Microscopy of spin hydrodynamics and cooperative light scattering in atomic Hubbard systems

David Wei

München 2023

Microscopy of spin hydrodynamics and cooperative light scattering in atomic Hubbard systems

David Wei

Dissertation
an der Fakultät für Physik
der Ludwig-Maximilians-Universität
München

vorgelegt von

Dawei David Wei

geboren in Karlsruhe

München, 8. August 2023

Erstgutachter:
Prof. Dr. Immanuel Bloch

Zweitgutachter:
Prof. Dr. Darrick Chang

Weitere Prüfungskommissionsmitglieder:
Prof. Dr. Ulrich Schollwöck
Prof. Dr. Dmitri Efetov

Tag der mündlichen Prüfung:
29. September 2023

Zusammenfassung

Wechselwirkungen zwischen quantenmechanischen Teilchen können zu kollektiven Phänomenen führen, deren Eigenschaften sich vom Verhalten einzelner Teilchen stark unterscheiden. Während solche Quanteneffekte im Allgemeinen schwierig zu beobachten sind, haben sich ultrakalte, in optischen Gittern gefangene atomare Gase als vielseitige experimentelle Plattform zur Erforschung der Quantenvielteilchenphysik erwiesen. In dieser Arbeit setzten wir ein Gitterplatz- und Einzelatom-aufgelöstes Quantengasmikroskop für bosonische ^{87}Rb Atome ein, um Vielteilchensysteme im und außerhalb des Gleichgewichts zu untersuchen.

Zunächst betrachteten wir den quantenmechanischen Phasenübergang zwischen dem suprafluiden und dem Mott-isolierenden Zustand im Bose-Hubbard-Modell, das nativ durch kalte Atome in optischen Gittern realisiert wird, und zeigten, dass sich die Brane-Parität eignet, um nichtlokale Ordnung im konventionell als ungeordnet erachteten zweidimensionalen Mott-Isolator zu identifizieren. Mithilfe eines mikroskopischen Ansatzes zur Realisierung einstellbarer Gittergeometrien und programmierbarer Einheitszellen implementierten wir Quadrats-, Dreiecks-, Kagome- und Lieb-Gitter und beobachteten die Skalierung des Phasenübergangspunkts mit der mittleren Koordinationszahl des Gitters.

In einem eindimensionalen Gitter untersuchten wir zudem den Hochtemperatur-Spintransport im Heisenberg-Modell, das durch Superaustausch in der Mott-isolierenden Phase eines zwei-Spezies Bose-Hubbard-Modells realisiert wurde. Durch Betrachten der Relaxationsdynamik eines als Domänenwand präparierten Anfangszustandes fanden wir eine superdiffusive Raum-Zeit-Skalierung mit einem anomalen dynamischen Exponenten von $3/2$. Anschließend untersuchten wir die theoretisch vorhergesagten mikroskopischen Voraussetzungen für Superdiffusion, indem wir reguläre Diffusion im nicht-integrablen, zweidimensionalen Heisenberg-Modell und ballistischen Transport für SU(2)-Symmetrie-gebrochene magnetisierte Anfangszustände nachwiesen. Weiterhin maßen wir die Zählstatistik der durch die Domänenwand transportierten Spins; die sich daraus ergebende schiefe Verteilung deutete auf einen nichtlinearen zugrundeliegenden Transportprozess hin, der an die dynamische Kardar-Parisi-Zhang Universalitätsklasse erinnert.

Mittels Mott-Isolatoren im Limit tiefer Gitter konnten wir darüber hinaus die durch Photonen vermittelten Wechselwirkungen in einem Spinsystem untersuchen, das aus zwei über einen geschlossenen optischen Übergang gekoppelten Zuständen besteht. Durch spektroskopische Untersuchung der Reflexion und Transmission konnten wir die direkte Anregung einer subradianten Eigenmode und kohärente Spiegelung beobachten, was auf die Realisierung einer effizienten, im freien Raum operierenden, paraxialen Licht-Materie-Schnittstelle hindeutet.

Abstract

The interplay of quantum particles can give rise to collective phenomena whose characteristics are distinct from the behavior of individual particles. While quantum effects are generally challenging to observe, ultracold atomic gases trapped in optical lattices have emerged as a versatile experimental platform to study quantum many-body physics. In this thesis, we employed a site– and single-atom–resolved quantum gas microscope of bosonic ^{87}Rb atoms to explore many-body systems in and out of equilibrium.

We first considered the ground-state quantum phase transition between the superfluid and Mott-insulating state in the Bose–Hubbard model, natively realized by cold atoms in optical lattices, for which we found brane parity to be suitable for detecting nonlocal order in the conventionally unordered two-dimensional Mott insulator. Using a microscopic approach to realizing tunable lattice geometries and programmable unit cells, we implemented square, triangular, kagome and Lieb lattices, and observed the mean-field scaling of the phase transition point with average coordination number.

In a one-dimensional lattice, we furthermore studied high-temperature spin transport in the Heisenberg model, realized by superexchange in the Mott-insulating phase of a two-species Bose–Hubbard model. By tracking the relaxation dynamics of an initial domain-wall state, we found superdiffusive space–time scaling with an anomalous dynamical exponent of $3/2$. We then probed the predicted microscopic requirements for superdiffusion, verifying regular diffusion for the integrability-broken two-dimensional Heisenberg model and ballistic transport for SU(2)-symmetry–broken net magnetized initial states. Subsequently, we measured the full counting statistics of spins transported across the domain wall; the resulting skewed distribution implied a nonlinear underlying transport process, reminiscent of the Kardar–Parisi–Zhang dynamical universality class.

Moving to Mott insulators in the deep-lattice limit, we could moreover study photon-mediated interactions on a subwavelength-spaced, array-ordered spin system consisting of states coupled by a closed optical transition. By spectroscopically probing the reflectance and transmittance, we demonstrated the direct excitation of a subradiant eigenmode and observed specular reflection, indicating the realization of an efficient free-space paraxial light–matter interface.

Contents

Chapter 1

Introduction

Since its inception more than a century ago, quantum mechanics has evolved into a central pillar of modern physics, providing a microscopic foundation to the understanding of a wide range of phenomena. The core challenge in studying the physics of interacting quantum particles lies in connecting the exponentially complex microscopic properties with the often simpler emergent behavior. A generic approach to answering such questions is given by quantum simulation, in which the abstract quantum-mechanical effects of an intractable system are implemented in a well-controlled alternate physical system [1]. Nowadays, theoretical models and experimental techniques in a variety of physical platforms have reached a level of maturity, in which desired quantum effects can often be engineered, solving problems ranging from quantum simulation and computation to communication and metrology [2–5]. The topic of this thesis is the platform of ultracold neutral atoms, which has become one of the leading systems for studying quantum physics [6], benefitting from high isolation, intrinsic indistinguishability, optical controllability and tunable interactions [7, 8].

Many-body physics with ultracold atoms

A major part of many-body physics is concerned with the equilibrium properties of an ensemble of particles; improving the understanding and control over these systems has been a driving force behind the advancements in the field of cold atoms. The study of many-body physics with dilute atomic gases in the quantum regime was enabled by the development of laser [9] and evaporative cooling, and began with the first realizations of atomic Bose–Einstein condensates (BECs) [10, 11] and degenerate Fermi gases [12]. Subsequent efforts focused on parametrically and adiabatically reaching the strongly correlated regime, where interaction effects compete with single-particle effects. For instance, the strong-interaction regime was reached in Fermi gases using Feshbach resonances to increase collisional interactions, and resulted in the observation of the crossover between BEC and Bardeen–Cooper–Schrieffer (BCS) pairing [13]. A complementary approach, most relevant for this thesis, employed optical lattice potentials, whose confinement allowed dilute atomic gases to undergo a quantum phase transition (QPT) between a superfluid (SF) and a Mott insulator (MI) phase [14]. These periodic systems give access to lower dimensionality and generically emulate condensed matter models; specifically, they realize bosonic or

fermionic Hubbard models [15], whose strong-interaction limit furthermore enabled the exploration of quantum magnets [16]. The use of static or driven optical lattices with more complex geometries [17–19] moreover enabled band engineering and the study of topological and frustration physics [20, 21].

The introduction of quantum gas microscopes (QGMs) [22–28] revolutionized experimental many-body physics, enabling projective Fock-basis measurements of the entire atomic Hilbert space using single-site– and single-atom–resolved imaging [29]. These techniques enabled the direct detection of quantum fluctuations of the atomic occupation or spin [30–36] and the observation of order with multi-point correlators [31, 37–39]. The high resolution provided by QGMs further allowed for single-site–resolved programmable potential shaping [40], granting local control for quantum-state and Hamiltonian engineering. These advances gave rise to the preparation of local excitations [41, 42], as well as the microscopic characterization of entanglement and emergent quasiparticles [43–46].

The well-isolated nature of ultracold atomic systems also lends itself well to the study of Hamiltonian quantum non-equilibrium phenomena, in which the many-body dynamics of interacting particles, typically prepared in states far from the ground state, are measured. A central question in this context relates to quantum thermalization and the breaking of ergodicity in the dynamical evolution of a non-equilibrium initial state [47–49]. Notably, this occurs in integrable models [50, 51], which feature extensive conservation laws, in many-body localized models [52, 53], in which disorder prevents thermal relaxation, or in models with fragmented Hilbert spaces [54–56], which give rise to strongly initial-state–dependent dynamics. Non-equilibrium dynamics is often studied in the context of atomic or spin transport phenomena, being most relevant for condensed matter systems [57], whereby the connection between microscopic properties and the emergent macroscopic behavior is of interest. In particular, this encompasses probing the dynamical scaling and possibly universal behavior of the arising hydrodynamics [58–62]; certain interacting quantum models display anomalous, i.e., non-diffusive and non-ballistic behavior [63, 64], whose microscopic origins are yet to be understood.

While the aforementioned approaches are based on the motional degree of freedom (DOF) of the atoms, their electronic DOFs in the form of microwave (MW) and optical transitions have also been directly employed. Notably, the inherent quantization of individual atoms is suited for the experimental study of quantum optics, enabling observations such as photon anti-bunching or deterministic quantum teleportation [65, 66]. Quantum-optical systems comprising atoms [67] have continued to play a major role in studying the foundations of quantum mechanics [68], the generation of exotic quantum states of light [69, 70], or applications in quantum information processing [71, 72]. Another focus of investigation involves the investigation of atom–photon interactions in ensembles of many atoms, where coherence in the light scattering pro-

cess can reveal collective emission properties [73, 74]. While such measurements have been performed in disordered atomic ensembles, collective quantum optics in spatially ordered systems, as enabled by ultracold atoms in optical lattices [75], has remained experimentally largely unexplored, and promises to give rise to rich physics [76].

1.1 Outline

In this thesis, we employ a QGM to experimentally study equilibrium properties of the Bose–Hubbard (BH) model, dynamical features of the isotropic Heisenberg (XXX) model and collective effects in many-atom light scattering. The emergence of this variety of quantum many-body models is summarized in Chapter 2, which furthermore reviews experimentally accessible observables and control parameters.

In Part I, we microscopically study the QPT of the two-dimensional (2D) BH model in different lattice geometries. We begin, in Chapter 3, by giving an overview of the experimental setup and describe the generation of programmable lattice structures, the extraction of site-resolved observables, the implementation of local control and the system calibration methods. We then introduce the BH model in more detail in Chapter 4, characterize quantum fluctuations and probe for nonlocal order in the MI phase in a variety of 2D lattice geometries.

In Part II, we consider anomalous spin transport in the one-dimensional (1D) XXX model and discuss its relation to the Kardar–Parisi–Zhang (KPZ) dynamical universality class. Chapter 5 serves as a theoretical overview of the properties of the KPZ class and provides an introduction to the main ideas of generalized hydrodynamics (GHD), used to describe transport in integrable systems. In Chapter 6, we focus on spin transport in generic Heisenberg (XXZ) chains and present measurements demonstrating superdiffusive dynamical scaling. We further explore the microscopic requirements to obtain superdiffusion and discuss the influence of initial states on far-from-equilibrium transport. Lastly, we exploit the single-atom sensitivity of our QGM to measure the full counting statistics (FCS) of the spin-transport problem, allowing us to characterize transport beyond a scaling exponent in Chapter 7.

In Part III, we study the cooperative optical response of an atomic array in the single-photon regime. We explain the effects of coherence in light-scattering processes in Chapter 8, highlighting the differences between array-ordered and disordered ensembles of dipole emitters. Subsequently, in Chapter 9, we present experimental measurements, showing a spectrally subradiant response and specular reflection. We discuss the role of positional order, cooperativity and the technical and physical limitations to mirror fidelity.

In Chapter 10, we summarize the results of the thesis, and give an outlook on possible extensions of the experiments shown in this thesis.

1.2 Publications

The following articles have been published in refereed journals in the context of this thesis. The articles most relevant for this thesis are shown in bold font.

- **Observation of brane parity order in programmable optical lattices.**
  D. Wei, D. Adler, K. Srakaew, S. Agrawal, P. Weckesser, I. Bloch, J. Zeiher.
  Phys. Rev. X **13**, 021042 (2023).

- A subwavelength atomic array switched by a single Rydberg atom.
  K. Srakaew, P. Weckesser, S. Hollerith, D. Wei, D. Adler, I. Bloch, J. Zeiher.
  Nat. Phys. **19**, 714–719 (2023).

- **Quantum gas microscopy of Kardar–Parisi–Zhang superdiffusion.**
  D. Wei, A. Rubio-Abadal, B. Ye, F. Machado, J. Kemp, K. Srakaew, S. Hollerith, J. Rui, S. Gopalakrishnan, N. Y. Yao, I. Bloch, J. Zeiher.
  Science **376**, 716–720 (2022).

- Realizing distance-selective interactions in a Rydberg-dressed atom array.
  S. Hollerith, K. Srakaew, D. Wei, A. Rubio-Abadal, D. Adler, P. Weckesser, A. Kruckenhauser, V. Walther, R. van Bijnen, J. Rui, C. Gross, I. Bloch, J. Zeiher.
  Phys. Rev. Lett. **128**, 113602 (2022).

- Microscopic electronic structure tomography of Rydberg macrodimers.
  S. Hollerith, J. Rui, A. Rubio-Abadal, K. Srakaew, D. Wei, J. Zeiher, C. Gross, I. Bloch.
  Phys. Rev. Research **3**, 013252 (2021).

- **A subradiant optical mirror formed by a single structured atomic layer.**
  J. Rui, D. Wei, A. Rubio-Abadal, S. Hollerith, J. Zeiher, D. M. Stamper-Kurn, C. Gross, I. Bloch.
  Nature **583**, 369–374 (2020).

- Floquet prethermalization in a Bose–Hubbard system.
  A. Rubio-Abadal, M. Ippoliti, S. Hollerith, D. Wei, J. Rui, S. L. Sondhi, V. Khemani, C. Gross, I. Bloch.
  Phys. Rev. X **10**, 021044 (2020).

Chapter 2

Quantum gas microscopy

Ultracold atoms trapped in optical dipole potentials have proven to be an outstanding experimental platform for studying quantum many-body systems [6, 77]. In particular, optical-lattice–based systems have given unprecedented insight into condensed matter phenomena [7, 14, 15, 78], given the engineered clean environment, intrinsic uniformity of the quantum particles studied and high isolation from external sources of decoherence. The advent of quantum gas microscopy has added valuable tools by providing access to observables on the single-atom level and by allowing for site-resolved control [22, 23, 29].

In this chapter, we will review the fundamentals of bosonic atoms in optical lattices and describe the main properties of the resulting Hubbard model. We then present effective models which emerge for extensions of the Bose–Hubbard (BH) model or when considering other aspects of the atomic system. Finally, we discuss the types of microscopically accessible observables and the role of local control in quantum gas microscopes (QGMs).

2.1 Ultracold atoms in optical lattices

Atoms in off-resonant light fields are subject to conservative optical dipole potentials [79], where the potential $V(\mathbf{r})$ is proportional to the light intensity $I(\mathbf{r})$. Optical lattices typically arise from periodic interference patterns formed by the coherent superposition of laser beams. These give rise to a periodic potential for the atoms, $V(\mathbf{r}) = V(\mathbf{r}+\mathbf{R})$, where $\mathbf{R}$ is a lattice vector. Typically, lattice depths, $V_0 \equiv V_{\max} - V_{\min}$, are expressed in units of the recoil energy, $E_{\mathrm{r}}^{a/\mathrm{nm}} = h^2/8ma^2$, where a denotes the lattice spacing and m the atomic mass.

2.1.1 From optical lattices to Hubbard models

Given a d-dimensional optical lattice potential, Bloch's theorem can be applied to obtain the band structure [80] with dispersion relation $E_{\mathbf{n},\mathbf{q}}$ and Bloch waves

$$\psi_{\mathbf{n},\mathbf{q}}(\mathbf{r}) = e^{i\mathbf{q}\cdot\mathbf{r}} u_{\mathbf{n},\mathbf{q}}(\mathbf{r}), \tag{2.1}$$

where $\mathbf{n}$ denotes the band indices, $\mathbf{q}$ the quasimomentum, and $u_{\mathbf{n},\mathbf{q}}$ a $\mathbf{R}$-periodic function. As we are interested in strongly correlated systems that interact via localized

interactions, we resort to the more suitable basis of Wannier states, which are exponentially localized around a given lattice site and form an orthonormal basis. Expressing the Wannier states as superpositions of the Bloch waves from a given band $\mathbf{n}$,

$$w_{\mathbf{n},\mathbf{R}}(\mathbf{r}) = \sum_{\mathbf{q}} c_{\mathbf{n},\mathbf{R}}(\mathbf{q})\psi_{\mathbf{n},\mathbf{q}}(\mathbf{r}), \tag{2.2}$$

the expansion coefficients $c_{\mathbf{n},\mathbf{R}}$ can be calculated using the notion of the Wannier states as eigenstates of the band-projected position operator along all reciprocal lattice vectors $\mathbf{G}_j$ [81], given by $\hat{P}_{\mathbf{n}}\,\hat{\mathbf{r}}\cdot\mathbf{G}_j\,\hat{P}_{\mathbf{n}}$. Here, $\hat{P}_{\mathbf{n}} = \sum_{\mathbf{q}}|\psi_{\mathbf{n},\mathbf{q}}\rangle\langle\psi_{\mathbf{n},\mathbf{q}}|$ denotes the projector onto the band $\mathbf{n}$, and the reciprocal lattice vectors are defined by $\mathbf{R}_i\cdot\mathbf{G}_j = 2\pi\delta_{i,j}$. In the following, we will restrict ourselves to the ground band, $\mathbf{n} = \mathbf{1}$. Note that the case of multiple sublattices (lattice sites within a unit cell) can be handled by constructing the Wannier states from a set containing multiple bands. For our purposes, we will treat multiple sublattices within the tight-binding approximation described below.

Having introduced the single-particle basis, we can expand the many-body Hamiltonian of collisionally interacting spinless bosons in the ground band Wannier states [82] as

$$\hat{H} = -\sum_{i,j} J_{i,j}\hat{a}_i^\dagger\hat{a}_j + \frac{1}{2}\sum_{i,j,k,l} U_{i,j,k,l}\hat{a}_i^\dagger\hat{a}_j^\dagger\hat{a}_k\hat{a}_l - \mu\sum_i \hat{n}_i, \tag{2.3}$$

with the hopping matrix elements $J_{i,j} = \int d^3r\, w^*_{\mathbf{R}_i}(\mathbf{r})(\hat{\mathbf{p}}^2/2m + V(\mathbf{r}))w_{\mathbf{R}_j}(\mathbf{r})$, the interaction matrix elements $U_{i,j,k,l} = g\int d^3r\, w^*_{\mathbf{R}_i}(\mathbf{r})w^*_{\mathbf{R}_j}(\mathbf{r})w_{\mathbf{R}_k}(\mathbf{r})w_{\mathbf{R}_l}(\mathbf{r})$, the momentum operator $\hat{\mathbf{p}}$, the bosonic creation (annihilation) operator $\hat{a}_i^\dagger(\hat{a}_i)$, and the number operator $\hat{n}_i$. The chemical potential is denoted by μ and the interaction parameter by $g = 4\pi\hbar^2 a_s/m$ with the s-wave scattering length a_s.

The Wannier-function overlap beyond nearest neighbors can be typically neglected for sufficiently deep lattices (e.g., $J_{i,i+2}/J_{i,i+1} \approx 0.1$ for $V_0 \approx 4E_\mathrm{r}$ in a one-dimensional (1D) sinusoidal lattice [83]), yielding the tight-binding approximation. We then obtain the standard BH Hamiltonian [84],

$$\hat{H}_\mathrm{BH} = -J\sum_{\langle i,j\rangle}\hat{a}_i^\dagger\hat{a}_j + \frac{U}{2}\sum_i \hat{n}_i(\hat{n}_i - 1) - \mu\sum_i \hat{n}_i, \tag{2.4}$$

where we sum over the nearest-neighbor (NN) sites i, j, and introduce the hopping energy $J = J_{i,j}$ and Hubbard interaction energy $U = U_{i,i,i,i}$. At high atomic densities, interaction-induced hopping processes can be of relevance, which are captured by the bond-charge tunnelling correction [85],

$$\hat{H}_\mathrm{BH} \mapsto \hat{H}_\mathrm{BH} - J_\mathrm{BC}\sum_{\langle i,j\rangle}(\hat{n}_i + \hat{n}_j - 1)\hat{a}_i^\dagger\hat{a}_j, \tag{2.5}$$

with hopping energy $J_\mathrm{BC} = U_{i,i,i,j}$.

2.1.2 Phases of the Bose–Hubbard model

The BH model constitutes a minimal quantum many-body lattice model of bosons which cannot be reduced to a single-particle problem [82] and features the celebrated Mott insulator (MI)–superfluid (SF) quantum phase transition (QPT) [86]. Despite its simplicity, the BH model is not analytically solvable and generally requires numerical approaches for quantitative predictions. In this section, we describe the fundamental properties of the phases in the BH model. In Part I we will perform more detailed analyses, consider nonlocal features and discuss the lattice-geometry dependence.

Superfluid phase

In the non-interacting limit, $J \gg U$, the ground state is given by a Bose–Einstein condensate (BEC), with all atoms populating the $\mathbf{q} = 0$ state of the ground band. For a large system with N atoms and a fixed density $\overline{n}_\gamma$ on each sublattice γ (as imposed by the ground band condition), the state factorizes into a product of local coherent states [6],

$$|\Psi\rangle_{U/J=0} \sim \exp\left(\sqrt{N}\,\hat{a}^\dagger_{\mathbf{q}=0}\right)|0\rangle \sim \prod_{i,\gamma}\left[\exp\left(\sqrt{\overline{n}_\gamma}\,\hat{a}^\dagger_{i,\gamma}\right)|0\rangle_{i,\gamma}\right]. \tag{2.6}$$

Thus, the number statistics of each lattice site follows a Poissonian distribution. At finite interaction strengths U, the distribution is modified as the repulsive interaction suppresses higher occupations.

Generally, the SF phase is characterized by a non-vanishing superfluid density and associated with off-diagonal (quasi-) long-range order [6, 87].

Mott-insulating phase

In the strongly interacting limit, $J \ll U$, the ground state at commensurate filling $\overline{n}$ is given by a tensor product of Fock states on the individual lattice sites,

$$|\Psi\rangle_{J/U=0} \sim \prod_{i,\gamma}\left[(\hat{a}^\dagger_{i,\gamma})^{\overline{n}}|0\rangle_{i,\gamma}\right], \tag{2.7}$$

and has vanishing number fluctuations. Finite values of the hopping energy, J, initiate number fluctuations in the form of particle–hole pairs, $\hat{a}^\dagger_{i,\gamma}\hat{a}_{j,\gamma'}$.

Typically, the MI phase is characterized by its incompressibility, $\partial n/\partial\mu = 0$, indicating the insensitivity of the total number of atoms [6, 84]. In contrast to this definition, which is based on the system response to external perturbation, a nonlocal order parameter has been devised which only depends on the given ground state itself [88–90], see Chapter 4.

System inhomogeneity

In actual experimental implementations of ultracold atoms in optical lattices, the available atom number is finite, so a confinement potential is required to limit the

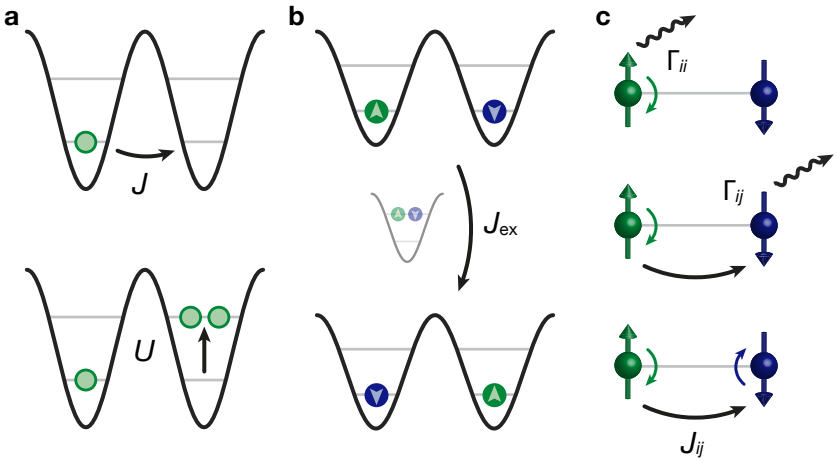

Figure 2.1: Quantum many-body models studied in this thesis. (**a**) The Bose–Hubbard (BH) model, studied in Part I, describes hopping between nearest-neighbor (NN) sites (top) and repulsive on-site interaction (bottom). (**b**) The Heisenberg model, studied in Part II, effectively describes the unity-filled strong-interaction limit of a two-species BH model. The coupling between NN spins (top, bottom) arises from spin exchange through virtual doublon formation (center). (**c**) Optical excitations (green) typically couple directly to propagating and thus dissipative electromagnetic modes (top). Cooperative atom–light interactions, studied in Part III, emerge at wavelength-scale interatomic distances, wherein coherent re-absorption processes occur, leading to cooperative dissipation (center) and energy shifts (bottom).

system size. For potential variations which are small compared to the ground band gap, the Wannier functions remain to be suitable wavefunctions for the tight-binding model, and the confinement manifests as a local potential shift ε_i with the correction Hamiltonian

$$\hat{H}_{\mathrm{BH}} \mapsto \hat{H}_{\mathrm{BH}} + \sum_i \varepsilon_i \hat{n}_i. \tag{2.8}$$

For spatially slowly varying confinement potentials, the local-density approximation (LDA) is applicable, in which we associate the local potential offset ε_i with a local phase corresponding to the uniform phase with chemical potential [15], $\mu_i = \mu - \varepsilon_i$. For a harmonic confinement potential—which the Gaussian beams forming the optical lattices realize—at small J/U, this gives rise to a concentrically layered coexistence of MI and SF phases, and thus results in atomic densities distributed in the shape of a wedding cake [23, 91].

System feature	Energy scale (h)
Hyperfine splitting	10^9 Hz
Zeeman splitting	10^7–10^8 Hz
Light scattering rate	10^6 Hz
Ground band gap	10^4–10^5 Hz
Hubbard interaction	10^2 Hz
Tunnelling	10^1–10^2 Hz
Spin exchange	10^0–10^1 Hz

Table 2.1: Typical energy scales of a ^{87}Rb quantum gas microscope. Ultracold atoms in optical lattices can be studied in a variety of independent contexts. Such experimental versatility is founded on, amongst others, the large separation of energy scales. The energies most relevant to this thesis are displayed in the table.

2.1.3 From optical lattices to spin models

In the previous section, we have focused on the motional state of the atoms. Taking into account the internal, electronic state, qualitatively different quantum many-body models can be realized. In the context of this thesis, models of relevance beyond the bare BH model are Heisenberg (XXZ) models and cooperative light scattering models. Illustrations of these models are depicted in Fig. 2.1. Note that these models operate on vastly different energy scales, see Tab. 2.1.

Heisenberg models (Part II)

Introducing an internal (pseudo-) spin state to the problem posed in Sec. 2.1.1, the single-species BH model, Eq. (2.4), is straightforwardly modified to yield the two-species BH model [92–95],

$$\hat{H}_{\mathrm{BH2}} = -J \sum_{\langle i,j\rangle,\sigma} \hat{a}^\dagger_{i,\sigma}\hat{a}_{j,\sigma} + \frac{1}{2}\sum_{i,\sigma} U_{\sigma\sigma}\hat{n}_{i,\sigma}(\hat{n}_{i,\sigma}-1) + U_{\uparrow\downarrow}\sum_i \hat{n}_{i,\uparrow}\hat{n}_{i,\downarrow} + \sum_{i,\sigma}(\varepsilon_{i,\sigma}-\mu)\hat{n}_{i,\sigma}, \tag{2.9}$$

for which we sum over the two spin states, $\sigma \in \{\uparrow,\downarrow\}$, and where $U_{\sigma\sigma'}$ indicates the Hubbard interaction between atoms with spins σ,σ'. In the limit of strong interactions, $J \ll U_{\sigma\sigma'}$, doublons can only form virtually, giving rise to perturbative spin exchange processes on top of regular tunnel coupling. Formally, Eq. (2.9) reduces to a bosonic t–J model [96]. When additionally demanding unity filling, $\hat{n}_{i,\uparrow}+\hat{n}_{i,\downarrow}=1$, we obtain the spin-1/2 XXZ model

$$\hat{H}_{\mathrm{XXZ}} = -\frac{J_{\mathrm{ex}}}{2}\sum_{\langle i,j\rangle}(\hat{S}^+_i\hat{S}^-_j + \Delta\hat{S}^z_i\hat{S}^z_j) + \sum_i h_i\hat{S}^z_i \tag{2.10}$$

with spin exchange energy $J_{\mathrm{ex}} = 4J^2/U_{\uparrow\downarrow}$, anisotropy $\Delta = U_{\uparrow\downarrow}/U_{\uparrow\uparrow} + U_{\uparrow\downarrow}/U_{\downarrow\downarrow} - 1$ and local effective magnetic field $h_i = 2(\varepsilon_{i,\uparrow} - \varepsilon_{i,\downarrow})$. The spin exchange operators are defined as $\hat{S}_i^+ = \hat{a}_{i,\uparrow}^\dagger \hat{a}_{i,\downarrow}$, $\hat{S}_i^- = \hat{a}_{i,\downarrow}^\dagger \hat{a}_{i,\uparrow}$, and the z-component as $\hat{S}_i^z = (\hat{n}_{i,\uparrow} - \hat{n}_{i,\downarrow})/2$. Note that, for the isotropic Heisenberg (XXX) model, $\Delta = 1$, the bond-charge correction of Eq. (2.5) reduces to a renormalization of the hopping energy J.

In Part II we will discuss the properties of the 1D XXZ model and focus on anomalous spin transport behavior.

Open long-range XY models (Part III)

More quantum models of interest arise when going even deeper into the atomic limit, where inter-site motional coupling is negligible, $J/U = 0$. To observe non-trivial effects away from the many-body low-energy regime of itinerant systems, we consider two states separated by a closed optical transition as a pseudo–spin-1/2 system. As this transition couples to the electromagnetic (EM) environment, we realize an open system of long-range–interacting dipoles, described by a master equation, $d\hat{\rho}/dt = -(i/\hbar)[\hat{H}, \hat{\rho}] + \mathcal{L}[\hat{\rho}]$, with the parameters in the rotating-wave approximation given by [76]

$$\begin{aligned} \hat{H} &= \sum_{i,j} J_{ij} \hat{\sigma}_i^+ \hat{\sigma}_j^- - \sum_i (\Omega_i \hat{\sigma}_i^+ + \Omega_i^* \hat{\sigma}_i^-), \\ \mathcal{L} &= \sum_{i,j} \frac{\Gamma_{ij}}{2} (2\hat{\sigma}_j^- \hat{\rho} \hat{\sigma}_i^+ - \hat{\sigma}_i^+ \hat{\sigma}_j^- \hat{\rho} - \hat{\rho} \hat{\sigma}_i^+ \hat{\sigma}_j^-), \\ J_{ij} &= -\mu_0 \omega_0^2 \mathbf{d}^* \cdot \mathrm{Re}\, \mathrm{G}(\mathbf{r}_i - \mathbf{r}_j, \omega_0) \cdot \mathbf{d}, \qquad J_{ii} = \Delta_i, \\ \Gamma_{ij} &= -2\mu_0 \omega_0^2 \mathbf{d}^* \cdot \mathrm{Im}\, \mathrm{G}(\mathbf{r}_i - \mathbf{r}_j, \omega_0) \cdot \mathbf{d}, \qquad \Gamma_{ii} = \Gamma_0. \end{aligned} \tag{2.11}$$

Here, $\hat{\sigma}_i^\pm$ indicate the local spin flip operators and $\hat{\rho}$ the atomic density matrix. The transition energy is denoted by $\hbar\omega_0$, its electric dipole moment as $\mathbf{d}$ with an associated single-body decay rate of $\Gamma_0/\hbar$, the EM Green's tensor as G and the Rabi frequency due to an external coherent drive field $\mathbf{E}$ (with a frequency detuning of Δ_i/h with respect to the bare transition frequency) as $\Omega_i/h = \mathbf{d} \cdot \mathbf{E}(\mathbf{r}_i)/h$. For our case of a three-dimensional (3D) vacuum as EM environment, G is given by the free-space Green's tensor,

$$\mathrm{G}(\mathbf{r}, \omega_0) = \frac{e^{ik_0 r}}{4\pi r} \left[\left(\frac{1}{k_0 r} + \frac{i}{k_0^2 r^2} - \frac{1}{k_0^3 r^3} \right) \mathbb{1} + \left(-\frac{1}{k_0 r} - \frac{3i}{k_0^2 r^2} + \frac{3}{k_0^3 r^3} \right) \frac{\mathbf{r} \otimes \mathbf{r}}{r^2} \right], \tag{2.12}$$

with wave number $k_0 = \omega_0/c$ and distance $r = |\mathbf{r}|$.

In Part III we will explore the weak-excitation limit of the model and discuss how structuring the atomic positions gives rise to novel light–matter interfaces.

2.2 Microscopic access

The development of QGMs has given unprecedented *in-situ* access to atomic observables and manipulation of atomic states [29]. In this section we give an overview over the observables and control parameters relevant to our experimental setup, with a primary focus on the models introduced in Sec. 2.1.

2.2.1 Experimental observables

The default observable of a QGM is the parity of the occupation on each lattice site, $\hat{s}_i = e^{i\pi(\hat{n}_i - \bar{n})}$, resulting from pair-wise losses caused by light-assisted inelastic collisions [97]. When working with lower-density clouds (i.e., typical $n_i < 2$), the local occupation, $\hat{n}_i \approx (1 + \hat{s}_i)/2$, can be deduced. Note that superlattice techniques in several QGMs have recently been implemented for absolute occupation measurements [33, 98, 99], see also Sec. 3.2.2. The local on-site potential ε_i (or the local chemical potential in LDA) can be characterized by analyzing the density distribution in the atomic limit [23].

In spinful systems, the local occupation of the hyperfine state (HFS) of interest can be measured by selective optical push-out of atoms in the respective other HFS [41]. At unity filling, as in the case of the effective XXZ model, we can assume that empty sites correspond to sites occupied by atoms in the other HFS prior to push-out. Hence, the z-projection of the local spin state is given by $\hat{S}_i^z = \hat{n}_i^{\uparrow} - \hat{n}_i^{\downarrow} \approx 1 - 2\hat{n}_i^{\downarrow}$. To measure the horizontal components of the spin state, $\pi/2$-pulses can be applied to rotate the spin axis of interest onto the z-axis. Generic measurements of $\hat{S}_i^{x,y}$ require a fully coherent system in the spin sector, which is not fulfilled on the time scales of the XXZ model in our implementation due to technical fluctuations of the absolute magnetic field. However, the ensemble-averaged horizontal component, $\langle \hat{S}_i^x \cos\theta + \hat{S}_i^y \sin\theta \rangle_\theta$, is only sensitive to the much smaller spatial *inhomogeneities* of the fluctuations, which can be well controlled.

The major benefit of a QGM lies in the fact that not only the mean value but also multi-point correlators of the operators specified above can be measured. This enables the observation of, e.g., full counting statistics (FCS) of site-resolved observables or fully resolved nonlocal correlations of spin or occupation parity. Even for observables that may be considered to be "global", the QGM has advantages. This includes, e.g., the total atom number, which can be accurately measured with single-atom precision, or the EM response of the atomic ensemble, like absorptance or reflectance, which are accessible with single-site resolution.

2.2.2 Experimental control

In this subsection, we summarize the model parameters controllable in our experiment. We elaborate on the experimental calibration procedures and accuracies in Sec. 3.3.

The extensive use of optical systems in experiments with ultracold atoms translates

the high precision of laser physics into widely tunable, clean and quickly switchable parameters of the BH Hamiltonian experienced by the atoms: While the scattering length of the ^{87}Rb atoms and therefore the Hubbard interaction, U, is by and large not tunable, the hopping energy, J, can be varied over an exponential scale by simply varying the power of the optical-lattice beam. This enables us to change the relevant BH energy ratio, J/U, and consequently also the spin exchange energy, J_{ex}, over multiple orders of magnitude. Another way to optically modify the Hamiltonian lies in the use of spatial light modulators (SLMs): By projecting spatially programmable intensity distributions of spectrally far detuned or fine-structure–resolved light, we can realize spin-independent local potentials, ε_i, or spin-dependent ones, h_i, respectively.

A complementary tool for generating spin-dependent potentials consists of magnetic fields generated in the far fields of (combinations of) coils: While optical fields allow for small-scale control, magnetic fields can be used for homogeneous global offset fields free of small-scale spatial inhomogeneities, $h_i = \text{const.}$, or for clean field gradients, $h_{i+1} - h_i = \text{const.}$

The electronic states are typically controlled by applying adiabatic or resonant EM pulses driving electric or magnetic dipole transitions. For the control of spin states in the XXZ model, the HFS can be manipulated by a microwave (MW) drive, acting as $\hat{S}_i^x$. Due to the narrow resonance feature, this technique cannot only be employed globally but also locally using optical addressing techniques. For the optical spin system, the quantization axis is set by a magnetic offset field, and the state can be globally driven by spectrally tunable laser beams, acting as $\hat{\sigma}^x$.

Part I

Bose–Hubbard models in variable lattice geometries

Chapter 3

Experimental platform

The experiments presented in this thesis were performed with a quantum gas microscope of bosonic ^{87}Rb atoms. In this chapter, we start by giving an overview over the experimental setup and describe the course of a typical sequence, available tools and the extraction of observables. We then describe the methods and the realization of programmable optical lattice geometries, based on the combination of structurally phase-stable lattices and dynamically variable unit cells. We conclude by summarizing optimization and calibration methods.

3.1 Experimental setup

The experimental setup builds on the work detailed in previous Ph.D. theses [101–107]. We first give an overview over the basic preparation sequence used in this setup and then discuss relevant technical details and upgrades implemented for the experiments described in this thesis. An overview of the level scheme of ^{87}Rb and the experimentally relevant transitions can be found in Fig. 3.1.

3.1.1 Experimental sequence

A typical experimental sequence has a duration of 25 s and can be separated into four main stages: the initial cooling and transport stage to prepare a cold atomic gas in the science chamber, an evaporative cooling stage to reach the ultracold quantum degenerate regime, the actual experimental sequence, and finally the detection stage.

Laser cooling, microwave evaporation and transport

The ^{87}Rb atoms start as a room-temperature gas and are loaded into a 2D$^+$ magneto-optical trap (MOT) within a vacuum chamber and form an atomic beam. This beam then travels through a differential pumping section into an auxiliary chamber at ultra-high vacuum, where the atoms are loaded into a three-dimensional (3D) MOT for 4 s. Following a compressed MOT stage, after which they are in the magnetic low-field–seeking $|\downarrow\rangle \equiv |F = 1, m_F = -1\rangle$ hyperfine state, the atoms are loaded into a magnetic quadrupole trap. Using a microwave (MW) knife on the transition to the high-field-seeking $|\uparrow\rangle \equiv |F = 2, m_F = -2\rangle$ state, we perform forced evaporative cooling for 6.5 s. We then load the atoms into an optical dipole trap (generated by an

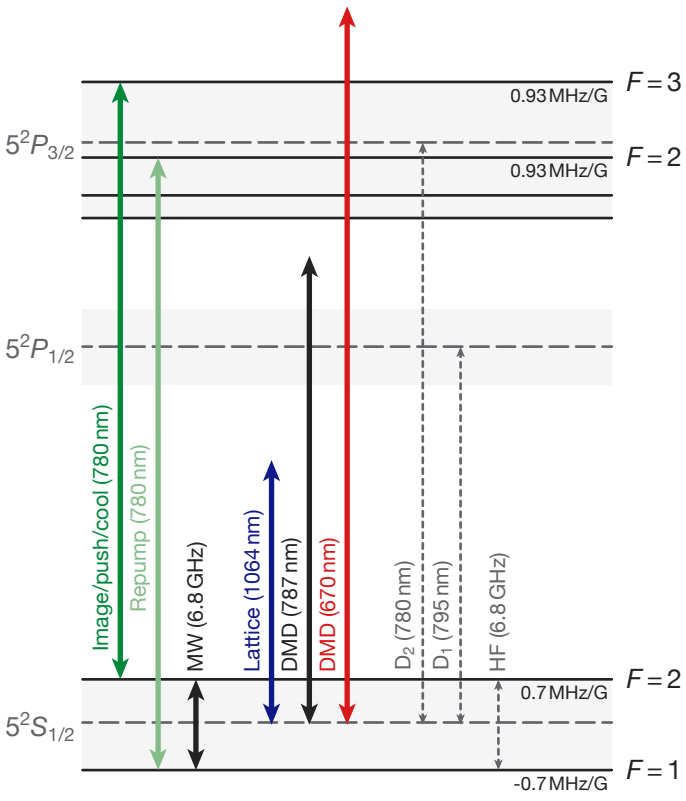

Figure 3.1: Electronic level scheme of ^{87}Rb. We show the most relevant hyperfine states (black) and their Zeeman shifts in the $5S$ ground and $5P$ excited state manifolds (gray) [100]. Transition frequencies are indicated by dashed arrows and experimentally driven transitions by solid arrows.

IPG YLR-50-1070-LP at a wavelength of 1070 nm) whose focus and thus trap position can be moved by a translation stage. Using this technique we transport the atoms into the science chamber in 2.5 s.

Preparation of a two-dimensional degenerate gas

From the transport trap, we load the atoms in the $|\downarrow\rangle$ state into a crossed dipole trap (CDT) formed by the incoming pass of the two horizontal lattice beams. All lattice beams are operated at a wavelength of 1064 nm (Coherent Mephisto master oscillator power amplifier (MOPA), 55 W model for horizontal lattices, 42 W model for vertical lattices). The retro-reflected beams are blocked by a mechanical shutter to prevent the formation of lattices. In the CDT, we perform forced evaporation by lowering the trap depth to about $2k_B \cdot 4\,\mu$K over 1 s. Using a MW sweep, we then transfer the atoms into the $|\uparrow\rangle$ state. Using a vertical magnetic gradient of 15 G/cm, we compensate the gravitational potential gradient to ensure that the atoms remain trapped in the center of the CDT, which reduces the beam alignment sensitivity. The sensitivity has increased compared to prior work in this setup, as we reduced the vertical waist of the horizontal lattice beams (see Sec. 3.2.2).

We load the atomic cloud into the mode-matched vertical physics lattice, which

yields substantial population in about 10 lattice layers. We then transfer the atoms into the smaller-waist vertical pinning lattice, and increase the magnetic gradient to 40 G/cm, corresponding to a Zeeman-shift–induced resonance detuning of 4.5 kHz between adjacent layers. In the tighter trap, the atomic cloud has a smaller horizontal extent, and therefore exhibits a more homogeneous magnetic field. Using a narrow MW sweep over less than 2 kHz, we transfer a single target layer back to the $|\downarrow\rangle$ state and remove the remaining atoms by a resonant push-out pulse on the D_2 cycling transition. This "slicing" procedure requires sub-10^{-5}–precise magnetic gradients which are created by a gradient coil driven by a unipolar precision current source (HighFinesse UCS 20A). The current, measured via a current transducer (Danfysik Ultrastab 768-60I), is furthermore stabilized with a feedback loop, with its setpoint fixed by a stable voltage source (Stahl Electronics DC 1-10). To compensate slow drifts, we use a secondary out-of-loop current transducer to independently measure the current with a 6-digit multimeter and use a digitally controlled voltage source—in parallel and weakly (gain of 10^{-4}) coupled to the voltage source—to correct the setpoint.

With all atoms populating a single two-dimensional (2D) layer of the vertical lattice, we perform a final 2 s evaporation stage: We introduce a horizontal magnetic gradient of 8.5 G/cm by generating a magnetic quadrupole field whose zero-field position is horizontally displaced from the cloud center. The quadrupole field is generated by reducing the vertical magnetic gradient and adding appropriate compensating offset fields. To improve evaporation efficiency and atom-number stability, we add a tight dimple trap by passing a laser beam (broadband laser diode at a wavelength of 850 nm) through the defocussed microscope objective. After this procedure, we end up with up to 3000 atoms in a nearly pure Bose–Einstein condensate (BEC) trapped in a single layer of the vertical lattice.

State preparation and experimental probe

In typical experiments, we then proceed to prepare a Mott insulator (MI) and initialize the system in a unity-filled product state. The exact sequence is described in the respective project-specific chapters. Details about the optical lattices can be found in Sec. 3.2.2.

When preparing larger system sizes, we first load the atoms back into the vertical physics lattice and optionally apply a local potential correction (see Sec. 3.1.3). We then adiabatically ramp up the horizontal lattices across the superfluid (SF)–MI phase transition into the atomic limit and obtain systems with 200–2000 atoms with typical fillings of 0.97–0.93. Starting from this state, local operations can be applied to manipulate occupation and hyperfine states of the atomic array (see Sec. 3.1.3).

Site-resolved fluorescence imaging

After conducting the experiments, the lattice powers are ramped up to a lattice depth of about $2000 E_r^{532} \approx k_B \cdot 200\,\mu K$. We shine in retro-reflected molasses beams in the

$\sigma^+\sigma^-$–polarization configuration along the horizontal axes and a spatially modulated vertical molasses beam. We collect the emitted fluorescence light through an objective with a numerical aperture (NA) of 0.68 and use an electron-multiplying charge-coupled device (EMCCD) camera (Andor iXon Ultra 897) for imaging. We obtain an overall photon detection efficiency of 7 %, accounting for the finite NA of the objective, losses along the optical path of 60 % and the quantum efficiency of the camera of 80 %. Using a piezo actuator (Physik Instrumente PIFOC P-726), the objective focus can be precisely optimized using feedback data from regularly run focus sequences [103]. With molasses temperatures far below the lattice depth, the hopping probability of less than 0.5 % (during an imaging time of 850 ms) is negligibly small. Due to light-assisted collisions, pairs of atoms get lost and the resulting fluorescence signal corresponds to the atom number parity of the lattice sites.

3.1.2 Reconstruction of local observables

In our experiment, local observables are generally restricted to measuring the atomic occupation of each lattice site. By performing quantum state manipulation and selective atomic push-out steps prior to imaging, further local observables like the hyperfine state can be deduced from the occupation data. For ultracold atoms in optical lattices, smaller lattice spacings tend to be advantageous due to overall higher energy scales, resulting in shorter required dynamics times and thus reduced decoherence. However, this comes at the expense that lattice spacings are close to or below the Rayleigh resolution of the imaging system.

The task of accurately reconstructing the occupation thus comprises deconvolving the image, accounting for prior knowledge of the lattice structure, and assigning the occupation of each site, i, by thresholding the deduced fluorescence emission state, F_i. Most reconstruction algorithms in quantum gas microscopy rely on iterative optimization of F_i to perform least-squares minimization of the deviation between convolved and actual image [23, 103] or use established algorithms like Wiener or Lucy–Richardson deconvolution [108]. Furthermore, following recent advances in machine learning techniques, alternative reconstruction approaches using both supervised [109] and unsupervised [110] learning have been realized, extending the reconstruction to account for nonlinearities in image formation.

In our case [111], we use a simple but computationally efficient approach to deconvolution based on linearly projecting the image onto the vector space spanned by the lattice sites [112]. This method has the advantage that it scales well to larger system sizes, is non-parametric and is robust due to its linearity. In the following, we first present the method itself and then describe how to extract the required parameters.

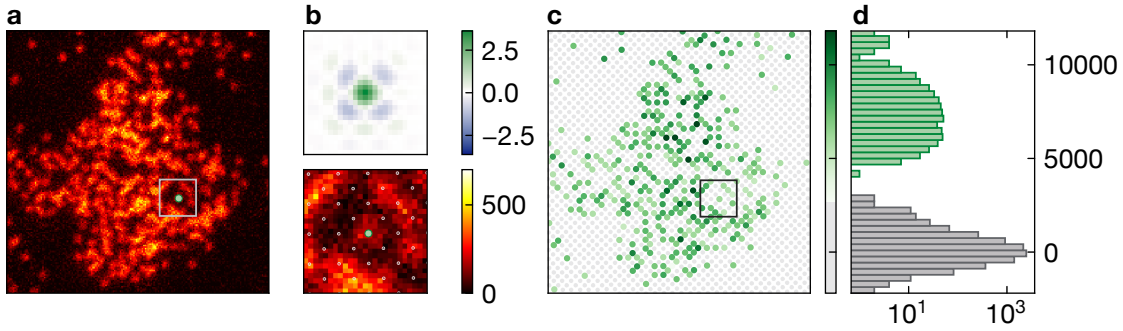

Figure 3.2: Reconstruction of the lattice site occupation. (**a**) The raw image is cropped in a region of interest (gray box) for every site to be reconstructed (green). (**b**) To obtain the fluorescence counts emitted by the given site, a scalar product is calculated between the projector (top) and the cropped image (bottom). (**c**) Repeating the process for every site yields a fully deconvolved image. The color map corresponds to the fluorescence counts emitted by the respective sites. (**d**) By thresholding the histogram of emission counts, we can separate empty (gray) from filled (green) sites.

Projection-based deconvolution

The molasses imaging technique used in our experimental setup can be largely regarded as incoherent microscopic fluorescence imaging since the fraction of coherently scattered light power is below 15 % even at highest atomic density [75]. Furthermore, image distortions within the area of interest are negligible, such that the point spread function (PSF) can be considered to be translationally invariant. Given a PSF, $p(\mathbf{r})$, this yields an image with a light distribution of

$$s(\mathbf{r}) = \sum_i F_i p(\mathbf{r} - \mathbf{r}_i), \tag{3.1}$$

given by the convolution of the PSF with the emitted light power, F_i, originating from a site located at $\mathbf{r}_i$.

Assuming the validity of Eq. (3.1), the linearity of the relation implies the existence of a kernel $k_i(\mathbf{r}) \equiv k(\mathbf{r} - \mathbf{r}_i)$, which serves as an inverse of the PSFs, such that $\int k_i(\mathbf{r}) p(\mathbf{r} - \mathbf{r}_j)\, d^2r = \delta_{ij}$. The application of the kernel to the image,

$$F_i = \int k_i(\mathbf{r}) s(\mathbf{r})\, d^2r, \tag{3.2}$$

then performs the deconvolution onto the space of lattice sites.

In practice, the fluorescence images $\tilde{S} \in \mathbb{R}^{\tilde{M}}$ are discretized with 8 px/µm, with the total number of pixels $\tilde{M}$ and with the magnification chosen as a compromise between resolution and signal-to-noise ratio (SNR) at low light levels. Hence, each lattice

site is only covered by a few pixels and a naive discretization of Eq. (3.2) becomes insufficient. With knowledge of the exact coordinate transformation between lattice sites and image pixels (for the extraction method, see the following subsection), the site position can be located inside a pixel with subpixel precision. The discretized PSF for each site, $P \in \mathbb{R}^{N\times M}$, is thus calculated by integrating the continuous PSF over the area of pixel m, $P_{j,m} = \int_{\mathcal{A}_m} p(\mathbf{r} - \mathbf{r}_j)\, d^2r$. N and M denote the number of lattice sites and camera pixels inside a region of interest (ROI) covering the vicinity of the site to be reconstructed. The projection kernels can then be obtained by calculating the Moore–Penrose inverse of the PSF matrix, $K = (P^{-1})^T$. The image projection onto site j is thus given by $F_j = S \cdot K_j$, with $S \in \mathbb{R}^N$ denoting the image cropped to the ROI. Repeated application of this procedure yields a full reconstruction of the emission state for each lattice site j (see Fig. 3.2).

The computationally most expensive step consists of calculating the matrix inverse to obtain the projection kernel. However, by exploiting the translational invariance of lattice and image, we can pre-calculate one kernel for each fractional position of the site center within a pixel; in our case we subdivide the pixel in 5×5 subpixel positions. For reconstructing a given site, we first determine the site's pixel and subpixel position, and choose the appropriate pre-calculated kernel for projection. The computational complexity for the projection step thus reduces to $\mathcal{O}(MN)$. For the 170×170 sites we choose to reconstruct for every image, and a kernel size of $M = 61 \times 61$, reconstruction times are reduced to about 100 ms.

Note that this reconstruction method works well in our setup featuring a Rayleigh resolution of $0.61\lambda/\mathrm{NA} = 700\,\mathrm{nm}$ and lattice spacings of $a = 532\,\mathrm{nm}$ or $752\,\mathrm{nm}$ (see Sec. 3.2.2). However, for potential technical upgrades discussed in Sec. 9.3 with lattice spacings of 370 nm, the assumption of linear image formation will likely be invalid, such that reconstruction might require nonlinear optimization approaches.

Extracting PSF, lattice orientation and lattice phase

The extraction of subpixel-resolved PSFs and coordinate transformations between lattice sites and camera pixels follows Ref. [103]: From images of hot and dilute clouds, we fit the center positions of each isolated atom. By aligning and averaging five-fold supersampled atom images with linear interpolation, we obtain the subpixel-resolved PSF. For determining the coordinate transformation parameters, we calculate the histogram of positions of the fitted site centers projected onto the lattice axes. By maximizing the histogram contrast between the positions in and out of the lattice phase, we obtain the optimum magnification and lattice angles with per mill precision.

While PSF and lattice orientation are long-term stable, the lattice phase can vary on the 10 min time scale due to thermal drifts. Every image therefore requires a subpixel-precise determination of the lattice phase. Contrary to common approaches for lattice spacings below the diffraction limit, where the center position of isolated atoms is fitted [103, 110], we exclusively make use of the kernel projection method. We

first subdivide the image into 8×8 subimages and calculate the variance over these subimages. By choosing the subimage with the maximum variance, we select the part of the image with highest dynamic range, which contains edges favorable for lattice phase detection. Optimizing over subpixel shifts, we then reconstruct the subimage and maximize the variance of the *projected* image. A higher variation of the projected emission suggests a higher contrast between filled and unfilled lattice sites, and serves as a proxy to determine the best subpixel shift and thus the lattice phase.

3.1.3 Potential projection using digital micromirror devices

The single-site resolution provided by the high-resolution objective can not only be used for detection but also for local control. Imaging a given light distribution through the objective allows us to project site-resolved optical dipole potentials in the atomic plane. Using spatial light modulators (SLMs), this light distribution can furthermore be programmatically and dynamically controlled. Such local control techniques can be classified in three main categories: sequential projection of a focussed beam [40], phase- or amplitude-SLM–based holography [42, 113], or amplitude-SLM–based direct imaging [35, 41, 114].

In our experiment, we employ a digital micromirror device (DMD) (Texas Instruments DLP Discovery 4100) in the direct-imaging configuration depicted in Fig. 3.3, which allows for generating both large- and small-scale potentials. The DMD consists of an array of 1024×768 micromirrors with a pitch of 13.68 µm, which can be individually programmed and quickly switched between two reflection states ($\pm 12°$). To generate gray-scale values from binary reflection states, we set the imaging system to have a 200-fold demagnification such that multiple DMD pixels illuminate each lattice site. By performing Floyd-Steinberg dithering [115] to binarize the reflectivity, followed by spatial filtering in the Fourier plane of the first demagnifying telescope, we obtain percent-level grayscaling [116]. After passing through a relay telescope and transmitting through a dichroic mirror, the DMD light is imaged into an intermediate image plane of the microscope imaging path through which it is projected onto the atoms. Its programmability makes the DMD a versatile tool, both for the manipulation of the hyperfine state (HFS) via MW addressing methods [40] as well as the occupation state via (HFS-independent) gray-scale potentials [117].

Spin addressing

When working with the internal degree of freedom (DOF) of the atoms, we typically restrict ourselves to the two stretched states $|\uparrow\rangle \equiv |F = 2, m_F = -2\rangle$ and $|\downarrow\rangle \equiv |F = 1, m_F = -1\rangle$. This spin-state combination is advantageous as it realizes a two-body–collisionally stable system [118], and is convenient as the $|\uparrow\rangle$ state can be cleanly pushed out via the closed D_2 transition.

Addressing the spin DOF of the atoms requires the projected light to induce a

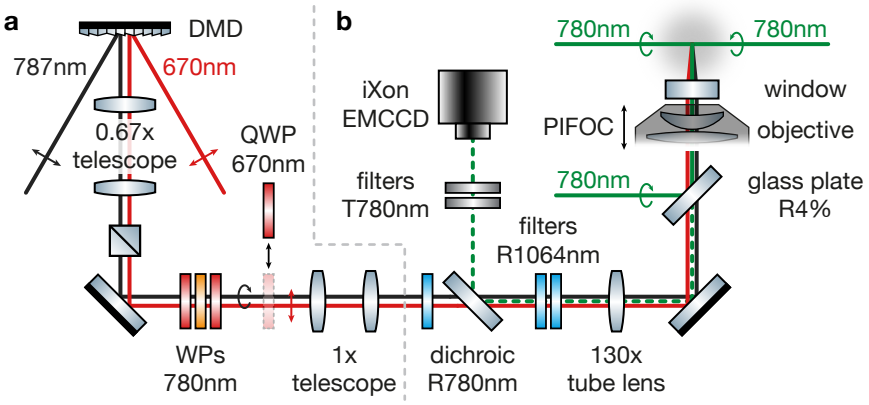

Figure 3.3: Imaging and DMD setup. (**a**) The DMD beams for both the spin-dependent (787 nm, black) and spin-independent (670 nm, red) potentials are linearly polarized and collimated. The beams are then combined by sending them to the DMD from opposite sides. After passing a first demagnifying telescope, they pass a stack of 780 nm quarter-wave plates (QWPs) (red) and half-wave plates (orange), generating σ^- polarization for the 787 nm beam. To minimize differential light shifts due to the 670 nm beam, an additional QWP can be mechanically flipped into the beam path to maintain linear polarization. Via a relay telescope, the DMD image is projected onto an intermediate image plane corresponding to the fluorescence camera position. After transmitting through a dichroic filter, the DMD light follows the imaging beam path in reverse to reach the atoms. (**b**) For fluorescence imaging, the horizontal and vertical molasses beams (780 nm, solid green) illuminate the atoms (gray-shaded area). The scattered photons (dashed green) are imaged via a high-resolution imaging system onto an EMCCD camera. Two 1064 nm-blocking short-pass filters (blue) were installed to prevent Lattice 3 light from continuing along the imaging beam path (see Fig. 3.6 for the lattice setup). Two 780 nm band pass filters (gray) in front of the camera additionally suppress photons from undesired wavelengths. For the most sensitive measurements, an additional 1064 nm short-pass filter was placed behind the dichroic splitter to guard against stray light originating from the nearby transport-trap laser.

differential light shift between the HFSs. For this purpose, we send in laser light at a wavelength between the D_1 and D_2 lines (Toptica TA pro 780) and can realize differential light shifts between 20 kHz for small-scale patterns and 200 kHz for large-scale patterns. At the position of the atoms, the beam has a (demagnified) Gaussian beam waist of 16.2 µm. Depending on the exact wavelength and polarization, configurations with particularly interesting properties can be generated. This includes a "tune-out" configuration at a wavelength of 787.5 nm and σ^- polarization, where the $|{\downarrow}\rangle$ state does not experience a potential at all [119], and an "anti-magic" configuration at 788.7 nm and σ^+ polarization, where the two spin states are subjected to mutually

inverted potentials.

To prepare local HFSs of arbitrary spatial pattern, we resort to a MW addressing approach [40]. We project a uniform amount of light on the sites to be addressed; due to the differential light shift, the MW resonance of the HFS transition is shifted on the addressed sites. By driving a global MW sweep, only the selected atoms are transferred into the other spin state. For patterns with only few addressed sites, we typically transfer the atoms on the illuminated (and thus resonance-shifted) sites, while for large-scale patterns we usually transfer the non-illuminated sites as their resonance location tends to be more uniform.

Furthermore, making use of the HFS-selective D_2 push-out, we can convert the prepared spin pattern into an occupation pattern, giving us additional access to locally controlling the "charge" DOF of an atomic array. By projecting such a differential–light-shift pattern during quantum evolution, we can furthermore realize an effective local magnetic field in the spin DOF.

Potential engineering

While controlling the initial spin state is a crucial capability, it relies on prior preparation of unity-filling MIs. The achievable system size therefore depends on the overall trapping potential and is typically provided by the harmonic confinement of the Gaussian lattice beams. Therefore, the capability to generate programmable spin-*independent* potentials is important for not only larger but also more consistently filled systems, and for well-defined system boundaries. Careful shaping of the local potential has been furthermore demonstrated to lower the entropy in a targeted area of the system [120, 121].

The diffraction-limited demagnifying projection of the desired light distributions poses stringent requirements onto the imaging system. For coherent light sources, imperfections like partial reflections or scatterers in the optical elements give rise to speckles, which significantly deteriorate imaging quality. As these effects are reduced with incoherent light [122], we employ a temporally incoherent superluminescent diode source (Superlum SLD-260-UHP at a wavelength of 670 nm with a spectral full width at half maximum (FWHM) of 7 nm, amplification by Toptica BoosTA 670L), which—upon angled incidence on the DMD—is also spatially incoherent along one axis. This source illuminates the same DMD as the 787 nm spin-addressing laser, but is coupled in from the opposite reflection angle (the "off"-state), and thus follows the same achromatic imaging system. At the position of the atoms, the beam has a (demagnified) Gaussian beam waist of 15.7 µm. The objective is the sole non-achromatic element and has to be shifted by about 17 µm when employing 670 nm light. Due to its blue detuning with respect to the D_2 line, this setup is particularly well-suited to project system-confining boundary potentials.

3.2 Realizing dynamically variable lattice geometries

Variations in the lattice geometry of quantum systems can give rise to a series of exotic phenomena, ranging from topological band structures [123] to geometric-frustration–induced flat band [124] or quantum spin liquid [125] physics. Neutral atom quantum simulators have proven capable in realizing countless novel quantum effects; a major factor for their success can be attributed to the high degree of controllability enabled by optical dipole potentials underlying the experimental platform [79]. Manipulations in the light intensity translate directly to variations in the atomic potentials, allowing for customizable and scalable yet environmentally isolated potentials. Optical lattices arise through the interference patterns of laser beams, hence providing wavelength-scale modulations with paraxial optics, which results in clean realizations of periodic potentials. In experimental setups, the lattice beam combinations and layouts are carefully chosen to produce a specific interference pattern designed to realize a target geometry [126, 127]. In 2D lattices, for example, this approach has led to geometries beyond square lattices, including triangular [128, 129], honeycomb [17], kagome [18] and Lieb [130] lattices. While optical lattices benefit from their inherent homogeneity and stability, the static nature of a given beam layout restricts systems to fixed spatial geometries.

In order to achieve dynamical tunability, two main approaches have been devised: Firstly, arrays of optical tweezers can be generated with almost freely programmable geometries [131]. While these systems have become popular for studying many-body spin models, reaching the itinerant regime by means of tunnel-coupled tweezers has proven difficult for large arrays, as individual tweezers suffer from inhomogeneities and thus a formidable calibration overhead [132, 133]. Secondly, adding additional lattice beams gives rise to so-called superlattices [134]; by varying the relative beam intensities, effective lattice geometries can be parametrically varied. However, superlattice setups typically require technically complex active phase stabilization schemes [17, 135] and furthermore lack free dynamical programmability. In this section, we address both of these points and describe our solution to realizing passively phase-stable, tunable lattices in combination with freely programmable unit cells.

3.2.1 Structural phase stability of optical lattices

The superposition of laser beams with scalar fields (here we consider common polarization) $A_l(\mathbf{r}) \propto \exp[i(\alpha_l(t) + \mathbf{k}_l \cdot \mathbf{r})]$ forms interference patterns with intensity $I(\mathbf{r}) = |\sum_{l=1}^{n} A_l(\mathbf{r})|^2$. Structural phase stability is achieved when phase shifts $\alpha_m \to \alpha_m + \Delta\alpha$ only lead to a translation of a pattern $I(\mathbf{r}) \to I(\mathbf{r} - \Delta\mathbf{r})$, i.e., that the phase shift can be absorbed into a translation $\Delta\alpha = -\mathbf{k}_m \cdot \Delta\mathbf{r}$. Setting $m = 1$ without loss of generality (w.l.o.g.), this structural phase stability condition for plane-wave interference patterns

can be shown to be equivalent to [136]

$$\mathrm{rank}(\mathcal{K}) = \mathrm{rank}(\mathcal{K}|\vec{\alpha})\ \forall\vec{\alpha}, \tag{3.3}$$

with $\mathcal{K} = (\mathbf{k}_2 - \mathbf{k}_1, \ldots, \mathbf{k}_n - \mathbf{k}_1)^T, \vec{\alpha} = (\alpha_2 - \alpha_1, \ldots, \alpha_n - \alpha_1)^T$. The rank of $\mathcal{K}$ corresponds to the number of spatial dimensions d spanned by the modulation of the interference pattern, thus $\mathrm{rank}(\mathcal{K}) = d \leq n - 1$ and the full pattern phase can be parameterized with d translational DOFs, $\vec{\varphi}(\vec{\alpha}) \in \mathbb{R}^d$, derived from the bare plane-wave phases $\vec{\alpha}$. Two strategies for creating phase-stable interference patterns were identified in Ref. [136]: (i) minimal lattices using exactly $n = d + 1$ plane waves or (ii) retro-reflected folded plane waves.

We can extend the classes of structurally phase-stable lattices further by additionally considering incoherent combinations of multiple such interference patterns, $I_{\mathrm{tot}}(\mathbf{r}) = \sum_i I_i(\mathbf{r})$. Incoherent overlapping can be achieved due to the patterns having, e.g., different frequencies or mutually orthogonal polarizations. Formally, this "incoherent" phase stability condition can be expressed as follows: For a pattern translation $\Delta\vec{\varphi}$ of any pattern j (w.l.o.g. let $j = 1$), there exists a displacement $\Delta\mathbf{r}$ such that

$$I_{\mathrm{tot}}(\mathbf{r}; \vec{\varphi}_1^{(0)} + \Delta\vec{\varphi}, \vec{\varphi}_2^{(0)}, \ldots) = I_{\mathrm{tot}}(\mathbf{r} - \Delta\mathbf{r}; \vec{\varphi}_1^{(0)}, \vec{\varphi}_2^{(0)}, \ldots). \tag{3.4}$$

As the individual interference patterns $I_i(\mathbf{r})$ could *a priori* be rather complicated, simplifications of Eq. (3.4) are difficult. In the following, we discuss two approaches realized in our experiment, in which phase stability is based on common-mode phase drifts and drifts along translationally invariant directions.

Combined minimal lattices

In $d = 1$ dimensions, $n = 2$ counter-propagating beams trivially fulfill Eq. (3.3) and thus form a structurally phase-stable one-dimensional (1D) lattice. Being 1D, the translational DOF is scalar, $\vec{\varphi} \equiv \varphi$, and can be identified with the phase of the sinusoidal pattern $\varphi = \alpha_2 - \alpha_1$ ("lattice phase"). In a setup consisting of two mutually non-interfering 1D lattices, the total intensity is given by

$$I_{\mathrm{tot}}(\mathbf{r}) = \sum_i I_i \left(\frac{1}{2} + \frac{1}{2}\cos(\mathbf{k}_i \cdot \mathbf{r}_i - \varphi_i)\right). \tag{3.5}$$

A lattice phase shift $\varphi_j \to \varphi_j + \Delta\varphi_j$ can then be equivalently expressed as $\mathbf{k}_i \cdot \mathbf{r}_i \to \mathbf{k}_i \cdot (\mathbf{r} - \Delta\mathbf{r}_j)$. Hence, Eq. (3.4) is fulfilled, proving the structural phase stability of typical retro-reflected 2D optical lattices (see Fig. 3.4).

In contrast, if all four beams interfere with each other and the beams are not phase locked, Eq. (3.3) is not fulfilled, $\mathrm{rank}(\mathcal{K}) = d = 2 \neq \mathrm{rank}(\mathcal{K}|\vec{\varphi}) = 3$, and there is $3 - 2 = 1$ excess DOF. As an explicit example, consider the case of retro-reflected orthogonally crossing beams with a light field given by $A(x, y) \propto e^{iky} + e^{-iky} + e^{i\alpha}e^{ikx} + e^{i\alpha}e^{-ikx}$. The resulting intensity of $I(x, y; \alpha) \propto \cos 2kx + \cos 2ky + 4\cos\alpha\cos kx\cos ky$ thus realizes an interference pattern whose structure depends on α.

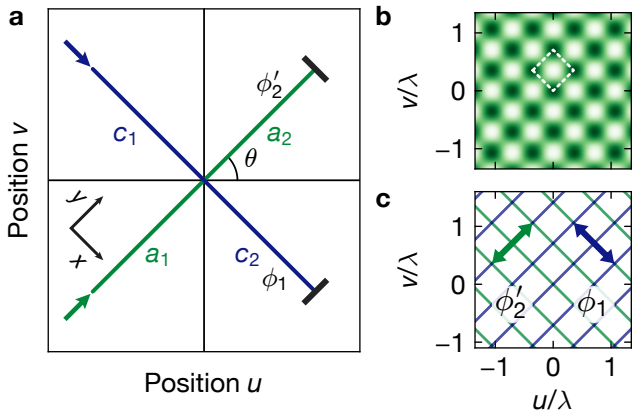

Figure 3.4: Square lattice beam layout. (**a**) Beam layout for mutually non-interfering 1D lattices (blue, green lines) intersecting at an angle of 2θ forming a 2D lattice. Light field amplitudes of the incoming pass, a_1, c_1, and the outgoing pass, a_2, c_2, retro-reflected from the mirrors are marked by black lines. The phases picked up in the retro-reflection path are denoted as ϕ_1, ϕ_2'. (**b**) Light intensity of the resulting square-lattice (light to dark color indicate low to high intensity). The ground band tunnel coupling (white dashed lines) can be tuned from pure 1D coupling to homogeneous 2D coupling by varying the beam power ratios or the beam intersection angle. (**c**) The colored lines indicate the potential minima of the respective 1D lattice. The arrows indicate how the lattices would shift when the marked phase changes, $\partial\Delta\mathbf{r}/\partial\phi_j$. The 2D lattice is structurally phase stable as phase changes only influence one lattice at a time and the resulting lattice shift occurs along the translationally invariant direction of the respective other lattice.

Tunable folded lattices

However, folding a lattice beam into the optical path of the other beam, realizes a bow-tie lattice [137] and reduces the number of phase DOFs. Generally, folded lattices (single beam intersecting multiple times and retro-reflected back through the same path) are structurally phase stable as they can be shown to fulfill Eq. (3.3) [136]. While the bow-tie lattice itself just realizes another square lattice, combining it non-interferometrically with a further 1D lattice gives rise to a highly versatile setup that allows us to qualitatively tune the lattice geometry exhibited by ground-band atoms [17, 135].

Concretely, we consider the setup depicted in Fig. 3.5a comprising lattice beams with the light fields given by

$$\begin{aligned} A_2(\mathbf{r}) &= a_1 e^{i\mathbf{k}_y\cdot\mathbf{r}} + b_1 e^{i\mathbf{k}_x\cdot\mathbf{r}+i\phi_2} + b_2 e^{-i\mathbf{k}_x\cdot\mathbf{r}+i\phi_2+2i\phi_1} + a_2 e^{-i\mathbf{k}_y\cdot\mathbf{r}+2i\phi_2+2i\phi_1} \text{ and} \\ A_1(\mathbf{r}) &= c_1 e^{i\mathbf{k}_x\cdot\mathbf{r}} + c_2 e^{-i\mathbf{k}_x\cdot\mathbf{r}+2i\phi_1+i\Delta\varphi}, \end{aligned} \tag{3.6}$$

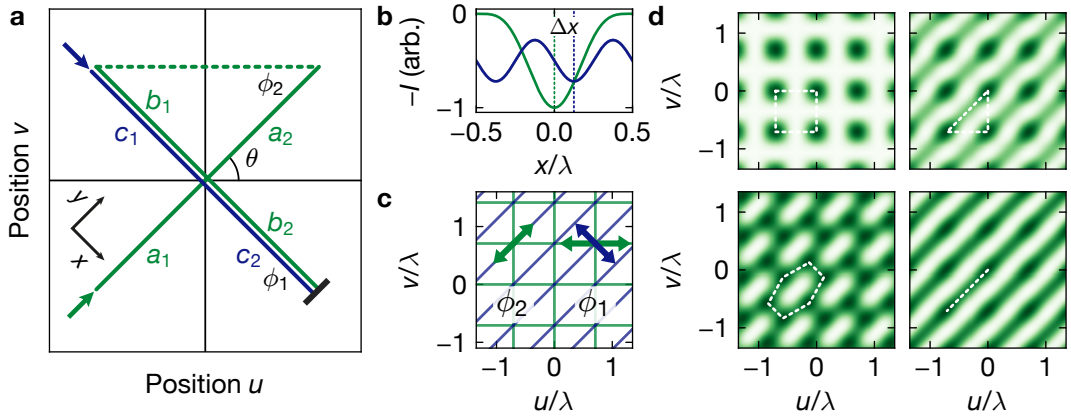

Figure 3.5: Tunable lattice beam layout and realizable geometries. (**a**) Passively phase-stable tunable 2D lattices can be formed by non-interferometrically combining a bow-tie lattice (green) with a 1D lattice (blue). Phase stability is retained for any light field amplitudes of incoming, a_1, b_1, c_1, and outgoing beams, a_2, b_2, c_2, and intersecting at an arbitrary angle θ. The translational degrees of freedom of the bow-tie lattice are the phases ϕ_1, ϕ_2. The 1D lattice shares a common phase ϕ_1 as both lattices are referenced to a common retro-reflection mirror. (**b**) There exists a third degree of freedom, the superlattice phase $\Delta\varphi$, that can be precisely and phase-stably controlled, as described in Sec. 3.2.2. $\Delta\varphi$ is defined as the phase difference between the two lattices along the cut $y = 0$, i.e., $\Delta\varphi \equiv 2\pi\Delta x/(\lambda/2)$. (**c**) The colored lines indicate the potential minima of the respective lattices. The arrows indicate the translational lattice shift upon phase drifts, $\partial\Delta\mathbf{r}/\partial\phi_j$. The 2D lattice is structurally phase stable as phase drifts are either common mode (ϕ_1) and/or occur along translationally invariant directions (ϕ_1 and ϕ_2). (**d**) Light intensity of selected lattices (light to dark color indicate low to high intensity). The beam parameters can be tuned to qualitatively change the tight-binding lattice geometry (white dashed lines). Realizable lattices include square lattices (top left), triangular lattices (top right), honeycomb lattices (bottom left), dimerized lattices or 1D lattices (bottom right).

where $\Delta\varphi$ indicates the superlattice phase, i.e., the phase difference between Lattice 1 (L1) and Lattice 2 (L2) illustrated in Fig. 3.5b. This yields an overall light intensity of

$$\begin{aligned} I(u,v) &= |A_1(u,v)|^2 + |A_2(u,v)|^2 \\ &= (a_1^2 + a_2^2 + b_1^2 + b_2^2 + c_1^2 + c_2^2) \\ &\quad + 2c_1c_2\cos[2k(u-u_0)\cos\theta - 2k(v-v_0)\sin\theta - \Delta\varphi] \\ &\quad + 2a_1a_2\cos[2k(u-u_0)\cos\theta + 2k(v-v_0)\sin\theta] \\ &\quad + 2b_1b_2\cos[2k(u-u_0)\cos\theta - 2k(v-v_0)\sin\theta] \\ &\quad + 2(a_1b_1 + a_2b_2)\cos[2k(v-v_0)\sin\theta] \\ &\quad + 2(a_1b_2 + a_2b_1)\cos[2k(u-u_0)\cos\theta] \end{aligned} \tag{3.7}$$

where we have defined $2ku_0\cos\theta = \phi_2 + 2\phi_1$ and $2kv_0\sin\theta = \phi_2$. Thus, the lattice potential only depends on a translated position $\mathbf{r} = (u,v) \to \mathbf{r} - \Delta\mathbf{r} = (u-u_0, v-v_0)$, which confirms that the lattice is structurally passively phase stable according to Eq. (3.4). To gain more intuitive understanding of the effects of phase shifts, we calculate the differential lattice translation given by

$$\frac{\partial k\Delta\mathbf{r}}{\partial\phi_2} = \begin{pmatrix} 1/\cos\theta \\ 0 \end{pmatrix} \text{ and } \frac{\partial k\Delta\mathbf{r}}{\partial\phi_1} = \frac{1}{2}\begin{pmatrix} 1/\cos\theta \\ 1/\sin\theta \end{pmatrix}, \tag{3.8}$$

which we visualize in Fig. 3.5c. Fig. 3.5d shows various optical lattice potentials realizable by varying the beam power ratios and/or the superlattice phase.

As an instructive example, we can consider the realization of triangular lattices in the tight-binding approximation using the topologically equivalent diagonal-neighbor (DN) tunnelling. At $\Delta\varphi = 0$, the effect of increasing the 1D lattice (L1) depth is to reduce nearest-neighbor (NN) tunnelling while the DN tunnelling is largely unaffected. By choosing suitable lattice power ratios, this realizes a ground-band triangular lattice.

3.2.2 Lattice setups

All lattices in our setup (see Fig. 3.6) have been chosen to fulfill the criteria for passive phase stability. In this subsection, we describe the lattice design considerations and properties, with more detailed technical information deferred to a future Ph.D. thesis [138].

Horizontal lattices

Both horizontal lattice beams are derived from a common 1064 nm laser (see also Sec. 3.1.1) with a linewidth below 1 kHz and thus have coherence lengths which are much larger than the dimensions of the experimental setup. The beams are frequency-detuned via acousto-optical modulators (AOMs) and guided through photonic-crystal fibers (PCFs) to the optical table.

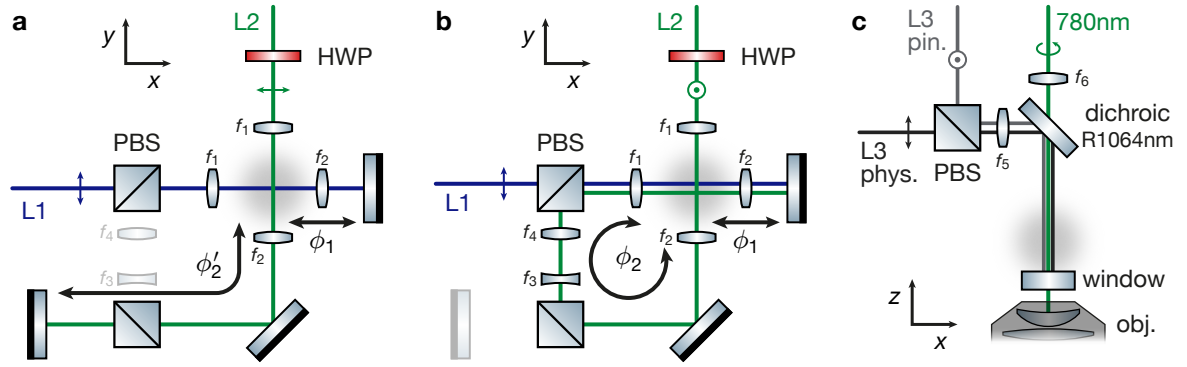

Figure 3.6: Horizontal and vertical lattice setups. (**a**) Square-lattice setup with a lattice spacing of $\lambda/2 = 532\,\text{nm}$ formed by the mutually non-interfering retro-reflected lattice beams L1 (blue) and L2 (green). The lattice beams are focussed onto the atoms with a $f_1 = 250\,\text{mm}$ and collimated with a $f_2 = 150\,\text{mm}$ lens. The colored arrows indicate the lattice beam polarization, chosen to be transmitting through the polarizing beam splitter (PBS). This setup realizes the lattice discussed in Fig. 3.4. (**b**) By rotating the half-wave plate (HWP), L2 is changed to out-of-plane polarization and reflects off the PBS. L2 exhibits four-fold interference, resulting in a square lattice with a spacing of 532 nm along the diagonals of the beam axes. To ensure equal beam sizes in the folded path, a telescope consisting of lenses $f_3 = -50\,\text{mm}$ and $f_4 = 75\,\text{mm}$ images the collimated L2 beam into the Fourier plane of the L1 focussing lens. By overlapping the mutually non-interfering L1 beam, complex ground band lattice geometries can be realized, ranging from 1D or square lattices to triangular or honeycomb geometries. This setup realizes the lattice discussed in Fig. 3.5. (**c**) The setup comprises two vertical lattice beams (L3), focussed onto the atoms with a $f_5 = 400\,\text{mm}$ lens. Most experiments are performed in the physics L3 (black), which has a larger waist for a reduced confinement potential. Fluorescence imaging is performed in the pinning L3 (gray) as it allows for deeper lattice depths for a reduced hopping rate during imaging. Both vertical lattice beams are retro-reflected at the vacuum window, coated for high reflection at the lattice wavelength. Analogous to the configuration (**b**), both lattice beams are referenced to a common retro-reflecting optical element, resulting in lattice phases that are passively stable to each other. An additional vertical resonant beam (sent to the atoms via a $f_6 = 300\,\text{mm}$ lens) is available for optical push-out and absorption imaging.

In the standard configuration of two mutually non-interfering, orthogonally crossing 1D lattices depicted in Fig. 3.6a, an optical square lattice with a spacing of $\lambda/2 = 532\,\mathrm{nm}$ arises. In comparison to the setup described in prior Ph.D. theses [101], both horizontal lattice beams were changed to a horizontal Gaussian beam waist of 330 µm. The reduced harmonic confinement potential then supports unity-filled MIs with larger system sizes. To minimize the laser-power demands during single-site–resolved imaging (which requires lattice depths of $2000E_\mathrm{r}^{532}$ per axis), we make use of requiring imaging in only a single 2D plane and introduced a strong ellipticity into the beam shape, resulting in a vertical Gaussian beam waist of 33 µm. Due to the ellipticity, the optical configuration for retro-reflection was changed such that the lens–mirror combination forms a $4f$-system which images the beam shape at the position of the atoms back onto itself.

The setup also supports a tunable bow-tie lattice configuration consisting of a folded L2 combined with a 1D lattice formed by L1. The optical layout was designed to allow for a flexible change of lattice configuration by simply rotating a half-wave plate (HWP) in the path of L2 before entering the vacuum chamber. To tune the superlattice phase $\Delta\varphi$, we make use of the long optical path length between atoms and retro-reflection mirror of $L = 300\,\mathrm{mm}$: As this distance corresponds to a number of standing wave nodes of $\varphi/2\pi = 2L/\lambda = 2L\nu/c$, we can tune the superlattice phase by varying the frequency difference $\Delta\nu$ between the lattices

$$\Delta\varphi = \frac{4\pi L}{c}\Delta\nu. \tag{3.9}$$

The lattice spacing is essentially unaffected by the frequency tuning as the relative frequency change is negligible, $\Delta\nu/\nu \sim \lambda/L \ll 1$. For our lattice parameters, we have a tuning slope of $\Delta\varphi/\Delta\nu = \pi/250\,\mathrm{MHz}$, which corresponds to a frequency range covered by AOM shifts. Note that although the frequency difference between the lattices can be tuned on an absolute scale, the absolute value of the superlattice phase has to be experimentally determined as optical coatings and imperfect focus overlap can lead to phase differences. Further care has to be taken to choose $\Delta\nu$ sufficiently large to avoid Raman transitions between Zeeman states, particularly during sweeps of the magnetic field.

Vertical lattices

Similar to the horizontal lattices, both vertical lattice beams are derived from a common 1064 nm narrow-band laser and are frequency-separated via AOMs. After passing separate PCFs and beam-shaping optics, the Lattice 3 (L3) beams are combined on a polarizing beam splitter (PBS) and reflected downwards into the vacuum chamber. Both beams are retro-reflected off the lower vacuum window, forming a vertical 1D lattice with a spacing of $\lambda/2 = 532\,\mathrm{nm}$.

The “physics” and “pinning” lattices have Gaussian beam waists of 350 µm and

75 µm, respectively, with their focus set to the plane of the reflective surface. As the atoms are located only $L = 5\,\mathrm{mm}$ above the window [101], Eq. (3.9) yields a tuning slope of the differential lattice phase of $\Delta\varphi/\Delta\nu = \pi/15\,\mathrm{GHz}$. Thus, typical AOM frequency shifts do not significantly affect the differential lattice phase, $\Delta\varphi$. A more important effect is related to the focus-induced Gouy phase, $\psi_\mathrm{G}(z) = \arctan z/z_R$, with the Rayleigh length z_R. While negligible for the large physics L3, we expect a phase shift for the pinning L3, resulting in a differential lattice phase of $\Delta\varphi = 2\psi_{\mathrm{G,pin.}}(L) = 0.1\pi$. Thus, the shift is sufficiently small to allow for adiabatic loading between the two vertical lattices.

The vertical lattice beams are furthermore of central importance for the atomic cloud shape, as they are largely responsible for the confining potential. For MIs loaded in the pinning L3, the confinement is harmonic and the position drifts with the beam alignment over a range of few micrometers. Hence, unity-filled MIs are circular with radii varying depending on the loaded atom number, with the maximum atom number of about 250 atoms limited by said harmonic confinement. Since the physics L3 has a substantially larger beam waist, we would expect it to feature strongly reduced harmonic confinement and thus much larger system sizes. However, (in our setup specifically) it turns out that there exist scatterers on the lower window which retro-reflects the vertical lattice beams. This leads to the formation of speckles with peak-to-peak intensity variations of up to 3 %—which correspond to the Bose–Hubbard (BH) energy scale—and a typical size of 10 µm, resulting in unity-filled MIs of similar size. Note that due to the small distance between the atoms and the window, the speckle pattern is largely insensitive to the small day-to-day drifts of the L3 alignment. By substantially beam-walking the lattice beam, a speckle potential minimum can be aligned to be centered with respect to the objective and camera. In this configuration, experiments can be performed in just the physics L3 confinement potential as long as evolution times are sufficiently short and tunnelling of atoms into other speckle potential minima can be neglected. Alternatively, the confinement potential can also be tailored to specific use cases, see Sec. 3.3.2.

3.2.3 Characterization of lattice phase stability

Having described the theoretical lattice design considerations in Sec. 3.2.1 and the experimental setup in Sec. 3.2.2, we characterize the horizontal lattice performance in this section.

Absolute lattice phase

While our lattices are structurally phase stable, the translational DOFs lead to drifts of the absolute lattice phase, as discussed in Sec. 3.2.1. The absolute phase depends on the optical path length between atoms and (retro-)reflection mirrors. Using our reconstruction method, we extract the lattice phase from each single-site–resolved

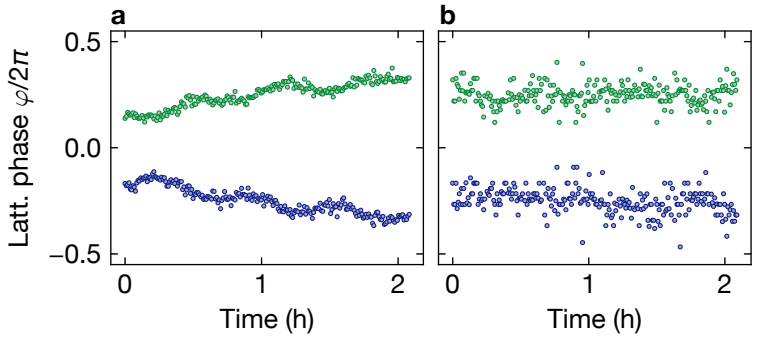

Figure 3.7: Absolute lattice phase stability. (**a**) For the 532 nm lattice, the absolute phase of both Lattice 1 (blue) and Lattice 2 (green) is shot-to-shot stable and drifts over time due to temperature variations. (**b**) For the 752 nm lattice, the absolute phase along both the u (blue) and v (green) axes varies significantly more. We attribute this behavior to the fact that the retro-reflection optical path is considerably longer and comprises more mirrors, which are susceptible to drifts. Nevertheless, typical shot-to-shot fluctuations occur below 50 nm and are sufficiently stable for DMD projection.

image to analyze the long-term stability of the absolute phase (see Fig. 3.7).

Generally, the absolute phase jump between subsequent shots is small for both lattices, indicating sufficient stability, e.g., for DMD projection purposes. Apart from uncontrolled long-term drifts, we can additionally observe drifts with periodicities of about 30 min. These can be correlated to the temperature drifts on the experimental table, indicating the importance of a stable thermal environment.

Superlattice phase

In the 752 nm lattice, the superlattice phase $\Delta\varphi$ is much more critical to realizing tunable lattice geometries. For the superlattice phase measurements shown in Fig. 3.8, we amplitude-modulate L1 within a deep L2 potential near the upper p-band resonance frequency. Due to the weak single-particle drive in an isolated system, we analyze the response assuming a two-level model with coupling Ω and modulation-frequency detuning Δ. This model yields a mean excited-state population of $P_e(\Omega,\Delta) = 2/(4 + \delta^2 + \sqrt{\delta^2(4+\delta^2)})$, with $\delta = \Delta/\Omega$. Close to the superlattice in-phase condition, $\Delta\varphi = 0$, the coupling is proportional to the superlattice phase, which we calculate from the band structure results. Considering the long and weak drive, we assume that Gaussian fluctuations in the superlattice phase ($\propto \sigma_\Omega$) and in the lattice depth ($\propto \sigma_\Delta$) dominate the shape of the resonance. Thus, the excitation probability on resonance is given by the two-fold convolution over the fluctuations, yielding

$$\overline{P}_e(\Omega) \sim 1 - \int f_{\mathcal{N}(\omega,\sigma^2)}(x) e^{x^2} \mathrm{erfc}|x|\, dx, \tag{3.10}$$

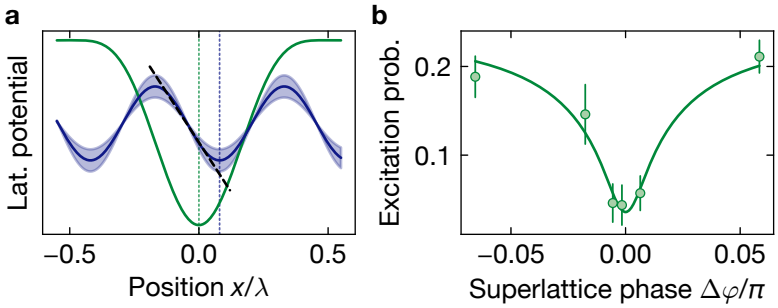

Figure 3.8: Superlattice phase stability. (**a**) The superlattice phase, $\Delta\varphi$, can be precisely calibrated by amplitude-modulating the 1D lattice, Lattice 1 (blue solid), near the band gap frequency of a much deeper bow-tie lattice, Lattice 2 (green solid). Single-band excitations require dipolar modulation (black dashed), which is minimal when the lattices are in phase ($\Delta\varphi = 0$). The vertical dotted lines represent the potential minima (and thus phase) of the respective lattices. (**b**) Single-band amplitude-modulation spectroscopy probing the resonant band excitation probability at the respective superlattice phase. The solid line shows a fit from which we extract a superlattice phase stability of $\sigma_{\Delta\varphi} = 0.01(1)\pi$.

where erfc denotes the complementary error function, and $f_{\mathcal{N}(\omega,\sigma^2)}$ the probability distribution of a normal distribution with center $\omega^2 = 2\Omega^2/\sigma_\Omega^2$ and variance $\sigma^2 = \sigma_\Omega^2/2\sigma_\Delta^2$.

At a L2 depth of $V_2 = 185(5)E_r^{752}$, where all dynamics in the lattice is frozen and where we can separate the lattice in its local potential wells, we modulated L1 at $V_1 = 5.0(2)E_r^{532}$ with a modulation depth of 25 % for 40 ms. As a spectroscopic signature, we measured the fraction of atoms remaining in the ground band after modulation by adiabatically lowering the lattice depth to $V_2 \approx 18E_r^{752}$, leading to the loss of atoms populating higher bands (see Fig. 3.8b). By fitting the functional shape of Eq. (3.10) to our experimental data and converting from coupling strength to the superlattice phase (for the given measurement parameters, band structure calculations yield $\Omega/\Delta\varphi \approx 660\,\mathrm{Hz}\,h/\pi$), this model allows us to extract a standard deviation (SD) of the superlattice phase of $\sigma_{\Delta\varphi} = 0.01(1)\pi$. Repeating this measurement weeks later gave a similar excitation probability, demonstrating the long-term stability of this lattice scheme.

3.2.4 Programmable unit cells

Our tunable lattice allows us to realize a wide range of tight-binding Bravais lattice geometries. An additional advantage lies in its enlarged lattice spacing of $\lambda/\sqrt{2} = 752\,\mathrm{nm}$, which relaxes resolution requirements for potential projection using the DMDs. In particular, the spin-independent DMD setup operating at 670 nm benefits from

DMD wavelength	Lattice spacing	Cross talk (single pixel/site pixels)		
		Single site	Stripe	Checkerboard
787 nm	532 nm	9/14 %	35/53 %	45/72 %
670 nm	532 nm	4/8 %	15/31 %	16/48 %
787 nm	752 nm	1/4 %	3/14 %	2/22 %
670 nm	752 nm	0/2 %	0/6 %	0/9 %

Table 3.1: Nominal cross talk of DMD projection. Assuming an ideal projective imaging system at a numerical aperture of 0.68, we compare the calculated ratio of light power (integrated over a $100 \times 100\,\mathrm{nm}^2$ area) at the nearest-neighbor site compared to the targeted site for different DMD wavelengths, lattice spacings and projected patterns. We assume fully coherent light and a Gaussian-approximated point spread function, and distinguish between a single active pixel and all pixels corresponding to a site active.

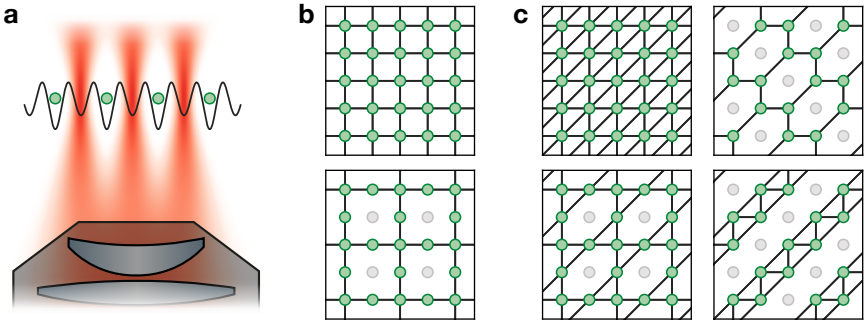

Figure 3.9: Programmable unit cells by site block-out. (**a**) Using the spin-independent DMD setup (see Sec. 3.1.3), we can project repulsive potentials (black lines) through the high-resolution objective on individual lattice sites in the 752 nm-spacing lattice, which prevent the population of the targeted sites (green circles). (**b**) We can project a block-out potential to remove a site (gray circles) from the ground-band Hilbert space. When using periodic block-out patterns, this corresponds to arbitrary unit cell engineering of tight-binding–coupled (black lines), occupiable lattice sites (green circles). Starting from a square Bravais lattice (top), we can create, e.g., a Lieb lattice (bottom). (**c**) Starting from a triangular Bravais lattice (top left), the same block-out pattern gives rise to a kagome lattice (bottom left). Other paradigmatic examples include the honeycomb lattice (top right) or a next-nearest-neighbor–coupled 1D chain.

substantially reduced cross talk, enabling us to project arbitrary single-site–resolved potential landscapes onto the atoms. In Tab. 3.1, we estimate the cross talk of coherent DMD-projected potentials based on the Gaussian-approximated theoretical PSF provided by our objective with a nominal NA of 0.68. Note that, firstly, the amount of cross talk strongly depends on the specific projected pattern, and, secondly, the partial spatial incoherence of the 670 nm will lead to further reduced cross talk. Indeed, when we project a checkerboard pattern with the 787 nm DMD setup in the 752 nm lattice, we can perform local MW spectroscopy (method described in Sec. 3.3.2) to measure the amount of cross talk to $21(4)$ %, in approximate agreement with Tab. 3.1.

As cross talk can be reduced to the percent level even for the most demanding high–spatial-frequency patterns, we do not have to restrict us to small projected potential depths, and instead project potentials with depths above the BH energy scale. In this case, addressed sites become energetically inaccessible to the atoms, effectively removing these sites from the Hilbert space of the tight-binding lattice. Hence, by projecting appropriate periodic block-out potentials, we obtain full control to engineer custom unit cells on top of base lattices with square or hexagonal Bravais symmetry. The block-out patterns required to realize some paradigmatic lattice geometries are shown in Fig. 3.9.

3.3 System optimization and calibration methods

Our experimental platform realizes a multitude of effective quantum many-body systems, see Sec. 2.1.3. However, the model parameters are often highly sensitive to the externally applied control parameters and therefore require direct calibration with the atoms. In this section, we describe optimization procedures and calibration methods to achieve this goal for the projects discussed in this thesis.

3.3.1 Lattice properties

The basis of all our experiments are the optical lattices. Thus, we require precise knowledge of the lattice properties; particularly, considering that the hopping energy depends exponentially on the lattice depth. We first discuss the calibration of the lattice depth itself, followed by an analysis of the lattice phases and a direct characterization of the hopping energy.

Lattice depth

A multitude of methods to measuring the depth of an optical lattice have been devised [139]. While many of these approaches are applicable for large atom numbers, our *in-situ* observables and small atom numbers benefit most from an approach based on parametric band excitation [140].

Due to the separability of our 532 nm lattice, we calibrate L1 and L2 independently

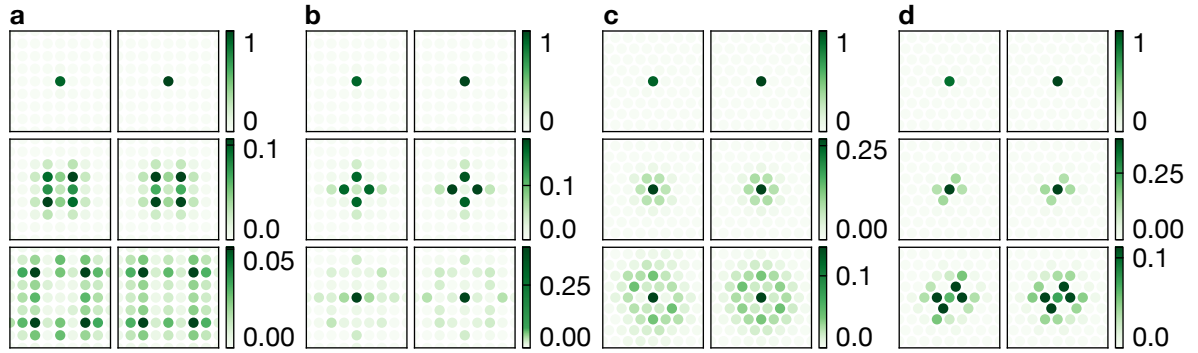

Figure 3.10: Quantum walks in various 2D lattice geometries. Evolution of atomic densities at times (top to bottom) $2J_h t/\hbar = 0.0, 1.8, 3.3$ for square base geometries (square (**a**) and Lieb (**b**) lattice) and $2J_h t/\hbar = 0.0, 0.9, 1.7$ for triangular base geometries (triangular (**c**) and kagome (**d**) lattice). We find good agreement between experiment (left) and simulation (right) and observe interference patterns characteristic of each geometry.

of each other. Starting from a 2D SF trapped in the pinning L3, we ramp up the 1D lattice to a given beam power. We then perform amplitude-modulation (AM) spectroscopy at a frequency resonant to the transition between first and third band corresponding to a depth of $10E_r^{532}$. By observing the atomic positional spread for varying beam powers, we find a resonance with which we calibrate a beam power to a $10E_r^{532}$ lattice depth. As the lattice depth varies linearly with the beam power, we extrapolate the $10E_r^{532}$ calibration point to other lattice depths. Compared to AM spectroscopy at deeper lattice depths, this protocol has the advantage that calibration is performed in the lattice depth regime typically of interest and with negligible interaction effects. An analogous sequence can be used to calibrate the vertical lattices.

In the 752 nm bow-tie L2, however, the potential is inseparable. We therefore create a unity-filled MI and increase the lattice depth to $180E_r^{752}$. Each lattice site can then be treated as an independent single-particle problem. We again perform AM spectroscopy between the s and d bands; after lowering the lattice depth, atoms in higher bands leave the system. Thus, the MI filling can be used as a spectroscopic signature. We can calibrate the lattice depth by identifying the two outer d band resonances.

These lattice AM spectroscopic methods allow us to calibrate the lattice depths with typically 1–2 % accuracy. Using the lattice depth, we then use band structure calculations to deduce the BH parameters for hopping energy and interaction energy.

Geometry	Lattice 1	Lattice 2	Axis	Calculations	Fit
Square	–	$10.0(3)E_r^{752}$	J_h/h	32.9(9) Hz	31.2(6) Hz
			J_v/h	30.8(9) Hz	28.8(6) Hz
Triangular	$8.5(3)E_r^{532}$	$3.9(2)E_r^{752}$	J_h/h	14.1(12) Hz	15.8(3) Hz
			J_v/h	13.4(12) Hz	15.1(3) Hz
			J_d/h	16.3(8) Hz	16.7(3) Hz

Table 3.2: Calibrated hopping energies in the tunable 2D lattice. For the square and triangular geometries in the folded lattice, we compare the hopping energies obtained from band structure calculations and lattice amplitude-modulation spectroscopy with fits from 2D quantum walks.

Quantum walk calibration

An alternative calibration method for the hopping energy makes use of quantum walks [141]. Despite being more time-consuming, this approach allows for a direct measurement of the kinetic energy term in both atomic and spin Hamiltonians [41, 42]. Using DMD addressing, we prepare a single atom (or spin) and quench the lattice depth to initiate dynamics. By measuring the time evolution of the wavefunction, we can fit the theoretical prediction, which only depends on the kinetic energy parameter and the lattice geometry. The quantum walk calibration typically yields a similar accuracy of 1–2 %.

In Fig. 3.10, we specifically show quantum walk measurements for the square, Lieb, triangular and kagome lattices (see Fig. 3.9), displaying characteristic interference patterns and agreeing well with numerical simulations. We quantitatively analyze the fitted hopping energies, J_h, J_v, J_d (along the plotted horizontal, vertical and diagonal lattice axis) in Tab. 3.2, where we additionally compare the results with the values obtained from band structure calculations using lattice depths measured through lattice AM spectroscopy. We first note the lattice-depth–dependent anisotropy in the square lattice, which we attribute to imperfect orthogonal alignment of the beam directions and which is captured by our calculations. We further find absolute agreement with deviations of up to 10 %, which could result from intensity imbalances or variations in the light polarization.

3.3.2 DMD projection

For accurate projection of DMD potentials, both the alignment with respect to the lattice sites and the local intensity have to be optimized. The procedure for determining rotation and magnification between lattice sites and DMD pixels is outlined in Ref. [104]. We optimize DMD pattern alignment to a precision of typically 10 % of the lattice spacing. To account for slow drifts of the lattice phase, we use the reconstructed lattice

phase to feedback the number of DMD pixels a given pattern has to be shifted to be aligned with the lattice [103].

Addressing patterns

To evaluate the homogeneity of addressing patterns used with the spin-dependent DMD setup, we perform site-resolved MW spectroscopy. Given a target pattern, we prepare a unity-filled atomic array and project the pattern with high intensity. By varying the spectral center of a narrowly swept MW transfer pulse between spin states $|\uparrow\rangle$ and $|\downarrow\rangle$, we can resolve the MW resonance and thus the DMD-induced differential light shift for each lattice site individually. Having a map of the absolute DMD power, we can iterate the local DMD grayscale reflectivity to homogenize the pattern intensity. Targeting homogeneous illumination, we can typically minimize the SD to about 5 %.

Potential shaping for large system sizes

Normally, the BH system size realized in our experiment is determined by the confining potential caused by the vertical lattice beam. In some cases, however, it is beneficial to work in larger system sizes or to have well-defined system boundaries. For these situations, we resort to potential shaping with the spin-independent 670 nm DMD setup.

In order to obtain a suitable base line for potential shaping, we start by iteratively correcting the potential into a flat box (typically of size 50×50 sites). For the correction procedure, we load a low-density SF from the pinning L3 into the DMD-corrected physics L3 potential and optimize the uniformity of the average density. To prevent atoms from leaving the correction area, we project a strong repulsive potential outside of the box area.

For the reliable creation of unity-filled MIs, however, this potential is not suitable because experimentally inevitable atom number fluctuations can lead to overfilling of the in-box lattice sites. To prevent overfilling, we ensure that the in-box sites have a higher potential than the bare (without DMD projection) sites outside of the box. Instead of retaining the high potential outside of the box, we project a repulsive wall with a width of few sites and a height of 0.5–1U, which is tapered down to zero at the outside. When adiabatically increasing the horizontal lattices, this potential has the effect that excess atoms (with interaction-induced excess energies of $\sim 1U$) are pushed over the boundary walls, vacating the in-box area and leaving behind a unity-filled MI. This potential engineering scheme is reminiscent of entropy redistribution approaches [120, 121] and could be optimized to increase the in-box MI filling further.

3.3.3 Spin transfers

An important capability of the experiment comprises the high-fidelity execution of desired changes of the atomic spin state and the prevention of undesired ones.

Microwave transfers

For general spin transfers, we perform a Landau–Zener sweep between two HFSs via MW Blackman pulses with a typical duration of 5 ms. We use this transfer approach for both global spin transfers and local transfers within the context of DMD addressing. We characterize the global transfer fidelity by performing multiple bidirectional transfers and fit the increase of the fraction of atoms in the wrong state, yielding typical fidelities of 99.96(1) %.

For global, coherent manipulations of the spin state we apply unswept MW pulses with Rabi frequencies in the range of 5–20 kHz. We typically obtain coherence times of the MW pulses of few ms.

Off-resonant light scattering

For sensitive experiments, off-resonant scattering in optical dipole potentials has to be taken into account. While the lattice beams at 1064 nm and the spin-independent DMD light at 670 nm is sufficiently detuned, the high intensities at 787 nm required during DMD addressing can be of significance: The first effect involves scattering-induced band excitations, which can be suppressed by addressing in deeper lattice potentials, which reduces the Lamb–Dicke parameter. The second effect involves scattering-induced spin flips, whereby the excited state may decay to ground states differing from the initial state according to the transitions' selection rules. This effect can also be suppressed when working with σ^- polarization, as off-resonant scattering then solely occurs on the closed D_2 transition.

3.3.4 Magnetic fields

When working with the $|\uparrow\rangle$ and $|\downarrow\rangle$ HFSs to probe spin physics, the differential Zeeman shift of $\Delta E_B/B = h \times 2.1\,\mathrm{MHz/G}$ between the spins lead to a system which is highly sensitive to the magnetic field. While the absolute value of the magnetic field is insignificant—as one can consider the spin model in a frame co-rotating with the trivial magnetic-field–induced dynamics—, fluctuations caused by ambient fields or variations in the magnetic coil currents can lead to dephasing. For the spin experiments discussed in this thesis, however, this is of no relevance as we are interested in either the $\hat{S}^z$ spin component or ensemble-averaged quantities [104]. Magnetic *gradients* are far more problematic as these cannot be transformed out and persist as field gradients within the spin model.

Spin-differential gradients can be precisely mapped out by performing Ramsey measurements on a spin-polarized, motionally frozen atomic array. By performing two MW $\pi/2$ pulses, interspersed with a hold time of up to $T = 600\,\mathrm{ms}$, the atoms accumulate a phase of $\Delta E_B T/\hbar$, visible as interference fringes. By fitting the interference patterns, we obtain a spatial magnetic-field map with which we can minimize magnetic gradients to less than 0.04 Hz per site using offset coils. This method also

allows us to benchmark deliberately generated magnetic-field gradients created by additional gradient coils.

3.3.5 Light polarization

Setting the correct polarization of light can be essential for both resonant and off-resonant beams.

DMD light

In the case of off-resonant (DMD) light, the polarization is critical to control differential light shifts. For our spin-dependent potentials using 787 nm light, the maximum ratio between light shift and off-resonant scattering is achieved for pure σ^- polarization. Using direct MW spectroscopy, the polarization purity can typically be optimized to more than 95 %. For spin-independent potentials, we conversely optimize for minimum differential light shift, realized for linear polarization. As the wavelength of 670 nm of the utilized light is already far off-resonant, differential shifts are small, and measurements rely on Ramsey sequences, see Sec. 3.3.4. In this case, we typically achieve estimated polarization purities of up to 90 % when differential light shifts of other sources start to become dominant.

Resonant light

Accurate control of the polarization of D_2 resonant light can also be critical for certain classes of experiments: For optical push-out of the $|\uparrow\rangle$ state, multiple scattering events are required, and a clean polarization prevents intermittent decay into a non-pushed ground state. With optimized parameters, we can achieve push fidelities up to 99.9(1) %. Resonant light can furthermore be used to probe the atoms' optical response by absorption imaging. For this purpose, high polarization purity is central to quantitatively deducing the optical absorptance.

We optimize the resonant beam for σ^- polarization by working in a regime where the Zeeman states are optically resolved. By tuning the laser to be resonant to the σ^+ transition, we minimize spin transfers after shining in the beam as spin flips indicate a residual σ^+ polarization. This optimization approach leads to polarization purities of more than 98 %.

Chapter 4

Nonlocal order in two-dimensional Mott insulators

Phase transitions describe the change of the collective behavior of a many-body system from a disordered to an ordered state. The order is indicated by an order parameter and is commonly given by a local correlation function whose value is zero in the disordered phase and finite in the ordered phase [86]. Indeed, for the paradigmatic example of a quantum phase transition (QPT), the superfluid (SF)–Mott insulator (MI) transition in the Bose–Hubbard (BH) model, the first detection was enabled by measuring the SF fraction as the order parameter of the SF phase [14]. In contrast, the MI phase is typically considered as a featureless state, and its presence defined indirectly through thermodynamic incompressibility, the excitation spectrum or parametric susceptibilities [6, 84, 142, 143]. In contrast, the notion of nonlocal order parameters gives rise to qualitatively different ordered phases [144–146], with the Haldane insulator as a prominent example [147]. Indeed, such order also exists in the MI phase, and has been experimentally demonstrated in one-dimensional (1D) BH chains [31, 88] and subsequently theoretically predicted for higher dimensions [89, 90, 148].

In this chapter, we first discuss the phase diagram of the BH model and provide a mean-field (MF) analysis, taking into account varying lattice geometries. We then analyze the doublon–hole correlations, which represent the quantum fluctuations driving the phase transition, and finally establish brane parity (BP) as a proxy for the nonlocal order parameter of two-dimensional (2D) MIs.

4.1 Bose–Hubbard model in the mean-field approximation

In this section, we analyze the BH model within the MF approximation, which has been shown to qualitatively capture the phase diagram [14, 149]. In MF theory, the full many-body Hamiltonian is approximated by the sum of local Hamiltonians, $\hat{H} \approx \sum_i \hat{H}_i$, by replacing nonlocal operator-valued quantities by their mean values.

Intuitively, MF theory is expected to be applicable to the BH model as it is exact in both the atomic and the non-interacting limit (see Sec. 2.1.2). For the BH model, the approximation amounts to $\hat{a}_i^\dagger \hat{a}_j \approx \hat{a}_i^\dagger \psi_j + \psi_i^* \hat{a}_j - \psi_i^* \psi_j$, with the expectation value of

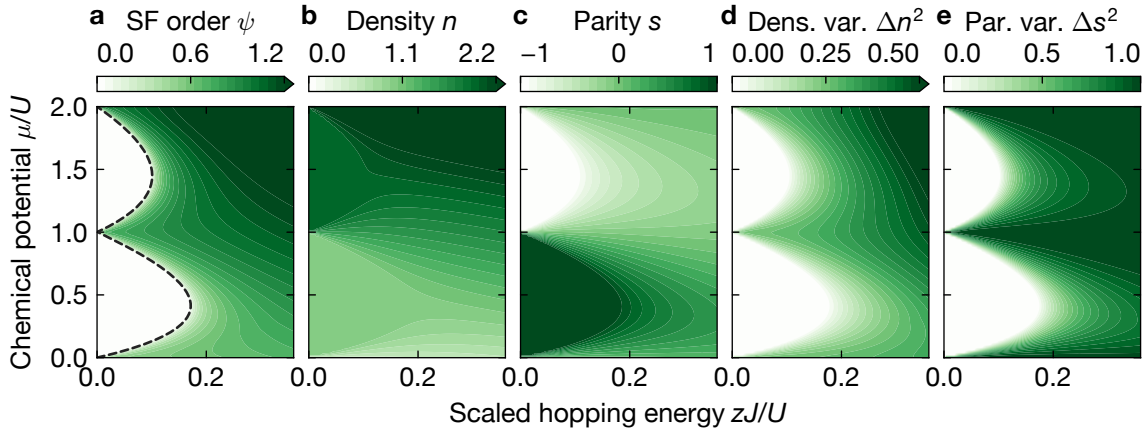

Figure 4.1: Mean-field Bose–Hubbard phase diagram in Bravais lattices. Various quantities of interest are plotted against the chemical potential, μ, and the hopping energy, J, scaled by the coordination number of the lattice, z. In the experiment, we typically operate around the $\mu/U \sim 0.5$ line. (**a**) The superfluid (SF) order parameter, $\psi = \langle \hat{a} \rangle$, reveals the presence of the SF phase outside of the Mott lobes. The dashed line indicates the phase boundary, Eq. (4.2). (**b**) The Mott insulator (MI) is characterized by incompressibility, visualized by the constant density in the Mott lobes. (**c**) Instead of the density, the experiment is subject to parity projection, $\hat{s} = e^{i\pi(\hat{n}-\overline{n})}$. (**d**) In the mean-field approximation, density fluctuations, $\Delta n^2 = \langle \hat{n}^2 \rangle - \langle \hat{n} \rangle^2$, suggest the presence of SF order. However, nonlocal fluctuations are not captured, which would lead to finite fluctuations already in the MI phase. (**e**) Visualization of the parity-projected density fluctuations, $\Delta s^2 = \langle \hat{s}^2 \rangle - \langle \hat{s} \rangle^2$.

the annihilation operator, $\psi_i = \langle \hat{a}_i \rangle$, serving as the local order parameter [86]. Hence, the BH MF Hamiltonian is given by [150]

$$\hat{H}_i = \frac{U}{2}\hat{n}_i(\hat{n}_i - 1) - \mu\hat{n}_i + \frac{J}{2}(\psi_i^*\phi_i + \phi_i^*\psi_i) - J(\phi_i^*\hat{a}_i + \phi_i\hat{a}_i^\dagger), \tag{4.1}$$

with ϕ_i the sum of the mean fields on the nearest-neighbor (NN)–connected sites, $\phi_i = \sum_{j\in\{j|\langle i,j\rangle\}} \psi_j$. This Hamiltonian can be numerically straightforwardly solved by taking into account the self-consistency condition between connected sites. The ground state is found by iteratively diagonalizing the system and calculating the mean field using the updated states.

4.1.1 Phase diagram

In the simplest case of a homogeneous system with one site per unit cell, e.g., square or triangular lattices, the NN fields are identical to the local field. Thus, $\phi_i = z\psi_i$, and the lattice-structure dependence reduces to a dependence on the coordination number

z only. The phase boundary can be perturbatively calculated [150] and is given by

$$\frac{zJ}{U} = \frac{(\lceil \mu/U \rceil - \mu/U)(1 - \lceil \mu/U \rceil + \mu/U)}{1 + \mu/U}, \tag{4.2}$$

showing the integer-filled Mott lobes for small J/U. Specifically, the critical point of the Mott lobe with integer filling $\overline{n} = \lceil (\mu/U)_c \rceil$ is located at

$$\left(\frac{\mu}{U}\right)_c = \sqrt{\overline{n}^2 + \overline{n}} - 1, \tag{4.3}$$

and scales with the coordination number, $(J/U)_c \propto 1/z$.

Fig. 4.1 shows a numerical calculation of the order parameter, the expected density and the experimentally relevant parity as a function of the BH parameters J/U and μ/U. In MF approximation, nonlocal effects are not captured so density fluctuations only appear in the SF phase. They grow with increasing J/U, reaching the Poissonian variance of $\Delta n^2 = n$ in the non-interacting limit.

4.1.2 Sublattice inhomogeneity

In the case of multiple sublattices in a unit cell, the MF calculation requires an inhomogeneous treatment, yielding separate states and fields on each sublattice [151, 152]. Here we focus on the tripartite Lieb lattice (see Fig. 4.2d) whose unit cell comprises a "hub" site (A), with local coordination number $z_{\text{hub}} = 4$, and two "rim" sites (B, C), with $z_{\text{rim}} = 2$. Each sublattice type is only connected to the respective other sublattice type.

In Fig. 4.2, we find that the phase diagram remains to be well-described by Eq. (4.2) when considering the arithmetic mean of the sublattices as effective coordination number, $z = (z_{\text{hub}} + 2z_{\text{rim}})/3$. The onset of nonzero SF density occurs at the same J/U parameter, indicating the global nature of the SF. Focussing on the spatial inhomogeneity of the order parameter, however, we find that close to the phase transition $\psi_{\text{hub}} \approx \sqrt{2}\psi_{\text{rim}}$, showing that higher connectivity leads to more phase rigidity responsible for SF formation. Following the contour line of equal density—which represents a homogeneous system with fixed atom number—, this relation persists.

Band structure

As a complementary view in the non-interacting limit, we can compute the system behavior from the band structure. Treating the system within the tight-binding model [153], we obtain the three sublattice bands

$$E^{(1,3)}(\mathbf{q}\cdot\mathbf{r}) = \mp J\sqrt{4 + 2\cos q_x x + 2\cos q_y y}, \quad E^{(2)}(\mathbf{q}\cdot\mathbf{r}) = 0, \tag{4.4}$$

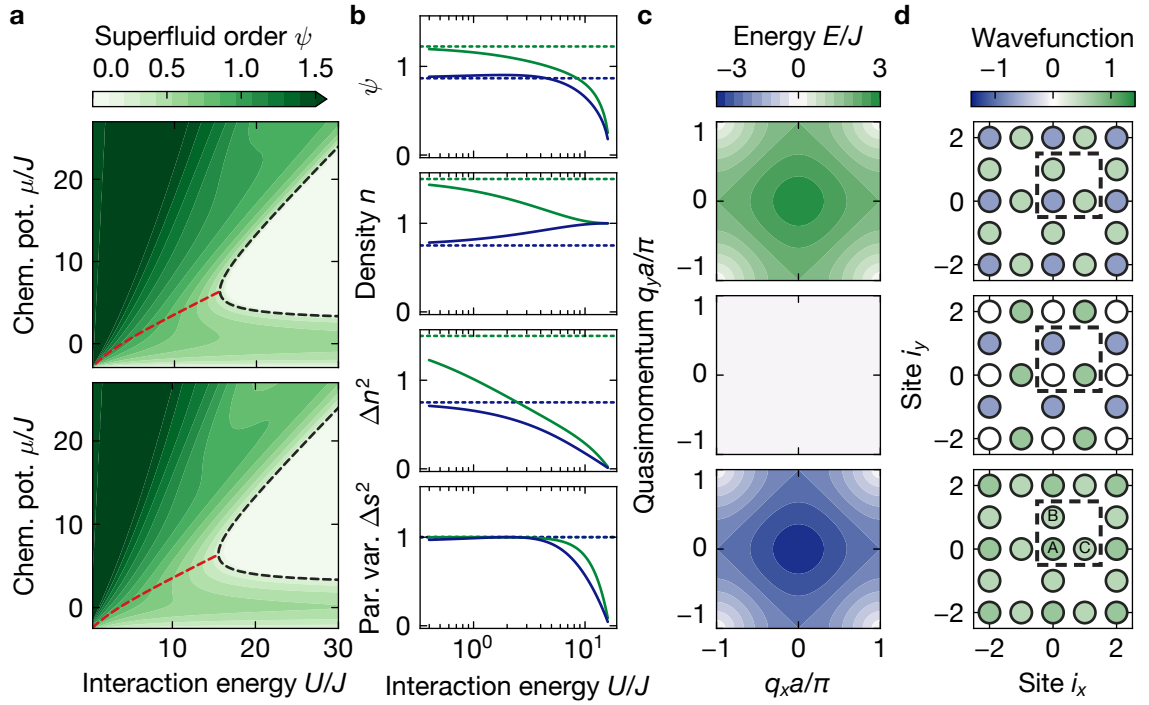

Figure 4.2: Mean-field phase diagram and band structure of the Lieb lattice. (**a**) The superfluid (SF) order parameter becomes nonzero at the same parameter regime on both the hub (top) and rim (bottom) sublattice. The phase boundary is shown as a black dashed line. The red dashed line marks the contour line of constant unit-cell–averaged density, $\sum_S \langle \hat{n}_S \rangle / 3 = 1$. (**b**) SF order parameter ψ, density n, density variance Δn^2 and parity variance Δs^2 (top to bottom) along the unity-filling contour line evaluated for the hub (green) and rim (blue) sites. The dashed lines indicate the non-interacting limit. (**c**) Band structure $E^{(1,2,3)}(\mathbf{q})$ for the three sublattice bands (bottom to top). (**d**) Eigenfunctions $\psi_{i,S}^{(1,2,3)}(\mathbf{q}=0)$ for the sublattice bands (bottom to top) and sublattice sites $S \in \{A, B, C\}$. The dashed box marks the Lieb lattice unit cell.

most notably, featuring a non-dispersive "flat" central band $E^{(2)}$. The eigenfunctions are given by

$$\begin{aligned} \vec{\psi}_i^{(1,3)} &\propto \frac{E^{(1,3)}(\mathbf{q}\cdot\mathbf{r}_i)}{2J}\vec{e}_\mathrm{A} + \cos\frac{q_x x_i}{2}\vec{e}_\mathrm{B} + \cos\frac{q_y y_i}{2}\vec{e}_\mathrm{C}, \\ \vec{\psi}_i^{(2)} &\propto \cos\frac{q_y y_i}{2}\vec{e}_\mathrm{B} - \cos\frac{q_x x_i}{2}\vec{e}_\mathrm{C}, \end{aligned} \tag{4.5}$$

where $\vec{e}_S$ denotes the sublattice S. Here we can observe that the flat-band states do not occupy the hub site at all, while the states in the dispersive bands have a density ratio between hub sites and rim sites of 2, consistent with the MF calculation.

4.2 Doublon–hole fluctuations

While the MF approximation captures on-site quantum fluctuations, nonlocal fluctuations are neglected, which play a prominent role in the MI phase at finite hopping $J \neq 0$. In the experimentally relevant case of commensurate filling deep in the MI phase, $J/U \ll (J/U)_c$, the BH model can be perturbatively treated through a strong-coupling expansion [154]. To first order, this yields a correction to the ground state of

$$|\Psi\rangle_{J/U\ll(J/U)_c} \propto |\Psi\rangle_{J/U=0} + \sum_{\langle i,j\rangle} \frac{J_{ij}}{U - \Delta\varepsilon_{ij}} \hat{a}_i^\dagger \hat{a}_j |\Psi\rangle_{J/U=0}, \tag{4.6}$$

where J_{ij} denotes the (possibly local) hopping energy and $\Delta\varepsilon_{ij} = \varepsilon_i - \varepsilon_j$ the variation of the on-site potential. The perturbative term describes the formation of virtual particle–hole pairs on adjacent sites, thus also rendering the on-site density fluctuations nonzero.

Notably, in a homogeneous lattice, $J_{ij} = J$ and $\Delta\varepsilon_{ij} = 0$, we would expect every lattice bond to give rise to an equal probability for the occurrence of these fluctuations and density correlation functions to show a dependence characteristic of the lattice geometry. Formally, the two-point connected correlator of the density at filling $\overline{n}$ is given by

$$\langle \hat{n}_i \hat{n}_j \rangle_c = 2\overline{n}(\overline{n}+1) \left(\frac{J}{U}\right)^2 (z_i \delta_{ij} + \delta_{\langle i,j\rangle}), \tag{4.7}$$

and can be deduced from parity-projected measurements as $\langle \hat{s}_i \hat{s}_j \rangle_c = 4|\langle \hat{n}_i \hat{n}_j \rangle_c|$.

4.2.1 Experimental scheme

The formation of virtual doublon–hole pairs has been experimentally detected in quantum gas microscopes (QGMs) of both bosonic and fermionic Hubbard systems [31, 36]. While these measurements were limited to 1D or square lattices, we analyze the dependence of the doublon–hole fluctuations on differing 2D lattice geometries. These are generated by our tunable lattices with a spacing of 752 nm (see Sec. 3.2.2) and demonstrate our ability to precisely control the geometry in the strongly interacting regime of 2D BH models.

In the experiment, we probe the many-body ground state of the 2D BH model for varying J/U parameters near unity filling in the square, triangular and Lieb lattices. The experimental approach is depicted in Fig. 4.3 and started with a 2D SF trapped in one layer of the physics Lattice 3 (L3). For the Lieb lattice, we additionally adiabatically ramped up the block-out potential to $V_b = h \cdot 450(120)$ Hz in 150 ms. We then adiabatically ramped up the horizontal lattices in 200 ms to a depth corresponding to the desired J/U value, resulting in the preparation of the associated BH ground state. The ramps were programmed such that the hopping energies remained largely isotropic.

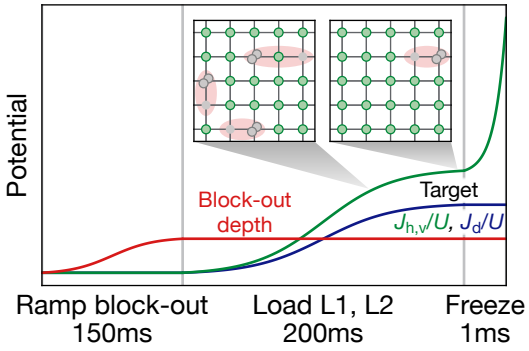

Figure 4.3: Experimental sequence for detecting doublon–hole pairs. To probe the Bose–Hubbard model in lattices with multi-site unit cells, we first ramp up the DMD-projected block-out potential (red). We then adiabatically ramp up the horizontal tunable lattices to the target lattice depths. The straight hopping strength is tunable via the Lattice 2 (L2) depth (green) and the diagonal hopping via Lattice 1 (L1) (blue). After reaching the target depth, we rapidly ramp up the Lattice 2 (L2) depth to freeze the occupation. (**Insets**) Depending on the lattice depths, different J/U value are realized, yielding varying strengths of doublon–hole fluctuations (red shaded) in the Mott insulator phase.

This is followed by a fast 1 ms quench to a lattice depth of $V = 90E_r^{752}$, freezing the occupation on each site and thus projecting the state into the local Fock basis upon imaging. Note that while the hopping energy, J, depends exponentially on the lattice depth, the interaction energy is rather insensitive, staying in the range of 200–300 Hz throughout the measurement parameters.

4.2.2 Geometry dependence of parity fluctuations

We average the parity fluctuation measurements over 200 experimental runs per data point. The correlations are analyzed on a region of interest (ROI) of 9×9 sites in the center of the cloud, where the potential is approximately homogeneous on the scale of the interaction energy, $\Delta\varepsilon_{ij} \lesssim 0.1U$. Due to the imperfect alignment of the lattice beams with an intersection angle of 90.7° and lattice-depth calibration uncertainties of 2–3 %, the hopping energies vary slightly between the horizontal, vertical and diagonal directions. In the case of the square Bravais lattice, the calculated anisotropy is given by $J_v/J_h \approx 0.92$–0.94, and in the case of the triangular Bravais lattice $J_d/J_h \approx 0.93$–0.99.

Parity correlations

By analyzing the dependence of the correlation strength on the BH parameter J/U (see Fig. 4.4), we can clearly observe quadratic growth, confirming the picture of NN–separated virtual doublon–hole pairs. These pairs, however, only form between

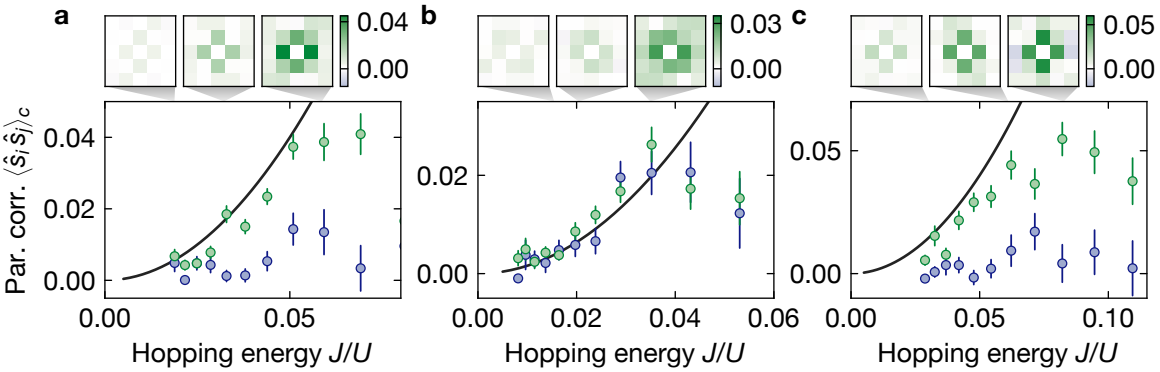

Figure 4.4: Parity correlation measurements. Connected parity correlations, $\langle \hat{s}_i \hat{s}_j \rangle_c$ between nearest-neighbor sites (green) and diagonal-neighbor sites along the triangular-lattice direction (blue) in the (**a**) square, (**b**) triangular and (**c**) Lieb lattice. In the case of the triangular lattice, both correlators grow equally, whereas in the cases with square Bravais lattice the diagonal correlators remain small. For all geometries, the onsets of the correlations agree well with the perturbative dependence, predicting proportionality with $(J/U)^2$ (black line). (**Insets**) show the 2D correlations at further locations (i, j), with the respective J/U parameter marked. For the Lieb lattice, the blocked-out sites have been excluded from the correlation analysis. Error bars denote the standard error of the mean (SEM).

sites that are directly tunnel-coupled. Particularly, we immediately find that only the triangular lattice builds up doublon–hole correlations across diagonal bonds whereas the lattices with square base geometry only show correlations along the straight NN sites. With increasing J/U, we can observe an increase of the diagonal-neighbor (DN) correlations also for the square lattices. We attribute this behavior to a diverging correlation length as the system approaches the phase transition. The doublon–hole pairs start to deconfine, and higher-order perturbations become relevant. In the SF phase after crossing the phase transition, parity fluctuations become increasingly global in nature, leading to a reduction in the NN correlations with further increasing J/U.

On-site parity fluctuations

Apart from two-point correlators, we can also analyze the on-site fluctuations of the parity, $\langle \hat{s}_i^2 \rangle_c$ (see Fig. 4.5a). In the MI phase, we again expect the parity variance to grow with $(J/U)^2$, due to the presence of the nonlocal doublon–hole fluctuations. Hence, in contrast to the NN correlators, the on-site variance depends on the local coordination number z_S. In the non-uniform Lieb lattice, we indeed find that the variance differs between hub and rim sites, agreeing well with perturbative analysis. The fact that the experimental data match the theoretical curve furthermore confirms that the block-out potentials used to create the Lieb lattice do not lead to significant potential disorder

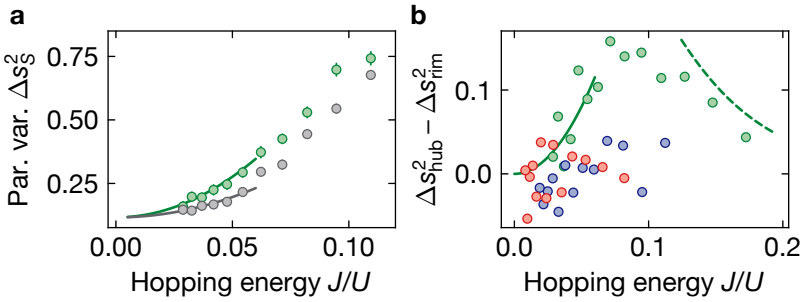

Figure 4.5: On-site parity fluctuations. (**a**) On-site parity variance, $\Delta s_S^2 = \langle \hat{s}_i^2 \rangle_{i \in S} - \langle \hat{s}_i \rangle_{i \in S}^2$, of the Lieb lattice, evaluated on the hub (green) and rim (gray) sublattice sites. The solid lines indicate predictions by perturbation theory, with an offset accounting for the finite filling of 0.97. Error bars show the SEM. (**b**) The parity variance difference between hub and rim sites evaluated for the Lieb (green), square (blue) and triangular (red) lattices. The solid line indicates strong-coupling perturbation theory, and the dashed line marks inhomogeneous mean-field theory.

on the non-blocked sites. Note that deep in the MI, we added an offset of $4\overline{n}(1-\overline{n})$ to the parity variance, which—using a Bernoulli distribution—classically accounts for uncorrelated holes present due to the finite filling of $\overline{n} = 0.97$.

In Fig. 4.5b we plot the difference of the parity variance between the sites (associated to the hub and rim sites in the Lieb lattice) also for the square and triangular lattices and clearly observe that only the Lieb lattice gives rise to the deviation. We can furthermore analyze the on-site fluctuations in the SF phase, where we observe a reduction of the variance with increasing J/U. At first glance, this appears counterintuitive as in the non-interacting limit band structure calculations predict that the number fluctuations on the hub sites are twice as large compared to the rim sites. However, due to parity projection, the experimentally observable fluctuations are limited, and number variances increasing above unity appear constant. Sufficiently far from the critical point, the data indeed follows MF predictions, consistent with Fig. 4.2b.

4.3 Two-dimensional nonlocal order

With Landau's theory of second order phase transitions, local order parameters have become a central concept for characterizing symmetry-broken phases in condensed matter physics [155]. However, certain systems can exhibit order that is not captured by such a two-point correlation function, requiring the introduction of extensive multi-point correlators as *nonlocal* order parameters [156]. Nonlocal string-order parameters have been particularly successful in revealing symmetry-protected topological phases [157, 158], and have revealed hidden order in various 1D chains and ladders

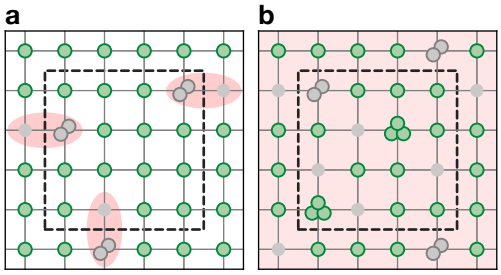

Figure 4.6: Brane parity order parameter. (**a**) Unity-filled Mott insulator with bound doublon–hole pairs (red shaded), which are experimentally observable by their parity (positive parity: green, negative parity: gray). The integer brane parity (BP) is determined by the number of pairs cut by the boundary of the analysis area $\mathcal{A}$ (dashed black box). For finite $\mathcal{A}$, the BP remains finite and scales with a perimeter law. (**b**) In the superfluid phase, no distinct pairs are present. For finite $\mathcal{A}$, the parities are largely uncorrelated, leading to a substantially smaller BP, which decays faster than the perimeter law.

of spins or Hubbard systems [88, 159–164]. Experimentally, microscopic access to site-resolved observables was crucial to detect nonlocal order, leading to observations of string order in Hubbard and Su–Schrieffer–Heeger models [31, 37, 39, 165].

In the 1D BH model, the parity order parameter, $O_P = \langle \prod_i \hat{s}_i \rangle$, turns out to serve as a string order parameter detecting the hidden order in the MI phase and has been experimentally demonstrated in Ref. [31]. In two dimensions, this concept was theoretically generalized to "brane parity", where the product over the parities runs over a 2D area [89, 90, 148]. In the following, we will discuss this quantity (partially following Ref. [102]) and present measurements, suggesting BP to be a suitable order parameter for the 2D MI phase.

4.3.1 Brane parity order in the Bose–Hubbard model

The BP order parameter can be written in a generalized form as

$$O_P^{(\theta)} = \left\langle \prod_{i \in \mathcal{A}} e^{i\theta\, \delta\hat{n}_i} \right\rangle = \left\langle e^{i\theta\, \delta\hat{N}} \right\rangle, \tag{4.8}$$

where $\delta\hat{n}_i = \hat{n}_i - \overline{n}$ and $\delta\hat{N} = \hat{N} - \overline{N}$ denote the fluctuation of the on-site occupation and of the total atom number within a ROI area, $\mathcal{A}$, respectively. The fractional parity phase θ is a generalization of the integer parity phase, $\theta = \pi$, which reproduces the standard parity.

To analyze the scaling behavior of the BP at large ROIs, $\mathcal{A} \sim L^2 \gg 1$, we can approximate $\delta\hat{N}$ as a normally distributed random variable. Then the higher statistical

moments become functions of the variance, and the BP value reduces to [89, 90]

$$\ln O_P^{(\theta)} \approx -\frac{\theta}{2}\langle \delta\hat{N}^2 \rangle \propto \begin{cases} -\theta^2\, L \log L & \text{(SF)}, \\ -\theta^1\, L & \text{(MI)}. \end{cases} \tag{4.9}$$

This implies that, for a fractional parity phase of $\theta = L^{-\gamma}$, $\gamma \geq 1/2$, BP serves as an order parameter in the thermodynamic limit, vanishing in the SF phase and becoming nonzero in the MI phase [90, 148]. For the experimentally accessible integer parity phase, $\theta = \pi$, the BP expectation value formally vanishes in both phases, however, with distinct scaling behavior. As, for finite ROIs, the absolute value of O_P in the MI phase is substantially larger compared with the SF phase, and the deviation grows with L due to the differing scaling laws, the integer BP is nevertheless suitable to detect order in cold atom experiments (see Sec. 4.3.2). Note that the use of such bipartite fluctuations to detect quantum critical points between gapped and gapless phases has been proposed on more general grounds in Ref. [166].

Integer brane parity

For the integer BP, $O_P \equiv O_P^{(\pi)}$, Eq. (4.8) can be written as [102]

$$O_P = \sum_{\delta N} p_{\mathcal{A}}(\delta N)(-1)^{\delta N} = 1 - 2P(\hat{O}_P = -1), \tag{4.10}$$

where $p_{\mathcal{A}}(\delta N)$ denotes the probability for an atom number deviation of δN within the ROI, $\mathcal{A}$, and $P(\hat{O}_P)$ the probability for the BP to have the value $\hat{O}_P$.

This relation permits a complementary, intuitive picture depicted in Fig. 4.6. Starting in the unity-filled strong-coupling limit, $J \ll U$, the ground state is a product Fock state, yielding $O_P(J/U = 0) = 1$. At finite perturbative hopping energies, J, doublon–hole pairs at NN sites form, which do not alter the BP as long as both constituents are located within $\mathcal{A}$. However, if the boundary of $\mathcal{A}$ cuts an odd number of doublon–hole pairs, the value of O_P flips sign. Thus, we can consider $P(\hat{O}_P)$ as a binomial distribution in the number of cut pairs along the perimeter of $\mathcal{A}$ and obtain $O_P = (1-2p)^{4L}$. Here, $p = z_b(J/U)^2$ is the perturbative on-perimeter probability for a cut pair, with $z_b = z/d - 1$ the average number of bonds cut on a perimeter site.

When approaching the phase transition, the doublon–hole pairs deconfine and higher perturbation orders have to be taken into account. As long as $\mathcal{A}$ is sufficiently large to capture all relevant perturbative clusters, the perimeter law, $\log O_P \propto -L$, holds true. In the SF phase, however, this picture becomes invalid, leading to the faster–than–perimeter-law decay, $\log O_P \propto -L \log L$, obtained from Eq. (4.9). Furthermore, in the MI phase, uncorrelated holes or doublons (e.g. originating from finite temperature) appearing in the bulk do not lead to the pairwise cancellation exhibited by the virtual doublon–hole pairs. In this case, the binomial distribution runs across the full ROI area instead of the perimeter, resulting in an area-law decay, $\log O_P \propto -L^2$.

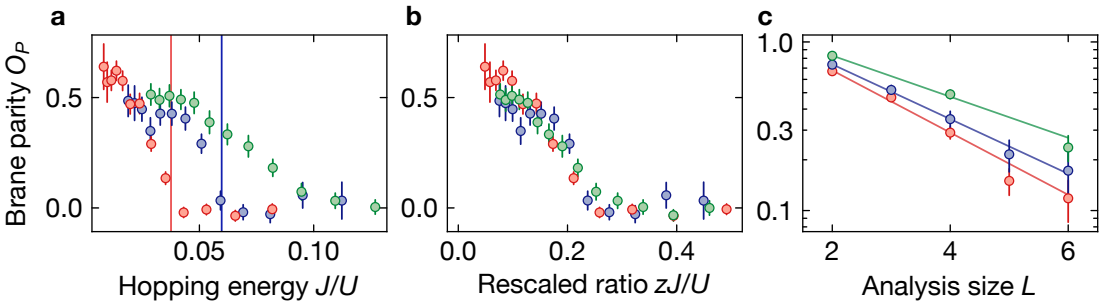

Figure 4.7: Brane parity order in various lattice geometries. (**a**) Integer brane parity (BP) evaluated over 4×4 sites in the triangular (red), square (blue) and Lieb (green) lattice. The vertical lines show Monte-Carlo predictions for the critical value, $(J/U)_c$, agreeing with the parameter value at which the BP becomes nonzero. (**b**) The same data rescaled with the (average) coordination number shows a collapse. This behavior is consistent with mean-field scaling, confirming the BP as a proxy for the order parameter of the Mott insulator (MI) phase. (**c**) In the MI phase at $J/U = 0.029$ (triangular, red), 0.029 (square, blue), and 0.033 (Lieb, green), we plot the BP evaluated over different ROIs of $L \times L$. The solid lines correspond to exponential fits, confirming the predicted perimeter-law scaling, $\log O_P \propto -L$. Error bars denote the SEM.

4.3.2 Geometry dependence of parity order

As quantum gas microscopy provides full access to site-resolved parities, images from a measurement following the protocol described in Sec. 4.2.1 immediately allow us to evaluate parity order. Particularly, we can leverage the experimental tunability of the lattice geometry to study the dependence of the BP value on the local connectivity.

For the analysis of the parity data, we crop the images to a ROI of 7×7 sites to sample only the homogeneous potential in the center of the trap. To improve the signal-to-noise ratio (SNR), we evaluate the BP on an area subset of size $\mathcal{A} \sim L \times L$ and average over all possible embeddings of $\mathcal{A}$ within the original 7×7 ROI.

Scaling with lattice geometry and system size

In Fig. 4.7a we show the results for $L = 4$, measured for the square, triangular and Lieb lattices. We can clearly observe that the integer BP indeed features a sudden increase in value when crossing below a critical $(J/U)_c$, consistent with its interpretation as an order parameter. Furthermore, in the case of both the square and the triangular lattice, the value agrees well with predictions by Monte-Carlo simulations [167, 168].

As outlined in Sec. 4.1.1, MF theory predicts that the phase diagram—including the critical point—depends on the lattice geometry only through the (averaged) coordination number of the lattice, z, and has been experimentally demonstrated by rescaling the measured SF order parameter [149]. This fact provides an alternative way to deter-

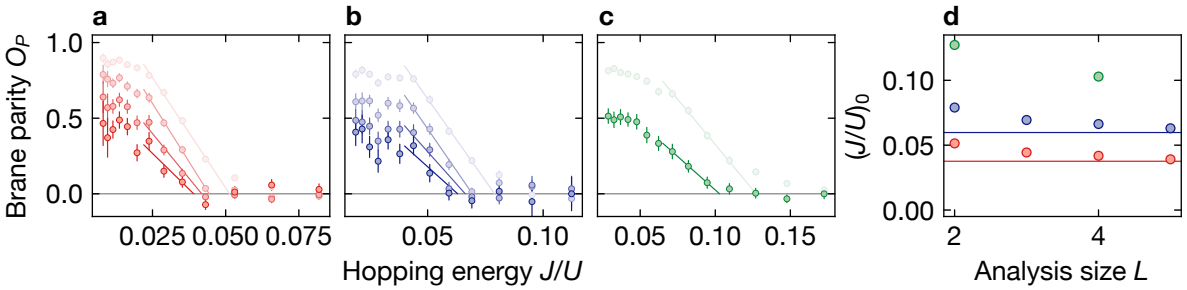

Figure 4.8: Critical point extraction from brane parity. (**a–c**) Brane parity in the triangular (red), square (blue) and Lieb (green) lattice for increasing analysis sizes (light to dark color), ranging from $L = 2$–5 for the triangular and square lattice, and $L = 2, 4$ for the Lieb lattice. The solid lines indicate linear fits, from which we extract the zero crossing as proxy for the critical point, $(J/U)_0$. Error bars denote the SEM. (**d**) The critical point proxy converges with increasing analysis size L. Solid lines mark the critical values predicted by Monte-Carlo simulations.

mining the role of BP: In Fig. 4.7b, we plot O_P as a function of the rescaled hopping energy, zJ/U. We find that the three curves approximately collapse, demonstrating BP as a complementary order parameter for the MI phase in the BH model. The data furthermore suggests that the transition of the Lieb lattice around the critical point is not as distinct as the other geometries. This could originate from finite-size effects due to the smaller number of sites covered in a given area $\mathcal{A}$, or hint at more non-trivial effects due to the presence of multiple sublattices.

In Fig. 4.7c, we analyze the dependence of the BP on the analysis size, L, in the MI phases of the three lattice geometries. By fitting an exponential decay to the data, we confirm that the integer BP indeed fulfills the perimeter law, $\log O_P \propto -L$, predicted in Eq. (4.9). In parts of the data, we can observe a slight faster-than-expected decrease of O_P with L, which we mainly attribute to two effects: First, finite temperatures correspond to the emergence of uncorrelated holes, giving rise to additional area-law scaling, $\log O_P \propto -L^2$. Second, evaluating data further away from the trap center is more susceptible to atom-number fluctuations, resulting in probing spatially inhomogeneous values of J/U, which can show signs of more SF character, which is expected to scale as $\log O_P \propto -L \log L$. Note that due to insufficient SNR, the scaling in the SF phase cannot be directly experimentally characterized.

Convergence behavior

As our analyses are performed on finite system sizes, $L < \infty$, and the experimental data are subject to noise, the exact critical point $(J/U)_c$ is difficult to locate. However, due to the difference of the system-size scaling in the different phases, we expect the

BP to grow more distinct with increasing system size (for sufficiently small thermal and inhomogeneity effects).

In Figs. 4.8 a–c we extract the convergence behavior by fitting a linear function to the sloped part of the BP data. We then use the zero crossing of the linear function, $(J/U)_0$, as a proxy for the critical point. In Fig. 4.8d, we indeed observe that the extracted value converges. Note that we expect our proxy to slightly underestimate the actual critical value due to both the expected nonlinear nature of the BP around the critical point and the spatial potential inhomogeneity. As we observe contrary behavior in the experimental data, this suggests that finite-size effects are still prevalent.

4.4 Conclusion and outlook

In this chapter, we have demonstrated the flexible realization of 2D BH models in geometries beyond the square lattice. By example of the square, triangular and Lieb lattice in the MI phase, we have observed NN parity correlations induced by doublon–hole fluctuations, which are characteristic of the particular geometry. We additionally observed that, in the strong-coupling regime, these fluctuations only depend on the local lattice connectivity by measuring the local coordination-number dependence of the on-site fluctuations. Leveraging the spatially resolved parity of the QGM, we experimentally established the integer BP as a parameter suitable to detect the nonlocal order of the 2D MI phase. We observed the perimeter-law decay of the BP in the MI phase and found that the BP as a function of the BH parameter J/U scales with the average coordination number.

A natural extension of this study could involve measuring the *fractional* BP as the formally true order parameter of the 2D MI phase, which would remain finite in the thermodynamic limit and could be achieved through doublon-resolved imaging in the honeycomb configuration of our tunable superlattice. Furthermore, as the presented data points were comparatively coarse in the vicinity of the critical point, a more detailed investigation could directly detect the critical scaling, characterizing the universality class of the QPT. Such a study would require larger and cleaner systems, and could be combined with the analysis of the influence of filling fractions and spatial potential inhomogeneity. Finally, while NN correlations per lattice bond do not depend on the exact lattice topology in first-order perturbation, characterization of higher-order correlations closer to the critical point could reveal the formation of more complex doublon–hole clusters.

Part II

Kardar–Parisi–Zhang universality and Heisenberg chains

Chapter 5

Kardar–Parisi–Zhang hydrodynamics

Universal scaling has proven to be a powerful concept in a variety of fields, ranging from physics, chemistry and biology to economics or social sciences [169]. The base idea involves analyzing the collective behavior of a many-body system in a scale-invariant limit, in which the microscopic details of a model become largely irrelevant and individual models can be grouped in universality classes [170, 171]. The most notable application constitutes the classification of equilibrium critical phenomena, for which not only static but also dynamical properties can be accounted for [172]. While these dynamical effects occur in the context of static criticality, there exists a wider range of genuine non-equilibrium scenarios, which are possibly independent of the static ground-state properties. Universal scaling can also be applied to such systems, even though a full characterization is still lacking [173].

A prominent member of such dynamical universality classes is the Kardar–Parisi–Zhang (KPZ) class, which will be the topic of this chapter. In Sec. 5.1, we will first discuss the properties of the one-dimensional (1D) KPZ universality class in its original context of interface growth, and then proceed with its relation to hydrodynamic transport in quantum models in Sec. 5.2.

5.1 KPZ universality class

The KPZ universality class has its origins in a stochastic partial differential equation (PDE),

$$\partial_t h(x,t) = v_0 + \nu \partial_x^2 h(x,t) + \frac{\lambda}{2}(\partial_x h(x,t))^2 + \sqrt{D}\eta(x,t), \tag{5.1}$$

which was devised by M. Kardar, G. Parisi and Y.-C. Zhang to model kinetic roughening and interface growth in $1+1$ spatial dimensions [174]. This PDE describes the height, h, of an interface as a stochastic process, with lateral position x and time t, under the influence of spatiotemporally uncorrelated noise, η. Due to its complexity as a stochastic nonlinear PDE, Eq. (5.1) remains an active field of study in mathematics [175] and could only recently be rigorously shown to belong to the KPZ universality class [176, 177], with the prefactors acting as nonuniversal parameters.

The first term, v_0, accounts for vertical height growth, and the second term, $\propto \nu$, describes diffusion, smoothening rough surfaces and giving rise to spatial correla-

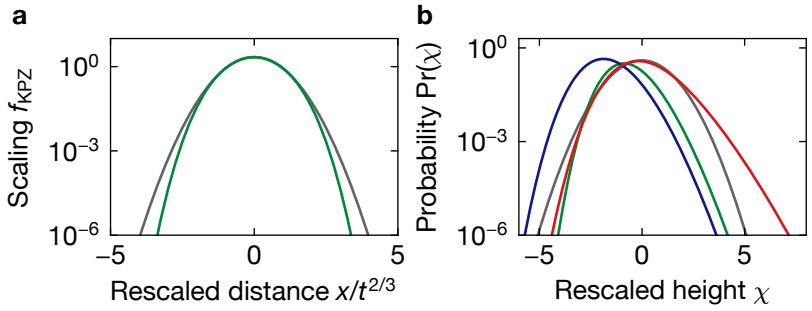

Figure 5.1: Characteristics of the KPZ universality class. (**a**) The KPZ scaling function (green) is characteristic of the KPZ universality class and features a small deviation from a Gaussian function (gray). (**b**) The distribution of the rescaled height fluctuations, $\chi = \delta h/t^{1/3}$, depend on the initial conditions. They are given by the Tracy–Widom GOE (flat initial condition, green), Tracy–Widom GUE (wedge, blue) and Baik–Rains (stationary, red) distributions. A normal distribution is depicted as a reference in gray.

tions. Growth processes modelled by these linear terms alone belong to the Edwards–Wilkinson universality class [178]. However, in most real growth processes, lateral growth needs to be taken into account, and is modelled by the third term, $\propto \lambda$. This nonlinear term remains relevant in the renormalization group sense and thus yields a distinct class—the KPZ universality class [179, 180]—, whose properties we will cover in this section.

5.1.1 Scaling functions

Dynamical universality classes are characterized by a set of scale-invariant correlation functions [173]. In particular the stationary-time two-point correlation function of the interface height follows Family–Vicsek scaling [181, 182],

$$C_h(x,t) \equiv \langle (h(x,t) - h(0,0) - v_\infty t)^2 \rangle \sim t^{2\beta} F_{\mathrm{KPZ}}\left(\frac{x}{t^{1/z}}\right), \tag{5.2}$$

where v_∞ is the asymptotic growth velocity of the interface and F_{KPZ} is a scaling function, with scaling exponents that are characteristic for a universality class. For the KPZ class, spatial correlations grow with $C_h(x \ll \xi, t) \sim x^{2\alpha}$ and spatial exponent $\alpha = 1/2$, and temporal correlations with $C_h(x \gg \xi, t) \sim t^{2\beta}$ and growth exponent $\beta = 1/3$. The correlation length, $\xi \sim t^{1/z}$, scales with the ratio of spatial and temporal correlations, with dynamical exponent $z = \alpha/\beta = 3/2$.

In the case of stationary initial conditions, the connected two-point function of the spatial derivatives of the height is of particular interest, and is given by [183]

$$\langle \partial_x h(x,t)\, \partial_x h(0,0) \rangle_c = \frac{1}{2}\partial_x^2 C_h(x,t) \sim t^{2\beta - 2/z} f_{\mathrm{KPZ}}\left(\frac{x}{t^{1/z}}\right) \tag{5.3}$$

with another scaling function (see Fig. 5.1a), $f_{\mathrm{KPZ}}(y) = F''_{\mathrm{KPZ}}(y)$, which has been exactly calculated and tabulated with high precision [184, 185]. We will refer to this function as the "KPZ scaling function".

5.1.2 Fluctuations

As the KPZ equation describes stochastic processes, the distributions of height fluctuations have also been investigated and found to exhibit universal behavior. Exact analysis of models in the KPZ universality class revealed that the KPZ class can be further subdivided into "KPZ subclasses" [186], which depend on the initial conditions, $h(x,0)$. Specifically, the height field can be written as

$$h(x,t) = v_\infty t + (\Gamma t)^\beta \chi\left(\frac{x}{\xi(t)}, t\right), \tag{5.4}$$

where χ denotes an initial-condition–dependent random process [184]. In the long-time limit, χ has been shown to universally converge in distribution and was termed Airy process $\mathcal{A}_i$ [187, 188]: For the "flat" initial condition, $h(x,0) = \text{const.}$, this yields $\chi \to \mathcal{A}_1$, for the "wedge" (also known as "droplet/circular") initial condition, $h(x,0) \sim |x|$, $\chi \to \mathcal{A}_2 - (x/\xi)^2$ and for the "stationary" initial state $\chi \to \mathcal{A}_{\mathrm{stat}}$.

Of particular interest are the universal distribution functions of the height fluctuations arising in these processes [183]. In Ref. [186], it was found that the distributions are related to the Tracy–Widom (TW) distribution [189], which describe the distribution of the largest eigenvalues of random matrices. For the flat initial state, the height fluctuations relate to random matrices in the Gaussian orthogonal ensemble (GOE), and for the wedge initial state the Gaussian unitary ensemble (GUE). The distribution for the stationary case is known as the Baik–Rains (BR) distribution [190]. Most notably, as shown in Fig. 5.1b, these fluctuation distributions are asymmetric, which is a hallmark of an underlying nonlinear effect and is reminiscent of the nonlinear KPZ equation. The asymmetry can be quantified by higher-order statistical central moments and provides an observable for detecting KPZ physics.

5.1.3 Models in the KPZ class

The KPZ universality class encompasses three broad categories of models: Apart from interface growth processes, these include paths in random environments and stochastic particle dynamics [191].

The category of interface-growth problems comprises the majority of both numerically and experimentally studied models. KPZ scaling was in fact observed to describe a variety of systems; notably, the fluctuations of paper combustion fronts or liquid-crystal phase boundaries even displayed the full distributions expected from KPZ universality [192, 193], experimentally confirming the initial-state–dependent KPZ subclasses. Models in the category involving paths in random environments are

often used to study percolation-type effects [194–197]. These include directed polymer problems, which have been vital in the precise determination of the KPZ fluctuations and scaling functions [185, 198].

The category of stochastic particle dynamics is most relevant to this thesis and typically consists of mapping the KPZ height field, $h(x,t)$, onto a particle density,

$$u(x,t) \sim \partial_x h(x,t). \tag{5.5}$$

This substitution is well-defined in the scaling limit and gives rise to the stochastic Burgers equation [199],

$$\partial_t u(x,t) = \nu \partial_x^2 u(x,t) + \lambda u(x,t)\partial_x u(x,t) + \sqrt{D}\partial_x \eta(x,t), \tag{5.6}$$

which is equivalent to the KPZ equation, Eq. (5.1), and serves as a model for turbulent fluid dynamics. Classical models of this type include asymmetric exclusion process (ASEP) particle-hopping models describing, e.g., biological transport or traffic flow [200–202].

KPZ behavior has also been discovered to arise in quantum many-body models: For instance, in the context of interface growth, experiments with driven 1D polariton condensates found the condensate phase front to follow KPZ scaling [203]. KPZ scaling was furthermore also predicted to arise as entanglement growth under random unitary dynamics, for which the problem was analyzed with respect to all three aforementioned KPZ categories [204]. These examples describe non-equilibrium settings subject to explicit noise, as typical for canonical models in the KPZ universality class. Recent numerical simulations, however, revealed that—despite the absence of these features—the linear-response spin transport in isotropic Heisenberg (XXX) spin chains exhibited KPZ scaling [63, 64]. This surprising finding is the topic of Part II of this thesis and will be discussed in detail in Chapter 6 and Chapter 7.

5.2 Hydrodynamics

Microscopic models in both classical and quantum many-body physics give rise to a wealth of dynamical phenomena. On macroscopic spatiotemporal scales, however, the details are often lost, and the time evolution becomes well-described by universal dynamics. This suggests the existence of a common framework to study macroscopic out-of-equilibrium phenomena, which is provided by hydrodynamics [205–207].

In this section we first discuss the general ideas of how coarse-graining gives rise to hydrodynamics. Then we review properties of integrable systems, which are relevant to this thesis, and describe how these systems thus lead to generalized hydrodynamics (GHD). We will restrict ourselves to 1D systems and follow Refs. [208, 209]. Note that we use a continuum notation but the discussion is readily applicable to discrete systems.

	Elementary dynamics	Fluid-cell dynamics		Stationary dynamics
System scale	Microscopic scale	Diffusive scale	Euler scale	Homogeneous system
Finite conserved quantities	Particle dynamics	Hydrodynamics		Gibbs ensemble thermodynamics
Infinite conserved quantities	Particle dynamics	Generalized hydrodynamics		Generalized Gibbs ensemble thermodynamics

Table 5.1: Scale-dependent theoretical descriptions of gases. With increasing temporal and spatial scales (left to right), the effective dynamics of a many-body system changes from considering individual particles to macroscopic densities. For integrable systems, the thermodynamics in macroscopically homogeneous systems is generalized to a GGE description. Analogously, for macroscopically inhomogeneous systems, hydrodynamics is generalized to GHD.

5.2.1 Coarse-grained dynamics

Hydrodynamics is a theory of conserved quantities: As, in general, any mixed initial state evolves towards a maximum-entropy state, the only nontrivial macroscopic dynamics can occur for conserved "charges" $\{Q_i\}$ (e.g., energy or particle number). Furthermore, microscopic charge conservation implies that a temporal change of a local charge density must be accompanied by a spatial charge-current inhomogeneity. This notion is encoded in a set of continuity equations,

$$\partial_t \hat{q}_i(x,t) + \partial_x \hat{j}_i(x,t) = 0, \tag{5.7}$$

where $\hat{q}_i$ and $\hat{j}_i$ denote the charge and current densities, respectively, for the total charge $\hat{Q}_i = \int dx\, \hat{q}_i(x)$. Entropy maximization under these constraints therefore implies evolution towards Gibbs ensembles (GEs), $\hat{\rho} \propto e^{-\sum_i \beta_i \hat{Q}_i}$, with the Lagrange multipliers $\{\beta_i\}$ (e.g., temperature or chemical potential) fully characterizing the thermodynamic state. Maximum entropy states have the useful property that susceptibilities of observables $\hat{o}$ can be expressed through connected correlation functions with respect to the charge densities [208],

$$-\frac{\partial}{\partial \beta_i}\langle \hat{o} \rangle_{\{\beta_i\}} = \int dx \langle \hat{o}\hat{q}_i(x,0)\rangle^c_{\{\beta_i\}}. \tag{5.8}$$

This in turn implies that the thermodynamic state can be equivalently expressed by the mean charge densities [208], $\{\overline{q}_i\} \Leftrightarrow \{\beta_i\}$.

Dynamics of locally thermodynamic states

The hydrodynamic approximation assumes the microscopic system to settle into locally equilibrated states within so-called fluid cells, which are described by locally varying GEs, i.e., that any observable $\hat{o}$ can be expressed as $\langle \hat{o}(x,t) \rangle \approx \langle \hat{o} \rangle_{\{\beta_i(x,t)\}}$. Hydrodynamics arises from spatial inhomogeneities of the charge densities between nearby fluid cells, which can be understood in a local-density approximation (LDA) sense. This picture thus relates thermodynamic susceptibilities to convective dynamics. The hydrodynamic equilibration obeys the fluid-cell–averaged continuity equations,

$$\partial_t \bar{q}_i(x,t) + \partial_x \bar{J}_i(x,t) = 0, \tag{5.9}$$

for which the currents can be expanded through the constitutive relations given by

$$\bar{J}_i(x,t) \approx \sum_j A_{ij}(\{\bar{q}_i(x,t)\})\bar{q}_j(x,t) - \frac{1}{2}\sum_j D_{ij}(\{\bar{q}_i(x,t)\})\partial_x \bar{q}_j(x,t), \tag{5.10}$$

where the expansion coefficients, A_{ij} and D_{ij}, generally depend on the local thermodynamic state.

To leading order, we obtain the Euler scale hydrodynamic equations, $\partial_t \bar{q}_i(x,t) + \sum_j A_{ij}\partial_x^2 \bar{q}_j(x,t) = 0$, whose core quantity is the flux Jacobian, $A_{ij} = \partial \bar{j}_i / \partial \bar{q}_j$, which describes a velocity response due to a spatial charge gradient. Indeed, its eigenbasis, $R_{ij} = \partial \rho_i / \partial \bar{q}_j$, can be written as the Jacobian of a mode density function, $\rho_i(\{\bar{q}_j\})$, and the eigenstates are known as the normal modes of hydrodynamics; the components of R_{ij} then describe the charge composition of the modes. The Euler hydrodynamic equations are then given by $\partial_t \rho_i + v_i^{\text{eff}} \partial_x \rho_i = 0$, where v_i^{eff} denote the eigenvalues of A and correspond to the generalized sound velocities of the normal modes. Euler hydrodynamics generally describes ballistic, reversible charge transport; charge diffusion is captured by the diffusion of the normal modes, which arises when accounting for higher orders in Eq. (5.10).

Note that the introduction of higher-order terms gives rise to nonlinear (fluctuating) hydrodynamics. One example are generic classical fluids with continuous Galilean symmetry (with only energy and momentum as conserved charges): When including the next-order term and assuming diagonal contributions to fluctuations to be dominant, Eq. (5.9) reduces to the Burgers equation (5.6) and thus features KPZ superdiffusion. However, in discrete systems, Galilean symmetry is broken, such that the momentum mode does not hold and one generally expects normal diffusion [210].

5.2.2 Generalized hydrodynamics

While the use of hydrodynamics in quantum systems with a finite number of conserved charges has been ubiquitous for decades, recent theoretical advances involved applying hydrodynamic ideas to integrable systems, resulting in the theory of GHD [211, 212].

Integrable models comprise an extensive number of (quasi-) local conserved charges and are known for being exactly solvable by the Bethe ansatz [213]. However, while thermodynamic quantities are readily accessible, calculations of nonequilibrium quantities on larger systems are generally challenging [214], motivating the development of GHD. An overview over the hydrodynamic scales and their suitable descriptions is shown in Tab. 5.1.

Integrable systems are described by stable quasiparticles, which correspond to asymptotically local excitations characterized by their rapidity θ (reminiscent of momenta). As rapidities are preserved in such systems, interactions can be reduced to elastic two-body collisions, which can only affect the phase of the quasiparticles. The effect of scattering between multiple quasiparticles can thus be thought of as a mutual dressing process between all quasiparticles. The hydrodynamic properties of integrable models can be obtained by identifying the quasiparticles as the hydrodynamic normal modes and the rapidity as parameterizing the space of conserved quantities. The generalized sound velocities are then given by the group velocities of the quasiparticles, $v^{\mathrm{eff}}(\theta) = \partial\varepsilon(\theta)/\partial k(\theta)$.

The transport behavior of a model is encoded in hydrodynamic correlation functions, with the dynamical structure factor (DSF) playing a central role. With GHD, the DSF can be expressed as [210]

$$\langle \overline{q}(x,t)\overline{q}(0,0)\rangle_c = \sum_s \int d\theta\, \rho_s^{\mathrm{tot}}(\theta) n_s(\theta)(1+\sigma n_s(\theta))[m_s^{\mathrm{dr}}(\theta)]^2 \varphi_t(x - v_s^{\mathrm{eff}}(\theta)t), \quad (5.11)$$

where $\sigma = 0, -1, 1$ accounts for classical, fermionic and bosonic particles statistics, and where $\varphi_t(\zeta)$ is the propagator of the respective quasiparticle. This dependence warrants a kinematic view of GHD, in which solitary wave packets—propagating ballistically with velocity v^{eff} and carrying a charge composition $m_i^{\mathrm{dr}}(\theta) = \partial\varepsilon(\theta)/\partial\beta_i$ dressed by elastic scattering—give rise to charge transport. A given state is represented by the distribution of quasiparticles, $\rho(\theta) = \rho^{\mathrm{tot}}(\theta)n(\theta)$, consisting of the density of states ρ^{tot} and the state occupation n, whose kinematic dynamics can be analyzed. Note that, generally, there can be multiple quasiparticle species s, when multiple bound states of elementary excitations exist.

5.2.3 Scaling behavior

In this thesis, we are interested in the low-frequency limit of hydrodynamic transport, which is commonly characterized through two transport coefficients [209, 215]: The Drude weight, $\mathcal{D}$, captures the ballistic mean transport due to convective modes, and the diffusion constant, D, describes fluctuations thereof. These coefficients arise from analyzing the dynamical spreading of a local disturbance of the equilibrium charge density, where the spatial variance [215],

$$\ell^2 = \langle x^2\rangle_c = \frac{1}{\chi}\int dx\, x^2 \langle \overline{q}(x,t)\overline{q}(0,0)\rangle_c \approx \frac{\mathcal{D}}{\chi}t^2 + Dt, \quad (5.12)$$

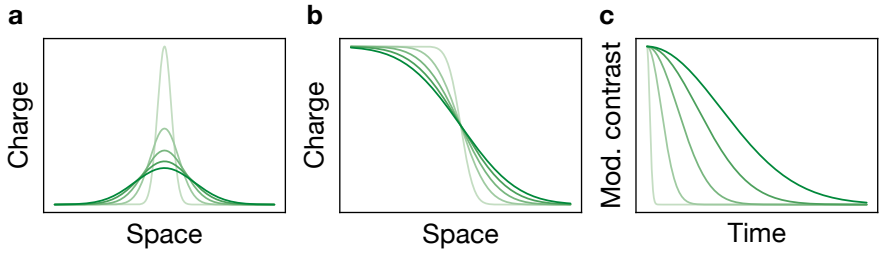

Figure 5.2: Extracting dynamical scaling. (**a**) The dynamical structure factor (DSF) can be directly measured through the spatial charge profile initialized with a localized perturbation. The scaling exponent is obtained by fitting the width growing with time (light to dark). (**b**) The spatial charge profile of a domain wall evolves into the spatially integrated DSF. Its width for increasing time (light to dark) again scales with the dynamical exponent. (**c**) Starting with a sinusoidal modulation, the reduction in modulation contrast follows the Fourier transform of the DSF. The dynamical exponent relates the decay time to the increasing modulation wavelength (light to dark).

shows a characteristic dominant dynamical scaling law, $\ell \sim t^{1/z}$, with dynamical exponent z. The susceptibility, $\chi = \partial\overline{q}/\partial\beta$, serves as a normalization of the DSF, see also Eq. (5.8).

Note that the charge transport behavior within linear response is fully captured by the DSF and thus represents the core quantity to study, from which the model's dynamical universality class can be determined. Through the height–charge mapping introduced in Eq. (5.5), the DSF can be related to a scaling function, f, in analogy to Eq. (5.3) as

$$\langle \overline{q}(x,t)\overline{q}(0,0)\rangle_c \sim \frac{1}{t^{1/z}} f\left(\frac{x}{t^{1/z}}\right). \tag{5.13}$$

Note that, due to charge conservation, the spatially integrated DSF is constant, implying a spatial exponent of $\alpha = 1/2$. Specifically, the model may be associated with the KPZ universality class if the dynamical exponent is $z = 3/2$ and the function f agrees with the KPZ scaling function f_{KPZ}, Eq. (5.3).

5.2.4 Measuring the dynamical structure factor

As DSFs are ubiquitous in the linear-response analysis of many-body physics, a wealth of methods have been developed to extract both the functional form and the scaling exponents. In a setting with time-domain dynamical access to local observables—as in numerics or in quantum gas microscopy—a generally applicable method is to prepare an initial mixed state with a charge distribution, $\varepsilon\langle\hat{q}(x,0)\rangle + \langle\hat{q}(x,0)\rangle_{\mathrm{eq}}$, which is slightly perturbed from equilibrium, $\varepsilon \ll 1$, yielding a density matrix of $\hat{\rho} \propto \exp[\int dx(\sum_i \beta_i(x)\hat{q}_i(x) - \varepsilon\beta(x)\hat{q}(x))]$. By measuring the time evolution of the

mean charge deviation [216],

$$\langle \hat{q}(x,t)\rangle - \langle \hat{q}(x,0)\rangle_{\mathrm{eq}} \approx \frac{\varepsilon}{\chi}\int dx' \langle \hat{q}(x',0)\rangle \langle \hat{q}(x,t)\hat{q}(x',0)\rangle_c, \tag{5.14}$$

the DSF and thus the transport properties can be deduced. In the following, we will discuss three experimentally relevant initial states, suitable for extracting the DSF as illustrated in Fig. 5.2.

- The most direct implementation of the scheme involves the preparation of a local perturbation, $\langle \hat{q}(x,0)\rangle \sim \delta(x)$. The evolving density profile then directly represents the DSF, realizing the scaling form

$$\langle \hat{q}(x,t)\rangle_{\mathrm{local}} \sim \langle \overline{q}(x,t)\overline{q}(0,0)\rangle_c \sim \frac{1}{t^{1/z}} f\left(\frac{x}{t^{1/z}}\right). \tag{5.15}$$

- Another scheme, known as the Riemann problem in the context of hydrodynamics, consists of preparing a domain wall (DW) initial state, $\langle \hat{q}(x,0)\rangle \sim \Theta(x)$. Here, the spatial derivatives of the density profiles evolve as the DSF [64] such that the densities scale with

$$\langle \hat{q}(x,t)\rangle_{\mathrm{DW}} \sim \int dx \langle \overline{q}(x,t)\overline{q}(0,0)\rangle_c \sim F\left(\frac{x}{t^{1/z}}\right), \tag{5.16}$$

  where $F'(\zeta) = f(\zeta)$.

- Finally, the linear-response hydrodynamics also permits a spatially spectral treatment, where the evolution of initial states $\langle \hat{q}(x,0)\rangle \sim e^{ikx}$ with varying wave numbers, k, are probed. The amplitude of the sinusoidal modulation then decays as

$$\langle \hat{q}(0,t)\rangle_{\mathrm{Fourier}} \sim \int_{-\infty}^{\infty} dx \langle \overline{q}(x,t)\overline{q}(0,0)\rangle_c \sim \tilde{f}(kt^{1/z}), \tag{5.17}$$

  with $\tilde{f}(\nu) = \int d\zeta\, e^{i\nu\zeta} f(\zeta)$.

Chapter 6

Spin transport in the Heisenberg model

The Heisenberg (XXZ) model is a quantum lattice model describing a system of interacting spins and forms a fundamental model for the understanding of quantum magnetism. Despite its simplicity, the XXZ model serves as a paradigmatic model to describe a range of quantum effects, enabling the study of magnetic phases and critical phenomena [217]. Especially in its one-dimensional (1D) form, the XXZ chain has proven vital for the discovery of theoretical methods and experimental approaches. Although the XXZ chain was formally analytically solved already a century ago by introducing the seminal Bethe ansatz [213], the analysis of long-time dynamics far from the ground state remains both an analytical and numerical challenge [214, 216].

Surprisingly, despite decades of investigation, recent numerical simulations found a novel feature in the isotropic Heisenberg (XXX) chain, revealing that infinite-temperature spin transport follows anomalous dynamical scaling [63, 64, 218], inconsistent with the usually occurring diffusive or ballistic transport. Moreover, the calculations suggested that the two-point functions of spin transport agreed with the scaling function of the Kardar–Parisi–Zhang (KPZ) universality class, triggering extensive studies on its fundamental origins [219–221].

In Sec. 6.1, we first give an overview over the transport regimes of the XXZ model and approaches to extracting the dynamical scaling. We then describe our experimental protocol to prepare domain wall (DW) initial states and report on the observation of superdiffusive spin transport in Sec. 6.2. This is followed, in Sec. 6.3, by an analysis of the microscopic requirements of superdiffusion, probing the validity of generalized hydrodynamics (GHD). Finally, in Sec. 6.4, we discuss how the choice of the initial state affects the extracted dynamical exponent.

6.1 Hydrodynamics of the Heisenberg model

The Hamiltonian of the XXZ chain is given by

$$\hat{H} = -J_{\mathrm{ex}} \sum_i (\hat{S}_i^x \hat{S}_{i+1}^x + \hat{S}_i^y \hat{S}_{i+1}^y + \Delta \hat{S}_i^z \hat{S}_{i+1}^z) + \sum_i h_i \hat{S}_i^z, \tag{6.1}$$

with nearest-neighbor (NN) coupling J_{ex}, local longitudinal field h_i, and anisotropy Δ. In the zero-field case, the model can be distinguished between the $\mathrm{SU}(2)$-symmetric case at $|\Delta| = 1$ and the anisotropic cases $|\Delta| \neq 1$ with reduced $\mathrm{U}(1)$ symmetry. In their respective limits, the anisotropic XXZ model reduces to the (anti-) ferromagnetic Ising model at $|\Delta| \gg 1$ and the XX model at $|\Delta| = 0$. At zero temperature, the isotropic point corresponds to a quantum critical point separating these two phases.

In this thesis, we are, however, interested in the dynamical properties of "typical" states. These generally correspond to states far from the ground state, and are therefore not subject to the critical physics near the ground-state phase transition. Thus, the well-studied theory of dynamical critical phenomena [172] is not applicable, rendering the direct analysis of out-of-equilibrium physics more difficult. However, as the XXZ chain is integrable, the GHD approach outlined in Sec. 5.2 is valid and will be the basis of our discussions about spin transport.

6.1.1 Dynamical exponents

Identifying the magnetization $\hat{S}^z$ as a hydrodynamic charge, the dynamical scaling behavior of spin transport phenomena in lattice systems is normally expected to fall into one of two classes: In generic non-integrable systems, only the energy mode is hydrodynamically relevant while (other) charge-carrying quasiparticle currents dissipate, resulting in diffusive transport with dynamical exponent $z = 2$. In integrable systems (which include non-interacting systems), the quasiparticles remain stable, typically resulting in ballistic transport with $z = 1$. However, for net-uncharged quasiparticles, e.g., due to screening by their environment, charge fluctuations need to be taken into account and can give rise to diffusive or anomalous transport properties.

In the XXZ chain, the elementary quasiparticles correspond to free magnons, which can form "s-strings", which are stable bound states consisting of s magnons [222]. As outlined in Sec. 5.2.2, these strings are treated as separate quasiparticle species within GHD and can be parameterized by the string length s. The transport properties of the model then depend on the bound-state structure, the two-body scattering phases and the quasiparticle spectrum. These are generally analyzed separately for the three regimes of anisotropy.

Easy-plane regime

In the easy-plane regime of the XXZ model, $|\Delta| < 1$, calculations have shown that spin transport is generally ballistic and comprises an anisotropy-dependent fractal Drude weight, reminiscent of the fractal bound-state structure [223–226]. Ballistic spin transport is most easily seen in the XX model limit, $|\Delta| \ll 1$. In this case, the many-body model can be mapped to a free-fermion system by a Jordan–Wigner transformation, yielding ballistically propagating single-particle dynamics.

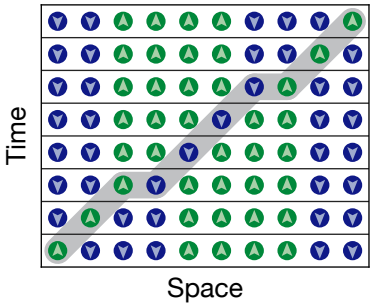

Figure 6.1: Propagating quasiparticles. In integrable models quasiparticles retain their momenta and propagate ballistically. In the illustrated case of the Ising model (with few excitations), an elementary quasiparticle (gray shaded) corresponds to a spin flip in a magnetization background. Upon collision with a larger quasiparticle (the domain of four up-spins), the lighter quasiparticle flips its magnetization and both quasiparticles are displaced.

Easy-axis regime

In the easy-axis regime, $|\Delta| > 1$, spin transport is, in contrast, expected to be diffusive. As the treatment is similar to the isotropic case, relevant for this thesis, we will describe this regime in more detail. In the following, we first outline an intuitive picture [214] for the quasiparticle and hydrodynamic description near the Ising limit, $|\Delta| \gg 1$, before moving to more general finite anisotropies.

In the Ising limit, the eigenstates are strings of s commonly polarized spins, which are related to the quasiparticles of species s and have magnetization s. Since the number of DWs is conserved due to energy conservation, these quasiparticles remain stable. Considering transversal coupling as a perturbation, elementary quasiparticles (i.e., single flipped spins) can propagate ballistically with a velocity given by the transversal coupling energy. "Heavier" s-strings can also move ballistically but only in a higher-order process scaling with $1/\Delta^s$, leading to a hierarchy of quasiparticle velocities which are exponentially suppressed with string length. In the presence of many quasiparticles, it follows that lighter s-strings move in a parametrically static spin background formed by heavier strings. However, while the bare quasiparticle carries a magnetization of s, its magnetization flips sign upon crossing a DW, as illustrated in Fig. 6.1. This means that the average magnetization of this quasiparticle becomes proportional to the net magnetization of the whole system, h. At $h \to 0$ the dressed magnetization thus vanishes, explaining the lack of ballistic transport in net unmagnetized systems despite integrability.

This intuitive picture can be generalized to finite anisotropies by thermodynamic Bethe ansatz calculations [227, 228]. In the high-temperature limit, $\beta \to 0$, these quantities have closed-form expressions independent of the rapidities [228]. Then,

GHD predicts a Drude weight which evaluates to $\mathcal{D} \propto h^2$ [214], which—in accordance with the intuitive picture—shows that in systems with vanishing net magnetization, $h \to 0$, ballistic transport is suppressed because the dressed quasiparticle magnetization vanishes. Therefore, spin transport is dominated by quasiparticle magnetization *fluctuations*, giving rise to a spin diffusion constant which scales as $D \propto 1/\sqrt{\Delta - 1}$ [228]. Evidently, the diffusion constant diverges with vanishing anisotropy, $\Delta \to 1$, demanding special attention at the isotropic point.

Isotropic point

The isotropic Heisenberg point, $|\Delta| = 1$, can be thought of as a dynamical critical point, separating the ballistic easy-plane regime from the diffusive easy-axis regime in an unmagnetized system, $h = 0$. The isotropic regime shares many features with the easy-axis regime and comprises a Drude weight that vanishes with $\mathcal{D} \propto h^2 |\log h|$. Spin transport is thus also dominated by fluctuations, but the diverging diffusion constant suggests anomalous superdiffusion instead of regular diffusion.

The dynamical exponent can be obtained within the kinetic picture of GHD following arguments devised in Ref. [214]: A bare quasiparticle retains its magnetization m_s as long as it does not collide with larger strings. This time scale is given by $\tau_s \sim \ell_s / v_s$, where v_s is the quasiparticle velocity and $\ell_s \sim 1/\sum_{s'>s} \rho_{s'}$ is the average spacing between larger strings. An initial spin current, $j_s \sim m_s v_s$, then decays as e^{-t/τ_s}. Hence, the total current correlation function is given by summing all quasiparticle contributions,

$$\int dx \langle j(x,t) j(0,0) \rangle_c \sim \sum_s j_s^2 \rho_s e^{-t/\tau_s} \sim \frac{D}{t}, \tag{6.2}$$

which yields the spin diffusion constant, D, through the Kubo formula.

In the XXX model, the quasiparticle magnetization is given by $m_s \sim s$, its density by $\rho_s \sim 1/s^3$ and its velocity by $v_s \sim 1/s$. Inserting these scaling relations into Eq. (6.2) gives rise to a diffusion constant of $D \sim t^{1/3}$, which implies a superdiffusive dynamical exponent of $z = 3/2$. This stands in contrast to the easy-axis regime, where the quasiparticle velocity scales as $v_s \sim e^{-s}$, yielding a diffusion constant that is constant in time. Note that GHD calculations at the isotropic point are not straightforward, since the quasiparticle velocity decays only polynomially with s and the hydrodynamic assumption of macroscopically small fluid cells, $s \ll L$, is technically not fulfilled [214].

6.1.2 Observing dynamical scaling

Quantum spin chains are experimentally realized in a multitude of platforms, ranging from solid-state bulk and surface systems to synthetic systems comprising ions or cold atoms. While solid-state samples feature large system sizes suitable for probing scaling behavior, direct observables of spin transport have generally proven challenging to obtain [216]. In contrast, quantum simulators provide microscopic access and

near-ideal model implementations but contain only relatively few lattice sites. This limitation partially motivates the extension of the system sizes realized in the context of this thesis. Their proximity to theoretical models allows these systems to explore numerically studied transport quantities using the schemes outlined in Sec. 5.2.4:

- For instance, an ion trap experiment observed the dynamical scaling functions in a long-range XX model [229] employing a local disturbance as initial state, Eq. (5.15). In the work, the authors could show superdiffusive transport and determine the functional forms of the dynamical structure factor (DSF) by rescaling the dynamical spin profiles, and could establish a temperature dependence by varying the background spin states.

- Ultracold atoms in optical lattices, realizing the XXZ model through superexchange, Eq. (2.10), have relied on measuring the scaling of the decay rates of sinusoidally modulated initial states with wavelength. In Ref. [60], the dynamical exponent of the isotropic XXX model was extracted to be diffusive in 1D and superdiffusive in 2D. Ref. [230] extended the 1D results to encompass varying anisotropies, Δ, of the XXZ model, yielding ballistic or superdiffusive exponents for $\Delta < 1$, diffusive ones for $\Delta = 1$, and subdiffusive ones for $\Delta > 1$. These measurements contradict the linear-response predictions, suggesting that the pure spin helix states employed may feature distinct far-from-equilibrium dynamics. We will discuss these effects in more detail in Sec. 6.4.

- The protocol using the DW initial state has been employed to study spin transport in a two-dimensional (2D) Fermi–Hubbard (FH) system [62], finding diffusive transport in the far-from-equilibrium regime.

The first measurements probing the high-temperature regime of the XXX model, for which numerics predicts KPZ superdiffusion, have been performed in the quantum material $KCuF_3$ [231]. This was accomplished through neutron scattering, which can be considered to be related to the Fourier-mode approach and probes the wavelength-dependent excitation spectrum of the high-temperature equilibrium state. Indeed, the measurements demonstrated that the system featured a superdiffusive dynamical exponent of $z \sim 3/2$; while this dynamical exponent is consistent with the KPZ exponent, it does not represent a sufficient condition for identifying the universality class, which requires agreement with a full scaling function and statistics of the transport fluctuations, and can be obtained from quantum simulators. For our high-temperature experiments in the XXX chain, we decided to follow the DW approach as the signal-to-noise ratio (SNR) is more beneficial compared to the local-excitation approach and our spatial resolution gives immediate access to the functional form of the DSF, in contrast to the Fourier-mode approach.

6.2 Superdiffusive spin transport

Studying the anomalous space–time scaling of spin transport in the XXX chain requires both a faithful realization of the model as well as large systems and long evolution times to reach the hydrodynamic regime. Optical lattice experiments with ^{87}Rb have been demonstrated to accurately implement the isotropic NN interaction necessary for the Heisenberg model (see Sec. 2.1.3), and experimental upgrades increased the available system size to 1D chains of up to 50 spins (see Sec. 3.1.3). Furthermore, the negligible dependence of the Heisenberg parameters on spin-independent potential inhomogeneities and access to precise calibrations of spin-dependent potentials make our setup ideal to study spin transport.

To achieve minimal spin-dependent inhomogeneities, we reduced magnetic gradients along the 1D systems by aligning and laterally slightly displacing the magnetic field minimum. Additionally, to minimize differential light shifts due to the 670 nm digital micromirror device (DMD)–projected local potentials while maintaining spin addressability with the 787 nm DMD light, we introduced a flippable quarter-wave plate (QWP) to cancel residual circular polarization in the 670 nm light on demand. As long evolution times of up to 1 s are required, we furthermore verified that no significant atom loss occurred even when holding the atoms in the most sensitive parameter regime near the Mott insulator (MI)–SF phase transition.

6.2.1 Experimental protocol

As argued in Sec. 6.1.2, we use the high-temperature DW protocol to study spin transport. To prepare the required initial state, we employ a multi-step process illustrated in Fig. 6.2: We start with a unity-filled, spin-polarized MI arranged in a bar shape to maximize the system size along one dimension while maintaining a stable, high filling fraction of 0.93. In the atomic limit, each atom evolves independently and is described by a spin-1/2 state, $\bigotimes_j |\downarrow\rangle_j$.

Using our local addressing scheme, we flip the spin on one half of the system, yielding $[\bigotimes_{j<0}|\downarrow\rangle_j] \otimes [\bigotimes_{j>0}|\uparrow\rangle_j]$. This preparation step has a fidelity of 0.99 in the bulk, and ~ 0.8 on the sites adjacent to the DW. We then reduce the $\hat{S}^z$ modulation by applying a resonant microwave (MW) pulse with pulse area θ. Since this state remains a pure state, we then use the 787 nm DMD to apply a shot-to-shot varying, spatially random spin-dependent potential, h_i. This procedure locally dephases the spins, $\varphi_i = h_i t$, and generates a high-entropy mixed state,

$$\left[\bigotimes_{j<0} e^{i\varphi_j}(-\sin\theta|\uparrow\rangle_j + \cos\theta|\downarrow\rangle_j)\right] \otimes \left[\bigotimes_{j>0} e^{i\varphi_j}(\cos\theta|\uparrow\rangle_j + \sin\theta|\downarrow\rangle_j)\right].$$

We parameterize these states by a purity parameter, η, and a net magnetization, δ,

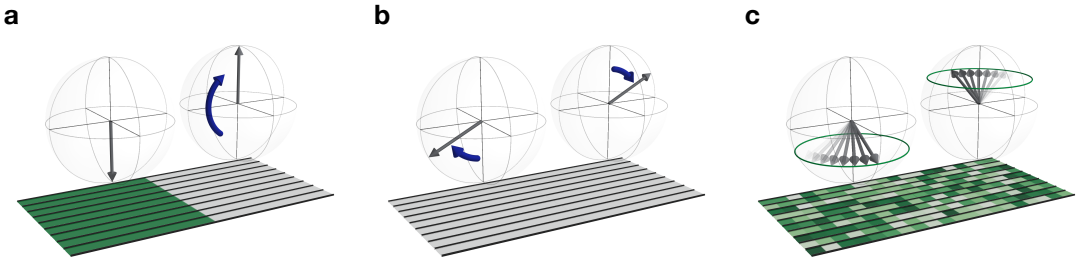

Figure 6.2: Preparation of high-temperature spin domain walls. The bar-shaped area shows our intrinsically 2D systems. During dynamics, one lattice axis is kept deep, effectively realising an ensemble of independent 1D chains (black lines). Above the atoms, we depict Bloch spheres representing the spin states of an atom on either side of the domain wall (DW). (**a**) A full-contrast spin DW is created by DMD addressing, where the green areas indicate the addressing light and the blue arrows the effect of the microwave (MW) drive. (**b**) A globally resonant MW pulse is used to reduce the $\hat{S}^z$ contrast. (**c**) To introduce entropy, a spatially random spin-dependent potential is projected, which controllably dephases each atom. By varying the random pattern from shot to shot, we realize a high-temperature mixed initial DW state.

which give rise to an average spin profile of

$$\langle \hat{S}_i^z(t=0)\rangle = \frac{1}{2}\begin{cases}\delta+\eta, & (i<0),\\ \delta-\eta, & (i>0).\end{cases} \tag{6.3}$$

To probe the spin dynamics, we follow the experimental sequence shown in Fig. 6.3: After ramping up the 670 nm DMD light to form the box-shaped on-site potential, we ramp down Lattice 1 (L1) to the lattice depth suitable for dynamics—typically at $10E_r^{532}$ (see Tab. 6.1)—while keeping Lattice 2 (L2) at $40E_r^{532}$ to obtain independent 1D systems. Following the evolution time, we freeze the spin dynamics by quickly increasing the L1 depth. Both quench and freeze ramp durations are chosen to be fast with respect to the superexchange time scale, which governs spin dynamics, while being more adiabatic on the hopping time scale to minimize excitations in the charge sector. Finally, we optically push out one spin species to measure the local occupation of a spin state. Using a MW sweep prior to push-out allows us to select which spin species to detect. We typically average over 1000 1D shots per data point.

Experimental observables

We separately measure the mean densities, $\langle \hat{n}_i^\sigma \rangle$, of each spin species, σ, and formally assign the mean spin value as $\langle \hat{S}_i^z \rangle = (\langle \hat{n}_i^\uparrow \rangle - \langle \hat{n}_i^\downarrow \rangle)/2$. We furthermore introduce the polarization transfer as a convenient integrated spin transport quantity, which is

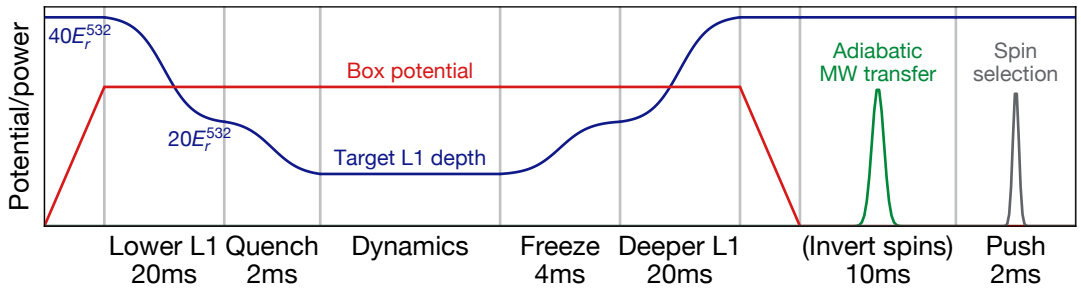

Figure 6.3: Experimental sequence for probing spin dynamics. 1D spin dynamics is initiated in a box potential by lowering the Lattice 1 (L1) depth while keeping Lattice 2 deep. After freezing the spin distributions arising through evolution times of up to 1 s, we perform single-site–resolved imaging of one spin species.

V_1	J/h	U/h	J_{ex}/h	$J_{\mathrm{ex}}^{\mathrm{QW}}/h$
$10.0(2)E_r^{532}$	42.7(9) Hz	737(26) Hz	9.9(2) Hz	10.2(2) Hz
$8.0(1)E_r^{532}$	66(1) Hz	686(24) Hz	27.5(6) Hz	27.0(2) Hz

Table 6.1: Calibrated Heisenberg model parameters. The other lattices were kept at a depth of $V_2 = 40.0(6)E_r^{532}$ and $V_3 = 15.0(3)E_r^{532}$, respectively. All lattice depths were calibrated by lattice AM spectroscopy. The Bose–Hubbard parameters were obtained through band structure calculations: J denotes the bond-charge–corrected hopping energy, see Eq. (2.5), U the Hubbard interaction energy, and J_{ex} the spin exchange energy. $J_{\mathrm{ex}}^{\mathrm{QW}}$ is extracted from a fit to a single-spin quantum walk and is consistent with the band structure calculations.

defined by

$$P(t) = \sum_{i<0} \langle \hat{S}_i^z(t) - \hat{S}_i^z(0) \rangle - \sum_{i>0} \langle \hat{S}_i^z(t) - \hat{S}_i^z(0) \rangle \tag{6.4}$$

and quantifies the number of spins which have crossed the DW by time t. As the spin profiles are related to the DSF and thus scale with the dynamical exponent according to Eq. (5.16) in the universal limit, the polarization transfer is expected to follow a power law, $P(t) \propto t^{1/z}$, which provides us with a higher–SNR observable to directly extract the dynamical exponent.

6.2.2 Spin transfer dynamics

In a first set of measurements, we study the equilibration dynamics of a net-unmagnetized DW with purity $\eta = 0.22(2)$. This purity serves as a compromise to provide a sufficient SNR against fluctuations in preparation while being close to the linear-response regime, for which superdiffusion has been predicted. As shown in Fig. 6.4, a power-law fit to

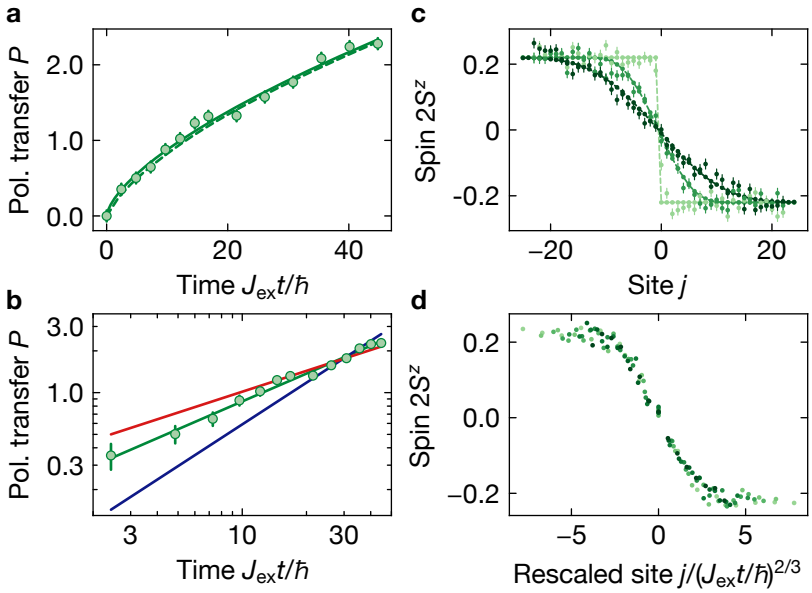

Figure 6.4: Observation of superdiffusive spin transport. (**a**) The polarization transfer across the domain wall shows a power-law growth with time, $P \propto t^{1/z}$. Fitting the data (solid line) yields a dynamical exponent of $z = 1.55(6)$, indicating superdiffusive spin transport. The experimental data furthermore show quantitative agreement with numerical simulations (dashed line). (**b**) Plotting the polarization transfer on a double-logarithmic scale, we can observe that the data is clearly inconsistent with both ballistic (blue) and diffusive (red) transport. (**c**) The agreement with theory holds also on the level of the evolving spin profiles, here shown for the time steps $J_{ex}t/\hbar = 0, 10, 26$ (bright to dark). (**d**) Rescaling the spatial axis by the KPZ dynamical exponent furthermore collapses the data (shown for the time range $J_{ex}t/\hbar = 5$–35), indicating superdiffusive universal scaling of the dynamical structure factor.

the growth of the polarization transfer yields a dynamical exponent of $z = 1.54(7)$, establishing anomalous superdiffusive transport, clearly distinct from both ballistic and diffusive exponents.

Since our quantum gas microscope (QGM) also gives access to spatially resolved data, we can furthermore extract the integrated DSF. After rescaling the spin profiles by the expected dynamical exponent, $j \to j/t^{2/3}$, we indeed find a collapse of the data, confirming superdiffusive hydrodynamics. Fitting the rescaling exponent to the evolving spin profiles yields an exponent of $z = 1.55(6)$, in agreement with the polarization-transfer analysis.

The functional form of the spin profiles are in addition consistent with the integrated KPZ scaling function. However, we note that this observation does not prove KPZ universality as the data quality does not allow us to discern the functional form from

an error function [64] (which would be expected for a Gaussian DSF). Finally, we can compare the experimental data to numerical simulations based on tensor-network techniques [232, 233], which show quantitative agreement on the level of the spin profiles.

After probing the low-contrast DW dynamics in the high-temperature regime closer to equilibrium, we also performed measurements starting from a pure-state DW. We describe the results in detail in Sec. 6.4.2 and note here that the contrast-normalized polarization transfer, $P(t)/\eta$, showed very similar superdiffusive behavior as the low-contrast case.

6.3 Microscopic origins of superdiffusion

Following the discovery of superdiffusion in the XXX model, theoretical studies were performed to identify more general requirements for a model to feature superdiffusive transport. This has led to the notion of "superuniversality" [220, 221], wherein spin superdiffusion generically occurs in integrable models with a non-abelian symmetry, including the SU(2)-symmetric integrable XXX chain. In terms of GHD (see Sec. 6.1.1), integrability ensures stable quasiparticles—which prevents regular diffusion—and the SU(2) symmetry ensures a vanishing net magnetization of the quasiparticles—which prevents a finite Drude weight—while retaining a diverging diffusion constant.

From an experimental point of view, this setup provides the opportunity to study the validity of the numerically proposed requirements and the GHD prediction. To probe potential changes in the transport behavior, our QGM allows us to controllably break both integrability—by realizing the non-integrable 2D XXX model—or the SU(2) symmetry—by preparing net magnetized initial states, which correspond to the equilibrium state under a symmetry-breaking external field.

6.3.1 Breaking integrability

As our experiment intrinsically works with 2D systems, whose coupling in either dimension can be adjusted by the applied lattice depth, we can realize 2D XXX models by introducing a finite inter-chain coupling, $J_{\mathrm{ex}}^{\perp}$. To realize 2D systems, we added a step in the experimental sequence after loading the MI, in which we remove all atoms outside a well-defined rectangle using local addressing. This procedure prevents global atom-number fluctuations to result in non-unity–filled states within the box potential, outside of the Hilbert space of the spin model.

In analogy to the 1D measurements, performed at a lattice depth of $10E_r^{532}$ along the 1D chains for near-pure DWs of $\eta \sim 0.9$, we track the evolution of the polarization transfer for varying inter–to–intra-chain coupling ratios, $J_{\mathrm{ex}}^{\perp}/J_{\mathrm{ex}}$. We then fit a power law to the data up to a time of $J_{\mathrm{ex}}t/\hbar \sim 50$ and extract the dynamical exponent z. As shown in Fig. 6.5, we find that spin transport indeed becomes diffusive when increasing

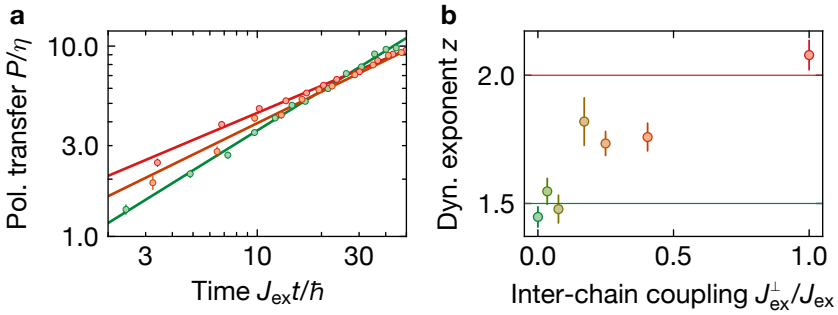

Figure 6.5: Diffusive spin transport under integrability breaking. (**a**) The time evolution of the normalized polarization transfer at inter-chain coupling ratios of $J_{ex}^{\perp}/J_{ex} = 0, 0.40(1), 1.00(5)$ (green to red) follows power laws, $P(t) \propto t^{1/z}$. (**b**) The fitted dynamical exponents, z, change from being superdiffusive in the 1D case, $J_{ex}^{\perp} = 0$, to being diffusive in the 2D case, $J_{ex}^{\perp} = J_{ex}$. The horizontal lines indicate the KPZ superdiffusive (green) and diffusive (red) exponents.

the inter-chain coupling, with $z = 2.08(4)$ in the fully 2D case. Interestingly, we observe superdiffusive exponents for $J_{ex}^{\perp}/J_{ex} \lesssim 0.1$ despite integrability being strictly broken, which we attribute to the limited experimentally accessible time scales. This behavior is in fact consistent with theoretical studies suggesting that superdiffusion is particularly robust to perturbations preserving the non-abelian symmetry [234].

Finally, we remark that the 2D systems do not fully conform to the XXX model anymore: First, given a constant lattice depth, the MI–superfluid (SF) phase transition grows closer with increasing inter-chain coupling. This leads to a reduction in the formal DW contrast from $\eta = 0.93(2)$ in 1D down to $\eta = 0.83(2)$ in the isotropic 2D case. Second, thermal holes in the 2D t–J model can re-order the spins on the hopping time scale, which is parametrically faster than the spin-exchange time scale, whereas in 1D both processes occur on the J_{ex} time scale. Despite these caveats, the measurements of the conserved spin degree of freedom (DOF) nevertheless serve as a suitable probe of integrability breaking, demonstrating diffusive behavior.

6.3.2 Breaking SU(2) symmetry

The second predicted prerequisite for superdiffusion in the XXX model is the presence of the SU(2) symmetry. We break the symmetry by initializing the system to a net-magnetized initial DW, $\delta > 0$.

To prepare half of the system with arbitrary mean magnetization, we apply a (not fully inverting) resonant MW pulse (instead of the adiabatic sweep used in Fig. 6.2a) with pulse area $\theta = \tilde{\Omega}t$ to a system, onto which a DW pattern is projected with the DMD. This procedure ideally results in the state $[\bigotimes_{j<0}(\sin\theta|\uparrow\rangle_j + \cos\theta|\downarrow\rangle_j)] \otimes [\bigotimes_{j>0}|\downarrow\rangle]$. However, the generalized Rabi frequency depends on the local detuning, $\tilde{\Omega}_i^2 \propto \delta h_i^2$,

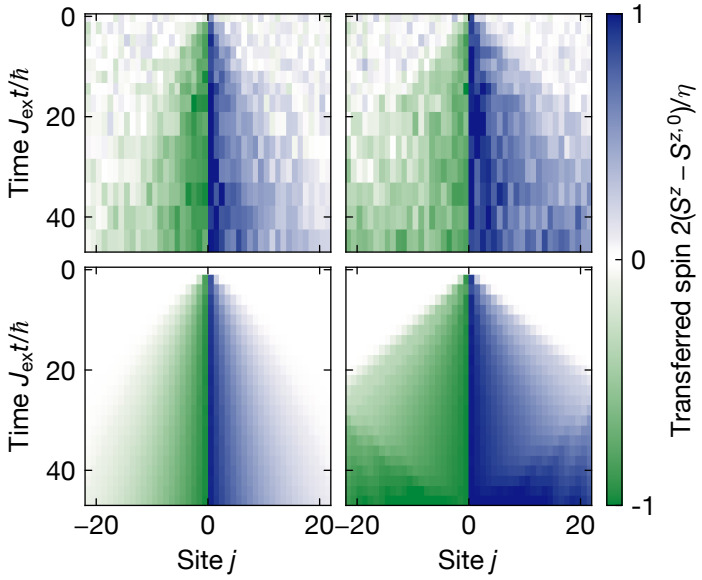

Figure 6.6: Ballistic spin transport under SU(2)-symmetry breaking. Time evolution of the spin profiles for an unmagnetized domain wall (DW) (left, $\delta = 0$, $\eta = 0.22(2)$) and a net-magnetized DW (right, $\delta = 0.80(1)$, $\eta = 0.12(1)$). The experimental data (top) agrees well with the numerical data (bottom), displaying a stark contrast depending on net magnetization. While the unmagnetized case shows superdiffusive behavior, the net-magnetized case exhibits ballistic transport, which can be seen by the overall increased spin transfer. Additionally, the net-magnetized case also transfers spins with the speed of the spin "light cone". After reaching the edge of the system at $J_{ex}t/\hbar \approx 25$, the magnons are reflected.

thus translating speckles on the DMD light, δh_i, directly onto the spin state. To minimize such effects, we decided to perform this preparation step on only half the system, keeping the other half spin-polarized, which gives access to DWs with $\eta \approx (1 - \delta)$. Using a subsequent dephasing DMD pulse (see Fig. 6.2c), we again obtain a high-entropy state.

The equilibration measurements were performed analogously to the 1D unmagnetized case and the spin dynamics are shown in Fig. 6.6. In the spatially resolved plots for the net-magnetized case, $\delta = 0.80(1), \eta = 0.12(1)$, a striking feature is the presence of spin transport with the speed of the spin "light cone", $c = \hbar/J_{ex}$. This contribution to spin transport may be attributed to single magnons, showing that even the fastest quasiparticles indeed retain a net magnetization [235]. Furthermore, the bulk of the spins—mediated by slower-moving, heavier quasiparticles—displays transport that is substantially faster than in the unmagnetized case. To quantify the transport dynamics, we fit the polarization transfer to a power law with offset, $P(t) \sim t^{1/z} + \text{const.}$ (with

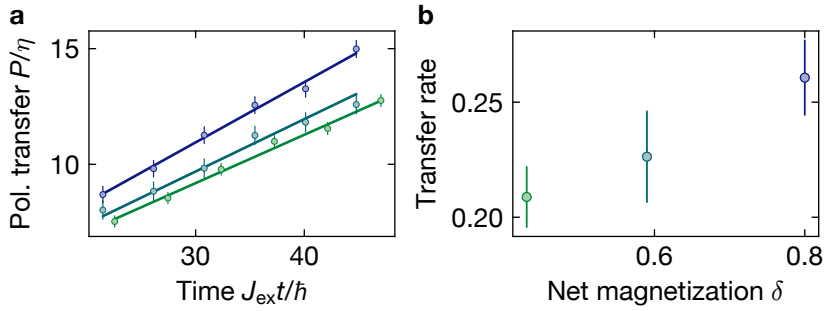

Figure 6.7: Ballistic polarization transfer rate. (**a**) We measure the normalized polarization transfer for increasing net magnetization δ (green to blue) and fit a linear function to the ballistic regime at $J_{ex}t/\hbar > 16$. (**b**) Using the fitted slope as the normalized polarization-transfer rate, $d(P/\eta)/d(J_{ex}t/\hbar)$, we observe an increase with δ, consistent with GHD.

the offset accounting for finite-time crossover behavior, which will be discussed in Sec. 6.3.3). The fit indeed reveals a departure from superdiffusion, yielding a dynamical exponent of $z = 0.9(3)$ and thus ballistic spin transport.

GHD does not only predict the dynamical exponent but also the amount of transported spins. In particular, following Sec. 5.2.2 for the XXX chain at small η, δ, we would expect the polarization transfer to grow as $P(t) \propto \delta t$ [117]. While the proportionality with net magnetization is not necessarily expected to hold for our experimentally accessible DW parameters, the increasing magnetization of the quasiparticles with δ suggests that the polarization transfer rate also increases [228]. In Fig. 6.7, we therefore measure the polarization transfer as a function of δ and calculate the transfer rate, dP/dt, from a linear fit of the polarization transfer for times $J_{ex}t/\hbar > 16$. Extracting the transport rate from the slope, we indeed find a growth with net magnetization.

6.3.3 Crossover dynamics

The assumption that the polarization transfer follows a simple power law is based on a late-time hydrodynamic approximation, where only a single scaling form is relevant. Apart from the local microscopic dynamics, which typically only gives rise to oscillations around a mean charge density, we can account for hydrodynamic finite-time effects by considering sub-leading terms. For instance, in the net-magnetized case, $\delta > 0$, we expect both ballistic and superdiffusive contributions to the polarization transfer, $P(t) = at^1 + bt^{2/3} + \cdots$. While the asymptotic power law is valid, a more accurate fit generally requires accounting for the additional transport through sub-leading terms. Since these terms are parametrically smaller, they can be better approximated by a constant after the crossover time scale t_c, such that the polarization transfer would be described by $P(t) \approx at^1 + bt_c^{2/3}$.

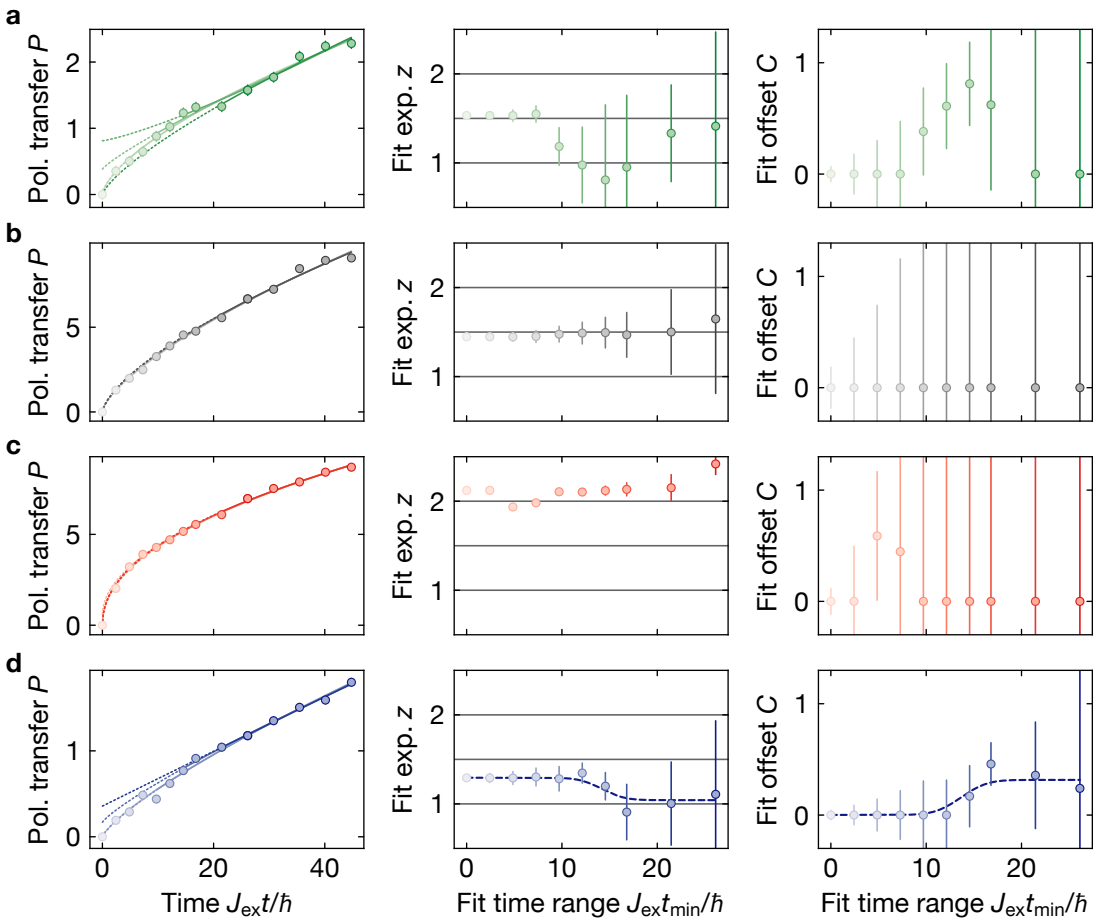

Figure 6.8: Crossover analysis of dynamical exponents. Data analysis of the polarization transfer for the 1D unmagnetized case with domain wall contrasts **(a)** $\eta = 0.22(2)$ and **(b)** $\eta = 0.95(2)$, **(c)** the 2D unmagnetized case with $\eta = 0.83(2)$ and **(d)** the 1D magnetized case with $\delta = 0.80(1), \eta = 0.12(1)$. We use the fit function $P(t) = At^{1/z} + C$ under the physical constraint $C \geq 0$ and analyze the data for the time range starting at t_{min}. By varying the fitted time window, we can account for initial-time crossover effects, see main text for details. The dotted lines in the left columns indicate the optimum fit function for a given fitted time window (light to dark for increasing t_{min}). The dashed lines in the center and right columns of (d) serve as a guide to the eye. The error bars denote the standard deviation (SD) of the fit.

As this discussion is generally valid for arbitrary leading-order exponents, we use the fit function $P(t > t_{\mathrm{min}}) = At^{1/z} + C$ to model-independently analyze our experimental data in Fig. 6.8. When varying the fitted time range, t_{min}, we expect convergent fit parameters after passing a crossover time scale, $t_{\mathrm{min}} \gtrsim t_c$.

For neither of the unmagnetized DWs, we can observe a crossover behavior, which is consistent with GHD which predicts the (super-) diffusive contribution to be dominant. Note that the $\eta = 0.22$ 1D data shows time-range–dependent variations of the optimum fit parameters; however, these occur due to the visually appreciable statistical fluctuations, and are not present at all for the $\eta = 0.95$ case which has a much lower SNR.

The only convergent change of the fitted exponent can be observed for the net-magnetized case. This finding is consistent with GHD reasoning at low net magnetization, see Sec. 6.1.1, where the magnetization of undressed quasiparticles requires a certain time scale to average to zero, which represents the time scale from which on ballistic transport becomes perceivable. Note that, for the large net magnetization of $\delta = 0.8$ studied here, XXX model simulations predict a shorter crossover time; however, the presence of thermal holes and further Bose–Hubbard (BH) effects could alter polarization-transfer and time scales [117].

6.4 Pure initial states far from equilibrium

In Sec. 6.2 we have discussed the observation of clearly superdiffusive spin transport in the XXX chain using the DW protocol. This result leads to an apparent contradiction with prior measurements based on the decay of Fourier modes [60, 96, 230], which obtained regular diffusive behavior. Notably, the experimental data of Ref. [230] disagreed with the expected dynamical exponents regimes for all probed Heisenberg anisotropies. However, recalling the deliberation in Sec. 6.1.1, these GHD predictions were based on the linear-response dynamics of high-entropy mixed states, whereas the aforementioned measurements started in pure states far from equilibrium. In this section we will discuss the role of purity in the evolution of such spin helix states as well as pure DW states.

6.4.1 Spin helices

In our experiment, spin helix states can be prepared using the protocol shown in Fig. 6.9 and introduced in Ref. [60]: Starting with a spin-polarized MI of 32 spins in the atomic limit, $\bigotimes_j |\downarrow\rangle_j$, we apply a magnetic-field gradient to generate a spin-dependent potential gradient, $\delta h = h \cdot 6.85(3)$ Hz, along the 1D chains. After applying a MW $\pi/2$ pulse, the spins start to precess in the $\hat{S}^{x,y}$ plane; the magnetic gradient causes adjacent spins to pick up a linear differential phase of $k = \delta h T/\hbar$ after a waiting time of T. We then apply another $\pi/2$ pulse, thus realizing the state $\bigotimes_j (\cos kj|\uparrow\rangle_j + \sin kj|\downarrow\rangle_j)$.

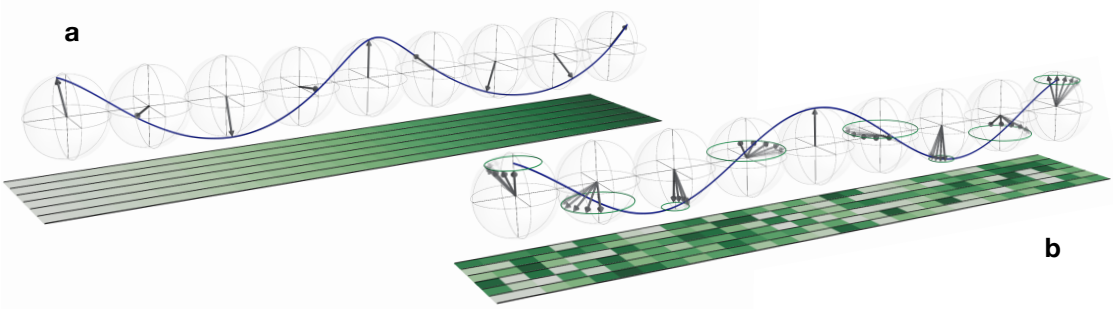

Figure 6.9: Preparation of spin-helix states. The helix preparation steps are shown in analogy to Fig. 6.2. (**a**) Starting in a spin-polarized state, we employ a Ramsey microwave pulse sequence under the presence of a magnetic-field gradient along the 1D chains to create full-contrast, pure spin-helix states. (**b**) By subsequently using the DMD to apply a shot-to-shot random spin-dependent potential, we can dephase the helix, yielding a mixed state with sinusoidal $\hat{S}^z$ modulation.

Note that we quickly switch off the gradient before the second MW pulse to prevent uncontrolled further spin precession. We then probe spin dynamics in the same way as for the DW measurements by ramping down L1 to a depth of $10E_r^{532}$ and freezing the spins after the desired evolution time.

In analogy to Sec. 6.2.1, we can furthermore reduce the modulation contrast to introduce entropy to the initial state by applying a global MW pulse and dephasing the $\hat{S}^{x,y}$ components of the spins through a spatially random DMD pulse before ramping down the lattice. Thus, we can study the evolution of an initial $\hat{S}^z$ modulation of

$$2\langle \hat{S}^z_j(t=0)\rangle = \eta \cos kj. \tag{6.5}$$

Note that the phase of the modulation is random from shot to shot as it depends on the absolute value of the global magnetic field (in contrast, the gradient of the magnetic field remains stable, resulting in a faithful preparation of the spin helix). To account for the random phase, we compute the equal-time connected correlator of the spin, $\langle \hat{S}^z_i(t)\hat{S}^z_{i+j}(t)\rangle^c_i \propto \langle \hat{S}^z_j(t)\rangle_{\varphi=\text{const.}} \sim C(k;t)\cos kj$. Fitting a sinusoidal function to the correlator allows us to extract the contrast over time, $C(k;t) \sim e^{-\gamma(k)t}$, which we in turn fit with an exponential decay (over a k-dependent time range corresponding to a dynamic range of one order of magnitude). By varying the wave number of the initial state, k, we finally obtain the dependence $\gamma(k) \propto k^z$ required to extract the dynamical exponent, z, following Eq. (5.17).

Spin helix purity

To probe the dependence of the dynamical exponents on the purity of the initial state, we perform measurements with and without dephasing. We furthermore compare

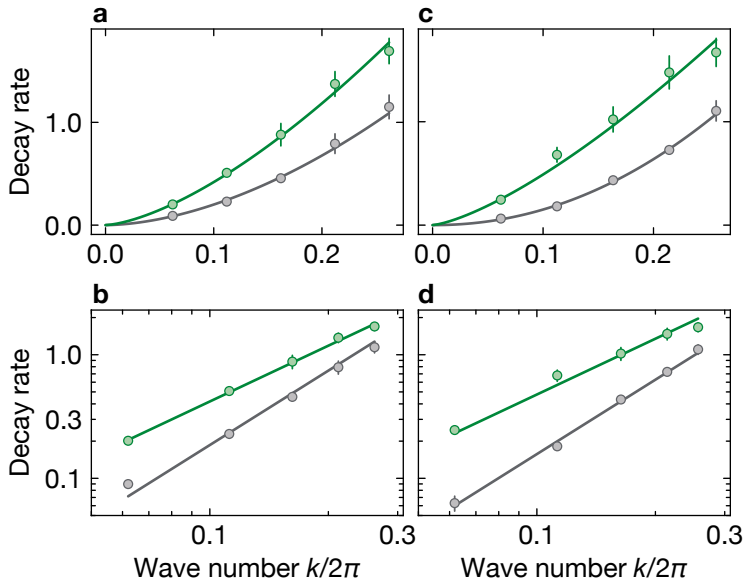

Figure 6.10: Decay-rate scaling of spin helices. (**a, c**) From the decay rate of the spin-helix contrast, $\hbar\gamma/J_{\mathrm{ex}}$, as a function of its wave number, we extract the dynamical exponent z by fitting the expected power-law growth (lines), $\gamma \propto k^z$. We compare dephased (green) with non-dephased (gray) helices at initial contrasts of $\eta \sim 0.86$ (left) and 0.35 (right). (**b, d**) The data plotted double-logarithmically show a significant difference between the dephased and pure cases. As a reference, the lines indicate power-law growth with a superdiffusive exponent of $z = 3/2$ (green) and diffusive exponent of $z = 2$ (gray).

whether a difference between full-contrast helices (with a formally fitted $\eta \sim 0.86$) and reduced-contrast ones ($\eta \sim 0.35$) exists, i.e., considering how far the initial state is from equilibrium. In Fig. 6.10, we find superdiffusive exponents in both dephased cases, $z = 1.5(1)$ and $1.4(1)$, for the pure- and low-contrast helices, respectively. On the contrary, both non-dephased cases—which are expected to be the same state in an XXX model—give fitted exponents of $z = 1.8(1)$ and $2.1(1)$, respectively. This difference suggests that the evolution of pure states in the XXX chain can be particularly distinct from "generic" states, whose superdiffusive spin transport relies on the presence of thermal fluctuations, in agreement with GHD.

Ref. [236] furthermore applied GHD to study the decay of full-contrast spin helices, finding diffusive exponents in the easy-axis regime, $|\Delta| > 1$, and ballistic ones in the easy-plane regime, $|\Delta| < 1$, albeit at inaccessibly late times and large helix wavelengths. At the isotropic point, realized in our experiment, GHD cannot be directly applied; however, a non-rigorous reasoning suggests an explanation for the observed exponent of $z = 2$ instead of the high-temperature exponent, $z = 3/2$: While quasiparticles of all

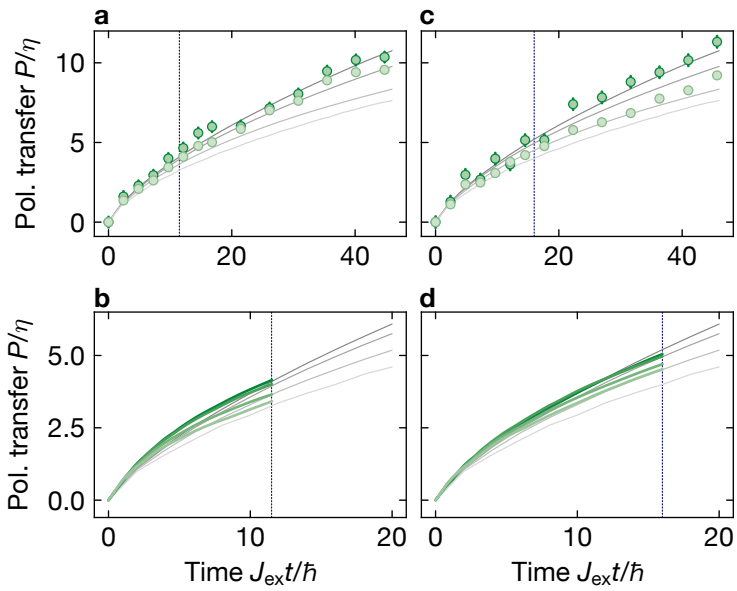

Figure 6.11: Polarization transfer for varying purity and lattice depth. (**a, c**) Experimental data (green) measured at a lattice depth of $10E_r^{532}$ (left) and $8E_r^{532}$ (right) with initial domain wall purities of $\eta \sim 0.2$ (dark) and $\eta \sim 0.9$ (light). Numerical simulations of the XXX model are shown in grey for $\eta = 0.1, 0.4, 0.7, 1.0$ (dark to light), suggesting a stronger dependence on η than the measured. (**b, d**) Numerical simulations of the Bose–Hubbard model (green) for a filling of 0.93 at the same purities as the XXX model simulations show a reduced sensitivity on η, qualitatively indicating that holes affect the observed polarization transfer dynamics. Note the different plotted time ranges between simulated and experimental data (blue line).

string sizes are populated for thermal states, the quasiparticle content for full-contrast spin helices of wavelength λ is dominated by strings of size $s = \lambda$. Following the discussion around Eq. (6.2), this then leads to diffusive spin transport.

6.4.2 Domain walls

A similar difference in spin transport behavior could be expected for the pure DW, as well. In fact, it has been shown that full-contrast DWs cannot thermalize at all in the easy-axis regime [237, 238] and give rise to diffusive transport with logarithmic corrections at the isotropic point [63, 239].

Full-contrast DWs are experimentally accessible by simply not performing the contrast-reducing MW and locally spin-dephasing DMD pulses during the initial-state preparation described in Sec. 6.2.1. In Fig. 6.11, we compare the polarization-transfer dynamics of a DW with $\eta \sim 0.2$ to a DW with $\eta \sim 0.9$. Interestingly, the contrast-normalized polarization transfer, P/η, does not show a strong difference and the fitted

dynamical exponent retains agreement with the KPZ exponent of $z \sim 3/2$ within experimental uncertainties. Numerical simulations of the XXX model confirm that the apparent dynamical exponent does not significantly change; at full contrast, $\eta = 1$, regular diffusion becomes noticeable only after a crossover duration of hundreds of exchange times, substantially exceeding experimentally accessible time scales. However, the simulations predict that the absolute growth of P/η should decrease with increasing purity. While we observe this trend, there remains a quantitative discrepancy.

One possible cause are imperfections in implementing the XXX model: As the physically underlying model is a two-species BH model, we perform simulations of the full BH model, accounting for our finite filling of ~ 0.93. The results qualitatively confirm that reduced filling reduces the sensitivity of P/η. To verify consistency, we additionally perform this measurement at a lattice depth of $8E_r^{532}$ instead of $10E_r^{532}$, which yields similar fitted exponents. In the $8E_r^{532}$ case, P/η is also reduced for higher purity (consistent with numerics), but displays a stronger dependence than in the $10E_r^{532}$ case. This could hint at the presence of system inhomogeneities, which affect the dynamics in the $10E_r^{532}$ case more since the hopping and spin-exchange energies are smaller on an absolute scale.

Finite domain-wall purity

The measurements furthermore raise the question about the fate of finite-purity DWs, $\eta < 1$. Classical simulations of the Landau–Lifshitz spin chain (modified to obey integrability) suggest DWs with any finite $\eta > 0$ to eventually become diffusive [240]. This would be consistent with the expectation that the pure DW state clearly comprises a broken non-abelian symmetry, which was identified as prerequisite for superdiffusion [220, 221, 241]. For *quantum* spin chains, however, it remains an open question as no analytic results are known, and both numerics and experiments are limited in evolution time [63]. In both quantum and classical cases, numerical data suggest that up to a crossover timescale—governed by the DW purity—the effective dynamical exponent appears to be consistent with superdiffusion. One explanation entails that in the space–time regime where the dynamics occur, local equilibration temporarily effectively realizes the required SU(2) symmetry. Regardless of the fundamental origin, this suggests that—at sufficiently early hydrodynamic time scales—it could be possible to observe features of KPZ universality even at $\eta \sim 1$, as will be discussed in detail in Chapter 7.

6.5 Conclusion and outlook

In this chapter we have studied spin transport in the 1D spin–1/2 XXX model. By measuring the equilibration dynamics of a high-temperature DW and utilizing the spatial resolution of our QGM, we have measured the spin DSF and found it to be con-

sistent with the superdiffusive KPZ scaling function. In order to test the microscopic understanding of spin transport based on GHD, we demonstrated that switching to a 2D XXX model restores regular diffusion, while preparing net magnetized 1D states results in ballistic transport. This corroborates theoretical studies suggesting integrability and non-abelian symmetry to be prerequisites for superdiffusion. With measurements of the evolution of dephased spin helices, we have furthermore demonstrated that, while pure initial states can show distinct behavior, thermal fluctuations recover superdiffusion.

Having probed spin transport at the isotropic point, an extension of the study could involve spin dynamics under general anisotropies, which could be implemented through laser-assisted hopping processes [242]. In particular, crossovers of the transport exponents (possibly for varying initial states) could be studied, which are expected to occur near the isotropic point, where (super-) diffusive fluctuations compete with ballistic modes. The spin transport regimes could be furthermore contrasted with energy transport, for which GHD predicts ballistic transport regardless of anisotropy [214], and could be measured through the time evolution of energy DWs. Finally, the effects of integrability breaking on spin transport could be studied in more detail: Notably, integrability-breaking but symmetry-preserving perturbations are predicted to only weakly affect superdiffusive transport, whereas symmetry-breaking ones quickly yield diffusion [234]. In a 2D arrangement of 1D XXX chains, such symmetry-breaking terms could comprise inter-chain Ising interactions implemented through spin-independent orthogonal potential gradients [243].

Chapter 7

Polarization transfer fluctuations

In Chapter 6, we have demonstrated that spin transport in the net-unmagnetized isotropic Heisenberg (XXX) chain is superdiffusive. However, the exponent of the space–time scaling behavior alone is generally insufficient to identify the universality class of the dynamics: The observed dynamical exponent of $z = 3/2$ could *a priori* not only result from nonlinear Kardar–Parisi–Zhang (KPZ) dynamics but also from linear underlying transport equations, such as rescaled diffusion or Lévy flights [63, 229]. The original numerical evidence, suggesting spin transport in the XXX chain to fall into the KPZ universality class, was based on comparing the dynamical structure factor (DSF) with the KPZ scaling function [64]. While our measurements of the DSF were consistent with this function, the finite experimental signal-to-noise ratio (SNR) did not allow us to exclude other transport mechanisms.

An alternative approach to classifying transport makes use of universal fluctuations of the transported quantity and is also applicable to quantum models. This concept arises naturally in two-terminal measurements, which are not only common in solid-state systems but have also found use in ultracold atom experiments [244]. In this context, quantum gas microscopes (QGMs) are uniquely suited to measure the spatio-temporally resolved full counting statistics (FCS), as they provide access to the transported quantities on the level of single sites and single charges. Microscopic control over initial states further enables the preparation of suitable non-equilibrium settings. In this chapter, we introduce our experimental approach to measuring the FCS of spin transport in Sec. 7.1 and show resulting signatures of KPZ–like dynamics in Sec. 7.2.

7.1 Counting statistics in spin transport

The core quantity for studying the spin transport fluctuations is the polarization transfer introduced in Eq. (6.4), $P(t) = P_0(t) - P_0(0)$, with $P_0(t) = \sum_{i<0}\langle \hat{S}_i^z(t)\rangle - \sum_{i>0}\langle \hat{S}_i^z(t)\rangle$. In experiments working on the basis of individual model realizations, like QGMs, the polarization transfer can be analyzed for each snapshot, yielding a distribution, $\Pr[\hat{P}(t) = P]$, characterizing the transport fluctuations. For a limited amount of data, these distributions can be evaluated through their statistical moments and compared to known distributions distinctive of the respective universality class.

7.1.1 Measurement protocol

As the polarization transfer measures the amount of magnetization which has crossed a given interface, it generally depends on the $\hat{S}^z$ distribution at two points in time. However, as we are working with a quantum system, this quantity cannot be directly evaluated since initial states may contain quantum fluctuations in S^z. A generally applicable measurement of $\hat{P}(t)$ would thus require an ancilla-based protocol [245, 246]. This requirement can be avoided in our setup, when limiting initial states to deterministically prepared S^z product states.

Specifically, we choose to measure the fluctuation dynamics starting from pure domain walls (DWs), which show superdiffusive behavior within experimentally accessible times, as described in Sec. 6.2.2. As we can simultaneously only detect the occupation of a single spin species in a snapshot, and the Mott insulator (MI) is reasonably close to unity-filled, we can approximate the spin as $\hat{S}_i^z \approx \hat{n}_i - 1/2$. Thus, the polarization transfer becomes $\hat{P}(t) \approx 2\hat{N}_T(t) \equiv 2\sum_{i>0} \hat{n}_i(t)$ and equates to counting the number of atoms on the initially empty side ($i > 0$), $\hat{N}_T(0) = 0$.

While the choice of a pure DW may be conceptually not ideal for probing the theoretically predicted near-equilibrium KPZ physics, it substantially alleviates the experimental challenge of reaching sufficiently low noise levels suitable for measuring FCS. This is achieved primarily by the fact that counting atoms above virtually no background yields the highest possible SNR. Furthermore, addressing large-scale patterns like the DW gives much higher preparation fidelities compared to, e.g., randomized local spin flips, which would be necessary to prepare high-entropy states. Finally, the non-equilibrium setting breaks the chiral symmetry present in equilibrium. Potential deviations from regular Gaussian fluctuations could thus manifest as *asymmetric* distributions, and may be observable already in the third instead of the fourth statistical moment. Specifically, we can then search for a non-vanishing skewness, $\mu_3[\hat{X}]/\mu_2^{3/2}[\hat{X}]$, where $\mu_k[\hat{X}]$ denotes the k-th central moment of the random variable $\hat{X}$.

Correcting for initial states

On experimentally accessible time scales, the number of transferred spins is relatively small, $\langle \hat{N}_T \rangle < 5$. Higher order statistics are thus very sensitive to additional atoms on the initially empty side due to imperfections in the initial-state preparation, $\langle \hat{N}_T(0) \rangle > 0$, which are typically introduced during addressing. The proper transport distribution, $\Delta\hat{N}_T(t) = \hat{N}_T(t) - \hat{N}_T(0)$, would thus require us to account for the initial state. If we assume the addressing defects to not significantly affect the rest of the spin dynamics (e.g. due to being far from the DW), $\hat{N}_T(t)$ and $\hat{N}_T(0)$ can be considered as independent random variables, for which cumulants are additive. Specifically, the k-th central moment of the corrected distribution can be written as $\mu_{k\leq 3}[\Delta\hat{N}_T(t)] = \mu_k[\hat{N}_T(t)] - \mu_k[\hat{N}_T(0)]$.

7.1.2 Central moments in linear transport

As noted in the introduction to this chapter, transport schemes with dynamical exponent $z = 3/2$ other than the KPZ universality class often follow linear transport equations, in contrast to the nonlinear KPZ equation (5.1). In linear transport, each spin moves according to the DSF as propagator, which scales as $\varphi(\Delta x, t) \sim (1/t^{1/z}) f(\Delta x/t^{1/z})$. The polarization transfer of this single spin is therefore a Bernoulli random variable, whose probability for crossing an interface at a distance x_0 from its starting point is thus given by $\Phi(x_0, t) = \int_{-\infty}^{x_0} \varphi(x, t)\, dx \sim F(x_0/t^{1/z})$; the single-spin cumulants then scale as a polynomial, $\mathfrak{P}[F(x_0/t^{1/z})]$.

In the case of many spins, linearity causes the cumulants of the polarization transfer to be additive. In a DW, all cumulants thus scale with $\int_{-\infty}^{0} \mathfrak{P}[F(x_0/t^{1/z})]\, dx_0 \propto t^{1/z}$, such that the skewness scales as $\mu_3/\mu_2^{3/2} \propto t^{-1/2z}$. Crucially, in linear models, the skewness always vanishes at late times, while possibly staying finite in nonlinear models.

7.2 KPZ fluctuations of the polarization transfer

The numerical simulations identifying spin transport in the XXX chain with the KPZ universality class were based on equating the spin DSF to the correlation function of the spatial derivative of the KPZ height field, h, see Eq. (5.3),

$$\langle \hat{S}^z(x,t)\hat{S}^z(0,0)\rangle_c \sim \frac{1}{t^{1/z}} f_{\mathrm{KPZ}}\left(\frac{x}{t^{1/z}}\right) \sim \langle \partial_x \hat{h}(x,t)\partial_x \hat{h}(0,0)\rangle. \tag{7.1}$$

In order to probe universal statistics of the KPZ class, first a suitable quantity representing the KPZ height field has to be identified. Informed by the mapping of the scaling function and canonical classical models in the KPZ class (see Sec. 5.1.3), the simplest option consists of assigning $\hat{S}^z(x,t) \sim \partial_x \hat{h}(x,t)$. This conjecture thus motivates studying the fluctuations of the polarization transfer,

$$\hat{h}(0,t) - \langle \hat{h}(0,t)\rangle \sim \int_{-\infty}^{0} dx \left(\hat{S}^z(x,t) - \hat{S}^z(0,t)\right) \sim \hat{P}(t), \tag{7.2}$$

whose statistical distribution can be compared to the KPZ distributions described in Sec. 5.1.2.

7.2.1 Asymmetric distributions in domain wall dynamics

We employ the experimental methods and parameters described in Sec. 6.2.1 to prepare the pure DW as initial state and evolve the system at a lattice depth of $10E_r^{532}$. We then analyze the polarization-transfer statistics according to Sec. 7.1.1. In addition to measurements of the one-dimensional (1D) spin model, we compare the results

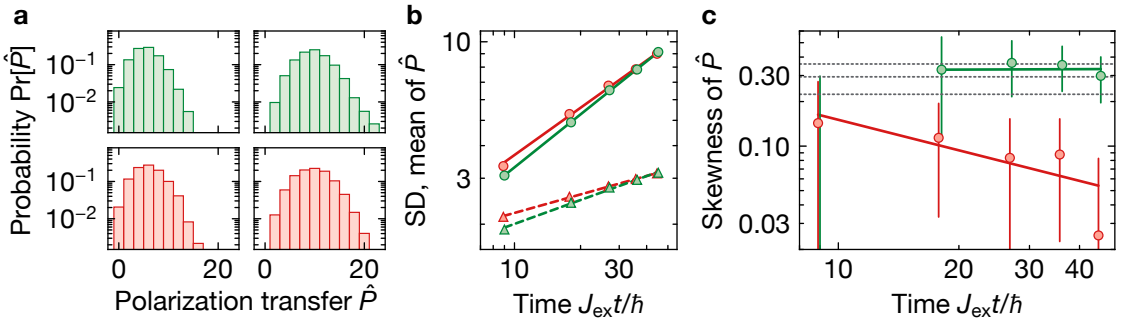

Figure 7.1: Fluctuations of the polarization transfer. (**a**) Distributions of the polarization transfer, $\Pr[\hat{P}(t)]$, after evolution times of $J_{ex}t/\hbar = 18.1$ (left) and 45.2 (right) of the XXX model in 1D (green) and 2D (red). (**b**) The mean of the polarization transfer (circles) is confirmed to scale with the inverse dynamical exponent, $1/z_{1D} = 2/3$ and $1/z_{2D} = 1/2$ (solid lines). The standard deviation (SD) (triangles) follows a power law with the growth exponent, $\beta_{1D} = 1/3$ and $\beta_{2D} = 1/4$ (dashed lines). (**c**) The evolution of the skewness of the 2D data suggests a decay towards zero, implying a Gaussian distribution associated with linear transport. In contrast, the skewness of the 1D case remains finite, implying nonlinear transport. The value of the skewness is furthermore consistent with the ones associated with the KPZ universality class (gray lines), namely the Tracy–Widom GUE, Tracy–Widom GOE and the Baik–Rains distribution (bottom to top).

to the two-dimensional (2D) case with an inter-chain coupling strength of $J_{ex}^{\perp}/J_{ex} = 0.25(1)$. This data serves as a reference of a non–KPZ model, for which we have demonstrated diffusive behavior in Sec. 6.3.1 and for which the formal DW contrast remains comparable, $\eta_{1D} = 0.91(2), \eta_{2D} = 0.89(1)$.

In Fig. 7.1, we first show the mean of the polarization transfer, $P(t) \propto t^{1/z}$, verifying the power law with dynamical exponents $1/z_{1D} = 0.67(1)$ and $1/z_{2D} = 0.60(2)$. Furthermore, we can analyze the scaling behavior of the variance, $\mu_2[\hat{P}(t)] \propto t^{2\beta}$, which represents a direct measurement of the KPZ growth exponent β, as outlined in Sec. 5.1.2. Power-law fits yield the exponents $\beta_{1D} = 0.31(1)$ and $\beta_{2D} = 0.24(1)$, consistent with the expected $\beta = 1/2z$ behavior.

Finally, we proceed to the analysis of the skewness, $\mu_3[\hat{P}(t)]/\mu_2^{3/2}[\hat{P}(t)]$: In 2D we find an overall small skewness, which is most consistent with a decay towards zero. This behavior follows the expectation that fluctuations in linear diffusive processes eventually become Gaussian. In contrast, the 1D case displays a substantially larger skewness, which furthermore remains constant over time. This observation indicates that the spin transport in 1D is governed by nonlinear transport processes and rules out several non-KPZ processes including, e.g., Lévy flights.

The value of the observed skewness, 0.33(8), can be furthermore compared to

the skewness of the KPZ distributions. Following the proposed spin–to–KPZ-height mapping, a pure spin DW corresponds to a wedge of the height, $h(x,0) \sim |x|$, which is associated with fluctuations following the Tracy–Widom (TW)–Gaussian unitary ensemble (GUE) distribution with skewness 0.224 [186]. The data appear to be more consistent with either 0.294 for the TW–Gaussian orthogonal ensemble (GOE) distribution associated with a flat initial condition, or 0.359 for the Baik–Rains (BR) distribution given for a stationary initial condition. However, we note that, firstly, the uncertainties of the values extracted from the measurements are high, and, secondly, the spin–height mapping may only be effective for our initial state at hydrodynamically early times.

7.2.2 Distributions near equilibrium

Finally, we note that the mapping $\hat{S}^z \leftrightarrow \partial_x \hat{h}$ can fundamentally not be exact [240, 247, 248]: The height derivative, $\partial_x \hat{h}$, leads to chiral dynamics, as can be seen by the signed nonlinear term in the Burgers equation (5.6), which is in stark contrast to the symmetric dynamics of the XXX model. Hence, this mapping can be considered to be an effective mapping, valid due to the initial large-contrast DW setting and up to a potential crossover time.

In a subsequent work, Ref. [249] employed a chain of superconducting qubits to perform a similar experiment for varying DW contrasts and with a higher cycle rate, allowing them to analyze the data up to the fourth statistical moment. To account for a crossover, they rescale time by $\eta t^{2/3}$, finding—within their experimentally accessible times of up to $J_{\mathrm{ex}} t/\hbar = 25$—a non-skewed distribution near equilibrium and a skewed distribution for large η, which both appear inconsistent with the known KPZ distributions. Even though numerical simulations of the classical Landau–Lifshitz model seem to capture the phenomenology at equilibrium [250], a full understanding of spin transport in the XXX chain remains elusive.

7.3 Conclusion and outlook

In this chapter, we have shown FCS measurements of the polarization transfer in the XXX chain starting from a full-contrast DW as initial state. The resulting distributions exhibited a persistent asymmetry, indicating the nonlinearity of the underlying spin transport process. Quantified by the skewness of the distributions, the asymmetry was furthermore found to be consistent with, though not evident of, distributions arising in the KPZ universality class.

While alternative quantum simulation platforms can generate higher statistics, cold-atoms systems benefit from comparatively substantially longer accessible evolution times, with measurements of the FCS challenging classical simulations. The time range probed in the present measurements were largely limited by system size, which could be straightforwardly enlarged by elliptically confining lattice beams. Improvements

in the MI filling [121] and of local addressing fidelities would also constitute a major step towards the fully deterministic preparation of arbitrary initial states [229, 249]. These could be used to access the near-equilibrium regime or to study the behavior of particular initial states. A related system, in which theoretical work has predicted KPZ universality, is the integrable 1D Fermi–Hubbard (FH) model, for which both spin and charge DSFs were associated with the KPZ scaling function [251]. Thus, analyzing the FCS in such a system and contrasting to the non-integrable 1D Bose–Hubbard (BH) model could reveal rich physics.

While the relation between KPZ statistics and transport phenomena in quantum models has only recently started to be uncovered, their relation to interface growth problems is more immediate, which offers possibilities to study KPZ statistics in a stricter sense—also in quantum models. As such, in a system of free fermions on a 1D lattice initialized in a pure DW, the position of the wave front has been predicted to follow TW–GUE statistics [252] and could be realized in our setup in the regime of 1D hard-core bosons.

Part III

Cooperative light scattering in atomic arrays

Chapter 8

Atomic light–matter interfaces

A central aim in quantum optics encompasses the creation of efficient and versatile atom–light interfaces, which represent a vital ingredient for quantum information processing. Atomic interfaces constitute a particularly promising platform [253, 254] as they unify the controllability of atomic states with the coherence of propagating photons. The challenge to realizing such interfaces typically lies in achieving strong atom–photon coupling in spite of the small scattering cross section in free space. Several approaches have been devised to overcome this problem, ranging from tightly focussing a photon onto a single atom [255, 256], which optimizes mode matching, to placing single atoms in optical cavities [257], where a photon passes a single atom multiple times, and utilizing large atomic ensembles [72], where a photon passes multiple different atoms.

Recently, a novel platform based on subwavelength-structured ensembles of atoms has been proposed [258–261], which employs cooperative scattering to achieve strong coupling to paraxial beams. In Sec. 8.1, we first describe the role of photon-mediated dipole–dipole interactions in atomic ensembles, and then discuss the consequences of array order in Sec. 8.2.

8.1 Cooperativity in atom–light interaction

The interaction between light and ensembles of atoms is often well-described by treating the light scattering process independently for each atom. At high densities, where typical interatomic distances reach the wavelength scale, this approximation breaks down since the scattering process occurs coherently across multiple atoms, requiring the ensemble to be treated as a single composite quantum object. Such collective systems can exhibit dramatically altered radiative properties, leading to a variety of phenomena like Dicke superradiance (subradiance) [262], in which spontaneous decay rates are increased (decreased) compared to the single-particle case, as illustrated in Fig. 8.1.

8.1.1 Experimental signatures

Effects of cooperative light–matter interaction have been observed in a wide range of systems—including neutral atoms, ions, and solid-state systems [263, 264]—in both

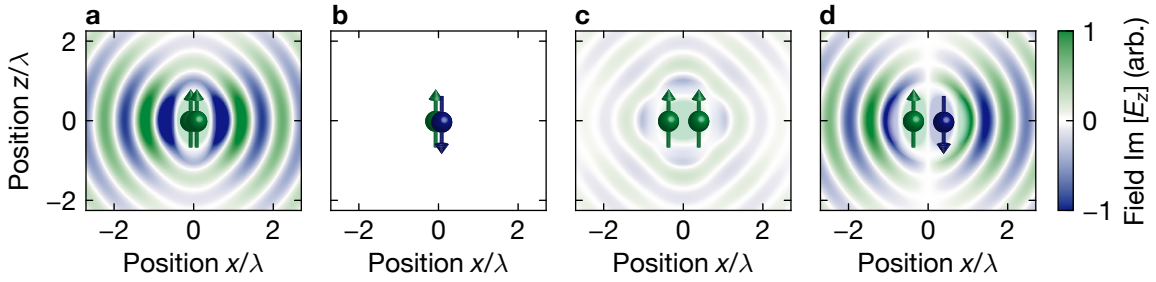

Figure 8.1: Single-photon super- and subradiance. Here, we show the emitted electromagnetic (EM) field, **E**, of ensembles of linearly polarized dipoles. (**a, b**) In the small-sample (Dicke) limit, where the inter-particle distances, Δx, are much smaller than the wavelength, λ, the spatial mode of the emitted EM field is identical to the single-dipole radiation lobe. However, given a total excited-state population in the system, the emission rate varies depending on the dipole state. If the dipoles oscillate in phase (**a**), their emission fields constructively interfere. Then, the collective dipole moment and thus the radiated power is larger, leading to a higher decay rate, i.e., superradiance. If the dipoles oscillate out of phase (**b**), their emission fields destructively interfere, leading to subradiance. (**c, d**) In extended samples, exemplarily shown for the case of $\Delta x = \lambda/2$, the in-phase condition changes as the phase shift associated with the propagation between the dipoles needs to be accounted for. Thus, we again obtain subradiance (**c**) or superradiance (**d**) depending on the dipole state, which additionally influences the spatial mode of the emitted field.

the optical and the microwave (MW) domain, and in a variety of electromagnetic (EM) environments. Typical experimental protocols are sketched in Fig. 8.2.

A first class of experiments probe the multi-photon regime, in which a large number of excitations are present in the system and can interact with each other. By preparing the system in a strongly inverted state, the collective spontaneous emission process has been studied by measuring the temporal dynamics of the emitted light. Such measurements have not only been performed in free space in both dilute [74] and dense ensembles [265], but also coupled through photonic waveguides [266, 267]. In such systems, superradiance (also called superfluorescence in this context) is often investigated [268], as the majority of excitations typically decay through a fast, non-exponential, superradiant burst; however, since a minority of excitations evolve in slowly decaying collective states, this scheme also allows for the study of subradiant effects at late times. A notable consequence of superfluorescence is the synchronization of the emission mode, resulting in directional emission in extended systems [269]. The structured recoil imparted on the emitting media can then give rise to motional self-organization, and has also been observed in atomic systems [73, 270].

Cooperative effects can, however, also arise in the single-photon regime, in which

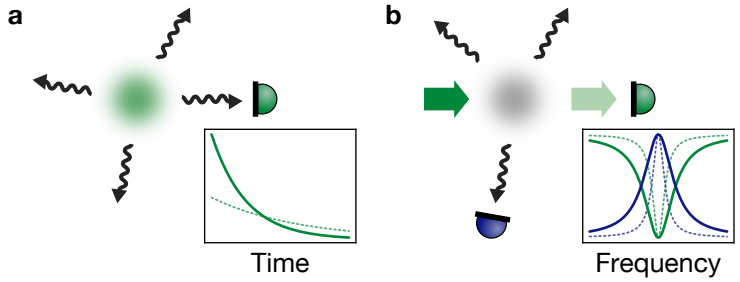

Figure 8.2: Experimental probes of cooperativity. (**a**) Cooperative light scattering is often studied by (strongly) exciting an atomic cloud (green shaded) and observing the decay dynamics of the emitted light (wavy arrows). (**b**) An alternative method makes use of the spectral response of the cloud (gray shaded) by measuring the extinction (light green arrow) of a weak probe beam (dark green arrow) or the scattered light (wavy arrows). (**Insets**) show typical photonic signals acquired at the respective detectors. In the single-photon regime, cooperative effects manifest through altered decay rates and spectral linewidths, respectively.

the Hilbert space is restricted to a single excitation. In this case, changes in the collective radiative properties are pure interference effects, corresponding to generally classical but coherent linear optics. This regime is experimentally probed by weak excitation beams, preventing any saturation effects. As subradiant states are only weakly coupled to propagating EM modes, they tend to be difficult to excite, such that experiments have largely focussed on small systems [271] or on studying single-photon superradiance in both dense and dilute atomic clouds. The latter can be achieved by measuring the temporal decay dynamics following repeated weak excitation pulses [272–274] or by probing the spectral width of the weak-excitation steady state through scattering experiments [275–277]. The spectroscopic approach has the additional advantage that the photon-mediated dipole–dipole interactions can be extracted from the shift of the resonance [277–280].

8.1.2 Collective light scattering

In the experiments performed in the context of this thesis, we probe two-level atomic dipoles with a spectroscopic scheme and are most interested in the system's cooperative light-scattering behavior. This quantum electrodynamics (QED) problem is typically treated by coupling the dipoles, with dipole matrix element $\mathbf{d}$, to the quantized EM modes [281, 282], potentially under the presence of a driving field, $\mathbf{E}_0(\mathbf{r})$. The emission field of a radiating electric dipole is given by $\mathbf{E}_i(\Delta\mathbf{r}) = \mu_0\omega_0^2 \mathrm{G}(\Delta\mathbf{r}) \cdot \mathbf{d}\langle\hat{\sigma}_i^-\rangle$, with the

free-space dyadic Green's tensor [283]

$$\mathrm{G}(\mathbf{r}) = (k_0^2 \mathbb{1} + \nabla \otimes \nabla) \frac{e^{ik_0 r}}{4\pi k_0^2 r}, \tag{8.1}$$

the dipole transition frequency $\omega_0/2\pi$ and its associated wave number $k_0 = \omega_0/c$. Due to linearity, the total scattered field therefore yields

$$\mathbf{E}(\mathbf{r}) = \mathbf{E}_0(\mathbf{r}) + \mu_0 \omega_0^2 \sum_j \mathrm{G}(\mathbf{r} - \mathbf{r}_j) \cdot \mathbf{d} \langle \hat{\sigma}_j^- \rangle. \tag{8.2}$$

This equation represents a generalized input–output relation [284], reducing the calculation of the resulting light field to solving the atomic dipole dynamics.

The scattering properties of the collective system are then commonly quantified with the differential cross section [285], which we define as the total energy flux propagating into the solid angle Ω, given by

$$\frac{d\sigma}{d\Omega} = \lim_{r\to\infty} \frac{1}{|\mathbf{E}_0|^2} \left(r^2 |\mathbf{E}(\mathbf{r})|^2 - |\mathbf{r} \cdot \mathbf{E}(\mathbf{r})| \right) \equiv \frac{d\sigma^{\mathrm{in}}}{d\Omega} + \frac{d\sigma^{\mathrm{sc}}}{d\Omega} + \frac{d\sigma^{\mathrm{intf}}}{d\Omega}, \tag{8.3}$$

where $\mathbf{E}_0 e^{ik_0 z}$ denotes the electric field of the incident plane wave. We formally separate the contributions into an incident, a scattered (power re-emitted from the dipoles) and an interfering part. The (integrated) scattering cross section, σ^{sc}, thus represents the total power scattered and measures the EM response of the atomic ensemble.

8.1.3 Collective dipole modes

The atomic dynamics in Born–Markov and rotating-wave approximation can be well described by the master equation introduced in Eq. (2.11), which—in the single-photon regime—can be reduced to the effective, non-Hermitian Hamiltonian [76, 286]

$$\begin{aligned} \hat{H} = &\sum_{i,j\neq i} \left(J_{ij} - i\frac{\Gamma_{ij}}{2} \right) \hat{\sigma}_i^+ \hat{\sigma}_j^- + \sum_i \left(\Delta_i - \Delta - i\frac{\Gamma_0}{2} \right) \hat{\sigma}_i^+ \hat{\sigma}_i^- + \sum_i \left(\Omega_i \hat{\sigma}_i^+ + \Omega_i^* \hat{\sigma}_i^- \right), \\ &\text{with } J_{ij} - i\frac{\Gamma_{ij}}{2} = -\mu_0 \omega_0^2 \mathbf{d}^* \cdot \mathrm{G}(\mathbf{r}_i - \mathbf{r}_j) \cdot \mathbf{d} \text{ and } \Omega_i = \mathbf{d} \cdot \mathbf{E}_0(\mathbf{r}_i). \end{aligned} \tag{8.4}$$

The Hamiltonian consists of single-atom terms, with local drive detuning $(\Delta - \Delta_i)/h$ and decay rate $\Gamma_0/\hbar$, and EM interaction terms, determined by the product of the dipole moment, $\mathbf{d}\hat{\sigma}_i^-$, and the local electric field, $\mathbf{E}(\mathbf{r}_i)$. As the local field at the position of dipole i itself depends on the dipole moments of all other dipoles $\{j\}$, the photon-mediated interaction term takes the form of $\mathbf{d}_i^* \cdot \mathrm{G}(\mathbf{r}_i - \mathbf{r}_j) \cdot \mathbf{d}_j$. This term warrants an intuitive interpretation, in which photons scattered at dipole j are re-scattered at

dipole i, and whose influence on the atomic state depends on both the strength of the rescattered field and its phase relative to the atomic dipole.

The collective eigenmodes of the dipole system can be obtained by diagonalizing the (symmetric) Hamiltonian without the drive term [76], yielding the structure of the collective dipole modes, $\mathbf{m}_{p,i}$. Since the drive-frequency–dependent part is diagonal, the spectral scattering properties are fully characterized by the eigenvalues, $\mu_p(\Delta)$. The driving field can then be decomposed into these modes, $\mathbf{E}_0(\mathbf{r}_i) = \sum_p b_p \mathbf{m}_{p,i}$, yielding the steady-state dipole moments $\mathbf{d}\langle\hat{\sigma}_i^-\rangle = \sum_p \alpha_p b_p \mathbf{m}_{p,i}$ with collective polarizability

$$\alpha_p(\Delta) = \alpha_0 \frac{\Gamma_0/2}{\mu_p(\Delta)} = \alpha_0 \frac{\Gamma_0/2}{(\Delta_p - \Delta) - i(\Gamma_p + \Gamma_0)/2}, \tag{8.5}$$

where $\alpha_0 = 6\pi\varepsilon_0/k_0^3$ denotes the resonant single-particle polarizability. Following Eq. (8.3), the total scattering cross section can be written in terms of the (generally non-orthogonal) eigenmodes as [285]

$$\sigma^{\mathrm{sc}}(\Delta) = \frac{k_0}{\varepsilon_0 |E_0|^2} \left(\sum_p |b_p \vec{\mathbf{m}}_p|^2 \,\mathrm{Im}[\alpha_p(\Delta)] + \sum_{p,q} \mathrm{Im}[\alpha_q(\Delta) b_p^* \vec{\mathbf{m}}_p^\dagger \cdot b_q \vec{\mathbf{m}}_q] \right). \tag{8.6}$$

Each eigenmode itself thus has a Lorentzian spectral response: The real term, Δ_p, captures virtual exchange processes, describing a coherent dipole–dipole energy shift known as the cooperative Lamb shift; the imaginary term, Γ_p, captures multiple-scattering processes that are dissipative to the system, giving rise to subradiance or superradiance.

8.1.4 Advantages of atomic dipoles

While cooperative EM effects can in principle be observed in a wide variety of platforms, atomic dipoles—apart from being inherently identical—offer distinct advantages for faithfully realizing such systems in the optical regime.

For instance, inhomogeneous broadening effects, i.e., large variations of the single-particle resonances $\{\Delta_i\}$, can occur due to the environment of the emitters or motional Doppler effects. The former is prevented by operating in free-space vacuum or through homogeneous trapping, and the latter through cooling to the motional ground state, as routinely achieved in cold-atom experiments. Homogeneous broadening effects typically arise due to nonradiative decay channels [261], $\Gamma_0 \to \Gamma_0 + \gamma_{\mathrm{nr}}$, and are commonly found in solid-state systems. In contrast, atomic ensembles are entirely decoupled from each other and the environment on the relevant time scales, so radiative transitions pose the only viable decay channels. Finally, dipolar scattering assumes point-like dipoles, i.e., emitters whose spatial extent is substantially smaller than the wavelength, which is well fulfilled by atoms near the electronic ground state.

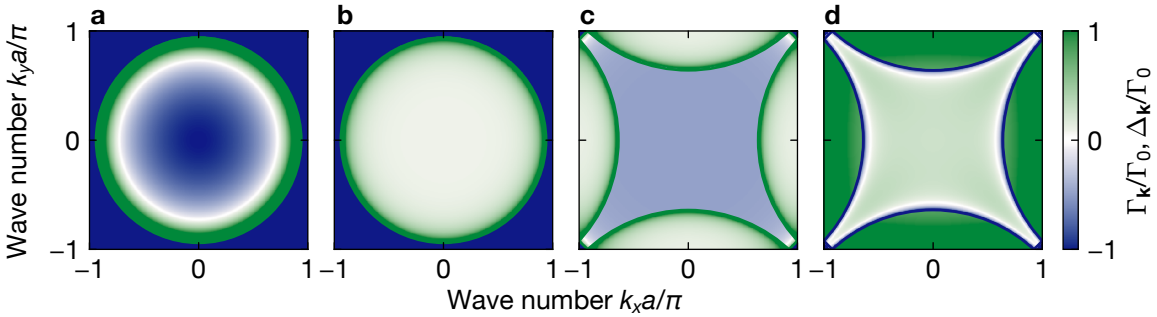

Figure 8.3: Cooperative spectra in a perfect square array of dipoles. (**a, b**) The cooperative correction to the decay rates, $\Gamma_{\mathbf{k}}$, of out-of-plane (**a**) and in-plane circular (**b**) polarized modes at a deeply subwavelength array spacing of $a/\lambda = 0.47$ show radiant states, $\Gamma_{\mathbf{k}} > -\Gamma_0$, within and non-radiant states, $\Gamma_{\mathbf{k}} = -\Gamma_0$, outside of the light cone. Their response diverges when the in-plane–projected spin wavelength approaches the light wavelength. (**c, d**) The cooperative decay rate (**c**) and cooperative Lamb shift, $\Delta_{\mathbf{k}}$ (**d**), for circular polarization at the experimentally realized array spacing of $a/\lambda = 0.68$ show similar behavior. The small dependence on the spin wave number indicates a robust behavior as a light–matter interface to more focussed or angled illumination. Note that the light cone folds back into the first Brillouin zone.

Note that Eq. (8.4) is written for a two-level system and can be realized in atoms on an optical cycling transition whose degeneracies are magnetically lifted by Zeeman shifts.

8.2 Light scattering in subwavelength arrays

While disordered ensembles of dipole emitters allow for studying fundamental aspects of collective light scattering, the involved EM modes are naturally non-deterministic. In contrast, structuring the dipole positions allows for engineering targeted, quantum-technologically relevant modes. A particularly interesting geometrical configuration involves structured arrays, which have been predicted to give rise to effects reminiscent of cavity QED systems [258, 287] and to provide efficient paraxial and non-dissipative atom–light interfaces in two-dimensional (2D) arrays [260, 261].

8.2.1 Two-dimensional arrays

For identical atoms located on an infinite 2D lattice, Bloch's theorem is applicable such that the eigenstates are given by (mutually orthogonal) spin waves, $\hat{S}^{\dagger}_{\mathbf{k}} = (1/\sqrt{N}) \sum_j e^{i\mathbf{k}\cdot\mathbf{r}_j} \hat{\sigma}^{+}_j$, with $\mathbf{k}$ denoting the 2D spin wave vector in the plane of the

array. The effective Hamiltonian can thus be written as

$$\hat{H} = \sum_{\mathbf{k}} \left(J_{\mathbf{k}} - i\frac{\Gamma_{\mathbf{k}} + \Gamma_0}{2} \right) \hat{S}^{\dagger}_{\mathbf{k}} \hat{S}_{\mathbf{k}}, \text{ with } J_{\mathbf{k}} - i\frac{\Gamma_{\mathbf{k}}}{2} = -\mu_0 \omega_0^2 \mathbf{d}^* \cdot \tilde{\mathrm{G}}(\mathbf{k}) \cdot \mathbf{d}. \tag{8.7}$$

The discrete Fourier transform of the regularized Green's tensor over the lattice vectors, $\{\mathbf{R}_i\}$, is given by

$$\begin{aligned} \tilde{\mathrm{G}}(\mathbf{k}) &= \sum_{\mathbf{R}_i \neq 0} e^{-i\mathbf{k}\cdot\mathbf{R}_i} \mathrm{G}(\mathbf{R}_i) \\ &= \frac{i}{8\pi^2 k_0^2} \int d^2 q_{\parallel} \frac{k_0^2 \mathbb{1} - \mathbf{q} \otimes \mathbf{q}}{q_z} \left[\frac{(2\pi)^2}{a^2} \sum_{\mathbf{g}_m} \delta(\mathbf{g}_m - \mathbf{k} + \mathbf{q}_{\parallel}) - 1 \right], \end{aligned} \tag{8.8}$$

with the in-plane wave vector $\mathbf{q}_{\parallel}$, and its generally complex out-of-plane component $q_z = \sqrt{k_0^2 - \mathbf{q}_{\parallel}^2}$. The first term reduces to a discrete sum over the reciprocal lattice vectors, $\{\mathbf{g}_m\}$, and the second term can be analytically integrated with a cutoff matched to the summation. The spectra for deeply subwavelength arrays and for the lattice spacing realized in our experiment, $a/\lambda = 0.68$, are shown in Fig. 8.3.

Relation to light cone

The imaginary part of the eigenvalues, $\Gamma_{\mathbf{k}}$, corresponding to the cooperative decay rates, can be further simplified: First, the in-plane and out-of-plane polarization components do not mix in a 2D array, and, second, the imaginary contributions only arise for purely real values of q_z. The cooperative decay rates are therefore given by [76]

$$\begin{aligned} \frac{\Gamma^{\parallel}_{\mathbf{k}}}{\Gamma_0} &= \frac{3\pi}{k_0^3 a^2} \sum_{\mathbf{g}_m, |\mathbf{k}+\mathbf{g}_m| \leq k_0} \frac{k_0^2 - |(\mathbf{k}+\mathbf{g}_m)\cdot\mathbf{e}_d|^2}{\sqrt{k_0^2 - |\mathbf{k}+\mathbf{g}_m|^2}} - 1, \\ \frac{\Gamma^{\perp}_{\mathbf{k}}}{\Gamma_0} &= \frac{3\pi}{k_0^3 a^2} \sum_{\mathbf{g}_m, |\mathbf{k}+\mathbf{g}_m| \leq k_0} \frac{|\mathbf{k}+\mathbf{g}_m|^2}{\sqrt{k_0^2 - |\mathbf{k}+\mathbf{g}_m|^2}} - 1, \end{aligned} \tag{8.9}$$

where $\mathbf{e}_d = \mathbf{d}/d$ denotes the polarization vector of the dipole.

Evidently, the decay rates at subwavelength spacings for spin waves with $|\mathbf{k}| > k_0$ vanishes, leading to non-radiative, evanescent modes in analogy to guided modes in photonic waveguides. Physically, this is caused by the fact that the phase-matching condition between light and spin wave cannot be fulfilled, preventing propagating light fields to couple to these collective modes. The remarkably long-lived nature of such states have since also been discussed in the context of quantum memories or many-body physics with light [288–290].

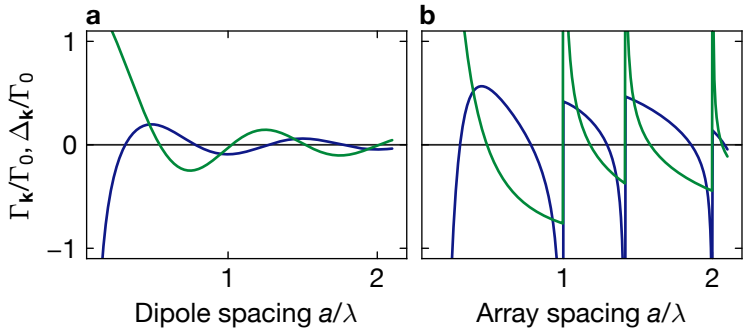

Figure 8.4: Cooperative response of the in-phase mode. Collective decay rate, $\Gamma_{\mathbf{k}}$ (green), and cooperative Lamb shift, $\Delta_{\mathbf{k}}$ (blue), as a function of the spacing. (**a**) Cooperative interactions between a pair of circularly polarized dipoles. The oscillatory behavior results from the accumulated phase upon light propagating between the dipoles, and the overall decay of the interaction is a consequence of the undirected emission pattern of a single dipole. (**b**) The cooperative response in a square array of in-plane circularly polarized dipoles also shows sign-changing behavior, reminiscent of the light-propagation phase. Furthermore, the array features divergences when higher diffraction orders arise and thus additional dissipation channels become available [261].

Perpendicularly incident modes

In this thesis, we are more interested in the array as a light–matter interface, which requires strong coupling to propagating EM modes, specifically the in-phase spin wave, $\mathbf{k} = 0$, corresponding to a perpendicularly incident optical mode. In subwavelength arrays (for which $|\mathbf{g}_m| > k_0$), one immediately finds that the out-of-plane–polarized mode does not radiate, $\Gamma^{\perp}_{\mathbf{k}=0} = 0$, as EM modes are transversal waves and emission in the in-plane direction is destructively interfering. In contrast, spin waves with in-plane polarization can couple to propagating EM modes, resulting in a decay rate in the subwavelength regime of [261]

$$\frac{\Gamma^{\parallel}_{\mathbf{k}=0}}{\Gamma_0} = \frac{3}{4\pi}\left(\frac{\lambda}{a}\right)^2 - 1 \quad \text{for} \quad a < \lambda, \tag{8.10}$$

with circular polarization being experimentally most relevant, as it supports closed dipole transitions in atoms with hyperfine state (HFS). In Fig. 8.4, we plot the cooperative response for varying lattice spacings, whose dependence is discontinuous and can be understood when considering the associated EM modes.

The discrete but periodic ordering of the emitters gives rise to a far-field emission pattern reminiscent of a homogeneously illuminated optical diffraction grating. A divergence in the collective eigenvalues occurs whenever the light's wave number

reaches an additional reciprocal lattice vector, corresponding to the emergence of another diffraction order. At subwavelength spacings, no higher-order diffraction occurs and the optical power remains fully confined to the zeroth order.

8.2.2 Paraxial interface

The light-scattering properties of atomic arrays can be furthermore treated in the context of quantum light–matter interfaces, in analogy to more established systems like atom ensembles in optical cavities. Following Ref. [291], a single-mode light–matter interface can be thought of as a device efficiently scattering light between two target modes. The main figure of merit is the cooperativity, $C = \Gamma/\gamma_{\mathrm{loss}}$, which describes the ratio between the power emission rate into targeted and untargeted modes, accounting for mode-matching effects and non-radiative losses. The scattering process can be intuitively understood as a two-step process consisting of absorption of the incident light and re-emission due to the resulting excitations of the atomic state; the efficiency of each step is equal to the classical field reflectivity, which is given by $r_0 = C/(C+1)$. The reflectivity has been shown to govern the fidelities of many quantum-optical applications, including quantum memory and correlation efficiencies [291], and thus serves as a convenient probe for the quality of the atom–light interface.

The experimentally most relevant target modes are Gaussian beams, as they retain a functionally similar form throughout propagation and can be straightforwardly refocussed through lenses. In infinite 2D atomic arrays, the eigenmodes have been identified with spin waves, which can be associated with plane waves as EM modes. As the distribution of plane-wave components of Gaussian beams with sufficiently large waists, $w_0 \gg \lambda$, is very narrow, the set of coupled spin waves are nearly degenerate and thus scatter the light phase-coherently. Contrasting to the cavity case, this yields ideal cooperativities of [291]

$$C_{\mathrm{array}} = \frac{3}{4\pi} \cdot \frac{\Gamma_0}{\gamma_{\mathrm{loss}}} \cdot \frac{\lambda^2}{a^2} \quad \text{and} \quad C_{\mathrm{cavity}} = \frac{3}{4\pi} \cdot \frac{\mathcal{F}}{\pi} \cdot \frac{\lambda^2}{\pi w_0^2/2}. \tag{8.11}$$

The technical challenges for array-based interfaces, analogous to the challenge of maximizing the cavity finesse $\mathcal{F}$, are thus to maintain a strict positional array order to prevent uncontrolled scattering.

Finally, we note that having plane waves as eigenmodes of the array implies a generally efficient way to realize technologically relevant paraxial interfaces. In particular, extensions to multimode interfaces by parallelly coupling multiple Gaussian beams is straightforward, and has been proposed to, e.g., realize quantum light modulators to flexibly generate correlated photonic states [292].

Chapter 9

Atomic arrays as subradiant mirrors

Control over the flow of light represents one of the fundamental aspects in the field of optics, driving research into light–matter interfaces. Progress in the creation of nanostructured devices has enabled the realization of classical metasurfaces, which allow for complex wavefront shaping based on subwavelength-structured light scatterers [293, 294]. Extending metasurface engineering to quantum optical scatterers thus poses a promising route to spatiotemporal quantum control of many-body states of both photons and scatterers [292, 295, 296].

The isolated nature of and the high degree of quantum control over individually trapped atoms render atomic arrays to be ideal candidates for realizing quantum metasurfaces. Homogeneous two-dimensional (2D) arrays of identical atoms constitute the foundational building blocks of such metasurfaces, and have been predicted to serve as ideal mirrors for resonant, paraxially incident light beams [260, 261]. Probing the reflective and spectral response of the array not only allows for testing the feasibility of the platform as a quantum light–matter interface [291], but also for revealing the underlying cooperative physics giving rise to directional scattering [258, 261, 297].

In our experiment, we trap atoms in a subwavelength-spaced optical lattice, allowing us to study such cooperative phenomena. In Sec. 9.1, we first show experimental light-scattering spectra and their dependence on the geometrical positioning of the atoms. In Sec. 9.2, we then present measurements probing the role of cooperativity based on varying the atomic density. Finally, in Sec. 9.3, we discuss technical and fundamental limitations to the achievable mirror fidelity.

9.1 Subradiant specular reflection

The fact that 2D atomic arrays can be used as mirrors for light beams propagating in three-dimensional (3D) free space is by itself remarkable for a variety of reasons: In contrast to mesoscopic engineered nano-antennae [294], the reflecting matter is dilute, with a typical ratio of 10^{-4} between atomic size and interatomic spacing. Furthermore considering that the array is truly 2D, the array realizes the conceptually lightest mirror possible. Alternative atomically thin mirrors have been demonstrated only in unstructured (and dense) emitter ensembles, e.g., through excitons in transition-metal dichalcogenide monolayers [298, 299]. In one-dimensional (1D) systems, where

photons propagate through classical waveguides, optical mirrors have been implemented by forming Bragg mirrors with trapped atoms evanescently coupled to the waveguide [300, 301].

A truly lower-dimensional analog of the cooperative mirror has been realized in the microwave (MW) domain, where 1D propagating photons were reflected at a 0D mirror realized using superconducting qubits [302]. By measuring the spectral response, MW-domain systems, including superconducting and metamolecular systems, have also enabled the observation of subradiant effects [279, 302, 303]. In contrast, deterministic excitation of subradiant modes in optical dipole ensembles, has only been realized in a small system of two ions [271].

Cold atoms trapped in optical lattices constitute a valuable platform for studying cooperative light-scattering phenomena in structured arrays: As discussed in Sec. 8.1.3, atoms represent ideal dipoles, Mott insulators (MIs) in the atomic limit realize unity-filled arrays, and the optical lattice guarantees the periodic array structure. While many quantum gas microscopes (QGMs) operate at larger lattice spacings to facilitate single-site–resolved detection, our experiment in the retro-reflected configuration yields a square lattice with a spacing of $a = 532\,\mathrm{nm}$, well within the subwavelength criterion, $a < \lambda = 780\,\mathrm{nm}$.

9.1.1 Experimental protocol

We realize the atomic arrays by loading a 2D MI in the pinning Lattice 3 (L3), as described in Sec. 3.1.1, and ramp up all three lattices to a depth of $300E_r^{532}$, yielding a square array with about 200 atoms at a typical filling of $\overline{n} = 0.92$ and a ground-state wave function with spatial SD of $s = 0.054a$. We furthermore apply a stabilized magnetic field of 3.3 G which is oriented out of the atomic plane to isolate a closed two-level transition between the $|5S_{1/2}, F = 2, m_F = -2\rangle$ and the $|5P_{3/2}, F' = 3, m'_F = -3\rangle$ states. To spectroscopically measure the cooperative light-scattering properties of the array, we use a σ^--polarized probe laser which is tunably offset-locked to an ultra-low–expansion cavity and has a laser linewidth of less than 50 kHz, much smaller than the natural linewidth, $\Gamma_0/h = 6.067\,\mathrm{MHz}$. The probe beam's Gaussian-beam waist at the position of the atoms is chosen to be much larger than the array size, such that the drive is well-approximated by a plane wave.

Our experimental setup, illustrated in Fig. 9.1, allows us to illuminate the array from above (or from below), giving us spatially resolved access to the transmitted (or reflected) light on the electron-multiplying charge-coupled device (EMCCD) camera. For the transmission measurements, we take an absorption image with atoms, $I_t(\mathbf{r})$, and an image of the beam without atoms, $I_{\mathrm{in}}(\mathbf{r})$ (and a background image to subtract systematic fluctuations), from which we can immediately calculate the absorptance, $A = 1 - \int I_t(\mathbf{r})/I_{\mathrm{in}}(\mathbf{r})\, d^2r$, which we evaluate over the central 11×11 sites to account for fluctuations in atom number and cloud position. For the reflection

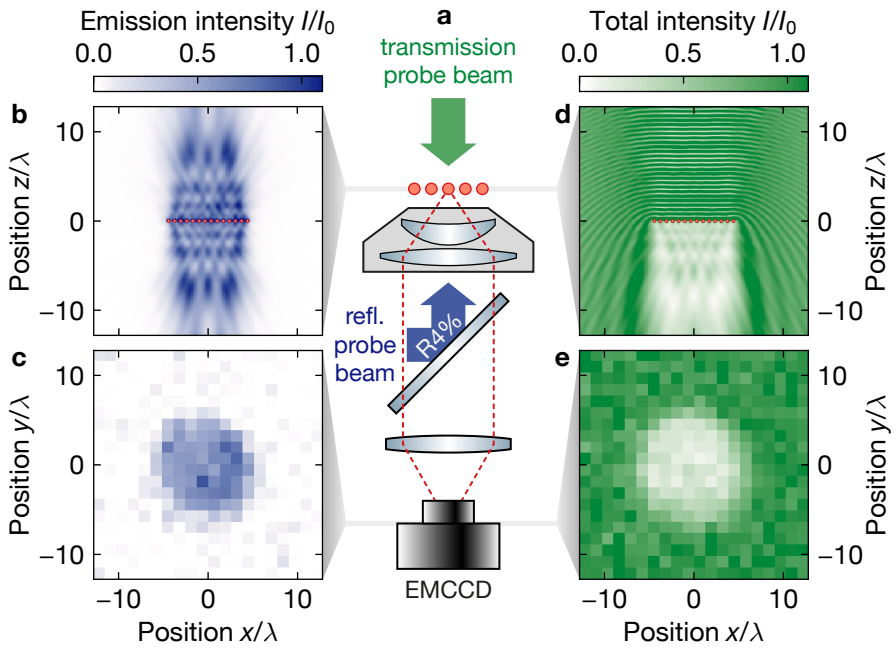

Figure 9.1: Experimental setup probing cooperative light scattering. (**a**) In our experiment, we send a vertically incident probe beam with intensity I_0 from either side onto the atomic array (red circles), allowing us to measure both reflection (blue, **b,c**) and transmission (green, **d,e**) spectra. We capture the probe light in an imaging configuration (red dashed) with an EMCCD camera. In the reflection configuration, we only observe the light emitted from the array; in the transmission configuration, we measure the destructively interfering superposition of emitted and incident light. (**b, d**) Numerically simulated light intensity in a plane orthogonal to the array with 14×14 sites, accounting for an array filling of $\overline{n} = 0.95$ and positional disorder with a standard deviation (SD) of $(s_\parallel, s_\perp) = (0.054, 0.13)a$. In the absorption-imaging case, we can see disorder-induced imperfect cancellation of the incident field in the forward direction, and formation of standing waves due to the mirror reflection in the backward direction. (**c, e**) Averaged experimental images (in the plane parallel to the array) taken at the cooperative resonance, showing interaction-enhanced specular reflection.

measurements, we analogously use the image with atoms to obtain the reflectance as $R = \int I_r(\mathbf{r})/I_{\text{in}}\, d^2r$. As we cannot directly image the reflective probe beam, we cross-calibrate the mean intensity by comparing the scattering-induced heating between the reflection and the well-characterizable transmission beam. Note that the polarization purity of the probe beams was optimized to more than 98 %, following the scheme outlined in Sec. 3.3.5.

Parameter optimization

In this experiment, the fundamental limitation lies in the fact that the absolute number of scattered (and therefore detectable) photons is limited by recoil-induced heating effects (see Sec. 9.3 for details). Therefore, the central technical challenge consists of handling the low signal-to-noise ratio (SNR) in photon detection. One approach involves increasing the photon-detection probability, however, these are practically limited to the given experimental setup: We estimate the transmission probability of the imaging path to be 61 % and the quantum efficiency of the camera to 80 %. Instead, we focus on reducing the residual noise to improve the SNR and to optimize the measurement parameters.

First, we ensure that the signal is not affected by background photons: These can be effectively reduced by installing additional spectral filters, which block both ambient light and high-power beams such as the lattice lasers. By varying the camera exposure time, we indeed find that ambient photons are not varying the camera counts and are thus not limiting the SNR.

Second, we minimize technical noise inherent to the EMCCD camera: We perform hardware-binning of 8×8 pixels (corresponding to about 3.5 lattice sites) to reduce the readout noise and increase the pixel shift speed to reduce noise from clock-induced charges, yielding a noise background with a SD over the binned pixels of about 16 photon-equivalents. We decide to operate at a SNR of around 1 near resonance, which—upon averaging over 15–30 shots per data point and spatial averaging—is expected to lead to a standard error of the mean (SEM) of about 3 %. We therefore choose a fluence of 6 (and 8–16) photons per lattice site in the transmission (and reflection) configuration. As we intend to probe the single-photon, steady-state regime, we illuminate the atoms with a photon flux of about $0.8\,\mathrm{ms}^{-1}$ per lattice site, which corresponds to a Rabi frequency of 7.5 kHz and is thus far below the saturation intensity. This value translates to pulse durations of 3 ms and 5–10 ms, respectively.

Numerical analysis

To facilitate the interpretation of the measurements, we simulate the experiment by solving the steady state of the dipole moments with Eq. (8.4) under a weak drive. The light-scattering properties can then be obtained by evaluating the differential cross section, Eq. (8.3), and integrating over the solid angle covered by the objective, $\sigma(\mathrm{NA}) = \int_{\sin\theta<\mathrm{NA}} (d\sigma/d\Omega) d\Omega$. In the reflection configuration, only the scattered light (i.e., the light emitted from the atomic ensemble) is detected, such that the reflectance is given by $R = \sigma^{\mathrm{sc}}/\sigma^{\mathrm{in}}$, where $\sigma^{\mathrm{in}} = Na^2$ denotes the area illuminated by the incident light and N the number of occupiable sites. In the transmission configuration, the coherent superposition of incident and scattered light is detected, such that the absorptance yields $A = -(\sigma^{\mathrm{sc}} + \sigma^{\mathrm{intf}})/\sigma^{\mathrm{in}}$. Note that here we are calculating the response in the far field and do not account for potential real-space inhomogeneities

as experimental fluctuations in the cloud size and position would average these out. The full finite-NA imaging configuration can be simulated by propagating back the far field using Debye–Wolf diffraction [304].

The motional degrees of freedom (DOFs) of the atoms can be treated as frozen because the dipole emission rates, $\Gamma/h \sim 10^6$ Hz, are far larger than the trap frequencies, $f_{\mathrm{tr}} \sim 10^4$ Hz. Motional effects can thus be captured by randomly sampling the positions of all atoms according to their (quantum-mechanical or thermal) probability distribution, and incoherently averaging the absorptances or reflectances. This Monte Carlo approach also allows us to account for imperfect array filling and for trap-induced inhomogeneities of the local atomic resonance frequency. By varying the drive frequency, we can calculate the spectral response, to which we fit a Lorentzian in order to obtain the collective linewidth and detuning.

The simulations, however, do not only give access to the spectra but also allow us to analyze the excited eigenmodes. To quantify the contribution of a given collective mode, $\vec{\mathbf{m}}_p$, with associated eigenvalue $\Delta_p + i\Gamma_p/2$, we define its population by $P_p = |b_p \vec{\mathbf{m}}_p|^2 / \sum_q |b_q \vec{\mathbf{m}}_q|^2$, with the driving field decomposed as $\mathbf{E}_0(\mathbf{r}_i) = \sum_p b_p \mathbf{m}_{p,i}$, according to Sec. 8.1.3. To account for the Monte Carlo sampling, we build a histogram in the space of the collective eigenvalues, finally yielding the probability distribution, $P(\Delta_{\mathrm{col}}, \Gamma_{\mathrm{col}})$, representing the mode structure.

9.1.2 Dependence on positional order

In a first set of experiments, we probe the influence of the atomic geometry on the optical response by measuring the transmission and reflection spectra of the respective atomic ensembles (see Fig. 9.2).

In the case of the 2D array, we can observe a pronounced subradiant response with a linewidth of $0.68(2)\Gamma_0/h$ in transmission and $0.66(2)\Gamma_0/h$ in reflection, clearly signalling cooperative behavior. Furthermore, the fits yield a small transmittance, $T = 0.23(1)$, and a large reflectance, $R = 0.58(3)$, indicating a directional response and thus demonstrating the specular reflection expected for a mirror. Note that the measured transmittance and reflectance do not add up to unity, $T + R \neq 1$, because light scattered at large angles is not collected by the finite-NA objective, which captures the light within a 43° cone around the optical axis. As a reference, we additionally take a standard absorption image of a dilute 3D cloud, whose response is well-described by the Beer–Lambert law. Analyzing the optical-density spectrum yields a Lorentzian linewidth of $1.00(2)\Gamma_0/h$, in agreement with the expected single-particle behavior and thus validating our subradiant result.

Comparing the measurement results with the spectra simulated on a 14×14 array, we find approximate agreement when accounting for experimental imperfections, with the main contribution arising from the positional uncertainty of the atoms, which increases beyond the spread of the ground-state wave function due to the scattered

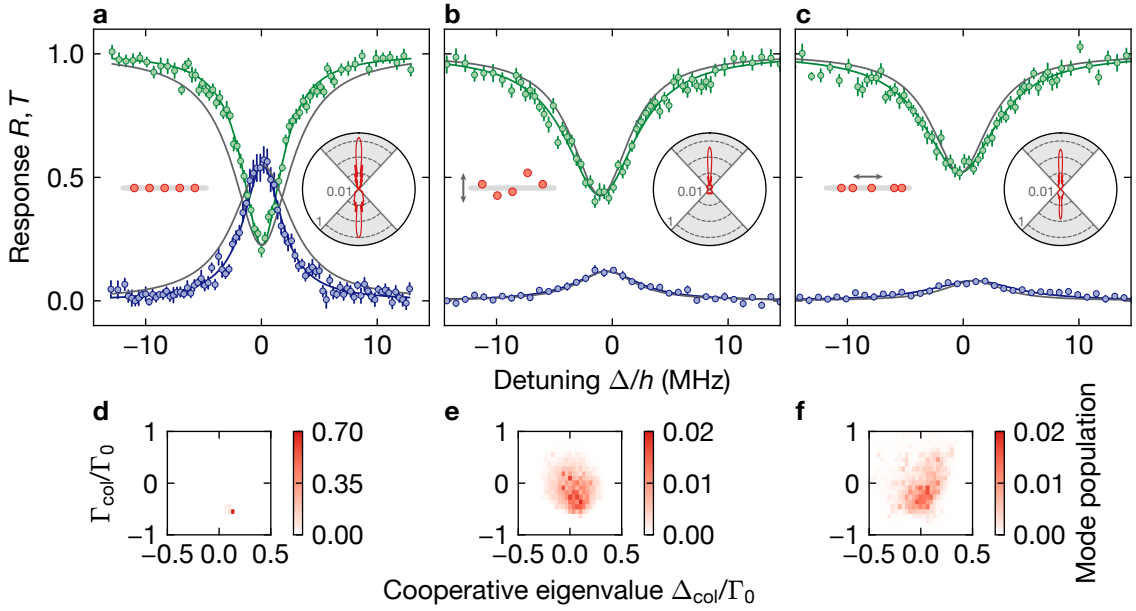

Figure 9.2: Cooperative response for varying geometries. (**a–c**) We measure the reflectance (green) and transmittance (blue) spectra for atoms in a square array (**a**), with out-of-plane disorder (**b**) and in-plane disorder (**c**). The colored solid lines show Lorentzian fits. Comparing to the natural linewidth, $\Gamma_0/h = 6.067\,\mathrm{MHz}$ (gray solid lines), the ordered array shows a clearly subradiant response with a linewidth of $4.09(11)\,\mathrm{MHz}$ and $4.04(12)\,\mathrm{MHz}$ in transmission and reflection, respectively. The high reflectance, $R = 0.58(3)$ (with transmittance $T = 0.23(1)$), indicates a mirror response. In stark contrast, neither disordered case yields a similar reflectance, demonstrating the importance of the array order. (**Insets**) Differential scattering cross section, $d\sigma^{\mathrm{sc}}/d\Omega$ (normalized to the array case), for light incident from below, and simulated accounting for experimental imperfections. While we find a strong directional response in the array case, the out-of-plane disordered case shows a large asymmetry, destroying any specular reflection. In the in-plane disordered case, we would expect a more pronounced reflection but are subjected to other effects (see main text). (**d–f**) Simulated eigenmode decomposition of the probed steady state. For a perfectly ordered array, we directly excite a subradiant eigenmode, whereas a large ensemble of modes are driven in the disordered cases, leading to both homogeneous and inhomogeneous broadening of the observed linewidth.

photons. We nevertheless consistently obtain directional emission from the array and find that the plane-wave drive largely excites a single subradiant eigenmode. Note that even in the ideal case of a defect-free array of perfectly ordered atoms, a multitude of modes are slightly excited, which is a consequence of the finite array size.

Vertical disorder

Next, we probe the response of an out-of-plane disordered cloud whose column density remains identical to the array case. To prepare the system, we start with a 2D unity-filled MI in a lattice with a horizontal depth of $V_{1,2} = 40E_r^{532}$ and a vertical depth of $V_3 = 13E_r^{532}$. Then, we suddenly switch off L3, allowing the atoms to vertically freely expand for 1 ms before freezing their position by rapidly ramping up L3 to $16E_r^{532}$. The vertical positions of the atoms are then normally distributed with a SD of 10 lattice sites. After ramping up all lattices to $300E_r^{532}$, we probe the electromagnetic (EM) response.

The most striking observation in the measured spectra is that while the transmittance, $T = 0.44(1)$, is slightly increased, the reflectance, $R = 0.13(1)$, has disproportionally reduced. This can be explained by the fact that the driving field imprints a vertical phase gradient. As a consequence, the symmetry between forward and backward emission is broken, leading to the difference between absorption and reflection. In addition, the phase gradient leads to a phase-matching condition, wherein the emitted field constructively interferes and may feature superradiant behavior.

Performing an eigenmode analysis, we can observe that, first, a random and large variety of collective modes are excited, indicating a generally cooperative response, and second, that the eigenvalues are scattered around the origin, indicating a change towards non-interacting behavior. Experimentally, this is observable as a both homogeneously and inhomogeneously broadened linewidth, with fitted linewidths of $1.22(5)\Gamma_0/h$ in transmission and $1.13(10)\Gamma_0/h$ in reflection.

Horizontal disorder

Finally, we consider the case of an in-plane disordered cloud whose mean density remains close to the array case. To prepare this geometry, we start with a 2D unity-filled MI with a vertical lattice depth of $V_3 = 300E_r^{532}$ and a horizontal depth of $V_{1,2} = 40E_r^{532} = h \cdot 80\,\mathrm{kHz}$. Then, we suddenly switch off the horizontal lattices in 100 µs, upon which the atoms randomly redistribute within the plane. As these atoms have a large kinetic energy and are horizontally insufficiently confined, we reduce the duration of the transmission (and reflection) probe pulses to 0.2 ms (and 2.3 ms) to minimize diluting the cloud.

In the transmission spectra, we find a similar transmittance of $T = 0.54(1)$ and a fitted linewidth of $1.26(6)\Gamma_0/h$, as in the vertically disordered case. The eigenmode decomposition analysis, however, suggests that the broadening is mainly inhomogeneous in nature, as no phase gradients are imprinted. Furthermore, the 2D symmetry implies that the reflectance should be similar to the non-transmittance, $1 - T$. In the ex-

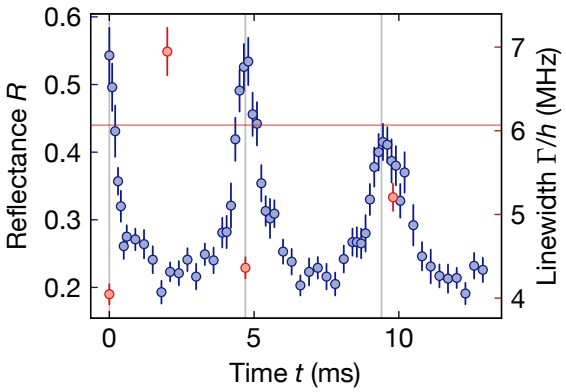

Figure 9.3: Cooperative response under Bloch oscillations. Starting from a 2D array, we let the atoms vertically tunnel under a gradient. The dynamics lead to Bloch oscillations, recovering the array order with a period of $T_B \approx 4.7\,\mathrm{ms}$ (gray lines). By measuring the reflectance (blue) at the array resonance, we also find an oscillatory behavior in the EM response. The linewidths (red circles) similarly show subradiant behavior in the ordered state and are broadened above the natural linewidth, $\Gamma_0/h = 6.067\,\mathrm{MHz}$ (red line), when disordered.

periment, however, we find that the reflectance of $R = 0.07(1)$ is substantially smaller. We attribute this behavior to density-reduction effects as the reflective probe pulses were about 10 times longer than the transmission pulses. The best agreement with calculations is obtained for a simulated density of $\overline{n} = 0.9$ (and 0.6) for the transmission (and reflection) data.

9.1.3 Bloch oscillations

To explore the importance of the planar array geometry further, we dynamically and periodically introduce controlled vertical disorder prior to probing the mirror response.

Experimentally, we again start with a unity-filled 2D MI with lattice depths of $V_{1,2} = 40E_r^{532}$ and $V_3 = 16E_r^{532}$. We initiate quantum dynamics by suddenly reducing the vertical lattice depth to $5E_r^{532}$. As the atoms are isolated within their own 1D systems and are subjected to a potential gradient (due to gravity and optical gradients), they independently perform Bloch oscillations in the out-of-plane direction [42, 305]. After freezing the dynamics by ramping up L3, the probability distribution after an evolution time t is thus given by

$$\langle \hat{n}_j(t) \rangle = J_j^2 \left(\frac{4J}{\delta V} \left| \sin \frac{\delta V t}{2\hbar} \right| \right), \tag{9.1}$$

where δV denotes the detuning between adjacent lattice sites and J_j the Bessel function of the first kind. We then perform a reflective measurement on the ordered-array

resonance at a lattice depth of $300E_r^{532}$.

Fig. 9.3 shows an oscillating behavior of the reflectance, with two peaks arising at the refocussing times of the Bloch oscillations, $T_B = 2h/\delta V \approx 4.7\,\mathrm{ms}$; the maximum half-width spread is thus given by $\delta z/a \approx 2.5$. The cooperative linewidth, spectrally measured at selected points, also oscillates between a subradiant value at the refocussing points and a value broadened beyond the natural linewidth when the atoms are maximally dispersed. The measurements furthermore reveal that, while the SD of the vertical spread varies sinusoidally, the reflectance decreases disproportionally quickly when introducing disorder, highlighting the central role of the array order. Note that we also observe a reduction in the reflectance at the refocussing times, which we attribute to dephasing Bloch oscillations caused by residual potential curvature, resulting in imperfect array formation.

9.2 Cooperativity of electromagnetic response

In Sec. 9.1, we have studied the role of the positioning of atoms on light scattering and found 2D arrays to perform well as mirrors. In contrast, for disordered samples several issues arise which prevent reflective behavior: In out-of-plane disordered samples, a phase gradient imprinted by the incident light along the propagation axis leads to phase-matched emission that breaks the mirror symmetry and fundamentally cannot work as a mirror. In in-plane disordered samples, atoms may come arbitrarily close, leading to strong photon-mediated pairwise interactions, which effectively shift the local resonance and result in strong inhomogeneous broadening [306]. To specifically probe the role of the many-atom cooperativity, it is therefore interesting to study the density-dependent response of a 2D sample with controlled minimum inter-particle distance.

9.2.1 Array filling fraction

We implement these requirements by working with atoms at variable filling in our optical lattice, which introduces the lattice spacing as minimum distance and confines the atoms to a 2D plane. Experimentally, we again start with a unity-filled 2D MI; by applying a variable-duration MW pulse between the ground hyperfine states (HFSs) and optically pushing out one spin species, we can precisely reduce the filling fraction. In Fig. 9.4, we show the Lorentzian spectral fit results for the transmissive and reflective measurements.

The fitted linewidth approaches the natural linewidth for low fillings, signalling a response reminiscent of independent single atoms. With increasing filling, the linewidth smoothly reduces to the previously measured subradiant value near unity filling. We also find a notable dependence of the cooperative resonance frequency on the filling, which can be identified as the cooperative Lamb shift and captures the

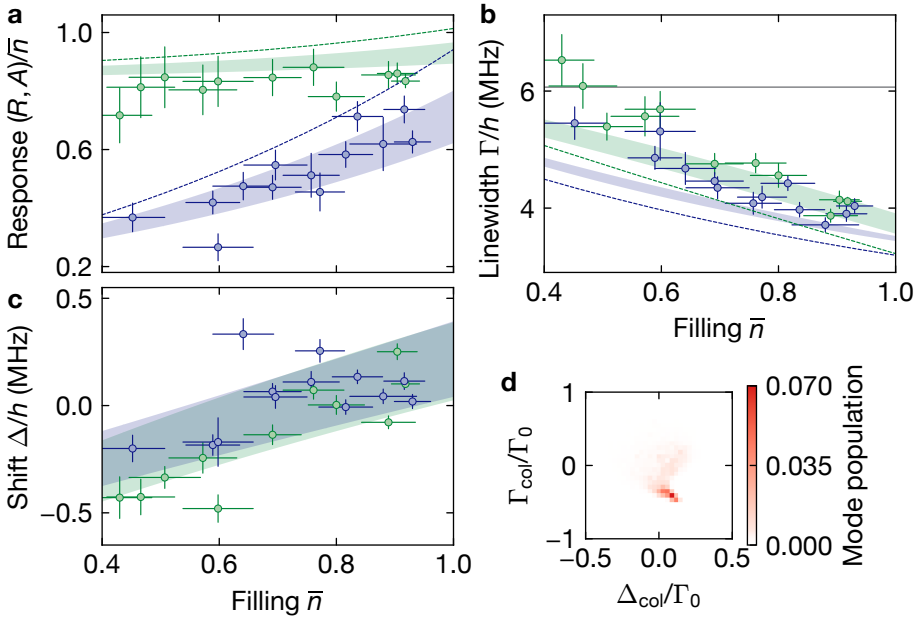

Figure 9.4: Cooperative response for arrays with varying filling. From experimentally measured reflective (blue) and transmissive (green) spectra, we fit a Lorentzian function and obtain the response amplitude, linewidth, and resonance shift. The dashed lines indicate numerical simulations of perfectly ordered arrays with reduced filling, the shaded areas account for a positional disorder of $s_{\parallel} = 0.054a$ and $s_{\perp} = 0.054$–$0.14a$ in the in-plane and out-of-plane direction, respectively. (**a**) The reflectance, R, and absorptance, $A = 1 - T$, normalized by the filling, $\overline{n}$, is expected to remain constant for independently responding atoms. The increase of the normalized reflectance with filling highlights the cooperative contribution to the directional reflection. (**b**) At high filling, the linewidth is clearly subradiant, and approaches the natural linewidth (gray line) with an increasing number of array defects. (**c**) By measuring the shift of the resonance frequency, we can furthermore observe the cooperative Lamb shift as the non-dissipative part of the dipole interaction. (**d**) An eigenmode decomposition simulated for perfectly ordered arrays at a filling of $\overline{n} = 0.4$ shows that mostly modes with similar properties as for the filled array are excited, in contrast to the disordered cases shown in Fig. 9.2.

non-dissipative part of the dipole–dipole interaction.

Finally, we analyze the filling-normalized reflectance and absorptance. In a dilute, non-cooperative medium, we would expect these quantities to be independent of the filling. The normalized reflectance, however, shows a clear increase with filling, which demonstrates the cooperative contribution to the directional reflection from the 2D array. The normalized absorptance, on the other hand, appears to be independent of filling: We attribute this effect to higher-order diffraction at low filling, which scatters light away from the collection angle of the objective. The reflection signal is not affected by this light and thus shows the cooperative response; in contrast, the absorption signal does not distinguish between randomly and specularly scattered light and normalized absorptance thus becomes insensitive to the filling.

Our numerical simulations agree quantitatively with the measured response when accounting for a positional spread of $s = 0.054$–$0.14a$. Possible reasons for the residual discrepancies in the linewidth at low filling include additional technical broadening effects and poorer SNR, diminishing the applicability of the Lorentzian fit.

9.3 Limitations to mirror fidelity

In our experiment, we have observed a strongly subradiant response and clearly specular reflection, and have demonstrated that atomic-array–based light–matter interfaces are feasible in principle. However, our measurements showed reflectances below 70 %, which are thus far below the ideal mirrors theoretically predicted and technologically envisioned. In this section, we will discuss both technical and fundamental limitations, and outline strategies to overcome these.

9.3.1 Technical limitations

Our experimental setup imposes several constraints to the available measurement configurations: The limited optical access in combination with comparatively small cloud sizes restricts us to use probe beams with waists that are much larger than the array size. In this case, even for an ideal mirror, diffraction off the array edges leads to light scattering away from the objective, resulting in a reduced reflectance, as suggested by our simulations in Fig. 9.5a. A related restriction to measuring the total scattered power is given by the limited numerical aperture (NA) of the collection objective, which misses light scattered at large angles, as shown in Fig. 9.5b. Note however that, in imperfectly ordered arrays, an increase in the NA mainly captures randomly scattered light and overestimates the specular reflectance.

Signal detection is furthermore limited by the comparatively high noise levels of our EMCCD camera, which requires the probe beam to scatter hundreds of photons. This leads to motional heating effects (as discussed in Sec. 9.3.2), exacerbating the array structure. By switching to a single-photon detector onto which the full array is

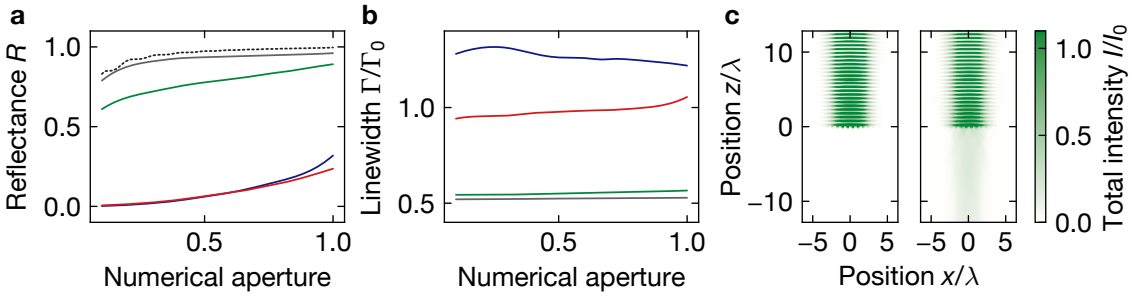

Figure 9.5: Technical limitations restricting observable mirror fidelity. (**a, b**) Simulated reflectance, R, and fitted linewidth, Γ/h, as a function of the objective numerical aperture (NA) for a perfectly ordered 14×14 array (gray), an array with a positional spread of $s = 0.054a$ (green), an out-of-plane disordered sample with SD $\Delta z = 10a$ (blue), and an in-plane disordered sample (red). The black dashed line indicates the response of an ideal mirror, demonstrating that the reduction in reflectance at low NA is a consequence of diffraction at the finite-size sample. (**c**) Simulating a probe beam with a waist smaller than the array, a perfectly ordered array (left) reflects nearly all incident light, whereas positional disorder, $(s_\parallel, s_\perp) = (0.054, 0.13)a$, leads to leakage (see also Fig. 9.1).

imaged, the response could be probed in the truly single-photon regime, which would substantially improve the observable reflectance.

9.3.2 Physical limitations

Neglecting any deterministic diffraction effects and technical limitations, atomic ensembles with ideal array order are expected to feature perfect reflectivity. However, atoms need to be trapped to form the array order, and imperfections in populating and creating the traps result in imperfect reflectivity.

Positional disorder

The most obvious imperfection, as discussed in Sec. 9.2.1, involves sub-unity filled arrays, and arises due to our preparation scheme of thermodynamically loading a MI of atoms in an optical lattice. Approaches to improve the array filling include selectively lowering the many-body system's entropy [120, 121] or deterministically implanting atoms from optical tweezers into the dense lattice [307]. Generally, missing atoms in denser ensembles appear to have a less detrimental effect on cooperativity [261], so operating in lattices with shorter spacing could result in a more robust mirror performance.

Another imperfection involves the positional uncertainty of each atom within its lattice site. For large lattice depths, V, each site can be harmonically approximated with trap frequency $\omega_{\mathrm{tr}}/2\pi = \sqrt{V/2ma^2}$, leading to a spatially Gaussian probability

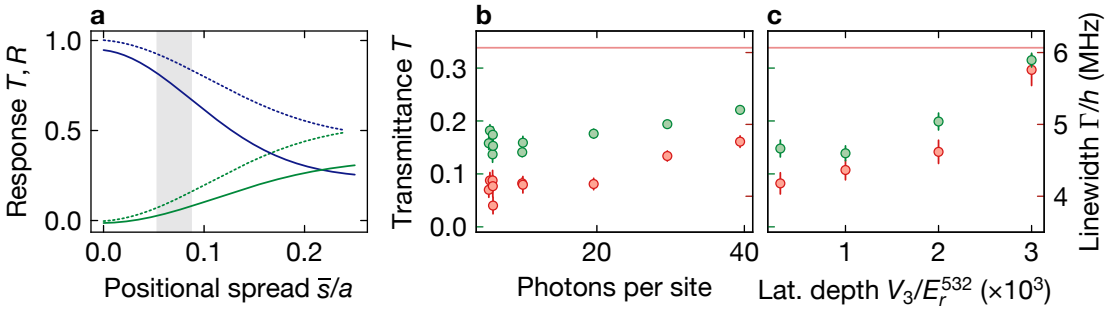

Figure 9.6: Limitations due to positional uncertainty. (**a**) Simulated transmittance (green) and reflectance (blue) as a function of the isotropic positional spread, $\bar{s}$. The solid lines correspond to the experimental configuration with a beam larger than the array and an objective with a numerical aperture of 0.68; the dashed lines considers the full 2π solid angle and a beam smaller than the array. The gray shaded region indicates the positional spread used in the simulations shown in Fig. 9.4. (**b**) Measurements at an isotropic lattice depth of $300E_{\mathrm{r}}^{532}$ for varying photon fluence. Recoil-induced heating leads to larger positional disorder and therefore an increased transmittance (green) and fitted linewidth (red). The red line marks the natural linewidth. (**c**) For a fixed fluence and horizontal lattice depth of $V_{1,2} = 1000E_{\mathrm{r}}^{532}$, we vary the vertical lattice depth, V_3. At low lattice depths (below the ones shown), the quantum fluctuations lead to substantial positional disorder, resulting in increased transmittance and linewidths. However, at higher lattice depths, we observe similar behavior due to the anti-trapped excited state.

distribution with a variance of

$$\delta r^2(\beta) = \frac{\hbar}{2m\omega_{\mathrm{tr}}} \frac{1}{\tanh(\beta\hbar\omega_{\mathrm{tr}}/2)}, \tag{9.2}$$

which accounts for both zero-point and thermal motion at a temperature of $1/k_B\beta$. In our experimental configuration, we scatter several photons per atom on average, whose recoil deposits a significant amount of kinetic energy, $K \approx 1/\beta$. The cooperative nature of the photon emission process also modifies the resulting recoil [308, 309] and, for the spontaneous emission of a single collective excitation in an infinite array, the added kinetic energy has been predicted to follow [310]

$$\frac{K_\perp}{E_{\mathrm{r}}^{780/2}} = \frac{2}{5}\frac{\Gamma_0}{\Gamma_{\mathrm{col}}}, \quad \frac{K_\parallel}{E_{\mathrm{r}}^{780/2}} \approx 0.7\frac{\Gamma_0}{\Gamma_{\mathrm{col}}}, \tag{9.3}$$

where $K_{\perp,\parallel}$ denote the out-of-plane and in-plane contribution of the kinetic energy. The inverse proportionality between kinetic energy and collective decay rate can be intuitively understood as recoil-imparting reabsorption processes within the atomic

ensemble extending the collective life time. Neglecting any motional effects on the EM response and accounting for both absorption and emission, we can extrapolate this relation to the experimental fluence of 6–16 photons per site, yielding a kinetic energy of $K \approx 54\text{–}144 E_\mathrm{r}^{532}$. Inserting into Eq. (9.2), we obtain a thermally increased positional SD of $\delta r/\delta r(\infty) \approx 1.8\text{–}3.0$, which roughly agrees with the amount of disorder we numerically identified in Sec. 9.2.1.

The correction to the EM response, numerically and experimentally analyzed in Figs. 9.6 a–b, can also be perturbatively evaluated, yielding a scaling behavior with positional spread of $\Delta_\mathrm{col} \propto \delta r/\lambda$ for the cooperative Lamb shift, and $R \propto (\delta r/\lambda)^2$ for the reflectance [261]. As the positional spread itself scales with the array spacing and harmonic trap frequency, employing shorter-wavelength and higher-power lattices constitutes a promising path to enhancing the mirror fidelity.

Trap-induced dephasing

While we expect increasing lattice depths to clearly improve the mirror response in the truly single-photon limit, we find additional deteriorating effects arising upon scattering larger numbers of photons, as shown in Fig. 9.6c. The core problem involves the optical dipole trap at a wavelength of 1064 nm, which creates an attractive potential for the $|5S\rangle$ ground state atoms but a repulsive one for the $|5P\rangle$ excited state. We experimentally characterized this effect by measuring the resonance shift with lattice depth and obtain a proportionality factor of $d\Delta/dV = h \cdot 5.06(10)\,\mathrm{kHz}/E_\mathrm{r}^{532}$.

For a large number of scattered photons, the atoms spend a significant amount of time in the excited state. As the excited state is anti-trapped, it accelerates motional spreading of the wave function, leading to an increased kinetic energy after projecting back to the ground state. With the additional positional spread, the atoms also populate areas away from the harmonic potential minimum; as the local optical transition also varies with the potential, this effect introduces inhomogeneities in the dipole resonance, further diminishing the mirror response. At small lattice depths, the motional acceleration is much slower and may not have significantly influenced the dynamics, such that the base positional spread dominates the mirror response. For a given photon fluence, we therefore expect an optimum lattice depth which maximizes the observed reflectance; experimentally, we indeed find a maximum reflectance at about $300 E_\mathrm{r}^{532}$, which we consequently chose as our measurement configuration.

This phenomenon can be entirely avoided by working with an optical lattice at a so-called magic wavelength [311], at which the light shift is equal for both the ground and excited states, which can be found for ^{87}Rb at, e.g., 740.07(1) nm [312]. At this wavelength, we expect to be able to substantially reduce positional disorder, and gain the previously discussed advantages for arrays with smaller spacings.

9.4 Conclusion and outlook

In this chapter, we have studied cooperative light scattering in 2D subwavelength arrays of atomic dipoles. By measuring the transmission and reflection spectra using a weak probe beam, we have observed a mirror response with a narrowed linewidth, indicating strong photon-mediated interactions and direct excitation of subradiant eigenmodes. Our experiments represent the realization of a novel class of light–matter interfaces, whose paraxial nature and intrinsically clean implementability yields great potential for applications in quantum optics. Although our mirror performance is presently limited, we found that effects arising from positional disorder pose the major obstacle and identified promising paths to qualitatively enhanced reflectivities.

Since our work was focussed on the linear (single-photon, classical) regime, this naturally raises the question about the EM response of dipole arrays in the nonlinear (quantum many-body) regime. While the spectral steady-state response for both low and high probe beam intensities are expected to obey semi-classical dynamics, intermediate intensities have been predicted to show quantum-correlation–induced deviations [313]. Better-controlled nonlinearities can, however, be achieved by introducing long-range Rydberg interactions [314]: Employing electromagnetically induced transparency (EIT) with the Rydberg state, the mirror can be turned into a single-photon saturable collective dipole [296]. In a subsequent work [315], we have furthermore applied EIT to demonstrate a mirror, whose reflectivity can be switched off with a single qubit, by adding an ancilla atom which can be excited to a Rydberg state as the control qubit. An extension of this scheme to multiple ancilla atoms in a larger array could then realize a quantum spatial light modulator (SLM), capable of engineering spatially multimode quantum states of light [292].

Chapter 10

Conclusion and outlook

In this thesis, we have experimentally studied ultracold atoms in optical lattices in versatile ways to advance the understanding of static and dynamic quantum many-body phenomena. In the following, we will summarize the novel conclusions drawn from our measurements, and discuss future experimental perspectives. For possible direct extensions of the experiments performed, refer also to the final sections in the respective chapters.

10.1 Conclusion

In Part I, we studied the equilibrium properties of the Bose–Hubbard (BH) model in various flexibly tunable two-dimensional (2D) lattice geometries, which were enabled by passively phase-stable optical lattices with tunable base geometry and programmable site-blocking potentials with minimized cross talk. By varying the BH parameter ratio across the superfluid (SF)–Mott insulator (MI) phase transition, we microscopically observed the geometry-dependent quantum fluctuations in the form of doublon–hole pairs. By extracting the brane parity (BP), we demonstrated a 2D generalization of the nonlocal order seen in one-dimensional (1D) MIs and furthermore found a scaling collapse when rescaling the kinetic energy by the mean lattice coordination number.

In Part II, we investigated hydrodynamic spin transport in the isotropic Heisenberg (XXX) chain by tracking the relaxation dynamics of a domain wall (DW) initial state. The well-defined and large system sizes obtained through increased lattice-beam waists and local potential shaping were crucial to realizing precise transport measurements. For the bare chain, we experimentally confirmed the predicted superdiffusive scaling with a dynamical exponent of $3/2$. In contrast, transport in a net magnetized chain showed ballistic behavior while 2D coupling led to diffusive evolution, highlighting the role of non-abelian symmetry and integrability for the emergence of superdiffusion. Exploiting the single-spin sensitivity of our quantum gas microscope (QGM), we furthermore measured the full counting statistics (FCS) of the transported magnetization. The resulting skewed distribution indicated a nonlinear underlying transport process, reminiscent of the Kardar–Parisi–Zhang (KPZ) universality class.

In Part III, we utilized the subwavelength spacing of our optical lattice to study cooperative light scattering in square arrays of atomic dipoles. By probing the steady-

state reflectance and transmittance spectra in the single-photon regime, we demonstrated the direct excitation of subradiant optical modes. We furthermore observed high specular reflectivity, indicating the utility of atomic arrays for quantum information processing, and characterized its sensitivity to positional disorder.

10.2 Outlook

The measurements and technical upgrades presented in this thesis have opened the door to a variety of future research directions in the fields of both quantum simulation of mobile bosons or spins on lattices and quantum optics with atomic dipole arrays.

Quantum simulation with itinerant atoms

The implementation of large-scale BH systems with homogeneous trapping potentials in principle enables studies of the quantum phase transition (QPT) beyond the coarse parametric resolution probed so far. This could allow for measurements of critical scaling near the transition [316], for which the experimental challenge lies in minimizing residual potential disorder far below the kinetic energy. The control over the lattice geometry and the presence of defined system edges could also enable microscopic studies of non-dispersive edge states [317, 318]; by implementing driven lattices [319], one could furthermore engineer flat ground bands, where geometric frustration in the BH model is predicted to give rise to supersolid or exotic superfluid phases [320, 321].

Lattice-dependent effects can also be observed when introducing the spin degree of freedom (DOF), enabling studies of the bosonic t–J model [96]. Using single-site addressing, hole propagation measurements [322] can be performed to study polaronic physics in otherwise undoped variable spin backgrounds, which could feature interference-driven spin ordering or frustration-induced magnon–hole binding [323–325], and could reveal differences to the fermionic model variant. Furthermore, by performing dynamics in site-resolved projected magnetic fields with a Néel-state spin background, staggered-field–assisted magnetic hole–hole binding could be studied. The main challenge for such experiments, in addition to homogeneous potentials and projection fidelity, lies in the preparation of a defect-free atomic background.

While we have studied the properties of 1D spin chains in detail, the 2D XXX model also hosts rich physics. Regarding equilibrium states, single-site control could allow for the adiabatic preparation of antiferromagnetic states [243], enabling the study of the inverted spectrum and negative-temperature properties of the ferromagnetic spin model [326]; furthermore, by subsequently changing the lattice geometry, one could potentially prepare spin liquid or chiral superfluid phases [327–329]. In the context of far-from-equilibrium physics, universal equilibration dynamics in 2D can be studied, including interface deformations of a DW initial state or the relaxation of spin helices [330]. In analogy to the hole-propagation measurements, mobile holes also

represent a limitation to studying 2D spin models, for which the separation of hopping and spin-exchange timescales hinders probing pure spin physics. A possible solution for dynamics experiments could involve adding a strong spin-independent potential gradient, which localizes the holes on relevant timescales.

Finally, Raman sideband imaging of a MI state prior to an experiment would constitute a valuable tool [331], aiding in the realization of better-filled arrays [307] and enabling the characterization of the exact initial many-body state of every experimental run. With this knowledge, one could measure the FCS of generic time-evolution experiments starting from product states [332, 333], or perform quantum information experiments, including benchmarking the many-body fidelity of itinerant quantum simulators [334].

Quantum optics with atom arrays

Atom arrays with optimized positional order constitute a promising quantum optics platform, as they can act as coherent, narrow-band and saturable optical elements. This could enable waveguide quantum electrodynamics (QED) studies of separately trapped impurity atoms, where the photonic waveguide is formed by atomic chains and its dispersion could be engineered through atomic positioning, enabling control over the interactions between the impurities [335]. Furthermore, two spatially separated 2D atomic layers could be prepared to realize optical cavities to generate interesting photonic states or to probe cavity QED [336, 337].

A photon detector with higher sensitivity could be added to substantially extend our experiments, in which we probed the control of the mirror reflectivity with a single atom through Rydberg–electromagnetically induced transparency (EIT) [315], and could be used to measure correlations between atomic and mirror states. Preparing the control atom in a superposition state, one could generate a photonic cat state [292], whose detection would require capturing and interfering both the transmitted and reflected part of the probe light in a phase-stabilized setup. Atomic multimode control over the array reflectivity could be demonstrated by preparing entangled states of multiple spatially separated control atoms [338], which switch the electromagnetic (EM) response on a subarea of the array. Correlations in the light field, which characterize the state of the control atoms, could be observable by interfering the light originating from the different subareas, and would naturally be detectable by imaging the far field of the reflected light.

As the mirror reflectivity characterizes the achievable fidelities in many quantum applications [291], improving the array order of the atoms is of central importance. This can be achieved using optical lattices at a magic wavelength for ^{87}Rb of 740 nm, which not only allows for a reduced strength of and sensitivity on positional disorder but would also grant access to strongly subradiant modes outside of the light cone [76]. While not directly excitable, these modes could be experimentally prepared through a weak drive of a three-photon transition or by geometric phase imprinting with fast

pulses [339, 340]. The long lifetimes associated with such states could then enable the realization of quantum memories or controlled photonic interactions [76, 290, 341, 342]. For finite-size arrays of dipoles with unique electronic ground states, local illumination could furthermore drive topologically protected edge states enabling controlled free-space emission [295, 343].

The introduction of a fast single-photon–sensitive detector could further expand the range of possible experiments to studying the decay dynamics of, e.g., metrologically interesting multi-photon excited states, including the observation of late-time subradiant power-law decay with interaction-induced spatial correlations [344]. Full inversion of the dipoles could in addition yield initial decay dynamics which show directional, array-spacing and dimensionality-dependent superradiant bursts [269].

Bibliography

[1] R. P. Feynman. *Simulating physics with computers*. Int. J. Theor. Phys. **21**, 467–488 (1982). (Cited on page **1**)

[2] I. M. Georgescu, S. Ashhab, and F. Nori. *Quantum simulation*. Rev. Mod. Phys. **86**, 153–185 (2014). (Cited on page **1**)

[3] L. Henriet, L. Beguin, A. Signoles, T. Lahaye, A. Browaeys, G.-O. Reymond, and C. Jurczak. *Quantum computing with neutral atoms*. Quantum **4**, 327 (2020). (Cited on page **1**)

[4] N. Gisin and R. Thew. *Quantum communication*. Nat. Photon. **1**, 165–171 (2007). (Cited on page **1**)

[5] L. Pezzè, A. Smerzi, M. K. Oberthaler, R. Schmied, and P. Treutlein. *Quantum metrology with nonclassical states of atomic ensembles*. Rev. Mod. Phys. **90**, 035005 (2018). (Cited on page **1**)

[6] I. Bloch, J. Dalibard, and W. Zwerger. *Many-body physics with ultracold gases*. Rev. Mod. Phys. **80**, 885–964 (2008). (Cited on pages **1**, **5**, **7**, and **41**)

[7] C. Gross and I. Bloch. *Quantum simulations with ultracold atoms in optical lattices*. Science **357**, 995–1001 (2017). (Cited on pages **1** and **5**)

[8] A. Periwal, E. S. Cooper, P. Kunkel, J. F. Wienand, E. J. Davis, and M. Schleier-Smith. *Programmable interactions and emergent geometry in an array of atom clouds*. Nature **600**, 630–635 (2021). (Cited on page **1**)

[9] S. Chu, L. Hollberg, J. E. Bjorkholm, A. Cable, and A. Ashkin. *Three-dimensional viscous confinement and cooling of atoms by resonance radiation pressure*. Phys. Rev. Lett. **55**, 48–51 (1985). (Cited on page **1**)

[10] M. H. Anderson, J. R. Ensher, M. R. Matthews, C. E. Wieman, and E. A. Cornell. *Observation of Bose-Einstein condensation in a dilute atomic vapor*. Science **269**, 198–201 (1995). (Cited on page **1**)

[11] K. B. Davis, M. O. Mewes, M. R. Andrews, N. J. van Druten, D. S. Durfee, D. M. Kurn, and W. Ketterle. *Bose-Einstein condensation in a gas of sodium atoms*. Phys. Rev. Lett. **75**, 3969–3973 (1995). (Cited on page **1**)

[12] B. DeMarco and D. S. Jin. *Onset of Fermi degeneracy in a trapped atomic gas*. Science **285**, 1703–1706 (1999). (Cited on page **1**)

[13] W. Zwerger, editor. *The BCS-BEC crossover and the unitary Fermi gas*, volume 836 of *Lecture Notes in Physics*. Springer, Berlin, Heidelberg (2012). ISBN 978-3-642-21978-8. (Cited on page **1**)

[14] M. Greiner, O. Mandel, T. Esslinger, T. W. Hänsch, and I. Bloch. *Quantum phase transition from a superfluid to a Mott insulator in a gas of ultracold atoms*. Nature **415**, 39–44 (2002). (Cited on pages **1**, **5**, and **41**)

[15] D. Jaksch, C. Bruder, J. I. Cirac, C. W. Gardiner, and P. Zoller. *Cold bosonic atoms in optical lattices*. Phys. Rev. Lett. **81**, 3108–3111 (1998). (Cited on pages **2**, **5**, and **8**)

[16] S. Trotzky, P. Cheinet, S. Fölling, M. Feld, U. Schnorrberger, A. M. Rey, A. Polkovnikov, E. A. Demler, M. D. Lukin, and I. Bloch. *Time-resolved observation and control of superexchange interactions with ultracold atoms in optical lattices*. Science **319**, 295–299 (2008). (Cited on page **2**)

[17] L. Tarruell, D. Greif, T. Uehlinger, G. Jotzu, and T. Esslinger. *Creating, moving and merging Dirac points with a Fermi gas in a tunable honeycomb lattice*. Nature **483**, 302–305 (2012). (Cited on pages **2**, **24**, and **26**)

[18] G.-B. Jo, J. Guzman, C. K. Thomas, P. Hosur, A. Vishwanath, and D. M. Stamper-Kurn. *Ultracold atoms in a tunable optical kagome lattice*. Phys. Rev. Lett. **108**, 045305 (2012). (Cited on pages **2** and **24**)

[19] M. Aidelsburger, M. Atala, S. Nascimbène, S. Trotzky, Y.-A. Chen, and I. Bloch. *Experimental realization of strong effective magnetic fields in an optical lattice*. Phys. Rev. Lett. **107**, 255301 (2011). (Cited on page **2**)

[20] J. Struck, C. Ölschläger, R. Le Targat, P. Soltan-Panahi, A. Eckardt, M. Lewenstein, P. Windpassinger, and K. Sengstock. *Quantum simulation of frustrated classical magnetism in triangular optical lattices*. Science **333**, 996–999 (2011). (Cited on page **2**)

[21] M. Aidelsburger, M. Lohse, C. Schweizer, M. Atala, J. T. Barreiro, S. Nascimbène, N. R. Cooper, I. Bloch, and N. Goldman. *Measuring the Chern number of Hofstadter bands with ultracold bosonic atoms*. Nat. Phys. **11**, 162–166 (2015). (Cited on page **2**)

[22] W. S. Bakr, J. I. Gillen, A. Peng, S. Fölling, and M. Greiner. *A quantum gas microscope for detecting single atoms in a Hubbard-regime optical lattice*. Nature **462**, 74–77 (2009). (Cited on pages **2** and **5**)

[23] J. F. Sherson, C. Weitenberg, M. Endres, M. Cheneau, I. Bloch, and S. Kuhr. *Single-atom-resolved fluorescence imaging of an atomic Mott insulator*. Nature **467**, 68–72 (2010). (Cited on pages **2**, **5**, **8**, **11**, and **18**)

[24] L. W. Cheuk, M. A. Nichols, M. Okan, T. Gersdorf, V. V. Ramasesh, W. S. Bakr, T. Lompe, and M. W. Zwierlein. *Quantum-gas microscope for fermionic atoms*. Phys. Rev. Lett. **114**, 193001 (2015). (Cited on page **2**)

[25] M. F. Parsons, F. Huber, A. Mazurenko, C. S. Chiu, W. Setiawan, K. Wooley-Brown, S. Blatt, and M. Greiner. *Site-resolved imaging of fermionic Li_6 in an optical lattice*. Phys. Rev. Lett. **114**, 213002 (2015). (Cited on page **2**)

[26] E. Haller, J. Hudson, A. Kelly, D. A. Cotta, B. Peaudecerf, G. D. Bruce, and S. Kuhr. *Single-atom imaging of fermions in a quantum-gas microscope*. Nat. Phys. **11**, 738–742 (2015). (Cited on page **2**)

[27] A. Omran, M. Boll, T. A. Hilker, K. Kleinlein, G. Salomon, I. Bloch, and C. Gross. *Microscopic observation of Pauli blocking in degenerate fermionic lattice gases*. Phys. Rev. Lett. **115**, 263001 (2015). (Cited on page **2**)

[28] G. J. A. Edge, R. Anderson, D. Jervis, D. C. McKay, R. Day, S. Trotzky, and J. H. Thywissen. *Imaging and addressing of individual fermionic atoms in an optical lattice*. Phys. Rev. A **92**, 063406 (2015). (Cited on page **2**)

[29] C. Gross and W. S. Bakr. *Quantum gas microscopy for single atom and spin detection*. Nat. Phys. **17**, 1316–1323 (2021). (Cited on pages **2**, **5**, and **11**)

[30] J. Simon, W. S. Bakr, R. Ma, M. E. Tai, P. M. Preiss, and M. Greiner. *Quantum simulation of antiferromagnetic spin chains in an optical lattice*. Nature **472**, 307–312 (2011). (Cited on page **2**)

[31] M. Endres, M. Cheneau, T. Fukuhara, C. Weitenberg, P. Schauß, C. Gross, L. Mazza, M. C. Bañuls, L. Pollet, I. Bloch, and S. Kuhr. *Observation of correlated particle-hole pairs and string order in low-dimensional Mott insulators*. Science **334**, 200–203 (2011). (Cited on pages **2**, **41**, **45**, and **49**)

[32] M. F. Parsons, A. Mazurenko, C. S. Chiu, G. Ji, D. Greif, and M. Greiner. *Site-resolved measurement of the spin-correlation function in the Fermi-Hubbard model*. Science **353**, 1253–1256 (2016). (Cited on page **2**)

[33] M. Boll, T. A. Hilker, G. Salomon, A. Omran, J. Nespolo, L. Pollet, I. Bloch, and C. Gross. *Spin- and density-resolved microscopy of antiferromagnetic correlations in Fermi-Hubbard chains*. Science **353**, 1257–1260 (2016). (Cited on pages **2** and **11**)

[34] L. W. Cheuk, M. A. Nichols, K. R. Lawrence, M. Okan, H. Zhang, E. Khatami, N. Trivedi, T. Paiva, M. Rigol, and M. W. Zwierlein. *Observation of spatial charge and spin correlations in the 2D Fermi-Hubbard model*. Science **353**, 1260–1264 (2016). (Cited on page **2**)

[35] A. Mazurenko, C. S. Chiu, G. Ji, M. F. Parsons, M. Kanász-Nagy, R. Schmidt, F. Grusdt, E. Demler, D. Greif, and M. Greiner. *A cold-atom Fermi–Hubbard antiferromagnet*. Nature **545**, 462–466 (2017). (Cited on pages **2** and **21**)

[36] T. Hartke, B. Oreg, N. Jia, and M. Zwierlein. *Doublon-hole correlations and fluctuation thermometry in a Fermi-Hubbard gas*. Phys. Rev. Lett. **125**, 113601 (2020). (Cited on pages **2** and **45**)

[37] T. A. Hilker, G. Salomon, F. Grusdt, A. Omran, M. Boll, E. Demler, I. Bloch, and C. Gross. *Revealing hidden antiferromagnetic correlations in doped Hubbard chains via string correlators*. Science **357**, 484–487 (2017). (Cited on pages **2** and **49**)

[38] C. S. Chiu, G. Ji, A. Bohrdt, M. Xu, M. Knap, E. Demler, F. Grusdt, M. Greiner, and D. Greif. *String patterns in the doped Hubbard model*. Science **365**, 251–256 (2019). (Cited on page **2**)

[39] P. Sompet, S. Hirthe, D. Bourgund, T. Chalopin, J. Bibo, J. Koepsell, P. Bojović, R. Verresen, F. Pollmann, G. Salomon, C. Gross, T. A. Hilker, and I. Bloch. *Realizing the symmetry-protected Haldane phase in Fermi–Hubbard ladders*. Nature **606**, 484–488 (2022). (Cited on pages **2** and **49**)

[40] C. Weitenberg, M. Endres, J. F. Sherson, M. Cheneau, P. Schauß, T. Fukuhara, I. Bloch, and S. Kuhr. *Single-spin addressing in an atomic Mott insulator*. Nature **471**, 319–324 (2011). (Cited on pages **2**, **21**, and **23**)

[41] T. Fukuhara, A. Kantian, M. Endres, M. Cheneau, P. Schauß, S. Hild, D. Bellem, U. Schollwöck, T. Giamarchi, C. Gross, I. Bloch, and S. Kuhr. *Quantum dynamics of a mobile spin impurity*. Nat. Phys. **9**, 235–241 (2013). (Cited on pages **2**, **11**, **21**, and **37**)

[42] P. M. Preiss, R. Ma, M. E. Tai, A. Lukin, M. Rispoli, P. Zupancic, Y. Lahini, R. Islam, and M. Greiner. *Strongly correlated quantum walks in optical lattices*. Science **347**, 1229–1233 (2015). (Cited on pages **2**, **21**, **37**, and **112**)

[43] R. Islam, R. Ma, P. M. Preiss, M. Eric Tai, A. Lukin, M. Rispoli, and M. Greiner. *Measuring entanglement entropy in a quantum many-body system*. Nature **528**, 77–83 (2015). (Cited on page **2**)

[44] M. Cheneau, P. Barmettler, D. Poletti, M. Endres, P. Schauß, T. Fukuhara, C. Gross, I. Bloch, C. Kollath, and S. Kuhr. *Light-cone-like spreading of correlations in a quantum many-body system*. Nature **481**, 484–487 (2012). (Cited on page **2**)

[45] J. Koepsell, J. Vijayan, P. Sompet, F. Grusdt, T. A. Hilker, E. Demler, G. Salomon, I. Bloch, and C. Gross. *Imaging magnetic polarons in the doped Fermi–Hubbard model*. Nature **572**, 358–362 (2019). (Cited on page **2**)

[46] J. Vijayan, P. Sompet, G. Salomon, J. Koepsell, S. Hirthe, A. Bohrdt, F. Grusdt, I. Bloch, and C. Gross. *Time-resolved observation of spin-charge deconfinement in fermionic Hubbard chains*. Science **367**, 186–189 (2020). (Cited on page **2**)

[47] A. Polkovnikov, K. Sengupta, A. Silva, and M. Vengalattore. *Colloquium: Nonequilibrium dynamics of closed interacting quantum systems*. Rev. Mod. Phys. **83**, 863–883 (2011). (Cited on page **2**)

[48] J. Eisert, M. Friesdorf, and C. Gogolin. *Quantum many-body systems out of equilibrium*. Nat. Phys. **11**, 124–130 (2015). (Cited on page **2**)

[49] A. Chandran, T. Iadecola, V. Khemani, and R. Moessner. *Quantum many-body scars: A quasiparticle perspective*. Annu. Rev. Condens. Matter Phys. **14**, 443–469 (2023). (Cited on page **2**)

[50] B. Paredes, A. Widera, V. Murg, O. Mandel, S. Fölling, I. Cirac, G. V. Shlyapnikov, T. W. Hänsch, and I. Bloch. *Tonks–Girardeau gas of ultracold atoms in an optical lattice*. Nature **429**, 277–281 (2004). (Cited on page **2**)

[51] T. Kinoshita, T. Wenger, and D. S. Weiss. *A quantum Newton's cradle*. Nature **440**, 900–903 (2006). (Cited on page **2**)

[52] M. Schreiber, S. S. Hodgman, P. Bordia, H. P. Lüschen, M. H. Fischer, R. Vosk, E. Altman, U. Schneider, and I. Bloch. *Observation of many-body localization of interacting fermions in a quasirandom optical lattice*. Science **349**, 842–845 (2015). (Cited on page **2**)

[53] J.-y. Choi, S. Hild, J. Zeiher, P. Schauß, A. Rubio-Abadal, T. Yefsah, V. Khemani, D. A. Huse, I. Bloch, and C. Gross. *Exploring the many-body localization transition in two dimensions*. Science **352**, 1547–1552 (2016). (Cited on page **2**)

[54] H. Bernien, S. Schwartz, A. Keesling, H. Levine, A. Omran, H. Pichler, S. Choi, A. S. Zibrov, M. Endres, M. Greiner, V. Vuletić, and M. D. Lukin. *Probing many-body dynamics on a 51-atom quantum simulator*. Nature **551**, 579–584 (2017). (Cited on page **2**)

[55] S. Scherg, T. Kohlert, P. Sala, F. Pollmann, B. Hebbe Madhusudhana, I. Bloch, and M. Aidelsburger. *Observing non-ergodicity due to kinetic constraints in tilted Fermi-Hubbard chains*. Nat. Commun. **12**, 4490 (2021). (Cited on page **2**)

[56] P. N. Jepsen, Y. K. E. Lee, H. Lin, I. Dimitrova, Y. Margalit, W. W. Ho, and W. Ketterle. *Long-lived phantom helix states in Heisenberg quantum magnets*. Nat. Phys. **18**, 899–904 (2022). (Cited on page **2**)

[57] C.-C. Chien, S. Peotta, and M. Di Ventra. *Quantum transport in ultracold atoms*. Nat. Phys. **11**, 998–1004 (2015). (Cited on page **2**)

[58] J.-P. Brantut, J. Meineke, D. Stadler, S. Krinner, and T. Esslinger. *Conduction of ultracold fermions through a mesoscopic channel*. Science **337**, 1069–1071 (2012). (Cited on page **2**)

[59] U. Schneider, L. Hackermüller, J. P. Ronzheimer, S. Will, S. Braun, T. Best, I. Bloch, E. Demler, S. Mandt, D. Rasch, and A. Rosch. *Fermionic transport and out-of-equilibrium dynamics in a homogeneous Hubbard model with ultracold atoms*. Nat. Phys. **8**, 213–218 (2012). (Cited on page **2**)

[60] S. Hild, T. Fukuhara, P. Schauß, J. Zeiher, M. Knap, E. Demler, I. Bloch, and C. Gross. *Far-from-equilibrium spin transport in Heisenberg quantum magnets*. Phys. Rev. Lett. **113**, 147205 (2014). (Cited on pages **2**, **71**, and **81**)

[61] P. T. Brown, D. Mitra, E. Guardado-Sanchez, R. Nourafkan, A. Reymbaut, C.-D. Hébert, S. Bergeron, A.-M. S. Tremblay, J. Kokalj, D. A. Huse, P. Schauß, and W. S. Bakr. *Bad metallic transport in a cold atom Fermi-Hubbard system*. Science **363**, 379–382 (2019). (Cited on page **2**)

[62] M. A. Nichols, L. W. Cheuk, M. Okan, T. R. Hartke, E. Mendez, T. Senthil, E. Khatami, H. Zhang, and M. W. Zwierlein. *Spin transport in a Mott insulator of ultracold fermions*. Science **363**, 383–387 (2019). (Cited on pages **2** and **71**)

[63] M. Ljubotina, M. Žnidarič, and T. Prosen. *Spin diffusion from an inhomogeneous quench in an integrable system*. Nat. Commun. **8**, 16117 (2017). (Cited on pages **2**, **60**, **67**, **84**, **85**, and **87**)

[64] M. Ljubotina, M. Žnidarič, and T. Prosen. *Kardar-Parisi-Zhang physics in the quantum Heisenberg magnet*. Phys. Rev. Lett. **122**, 210602 (2019). (Cited on pages **2**, **60**, **65**, **67**, **76**, and **87**)

[65] H. J. Kimble, M. Dagenais, and L. Mandel. *Photon antibunching in resonance fluorescence*. Phys. Rev. Lett. **39**, 691–695 (1977). (Cited on page **2**)

[66] M. Riebe, H. Häffner, C. F. Roos, W. Hänsel, J. Benhelm, G. P. T. Lancaster, T. W. Körber, C. Becher, F. Schmidt-Kaler, D. F. V. James, and R. Blatt. *Deterministic quantum teleportation with atoms*. Nature **429**, 734–737 (2004). (Cited on page **2**)

[67] C. Gardiner and P. Zoller. *The quantum world of ultra-cold atoms and light. Book II: The physics of quantum-optical devices*. World Scientific Publishing Company (2015). ISBN 978-1-78326-615-9. (Cited on page **2**)

[68] W. Rosenfeld, D. Burchardt, R. Garthoff, K. Redeker, N. Ortegel, M. Rau, and H. Weinfurter. *Event-ready Bell test using entangled atoms simultaneously closing detection and locality loopholes*. Phys. Rev. Lett. **119**, 010402 (2017). (Cited on page **2**)

[69] P. Thomas, L. Ruscio, O. Morin, and G. Rempe. *Efficient generation of entangled multiphoton graph states from a single atom*. Nature **608**, 677–681 (2022). (Cited on page **2**)

[70] C.-W. Yang, Y. Yu, J. Li, B. Jing, X.-H. Bao, and J.-W. Pan. *Sequential generation of multiphoton entanglement with a Rydberg superatom*. Nat. Photon. **16**, 658–661 (2022). (Cited on page **2**)

[71] A. I. Lvovsky, B. C. Sanders, and W. Tittel. *Optical quantum memory*. Nat. Photon. **3**, 706–714 (2009). (Cited on page **2**)

[72] K. Hammerer, A. S. Sørensen, and E. S. Polzik. *Quantum interface between light and atomic ensembles*. Rev. Mod. Phys. **82**, 1041–1093 (2010). (Cited on pages **2** and **95**)

[73] S. Inouye, A. P. Chikkatur, D. M. Stamper-Kurn, J. Stenger, D. E. Pritchard, and W. Ketterle. *Superradiant Rayleigh scattering from a Bose-Einstein condensate*. Science **285**, 571–574 (1999). (Cited on pages **3** and **96**)

[74] W. Guerin, M. O. Araújo, and R. Kaiser. *Subradiance in a large cloud of cold atoms*. Phys. Rev. Lett. **116**, 083601 (2016). (Cited on pages **3** and **96**)

[75] C. Weitenberg, P. Schauß, T. Fukuhara, M. Cheneau, M. Endres, I. Bloch, and S. Kuhr. *Coherent light scattering from a two-dimensional Mott insulator*. Phys. Rev. Lett. **106**, 215301 (2011). (Cited on pages **3** and **19**)

[76] A. Asenjo-Garcia, M. Moreno-Cardoner, A. Albrecht, H. J. Kimble, and D. E. Chang. *Exponential improvement in photon storage fidelities using subradiance and "selective radiance" in atomic arrays*. Phys. Rev. X **7**, 031024 (2017). (Cited on pages **3**, **10**, **98**, **99**, **101**, **123**, and **124**)

[77] I. Bloch, J. Dalibard, and S. Nascimbène. *Quantum simulations with ultracold quantum gases*. Nat. Phys. **8**, 267–276 (2012). (Cited on page **5**)

[78] R. Jördens, N. Strohmaier, K. Günter, H. Moritz, and T. Esslinger. *A Mott insulator of fermionic atoms in an optical lattice*. Nature **455**, 204–207 (2008). (Cited on page **5**)

[79] R. Grimm, M. Weidemüller, and Y. B. Ovchinnikov. *Optical dipole traps for neutral atoms*. Adv. At. Mol. Opt. Phys. **42**, 95–170 (2000). (Cited on pages **5** and **24**)

[80] N. W. Ashcroft and N. D. Mermin. *Solid state physics*. Cengage (2021). ISBN 978-0-357-67081-1. (Cited on page **5**)

[81] U. Bissbort. *Dynamical effects and disorder in ultracold bosonic matter*. Ph.D. thesis, Johann Wolfgang Goethe-Universität Frankfurt (2012). (Cited on page **6**)

[82] M. Lewenstein, A. Sanpera, and V. Ahufinger. *Ultracold atoms in optical lattices: Simulating quantum many-body systems*. OUP Oxford (2012). ISBN 978-0-19-162743-9. (Cited on pages **6** and **7**)

[83] M. Arzamasovs and B. Liu. *Tight-binding tunneling amplitude of an optical lattice*. Eur. J. Phys. **38**, 065405 (2017). (Cited on page **6**)

[84] M. P. A. Fisher, P. B. Weichman, G. Grinstein, and D. S. Fisher. *Boson localization and the superfluid-insulator transition*. Phys. Rev. B **40**, 546–570 (1989). (Cited on pages **6**, **7**, and **41**)

[85] D.-S. Lühmann, O. Jürgensen, and K. Sengstock. *Multi-orbital and density-induced tunneling of bosons in optical lattices*. New J. Phys. **14**, 033021 (2012). (Cited on page **6**)

[86] S. Sachdev. *Quantum phase transitions*. Cambridge University Press (2011). ISBN 978-0-521-51468-2. (Cited on pages **7**, **41**, and **42**)

[87] A. J. Leggett. *Quantum liquids: Bose condensation and Cooper pairing in condensed-matter systems*. OUP Oxford (2006). ISBN 978-0-19-852643-8. (Cited on page **7**)

[88] E. Berg, E. G. Dalla Torre, T. Giamarchi, and E. Altman. *Rise and fall of hidden string order of lattice bosons*. Phys. Rev. B **77**, 245119 (2008). (Cited on pages **7**, **41**, and **49**)

[89] S. P. Rath, W. Simeth, M. Endres, and W. Zwerger. *Non-local order in Mott insulators, duality and Wilson loops*. Ann. Phys. **334**, 256–271 (2013). (Cited on pages **7**, **41**, **49**, and **50**)

[90] S. Fazzini, F. Becca, and A. Montorsi. *Nonlocal parity order in the two-dimensional Mott insulator*. Phys. Rev. Lett. **118**, 157602 (2017). (Cited on pages **7**, **41**, **49**, and **50**)

[91] N. Gemelke, X. Zhang, C.-L. Hung, and C. Chin. *In situ observation of incompressible Mott-insulating domains in ultracold atomic gases*. Nature **460**, 995–998 (2009). (Cited on page **8**)

[92] A. B. Kuklov and B. V. Svistunov. *Counterflow superfluidity of two-species ultracold atoms in a commensurate optical lattice*. Phys. Rev. Lett. **90**, 100401 (2003). (Cited on page **9**)

[93] J. J. García-Ripoll and J. I. Cirac. *Spin dynamics for bosons in an optical lattice*. New J. Phys. **5**, 76 (2003). (Cited on page **9**)

[94] L.-M. Duan, E. Demler, and M. D. Lukin. *Controlling spin exchange interactions of ultracold atoms in optical lattices*. Phys. Rev. Lett. **91**, 090402 (2003). (Cited on page **9**)

[95] E. Altman, W. Hofstetter, E. Demler, and M. D. Lukin. *Phase diagram of two-component bosons on an optical lattice*. New J. Phys. **5**, 113 (2003). (Cited on page **9**)

[96] P. N. Jepsen, W. W. Ho, J. Amato-Grill, I. Dimitrova, E. Demler, and W. Ketterle. *Transverse spin dynamics in the anisotropic Heisenberg model realized with ultracold atoms*. Phys. Rev. X **11**, 041054 (2021). (Cited on pages **9**, **81**, and **122**)

[97] M. T. DePue, C. McCormick, S. L. Winoto, S. Oliver, and D. S. Weiss. *Unity occupation of sites in a 3D optical lattice*. Phys. Rev. Lett. **82**, 2262–2265 (1999). (Cited on page **11**)

[98] P. M. Preiss, R. Ma, M. E. Tai, J. Simon, and M. Greiner. *Quantum gas microscopy with spin, atom-number, and multilayer readout*. Phys. Rev. A **91**, 041602 (2015). (Cited on page **11**)

[99] J. Koepsell, S. Hirthe, D. Bourgund, P. Sompet, J. Vijayan, G. Salomon, C. Gross, and I. Bloch. *Robust bilayer charge pumping for spin- and density-resolved quantum gas microscopy*. Phys. Rev. Lett. **125**, 010403 (2020). (Cited on page **11**)

[100] D. A. Steck. *Rubidium 87 D line data*. Rev. 1.6, steck.us/alkalidata (2003). (Cited on page **16**)

[101] C. Weitenberg. *Single-atom resolved imaging and manipulation in an atomic Mott insulator*. Ph.D. thesis, Ludwig-Maximilians-Universität München (2011). (Cited on pages **15**, **30**, and **31**)

[102] M. Endres. *Probing correlated quantum many-body systems at the single-particle level*. Ph.D. thesis, Ludwig-Maximilians-Universität München (2014). (Cited on pages **15**, **49**, and **50**)

[103] P. Schauss. *High-resolution imaging of ordering in Rydberg many-body systems*. Ph.D. thesis, Ludwig-Maximilians-Universität München (2014). (Cited on pages **15**, **18**, **20**, and **38**)

[104] S. Hild. *Microscopy of quantum many-body systems out of equilibrium*. Ph.D. thesis, Ludwig-Maximilians-Universität München (2016). (Cited on pages **15**, **37**, and **39**)

[105] J. Zeiher. *Realization of Rydberg-dressed quantum magnets*. Ph.D. thesis, Ludwig-Maximilians-Universität München (2017). (Cited on page **15**)

[106] A. Rubio Abadal. *Probing quantum thermalization and localization in Bose-Hubbard systems*. Ph.D. thesis, Ludwig-Maximilians-Universität München (2020). (Cited on page **15**)

[107] S. J. Hollerith. *A microscopically and vibrationally resolved study of Rydberg macrodimers*. Ph.D. thesis, Ludwig-Maximilians-Universität München (2022). (Cited on page **15**)

[108] A. La Rooij, C. Ulm, E. Haller, and S. Kuhr. *A comparative study of deconvolution techniques for quantum-gas microscope images*. New J. Phys. **25**, 083036 (2023). (Cited on page **18**)

[109] L. R. B. Picard, M. J. Mark, F. Ferlaino, and R. van Bijnen. *Deep learning-assisted classification of site-resolved quantum gas microscope images*. Meas. Sci. Technol. **31**, 025201 (2019). (Cited on page **18**)

[110] A. Impertro, J. F. Wienand, S. Häfele, H. von Raven, S. Hubele, T. Klostermann, C. R. Cabrera, I. Bloch, and M. Aidelsburger. *An unsupervised deep learning algorithm for single-site reconstruction in quantum gas microscopes*. Commun. Phys. **6**, 1–8 (2023). (Cited on pages **18** and **20**)

[111] D. Wei. *State reconstruction*. GitHub/david-wei (2023). (Cited on page **18**)

[112] D. Greif, M. F. Parsons, A. Mazurenko, C. S. Chiu, S. Blatt, F. Huber, G. Ji, and M. Greiner. *Site-resolved imaging of a fermionic Mott insulator*. Science **351**, 953–957 (2016). (Cited on page **18**)

[113] F. Nogrette, H. Labuhn, S. Ravets, D. Barredo, L. Béguin, A. Vernier, T. Lahaye, and A. Browaeys. *Single-atom trapping in holographic 2D arrays of microtraps with arbitrary geometries*. Phys. Rev. X **4**, 021034 (2014). (Cited on page **21**)

[114] G. Gauthier, I. Lenton, N. M. Parry, M. Baker, M. J. Davis, H. Rubinsztein-Dunlop, and T. W. Neely. *Direct imaging of a digital-micromirror device for configurable microscopic optical potentials*. Optica **3**, 1136–1143 (2016). (Cited on page **21**)

[115] R. W. Floyd and L. Steinberg. *An adaptive algorithm for spatial grayscale*. Proc. Soc. Inf. Disp. **17**, 75–77 (1976). (Cited on page **21**)

[116] D. Bellem. *Generation of spatially and temporally varying light potentials in optical lattices*. Master's thesis, Ludwig-Maximilians-Universität München (2011). (Cited on page **21**)

[117] D. Wei, A. Rubio-Abadal, B. Ye, F. Machado, J. Kemp, K. Srakaew, S. Hollerith, J. Rui, S. Gopalakrishnan, N. Y. Yao, I. Bloch, and J. Zeiher. *Quantum gas microscopy of Kardar-Parisi-Zhang superdiffusion*. Science **376**, 716–720 (2022). (Cited on pages **21**, **79**, and **81**)

[118] M. Egorov, B. Opanchuk, P. Drummond, B. V. Hall, P. Hannaford, and A. I. Sidorov. *Measurement of s-wave scattering lengths in a two-component Bose-Einstein condensate*. Phys. Rev. A **87**, 053614 (2013). (Cited on page **21**)

[119] A. Rubio-Abadal, J.-y. Choi, J. Zeiher, S. Hollerith, J. Rui, I. Bloch, and C. Gross. *Many-body delocalization in the presence of a quantum bath*. Phys. Rev. X **9**, 041014 (2019). (Cited on page **22**)

[120] C. S. Chiu, G. Ji, A. Mazurenko, D. Greif, and M. Greiner. *Quantum state engineering of a Hubbard system with ultracold fermions*. Phys. Rev. Lett. **120**, 243201 (2018). (Cited on pages **23**, **38**, and **116**)

[121] B. Yang, H. Sun, C.-J. Huang, H.-Y. Wang, Y. Deng, H.-N. Dai, Z.-S. Yuan, and J.-W. Pan. *Cooling and entangling ultracold atoms in optical lattices*. Science **369**, 550–553 (2020). (Cited on pages **23**, **38**, **92**, and **116**)

[122] D. Wei. *Development of a spatially incoherent laser source*. Master's thesis, Technische Universität München (2019). (Cited on page **23**)

[123] N. R. Cooper, J. Dalibard, and I. B. Spielman. *Topological bands for ultracold atoms*. Rev. Mod. Phys. **91**, 015005 (2019). (Cited on page **24**)

[124] D. Leykam, A. Andreanov, and S. Flach. *Artificial flat band systems: From lattice models to experiments*. Adv. Phys. X **3**, 1473052 (2018). (Cited on page **24**)

[125] L. Balents. *Spin liquids in frustrated magnets*. Nature **464**, 199–208 (2010). (Cited on page **24**)

[126] P. Windpassinger and K. Sengstock. *Engineering novel optical lattices*. Rep. Prog. Phys. **76**, 086401 (2013). (Cited on page **24**)

[127] X. Li and W. V. Liu. *Physics of higher orbital bands in optical lattices: A review*. Rep. Prog. Phys. **79**, 116401 (2016). (Cited on page **24**)

[128] R. Yamamoto, H. Ozawa, D. C. Nak, I. Nakamura, and T. Fukuhara. *Single-site-resolved imaging of ultracold atoms in a triangular optical lattice*. New J. Phys. **22**, 123028 (2020). (Cited on page **24**)

[129] J. Yang, L. Liu, J. Mongkolkiattichai, and P. Schauss. *Site-resolved imaging of ultracold fermions in a triangular-lattice quantum gas microscope*. PRX Quantum **2**, 020344 (2021). (Cited on page **24**)

[130] S. Taie, H. Ozawa, T. Ichinose, T. Nishio, S. Nakajima, and Y. Takahashi. *Coherent driving and freezing of bosonic matter wave in an optical Lieb lattice*. Sci. Adv. **1**, e1500854 (2015). (Cited on page **24**)

[131] D. Barredo, S. de Léséleuc, V. Lienhard, T. Lahaye, and A. Browaeys. *An atom-by-atom assembler of defect-free arbitrary two-dimensional atomic arrays*. Science **354**, 1021–1023 (2016). (Cited on page **24**)

[132] A. M. Kaufman, B. J. Lester, C. M. Reynolds, M. L. Wall, M. Foss-Feig, K. R. A. Hazzard, A. M. Rey, and C. A. Regal. *Two-particle quantum interference in tunnel-coupled optical tweezers*. Science **345**, 306–309 (2014). (Cited on page **24**)

[133] B. M. Spar, E. Guardado-Sanchez, S. Chi, Z. Z. Yan, and W. S. Bakr. *Realization of a Fermi-Hubbard optical tweezer array*. Phys. Rev. Lett. **128**, 223202 (2022). (Cited on page **24**)

[134] T. Chalopin. *Optical superlattices in quantum gas microscopy*. Nat. Rev. Phys. **3**, 605–605 (2021). (Cited on page **24**)

[135] M. Xu, L. H. Kendrick, A. Kale, Y. Gang, G. Ji, R. T. Scalettar, M. Lebrat, and M. Greiner. *Frustration- and doping-induced magnetism in a Fermi–Hubbard simulator*. Nature **620**, 971–976 (2023). (Cited on pages **24** and **26**)

[136] G. Di Domenico, N. Castagna, M. D. Plimmer, P. Thomann, A. V. Taichenachev, and V. I. Yudin. *On the stability of optical lattices*. Laser Phys. **15**, 1674 (2005). (Cited on pages **25** and **26**)

[137] J. Sebby-Strabley, M. Anderlini, P. S. Jessen, and J. V. Porto. *Lattice of double wells for manipulating pairs of cold atoms*. Phys. Rev. A **73**, 033605 (2006). (Cited on page **26**)

[138] K. Srakaew. Future Ph.D. thesis. (Cited on page **28**)

[139] O. Morsch and M. Oberthaler. *Dynamics of Bose-Einstein condensates in optical lattices*. Rev. Mod. Phys. **78**, 179–215 (2006). (Cited on page **35**)

[140] S. Friebel, C. D'Andrea, J. Walz, M. Weitz, and T. W. Hänsch. *CO_2-laser optical lattice with cold rubidium atoms*. Phys. Rev. A **57**, R20–R23 (1998). (Cited on page **35**)

[141] T. Hartmann, F. Keck, H. J. Korsch, and S. Mossmann. *Dynamics of Bloch oscillations*. New J. Phys. **6**, 2 (2004). (Cited on page **37**)

[142] S. D. Huber, E. Altman, H. P. Büchler, and G. Blatter. *Dynamical properties of ultracold bosons in an optical lattice*. Phys. Rev. B **75**, 085106 (2007). (Cited on page **41**)

[143] M. Łącki, B. Damski, and J. Zakrzewski. *Locating the quantum critical point of the Bose-Hubbard model through singularities of simple observables*. Sci. Rep. **6**, 38340 (2016). (Cited on page **41**)

[144] M. den Nijs and K. Rommelse. *Preroughening transitions in crystal surfaces and valence-bond phases in quantum spin chains*. Phys. Rev. B **40**, 4709–4734 (1989). (Cited on page **41**)

[145] T. Kennedy and H. Tasaki. *Hidden $Z_2 \times Z_2$ symmetry breaking in Haldane-gap antiferromagnets*. Phys. Rev. B **45**, 304–307 (1992). (Cited on page **41**)

[146] H. V. Kruis, I. P. McCulloch, Z. Nussinov, and J. Zaanen. *Geometry and topological order in the Luttinger liquid state*. Europhys. Lett. **65**, 512 (2004). (Cited on page **41**)

[147] F. D. M. Haldane. *Nonlinear field theory of large-spin Heisenberg antiferromagnets: Semiclassically quantized solitons of the one-dimensional easy-axis Néel state*. Phys. Rev. Lett. **50**, 1153–1156 (1983). (Cited on page **41**)

[148] C. Degli Esposti Boschi, A. Montorsi, and M. Roncaglia. *Brane parity orders in the insulating state of Hubbard ladders*. Phys. Rev. B **94**, 085119 (2016). (Cited on pages **41**, **49**, and **50**)

[149] C. K. Thomas, T. H. Barter, T.-H. Leung, M. Okano, G.-B. Jo, J. Guzman, I. Kimchi, A. Vishwanath, and D. M. Stamper-Kurn. *Mean-field scaling of the superfluid to Mott insulator transition in a 2D optical superlattice*. Phys. Rev. Lett. **119**, 100402 (2017). (Cited on pages **41** and **51**)

[150] K. V. Krutitsky. *Ultracold bosons with short-range interaction in regular optical lattices*. Phys. Rep. **607**, 1–101 (2016). (Cited on pages **42** and **43**)

[151] M. Rizzi, V. Cataudella, and R. Fazio. *Phase diagram of the Bose-Hubbard model with T_3 symmetry*. Phys. Rev. B **73**, 144511 (2006). (Cited on page **43**)

[152] B. Grygiel and K. Patucha. *Excitation spectra of strongly interacting bosons in the flat-band Lieb lattice*. Phys. Rev. B **106**, 224514 (2022). (Cited on page **43**)

[153] W. Jiang, M. Kang, H. Huang, H. Xu, T. Low, and F. Liu. *Topological band evolution between Lieb and kagome lattices*. Phys. Rev. B **99**, 125131 (2019). (Cited on page **43**)

[154] J. K. Freericks and H. Monien. *Strong-coupling expansions for the pure and disordered Bose-Hubbard model*. Phys. Rev. B **53**, 2691–2700 (1996). (Cited on page **45**)

[155] L. D. Landau and E. M. Lifshitz. *Statistical physics*. Elsevier (2013). ISBN 978-0-08-057046-4. (Cited on page **48**)

[156] F. Anfuso and A. Rosch. *Fragility of string orders*. Phys. Rev. B **76**, 085124 (2007). (Cited on page **48**)

[157] T. Senthil. *Symmetry-protected topological phases of quantum matter*. Annu. Rev. Condens. Matter Phys. **6**, 299–324 (2015). (Cited on page **48**)

[158] X.-G. Wen. *Colloquium: Zoo of quantum-topological phases of matter*. Rev. Mod. Phys. **89**, 041004 (2017). (Cited on page **48**)

[159] E. H. Kim, G. Fáth, J. Sólyom, and D. J. Scalapino. *Phase transitions between topologically distinct gapped phases in isotropic spin ladders*. Phys. Rev. B **62**, 14965–14974 (2000). (Cited on page **49**)

[160] E. G. Dalla Torre, E. Berg, and E. Altman. *Hidden order in 1D Bose insulators*. Phys. Rev. Lett. **97**, 260401 (2006). (Cited on page **49**)

[161] F. Anfuso and A. Rosch. *String order and adiabatic continuity of Haldane chains and band insulators*. Phys. Rev. B **75**, 144420 (2007). (Cited on page **49**)

[162] D. Pérez-García, M. M. Wolf, M. Sanz, F. Verstraete, and J. I. Cirac. *String order and symmetries in quantum spin lattices*. Phys. Rev. Lett. **100**, 167202 (2008). (Cited on page **49**)

[163] A. Montorsi and M. Roncaglia. *Nonlocal order parameters for the 1D Hubbard model*. Phys. Rev. Lett. **109**, 236404 (2012). (Cited on page **49**)

[164] F. Pollmann, E. Berg, A. M. Turner, and M. Oshikawa. *Symmetry protection of topological phases in one-dimensional quantum spin systems*. Phys. Rev. B **85**, 075125 (2012). (Cited on page **49**)

[165] S. de Léséleuc, V. Lienhard, P. Scholl, D. Barredo, S. Weber, N. Lang, H. P. Büchler, T. Lahaye, and A. Browaeys. *Observation of a symmetry-protected topological phase of interacting bosons with Rydberg atoms*. Science **365**, 775–780 (2019). (Cited on page **49**)

[166] S. Rachel, N. Laflorencie, H. F. Song, and K. Le Hur. *Detecting quantum critical points using bipartite fluctuations*. Phys. Rev. Lett. **108**, 116401 (2012). (Cited on page **50**)

[167] B. Capogrosso-Sansone, Ş. G. Söyler, N. Prokof'ev, and B. Svistunov. *Monte Carlo study of the two-dimensional Bose-Hubbard model*. Phys. Rev. A **77**, 015602 (2008). (Cited on page **51**)

[168] N. Teichmann, D. Hinrichs, and M. Holthaus. *Reference data for phase diagrams of triangular and hexagonal bosonic lattices*. Europhys. Lett. **91**, 10004 (2010). (Cited on page **51**)

[169] T. Tao. *E pluribus unum: From complexity, universality*. Daedalus **141**, 23–34 (2012). (Cited on page **57**)

[170] L. P. Kadanoff. *Scaling and universality in statistical physics*. Physica A **163**, 1–14 (1990). (Cited on page **57**)

[171] M. E. Fisher. *Renormalization group theory: Its basis and formulation in statistical physics*. Rev. Mod. Phys. **70**, 653–681 (1998). (Cited on page **57**)

[172] P. C. Hohenberg and B. I. Halperin. *Theory of dynamic critical phenomena*. Rev. Mod. Phys. **49**, 435–479 (1977). (Cited on pages **57** and **68**)

[173] G. Ódor. *Universality classes in nonequilibrium lattice systems*. Rev. Mod. Phys. **76**, 663–724 (2004). (Cited on pages **57** and **58**)

[174] M. Kardar, G. Parisi, and Y.-C. Zhang. *Dynamic scaling of growing interfaces*. Phys. Rev. Lett. **56**, 889–892 (1986). (Cited on page **57**)

[175] M. Hairer. *Solving the KPZ equation*. Ann. Math. **178**, 559–664 (2013). (Cited on page **57**)

[176] T. Sasamoto and H. Spohn. *One-dimensional Kardar-Parisi-Zhang equation: An exact solution and its universality*. Phys. Rev. Lett. **104**, 230602 (2010). (Cited on page **57**)

[177] G. Amir, I. Corwin, and J. Quastel. *Probability distribution of the free energy of the continuum directed random polymer in 1 + 1 dimensions*. Commun. Pure Appl. Math. **64**, 466–537 (2011). (Cited on page **57**)

[178] S. F. Edwards and D. R. Wilkinson. *The surface statistics of a granular aggregate*. Proc. R. Soc. A **381**, 17–31 (1982). (Cited on page **58**)

[179] T. Halpin-Healy and Y.-C. Zhang. *Kinetic roughening phenomena, stochastic growth, directed polymers and all that. Aspects of multidisciplinary statistical mechanics*. Phys. Rep. **254**, 215–414 (1995). (Cited on page **58**)

[180] I. Corwin. *The Kardar–Parisi–Zhang equation and universality class*. Random Matrices: Theory and Appl. (2012). (Cited on page **58**)

[181] T. Vicsek and F. Family. *Dynamic scaling for aggregation of clusters*. Phys. Rev. Lett. **52**, 1669–1672 (1984). (Cited on page **58**)

[182] F. Family and T. Vicsek. *Scaling of the active zone in the Eden process on percolation networks and the ballistic deposition model*. J. Phys. A **18**, L75 (1985). (Cited on page **58**)

[183] M. Prähofer. *Stochastic surface growth*. Ph.D. thesis, Technische Universität München (2003). (Cited on pages **58** and **59**)

[184] M. Prähofer and H. Spohn. *The scaling function g(y)*. www-m5.ma.tum.de/KPZ (2002). (Cited on page **59**)

[185] M. Prähofer and H. Spohn. *Exact scaling functions for one-dimensional stationary KPZ growth*. J. Stat. Phys. **115**, 255–279 (2004). (Cited on pages **59** and **60**)

[186] M. Prähofer and H. Spohn. *Universal distributions for growth processes in 1+1 dimensions and random matrices*. Phys. Rev. Lett. **84**, 4882–4885 (2000). (Cited on pages **59** and **91**)

[187] J. Quastel and D. Remenik. *Airy processes and variational problems*. Springer Proc. Math. Stat. **69**, 121–171 (2014). (Cited on page **59**)

[188] K. A. Takeuchi. *An appetizer to modern developments on the Kardar–Parisi–Zhang universality class*. Physica A **504**, 77–105 (2018). (Cited on page **59**)

[189] C. A. Tracy and H. Widom. *Level-spacing distributions and the Airy kernel*. Commun. Math. Phys. **159**, 151–174 (1994). (Cited on page **59**)

[190] J. Baik and E. M. Rains. *Limiting distributions for a polynuclear growth model with external sources*. J. Stat. Phys. **100**, 523–541 (2000). (Cited on page **59**)

[191] I. Corwin. *Kardar–Parisi–Zhang universality*. Not. Am. Math. Soc. **63**, 230–239 (2016). (Cited on page **59**)

[192] L. Miettinen, M. Myllys, J. Merikoski, and J. Timonen. *Experimental determination of KPZ height-fluctuation distributions*. Eur. Phys. J. B **46**, 55–60 (2005). (Cited on page **59**)

[193] K. A. Takeuchi and M. Sano. *Universal fluctuations of growing interfaces: Evidence in turbulent liquid crystals*. Phys. Rev. Lett. **104**, 230601 (2010). (Cited on page **59**)

[194] M. Kardar. *Replica Bethe ansatz studies of two-dimensional interfaces with quenched random impurities*. Nucl. Phys. B **290**, 582–602 (1987). (Cited on page **60**)

[195] T. Halpin-Healy. *Directed polymers versus directed percolation*. Phys. Rev. E **58**, R4096–R4099 (1998). (Cited on page **60**)

[196] J. Baik, P. Deift, and K. Johansson. *On the distribution of the length of the longest increasing subsequence of random permutations*. J. Am. Math. Soc. **12**, 1119–1178 (1999). (Cited on page **60**)

[197] K. Johansson. *Shape fluctuations and random matrices*. Comm. Math. Phys. **209**, 437–476 (2000). (Cited on page **60**)

[198] M. Prähofer and H. Spohn. *Scale invariance of the PNG droplet and the Airy process*. J. Stat. Phys. **108**, 1071–1106 (2002). (Cited on page **60**)

[199] G. Da Prato, A. Debussche, and R. Temam. *Stochastic Burgers' equation*. Nonlinear Differ. Equ. Appl. **1**, 389–402 (1994). (Cited on page **60**)

[200] L. Bertini and G. Giacomin. *Stochastic Burgers and KPZ equations from particle systems*. Comm. Math. Phys. **183**, 571–607 (1997). (Cited on page **60**)

[201] T. Chou, K. Mallick, and R. K. P. Zia. *Non-equilibrium statistical mechanics: From a paradigmatic model to biological transport*. Rep. Prog. Phys. **74**, 116601 (2011). (Cited on page **60**)

[202] J. de Gier, A. Schadschneider, J. Schmidt, and G. M. Schütz. *Kardar-Parisi-Zhang universality of the Nagel-Schreckenberg model*. Phys. Rev. E **100**, 052111 (2019). (Cited on page **60**)

[203] Q. Fontaine, D. Squizzato, F. Baboux, I. Amelio, A. Lemaître, M. Morassi, I. Sagnes, L. Le Gratiet, A. Harouri, M. Wouters, I. Carusotto, A. Amo, M. Richard, A. Minguzzi, L. Canet, S. Ravets, and J. Bloch. *Kardar–Parisi–Zhang universality in a one-dimensional polariton condensate*. Nature **608**, 687–691 (2022). (Cited on page **60**)

[204] A. Nahum, J. Ruhman, S. Vijay, and J. Haah. *Quantum entanglement growth under random unitary dynamics*. Phys. Rev. X **7**, 031016 (2017). (Cited on page **60**)

[205] H. Spohn. *Large scale dynamics of interacting particles*. Theoretical and Mathematical Physics. Springer, Berlin Heidelberg (1991). ISBN 978-3-642-84373-0. (Cited on page **60**)

[206] R. E. Wyatt. *Quantum dynamics with trajectories: Introduction to quantum hydrodynamics*. Interdisciplinary Applied Mathematics. Springer, New York (2005). ISBN 978-0-387-22964-5. (Cited on page **60**)

[207] G. Birkhoff. *Hydrodynamics*. Princeton University Press (2015). ISBN 978-1-4008-7777-5. (Cited on page **60**)

[208] B. Doyon. *Lecture notes on generalised hydrodynamics*. SciPost Phys. Lect. Notes **18** (2020). (Cited on pages **60** and **61**)

[209] J. De Nardis, B. Doyon, M. Medenjak, and M. Panfil. *Correlation functions and transport coefficients in generalised hydrodynamics*. J. Stat. Mech. **2022**, 014002 (2022). (Cited on pages **60** and **63**)

[210] B. Doyon and H. Spohn. *Drude weight for the Lieb-Liniger Bose gas*. SciPost Phys. **3**, 039 (2017). (Cited on pages **62** and **63**)

[211] B. Bertini, M. Collura, J. De Nardis, and M. Fagotti. *Transport in out-of-equilibrium XXZ chains: Exact profiles of charges and currents*. Phys. Rev. Lett. **117**, 207201 (2016). (Cited on page **62**)

[212] O. A. Castro-Alvaredo, B. Doyon, and T. Yoshimura. *Emergent hydrodynamics in integrable quantum systems out of equilibrium*. Phys. Rev. X **6**, 041065 (2016). (Cited on page **62**)

[213] H. Bethe. *Zur Theorie der Metalle*. Z. Physik **71**, 205–226 (1931). (Cited on pages **63** and **67**)

[214] V. B. Bulchandani, S. Gopalakrishnan, and E. Ilievski. *Superdiffusion in spin chains*. J. Stat. Mech. **2021**, 084001 (2021). (Cited on pages **63**, **67**, **69**, **70**, and **86**)

[215] M. Medenjak, J. De Nardis, and T. Yoshimura. *Diffusion from convection*. SciPost Physics **9**, 075 (2020). (Cited on page **63**)

[216] B. Bertini, F. Heidrich-Meisner, C. Karrasch, T. Prosen, R. Steinigeweg, and M. Žnidarič. *Finite-temperature transport in one-dimensional quantum lattice models*. Rev. Mod. Phys. **93**, 025003 (2021). (Cited on pages **65**, **67**, and **70**)

[217] S. Sachdev. *Quantum magnetism and criticality*. Nat. Phys. **4**, 173–185 (2008). (Cited on page **67**)

[218] M. Žnidarič. *Spin transport in a one-dimensional anisotropic Heisenberg model*. Phys. Rev. Lett. **106**, 220601 (2011). (Cited on page **67**)

[219] V. B. Bulchandani. *Kardar-Parisi-Zhang universality from soft gauge modes*. Phys. Rev. B **101**, 041411 (2020). (Cited on page **67**)

[220] Ž. Krajnik and T. Prosen. *Kardar–Parisi–Zhang physics in integrable rotationally symmetric dynamics on discrete space–time lattice*. J. Stat. Phys. **179**, 110–130 (2020). (Cited on pages **67**, **76**, and **85**)

[221] E. Ilievski, J. De Nardis, S. Gopalakrishnan, R. Vasseur, and B. Ware. *Superuniversality of superdiffusion*. Phys. Rev. X **11**, 031023 (2021). (Cited on pages **67**, **76**, and **85**)

[222] P. Lu, G. Müller, and M. Karbach. *Quasiparticles in the XXZ model*. Condens. Matter Phys. **12**, 381–398 (2009). (Cited on page **68**)

[223] T. Prosen and E. Ilievski. *Families of quasilocal conservation laws and quantum spin transport*. Phys. Rev. Lett. **111**, 057203 (2013). (Cited on page **68**)

[224] E. Ilievski and J. De Nardis. *Microscopic origin of ideal conductivity in integrable quantum models*. Phys. Rev. Lett. **119**, 020602 (2017). (Cited on page **68**)

[225] V. B. Bulchandani, R. Vasseur, C. Karrasch, and J. E. Moore. *Bethe-Boltzmann hydrodynamics and spin transport in the XXZ chain*. Phys. Rev. B **97**, 045407 (2018). (Cited on page **68**)

[226] M. Collura, A. De Luca, and J. Viti. *Analytic solution of the domain-wall nonequilibrium stationary state*. Phys. Rev. B **97**, 081111 (2018). (Cited on page **68**)

[227] E. Ilievski, J. De Nardis, M. Medenjak, and T. Prosen. *Superdiffusion in one-dimensional quantum lattice models*. Phys. Rev. Lett. **121**, 230602 (2018). (Cited on page **69**)

[228] S. Gopalakrishnan, R. Vasseur, and B. Ware. *Anomalous relaxation and the high-temperature structure factor of XXZ spin chains*. Proc. Natl. Acad. Sci. **116**, 16250–16255 (2019). (Cited on pages **69**, **70**, and **79**)

[229] M. K. Joshi, F. Kranzl, A. Schuckert, I. Lovas, C. Maier, R. Blatt, M. Knap, and C. F. Roos. *Observing emergent hydrodynamics in a long-range quantum magnet*. Science **376**, 720–724 (2022). (Cited on pages **71**, **87**, and **92**)

[230] P. N. Jepsen, J. Amato-Grill, I. Dimitrova, W. W. Ho, E. Demler, and W. Ketterle. *Spin transport in a tunable Heisenberg model realized with ultracold atoms*. Nature **588**, 403–407 (2020). (Cited on pages **71** and **81**)

[231] A. Scheie, N. E. Sherman, M. Dupont, S. E. Nagler, M. B. Stone, G. E. Granroth, J. E. Moore, and D. A. Tennant. *Detection of Kardar–Parisi–Zhang hydrodynamics in a quantum Heisenberg spin-1/2 chain*. Nat. Phys. **17**, 726–730 (2021). (Cited on page **71**)

[232] C. D. White, M. Zaletel, R. S. K. Mong, and G. Refael. *Quantum dynamics of thermalizing systems*. Phys. Rev. B **97**, 035127 (2018). (Cited on page **76**)

[233] B. Ye, F. Machado, C. D. White, R. S. K. Mong, and N. Y. Yao. *Emergent hydrodynamics in nonequilibrium quantum systems*. Phys. Rev. Lett. **125**, 030601 (2020). (Cited on page **76**)

[234] J. De Nardis, S. Gopalakrishnan, R. Vasseur, and B. Ware. *Stability of superdiffusion in nearly integrable spin chains*. Phys. Rev. Lett. **127**, 057201 (2021). (Cited on pages **77** and **86**)

[235] F. Weiner, P. Schmitteckert, S. Bera, and F. Evers. *High-temperature spin dynamics in the Heisenberg chain: Magnon propagation and emerging Kardar-Parisi-Zhang scaling in the zero-magnetization limit*. Phys. Rev. B **101**, 045115 (2020). (Cited on page **78**)

[236] G. Cecile, S. Gopalakrishnan, R. Vasseur, and J. De Nardis. *Hydrodynamic relaxation of spin helices*. Phys. Rev. B **108**, 075135 (2023). (Cited on page **83**)

[237] D. Gobert, C. Kollath, U. Schollwöck, and G. Schütz. *Real-time dynamics in spin-1/2 chains with adaptive time-dependent density matrix renormalization group*. Phys. Rev. E **71**, 036102 (2005). (Cited on page **84**)

[238] J. Mossel and J.-S. Caux. *Relaxation dynamics in the gapped XXZ spin-1/2 chain*. New J. Phys. **12**, 055028 (2010). (Cited on page **84**)

[239] G. Misguich, K. Mallick, and P. L. Krapivsky. *Dynamics of the spin-1/2 Heisenberg chain initialized in a domain-wall state*. Phys. Rev. B **96**, 195151 (2017). (Cited on page **84**)

[240] Ž. Krajnik, E. Ilievski, and T. Prosen. *Absence of normal fluctuations in an integrable magnet*. Phys. Rev. Lett. **128**, 090604 (2022). (Cited on pages **85** and **91**)

[241] B. Ye, F. Machado, J. Kemp, R. B. Hutson, and N. Y. Yao. *Universal Kardar-Parisi-Zhang dynamics in integrable quantum systems*. Phys. Rev. Lett. **129**, 230602 (2022). (Cited on page **85**)

[242] M. Mamaev, I. Kimchi, R. M. Nandkishore, and A. M. Rey. *Tunable-spin-model generation with spin-orbit-coupled fermions in optical lattices*. Phys. Rev. Res. **3**, 013178 (2021). (Cited on page **86**)

[243] H. Sun, B. Yang, H.-Y. Wang, Z.-Y. Zhou, G.-X. Su, H.-N. Dai, Z.-S. Yuan, and J.-W. Pan. *Realization of a bosonic antiferromagnet*. Nat. Phys. **17**, 990–994 (2021). (Cited on pages **86** and **122**)

[244] S. Krinner, T. Esslinger, and J.-P. Brantut. *Two-terminal transport measurements with cold atoms*. J. Phys.: Condens. Matter **29**, 343003 (2017). (Cited on page **87**)

[245] L. S. Levitov, H. Lee, and G. B. Lesovik. *Electron counting statistics and coherent states of electric current*. J. Math. Phys. **37**, 4845–4866 (1996). (Cited on page **88**)

[246] R. Samajdar, E. McCulloch, V. Khemani, R. Vasseur, and S. Gopalakrishnan. *Quantum turnstiles for robust measurement of full counting statistics*. arXiv:2305.15464 (2023). (Cited on page **88**)

[247] J. De Nardis, S. Gopalakrishnan, and R. Vasseur. *Non-linear fluctuating hydrodynamics for KPZ scaling in isotropic spin chains*. arXiv:2212.03696 (2023). (Cited on page **91**)

[248] S. Gopalakrishnan and R. Vasseur. *Superdiffusion from nonabelian symmetries in nearly integrable systems*. arXiv:2305.15463 (2023). (Cited on page **91**)

[249] E. Rosenberg, T. Andersen, R. Samajdar, A. Petukhov, J. Hoke, D. Abanin, A. Bengtsson, I. Drozdov, C. Erickson, P. Klimov, X. Mi, A. Morvan, M. Neeley, C. Neill, R. Acharya, I. Aleiner, R. Allen, K. Anderson, M. Ansmann, F. Arute, K. Arya, A. Asfaw, J. Atalaya, J. Bardin, A. Bilmes, G. Bortoli, A. Bourassa, J. Bovaird, L. Brill, M. Broughton, B. B. Buckley, D. Buell, T. Burger, B. Burkett, N. Bushnell, J. Campero, H.-S. Chang, Z. Chen, B. Chiaro, D. Chik, J. Cogan, R. Collins, P. Conner, W. Courtney, A. Crook, B. Curtin, D. Debroy, A. D. T. Barba, S. Demura, A. Di Paolo, A. Dunsworth, C. Earle, E. Farhi, R. Fatemi, V. Ferreira, L. Flores, E. Forati, A. Fowler, B. Foxen, G. Garcia, É. Genois, W. Giang, C. Gidney, D. Gilboa, M. Giustina, R. Gosula, A. G. Dau, J. Gross, S. Habegger, M. Hamilton, M. Hansen, M. Harrigan, S. Harrington, P. Heu, G. Hill, M. Hoffmann, S. Hong, T. Huang, A. Huff, W. Huggins, L. Ioffe, S. Isakov, J. Iveland, E. Jeffrey, Z. Jiang, C. Jones, P. Juhas, D. Kafri, T. Khattar, M. Khezri, M. Kieferová, S. Kim, A. Kitaev, A. Klots, A. Korotkov, F. Kostritsa, J. M. Kreikebaum, D. Landhuis, P. Laptev, K. M. Lau, L. Laws, J. Lee, K. Lee, Y. Lensky, B. Lester, A. Lill, W. Liu, W. P. Livingston, A. Locharla, S. Mandrà, O. Martin, S. Martin, J. McClean, M. McEwen, S. Meeks, K. Miao, A. Mieszala, S. Montazeri, R. Movassagh, W. Mruczkiewicz, A. Nersisyan, M. Newman, J. H. Ng, A. Nguyen, M. Nguyen, M. Niu, T. O'Brien, S. Omonije, A. Opremcak, R. Potter, L. Pryadko, C. Quintana, D. Rhodes, C. Rocque, N. Rubin, N. Saei, D. Sank, K. Sankaragomathi, K. Satzinger, H. Schurkus, C. Schuster, M. Shearn, A. Shorter, N. Shutty, V. Shvarts, V. Sivak, J. Skruzny, C. Smith, R. Somma, G. Sterling,

D. Strain, M. Szalay, D. Thor, A. Torres, G. Vidal, B. Villalonga, C. V. Heidweiller, T. White, B. Woo, C. Xing, J. Yao, P. Yeh, J. Yoo, G. Young, A. Zalcman, Y. Zhang, N. Zhu, N. Zobrist, H. Neven, R. Babbush, D. Bacon, S. Boixo, J. Hilton, E. Lucero, A. Megrant, J. Kelly, Y. Chen, V. Smelyanskiy, V. Khemani, S. Gopalakrishnan, T. Prosen, and P. Roushan. *Dynamics of magnetization at infinite temperature in a Heisenberg spin chain*. arXiv:2306.09333 (2023). (Cited on pages **91** and **92**)

[250] Ž. Krajnik, J. Schmidt, E. Ilievski, and T. Prosen. *Universal distributions of magnetization transfer in integrable spin chains*. arXiv:2303.16691 (2023). (Cited on page **91**)

[251] M. Fava, B. Ware, S. Gopalakrishnan, R. Vasseur, and S. A. Parameswaran. *Spin crossovers and superdiffusion in the one-dimensional Hubbard model*. Phys. Rev. B **102**, 115121 (2020). (Cited on page **92**)

[252] V. Eisler and Z. Rácz. *Full counting statistics in a propagating quantum front and random matrix spectra*. Phys. Rev. Lett. **110**, 060602 (2013). (Cited on page **92**)

[253] D. E. Chang, J. S. Douglas, A. González-Tudela, C.-L. Hung, and H. J. Kimble. *Colloquium: Quantum matter built from nanoscopic lattices of atoms and photons*. Rev. Mod. Phys. **90**, 031002 (2018). (Cited on page **95**)

[254] D. E. Chang, V. Vuletić, and M. D. Lukin. *Quantum nonlinear optics — photon by photon*. Nat. Photon. **8**, 685–694 (2014). (Cited on page **95**)

[255] S. J. van Enk and H. J. Kimble. *Strongly focused light beams interacting with single atoms in free space*. Phys. Rev. A **63**, 023809 (2001). (Cited on page **95**)

[256] M. K. Tey, Z. Chen, S. A. Aljunid, B. Chng, F. Huber, G. Maslennikov, and C. Kurtsiefer. *Strong interaction between light and a single trapped atom without the need for a cavity*. Nat. Phys. **4**, 924–927 (2008). (Cited on page **95**)

[257] A. Reiserer and G. Rempe. *Cavity-based quantum networks with single atoms and optical photons*. Rev. Mod. Phys. **87**, 1379–1418 (2015). (Cited on page **95**)

[258] D. Porras and J. I. Cirac. *Collective generation of quantum states of light by entangled atoms*. Phys. Rev. A **78**, 053816 (2008). (Cited on pages **95**, **100**, and **105**)

[259] S. D. Jenkins and J. Ruostekoski. *Controlled manipulation of light by cooperative response of atoms in an optical lattice*. Phys. Rev. A **86**, 031602 (2012). (Cited on page **95**)

[260] R. J. Bettles, S. A. Gardiner, and C. S. Adams. *Enhanced optical cross section via collective coupling of atomic dipoles in a 2D array*. Phys. Rev. Lett. **116**, 103602 (2016). (Cited on pages **95**, **100**, and **105**)

[261] E. Shahmoon, D. S. Wild, M. D. Lukin, and S. F. Yelin. *Cooperative resonances in light scattering from two-dimensional atomic arrays*. Phys. Rev. Lett. **118**, 113601 (2017). (Cited on pages **95**, **99**, **100**, **102**, **105**, **116**, and **118**)

[262] R. H. Dicke. *Coherence in spontaneous radiation processes*. Phys. Rev. **93**, 99–110 (1954). (Cited on page **95**)

[263] M. O. Scully and A. A. Svidzinsky. *The super of superradiance*. Science **325**, 1510–1511 (2009). (Cited on page **95**)

[264] K. Cong, Q. Zhang, Y. Wang, G. T. Noe, A. Belyanin, and J. Kono. *Dicke superradiance in solids*. J. Opt. Soc. Am. B **33**, C80–C101 (2016). (Cited on page **95**)

[265] G. Ferioli, A. Glicenstein, L. Henriet, I. Ferrier-Barbut, and A. Browaeys. *Storage and release of subradiant excitations in a dense atomic cloud*. Phys. Rev. X **11**, 021031 (2021). (Cited on page **96**)

[266] P. Solano, P. Barberis-Blostein, F. K. Fatemi, L. A. Orozco, and S. L. Rolston. *Superradiance reveals infinite-range dipole interactions through a nanofiber*. Nat. Commun. **8**, 1–7 (2017). (Cited on page **96**)

[267] C. Liedl, S. Pucher, F. Tebbenjohanns, P. Schneeweiss, and A. Rauschenbeutel. *Collective radiation of a cascaded quantum system: From timed Dicke states to inverted ensembles*. Phys. Rev. Lett. **130**, 163602 (2023). (Cited on page **96**)

[268] M. Gross and S. Haroche. *Superradiance: An essay on the theory of collective spontaneous emission*. Phys. Rep. **93**, 301–396 (1982). (Cited on page **96**)

[269] S. J. Masson and A. Asenjo-Garcia. *Universality of Dicke superradiance in arrays of quantum emitters*. Nat. Commun. **13**, 2285 (2022). (Cited on pages **96** and **124**)

[270] S. L. Bromley, B. Zhu, M. Bishof, X. Zhang, T. Bothwell, J. Schachenmayer, T. L. Nicholson, R. Kaiser, S. F. Yelin, M. D. Lukin, A. M. Rey, and J. Ye. *Collective atomic scattering and motional effects in a dense coherent medium*. Nat. Commun. **7**, 11039 (2016). (Cited on page **96**)

[271] R. G. DeVoe and R. G. Brewer. *Observation of superradiant and subradiant spontaneous emission of two trapped ions*. Phys. Rev. Lett. **76**, 2049–2052 (1996). (Cited on pages **97** and **106**)

[272] A. Goban, C.-L. Hung, J. D. Hood, S.-P. Yu, J. A. Muniz, O. Painter, and H. J. Kimble. *Superradiance for atoms trapped along a photonic crystal waveguide*. Phys. Rev. Lett. **115**, 063601 (2015). (Cited on page **97**)

[273] M. O. Araújo, I. Krešić, R. Kaiser, and W. Guerin. *Superradiance in a large and dilute cloud of cold atoms in the linear-optics regime*. Phys. Rev. Lett. **117**, 073002 (2016). (Cited on page **97**)

[274] T. S. do Espirito Santo, P. Weiss, A. Cipris, R. Kaiser, W. Guerin, R. Bachelard, and J. Schachenmayer. *Collective excitation dynamics of a cold atom cloud*. Phys. Rev. A **101**, 013617 (2020). (Cited on page **97**)

[275] J. Pellegrino, R. Bourgain, S. Jennewein, Y. R. P. Sortais, A. Browaeys, S. D. Jenkins, and J. Ruostekoski. *Observation of suppression of light scattering induced by dipole-dipole interactions in a cold-atom ensemble*. Phys. Rev. Lett. **113**, 133602 (2014). (Cited on page **97**)

[276] S. Jennewein, M. Besbes, N. J. Schilder, S. D. Jenkins, C. Sauvan, J. Ruostekoski, J.-J. Greffet, Y. R. P. Sortais, and A. Browaeys. *Coherent scattering of near-resonant light by a dense microscopic cold atomic cloud*. Phys. Rev. Lett. **116**, 233601 (2016). (Cited on page **97**)

[277] S. J. Roof, K. J. Kemp, M. D. Havey, and I. M. Sokolov. *Observation of single-photon superradiance and the cooperative Lamb shift in an extended sample of cold atoms*. Phys. Rev. Lett. **117**, 073003 (2016). (Cited on page **97**)

[278] J. Keaveney, A. Sargsyan, U. Krohn, I. G. Hughes, D. Sarkisyan, and C. S. Adams. *Cooperative Lamb shift in an atomic vapor layer of nanometer thickness*. Phys. Rev. Lett. **108**, 173601 (2012). (Cited on page **97**)

[279] A. F. van Loo, A. Fedorov, K. Lalumière, B. C. Sanders, A. Blais, and A. Wallraff. *Photon-mediated interactions between distant artificial atoms*. Science **342**, 1494–1496 (2013). (Cited on pages **97** and **106**)

[280] Z. Meir, O. Schwartz, E. Shahmoon, D. Oron, and R. Ozeri. *Cooperative Lamb shift in a mesoscopic atomic array*. Phys. Rev. Lett. **113**, 193002 (2014). (Cited on page **97**)

[281] R. H. Lehmberg. *Radiation from an N-atom system. I. General formalism*. Phys. Rev. A **2**, 883–888 (1970). (Cited on page **97**)

[282] J. Ruostekoski and J. Javanainen. *Quantum field theory of cooperative atom response: Low light intensity*. Phys. Rev. A **55**, 513–526 (1997). (Cited on page **97**)

[283] L. Novotny and B. Hecht. *Principles of nano-optics*. Cambridge University Press (2006). ISBN 978-1-139-45205-2. (Cited on page **98**)

[284] T. Caneva, M. T. Manzoni, T. Shi, J. S. Douglas, J. I. Cirac, and D. E. Chang. *Quantum dynamics of propagating photons with strong interactions: A generalized input–output formalism*. New J. Phys. **17**, 113001 (2015). (Cited on page **98**)

[285] R. Bettles. *Cooperative interactions in lattices of atomic dipoles*. Ph.D. thesis, Durham University (2017). (Cited on pages **98** and **99**)

[286] A. Asenjo-Garcia, J. D. Hood, D. E. Chang, and H. J. Kimble. *Atom-light interactions in quasi-one-dimensional nanostructures: A Green's-function perspective*. Phys. Rev. A **95**, 033818 (2017). (Cited on page **98**)

[287] R. J. Bettles, S. A. Gardiner, and C. S. Adams. *Cooperative eigenmodes and scattering in one-dimensional atomic arrays*. Phys. Rev. A **94**, 043844 (2016). (Cited on page **100**)

[288] C. Noh and D. G. Angelakis. *Quantum simulations and many-body physics with light*. Rep. Prog. Phys. **80**, 016401 (2016). (Cited on page **101**)

[289] G. Facchinetti, S. D. Jenkins, and J. Ruostekoski. *Storing light with subradiant correlations in arrays of atoms*. Phys. Rev. Lett. **117**, 243601 (2016). (Cited on page **101**)

[290] M. T. Manzoni, M. Moreno-Cardoner, A. Asenjo-Garcia, J. V. Porto, A. V. Gorshkov, and D. E. Chang. *Optimization of photon storage fidelity in ordered atomic arrays*. New J. Phys. **20**, 083048 (2018). (Cited on pages **101** and **124**)

[291] Y. Solomons, R. Ben-Maimon, and E. Shahmoon. *Universal approach for quantum interfaces with atomic arrays*. arXiv:2302.04913 (2023). (Cited on pages **103**, **105**, and **123**)

[292] R. Bekenstein, I. Pikovski, H. Pichler, E. Shahmoon, S. F. Yelin, and M. D. Lukin. *Quantum metasurfaces with atom arrays*. Nat. Phys. **16**, 676–681 (2020). (Cited on pages **103**, **105**, **119**, and **123**)

[293] A. V. Kildishev, A. Boltasseva, and V. M. Shalaev. *Planar photonics with metasurfaces*. Science **339**, 1232009 (2013). (Cited on page **105**)

[294] N. Yu and F. Capasso. *Flat optics with designer metasurfaces*. Nat. Mater. **13**, 139–150 (2014). (Cited on page **105**)

[295] J. Perczel, J. Borregaard, D. E. Chang, H. Pichler, S. F. Yelin, P. Zoller, and M. D. Lukin. *Topological quantum optics in two-dimensional atomic arrays*. Phys. Rev. Lett. **119**, 023603 (2017). (Cited on pages **105** and **124**)

[296] M. Moreno-Cardoner, D. Goncalves, and D. E. Chang. *Quantum nonlinear optics based on two-dimensional Rydberg atom arrays*. Phys. Rev. Lett. **127**, 263602 (2021). (Cited on pages **105** and **119**)

[297] S. D. Jenkins and J. Ruostekoski. *Metamaterial transparency induced by cooperative electromagnetic interactions*. Phys. Rev. Lett. **111**, 147401 (2013). (Cited on page **105**)

[298] P. Back, S. Zeytinoglu, A. Ijaz, M. Kroner, and A. Imamoğlu. *Realization of an electrically tunable narrow-bandwidth atomically thin mirror using monolayer $MoSe_2$*. Phys. Rev. Lett. **120**, 037401 (2018). (Cited on page **105**)

[299] G. Scuri, Y. Zhou, A. A. High, D. S. Wild, C. Shu, K. De Greve, L. A. Jauregui, T. Taniguchi, K. Watanabe, P. Kim, M. D. Lukin, and H. Park. *Large excitonic reflectivity of monolayer $MoSe_2$ encapsulated in hexagonal boron nitride*. Phys. Rev. Lett. **120**, 037402 (2018). (Cited on page **105**)

[300] N. V. Corzo, B. Gouraud, A. Chandra, A. Goban, A. S. Sheremet, D. V. Kupriyanov, and J. Laurat. *Large Bragg reflection from one-dimensional chains of trapped atoms near a nanoscale waveguide*. Phys. Rev. Lett. **117**, 133603 (2016). (Cited on page **106**)

[301] H. L. Sørensen, J.-B. Béguin, K. W. Kluge, I. Iakoupov, A. S. Sørensen, J. H. Müller, E. S. Polzik, and J. Appel. *Coherent backscattering of light off one-dimensional atomic strings*. Phys. Rev. Lett. **117**, 133604 (2016). (Cited on page **106**)

[302] M. Mirhosseini, E. Kim, X. Zhang, A. Sipahigil, P. B. Dieterle, A. J. Keller, A. Asenjo-Garcia, D. E. Chang, and O. Painter. *Cavity quantum electrodynamics with atom-like mirrors*. Nature **569**, 692–697 (2019). (Cited on page **106**)

[303] S. D. Jenkins, J. Ruostekoski, N. Papasimakis, S. Savo, and N. I. Zheludev. *Many-body subradiant excitations in metamaterial arrays: Experiment and theory*. Phys. Rev. Lett. **119**, 053901 (2017). (Cited on page **106**)

[304] P. Török, P. R. T. Munro, and E. E. Kriezis. *High numerical aperture vectorial imaging in coherent optical microscopes*. Opt. Express **16**, 507–523 (2008). (Cited on page **109**)

[305] M. Ben Dahan, E. Peik, J. Reichel, Y. Castin, and C. Salomon. *Bloch oscillations of atoms in an optical potential*. Phys. Rev. Lett. **76**, 4508–4511 (1996). (Cited on page **112**)

[306] F. Andreoli, M. J. Gullans, A. A. High, A. Browaeys, and D. E. Chang. *Maximum refractive index of an atomic medium*. Phys. Rev. X **11**, 011026 (2021). (Cited on page **113**)

[307] N. Schine, A. W. Young, W. J. Eckner, M. J. Martin, and A. M. Kaufman. *Long-lived Bell states in an array of optical clock qubits*. Nat. Phys. **18**, 1067–1073 (2022). (Cited on pages **116** and **123**)

[308] F. Robicheaux and S. Huang. *Atom recoil during coherent light scattering from many atoms*. Phys. Rev. A **99**, 013410 (2019). (Cited on page **117**)

[309] E. Shahmoon, M. D. Lukin, and S. F. Yelin. *Quantum optomechanics of a two-dimensional atomic array*. Phys. Rev. A **101**, 063833 (2020). (Cited on page **117**)

[310] D. A. Suresh and F. Robicheaux. *Photon-induced atom recoil in collectively interacting planar arrays*. Phys. Rev. A **103**, 043722 (2021). (Cited on page **117**)

[311] J. Ye, H. J. Kimble, and H. Katori. *Quantum state engineering and precision metrology using state-insensitive light traps*. Science **320**, 1734–1738 (2008). (Cited on page **118**)

[312] B. Arora, M. S. Safronova, and C. W. Clark. *Magic wavelengths for the np-ns transitions in alkali-metal atoms*. Phys. Rev. A **76**, 052509 (2007). (Cited on page **118**)

[313] R. J. Bettles, M. D. Lee, S. A. Gardiner, and J. Ruostekoski. *Quantum and nonlinear effects in light transmitted through planar atomic arrays*. Commun. Phys. **3**, 1–9 (2020). (Cited on page **119**)

[314] D. Petrosyan, J. Otterbach, and M. Fleischhauer. *Electromagnetically induced transparency with Rydberg atoms*. Phys. Rev. Lett. **107**, 213601 (2011). (Cited on page **119**)

[315] K. Srakaew, P. Weckesser, S. Hollerith, D. Wei, D. Adler, I. Bloch, and J. Zeiher. *A subwavelength atomic array switched by a single Rydberg atom*. Nat. Phys. **19**, 714–719 (2023). (Cited on pages **119** and **123**)

[316] S. Wessel, F. Alet, M. Troyer, and G. G. Batrouni. *Quantum Monte Carlo simulations of confined bosonic atoms in optical lattices*. Phys. Rev. A **70**, 053615 (2004). (Cited on page **122**)

[317] S. Flannigan and A. J. Daley. *Enhanced repulsively bound atom pairs in topological optical lattice ladders*. Quantum Sci. Technol. **5**, 045017 (2020). (Cited on page **122**)

[318] S. Flannigan, L. Madail, R. G. Dias, and A. J. Daley. *Hubbard models and state preparation in an optical Lieb lattice*. New J. Phys. **23**, 083014 (2021). (Cited on page **122**)

[319] A. Eckardt, C. Weiss, and M. Holthaus. *Superfluid-insulator transition in a periodically driven optical lattice*. Phys. Rev. Lett. **95**, 260404 (2005). (Cited on page **122**)

[320] S. D. Huber and E. Altman. *Bose condensation in flat bands*. Phys. Rev. B **82**, 184502 (2010). (Cited on page **122**)

[321] Y.-Z. You, Z. Chen, X.-Q. Sun, and H. Zhai. *Superfluidity of bosons in kagome lattices with frustration*. Phys. Rev. Lett. **109**, 265302 (2012). (Cited on page **122**)

[322] G. Ji, M. Xu, L. H. Kendrick, C. S. Chiu, J. C. Brüggenjürgen, D. Greif, A. Bohrdt, F. Grusdt, E. Demler, M. Lebrat, and M. Greiner. *Coupling a mobile hole to an antiferromagnetic spin background: Transient dynamics of a magnetic polaron*. Phys. Rev. X **11**, 021022 (2021). (Cited on page **122**)

[323] M. Kanász-Nagy, I. Lovas, F. Grusdt, D. Greif, M. Greiner, and E. A. Demler. *Quantum correlations at infinite temperature: The dynamical Nagaoka effect*. Phys. Rev. B **96**, 014303 (2017). (Cited on page **122**)

[324] S.-S. Zhang, W. Zhu, and C. D. Batista. *Pairing from strong repulsion in triangular lattice Hubbard model*. Phys. Rev. B **97**, 140507 (2018). (Cited on page **122**)

[325] I. Morera, A. Bohrdt, W. W. Ho, and E. Demler. *Attraction from frustration in ladder systems*. arXiv:2106.09600 (2021). (Cited on page **122**)

[326] S. Braun, J. P. Ronzheimer, M. Schreiber, S. S. Hodgman, T. Rom, I. Bloch, and U. Schneider. *Negative absolute temperature for motional degrees of freedom*. Science **339**, 52–55 (2013). (Cited on page **122**)

[327] S. Yunoki and S. Sorella. *Two spin liquid phases in the spatially anisotropic triangular Heisenberg model*. Phys. Rev. B **74**, 014408 (2006). (Cited on page **122**)

[328] S. Yan, D. A. Huse, and S. R. White. *Spin-liquid ground state of the S = 1/2 kagome Heisenberg antiferromagnet*. Science **332**, 1173–1176 (2011). (Cited on page **122**)

[329] D. Yamamoto, T. Fukuhara, and I. Danshita. *Frustrated quantum magnetism with Bose gases in triangular optical lattices at negative absolute temperatures*. Commun. Phys. **3**, 1–10 (2020). (Cited on page **122**)

[330] J. F. Rodriguez-Nieva, A. Piñeiro Orioli, and J. Marino. *Far-from-equilibrium universality in the two-dimensional Heisenberg model*. Proc. Natl. Acad. Sci. **119**, e2122599119 (2022). (Cited on page **122**)

[331] K. D. Nelson, X. Li, and D. S. Weiss. *Imaging single atoms in a three-dimensional array*. Nat. Phys. **3**, 556–560 (2007). (Cited on page **123**)

[332] M. Rispoli, A. Lukin, R. Schittko, S. Kim, M. E. Tai, J. Léonard, and M. Greiner. *Quantum critical behaviour at the many-body localization transition*. Nature **573**, 385–389 (2019). (Cited on page **123**)

[333] J. F. Wienand, S. Karch, A. Impertro, C. Schweizer, E. McCulloch, R. Vasseur, S. Gopalakrishnan, M. Aidelsburger, and I. Bloch. *Emergence of fluctuating hydrodynamics in chaotic quantum systems*. arXiv:2306.11457 (2023). (Cited on page **123**)

[334] J. Choi, A. L. Shaw, I. S. Madjarov, X. Xie, R. Finkelstein, J. P. Covey, J. S. Cotler, D. K. Mark, H.-Y. Huang, A. Kale, H. Pichler, F. G. S. L. Brandão, S. Choi, and M. Endres. *Preparing random states and benchmarking with many-body quantum chaos*. Nature **613**, 468–473 (2023). (Cited on page **123**)

[335] S. J. Masson and A. Asenjo-Garcia. *Atomic-waveguide quantum electrodynamics*. Phys. Rev. Res. **2**, 043213 (2020). (Cited on page **123**)

[336] P.-O. Guimond, A. Grankin, D. V. Vasilyev, B. Vermersch, and P. Zoller. *Subradiant Bell states in distant atomic arrays*. Phys. Rev. Lett. **122**, 093601 (2019). (Cited on page **123**)

[337] O. Černotík, A. Dantan, and C. Genes. *Cavity quantum electrodynamics with frequency-dependent reflectors*. Phys. Rev. Lett. **122**, 243601 (2019). (Cited on page **123**)

[338] P. Schauß, J. Zeiher, T. Fukuhara, S. Hild, M. Cheneau, T. Macrì, T. Pohl, I. Bloch, and C. Gross. *Crystallization in Ising quantum magnets*. Science **347**, 1455–1458 (2015). (Cited on page **123**)

[339] D. Plankensteiner, L. Ostermann, H. Ritsch, and C. Genes. *Selective protected state preparation of coupled dissipative quantum emitters*. Sci. Rep. **5**, 16231 (2015). (Cited on page **124**)

[340] Y. He, L. Ji, Y. Wang, L. Qiu, J. Zhao, Y. Ma, X. Huang, S. Wu, and D. E. Chang. *Geometric control of collective spontaneous emission*. Phys. Rev. Lett. **125**, 213602 (2020). (Cited on page **124**)

[341] C. C. Rusconi, T. Shi, and J. I. Cirac. *Exploiting the photonic nonlinearity of free-space subwavelength arrays of atoms*. Phys. Rev. A **104**, 033718 (2021). (Cited on page **124**)

[342] F. Shah, T. L. Patti, O. Rubies-Bigorda, and S. F. Yelin. *Quantum computing with subwavelength atomic arrays*. arXiv:2306.08555 (2023). (Cited on page **124**)

[343] R. J. Bettles, J. Minář, C. S. Adams, I. Lesanovsky, and B. Olmos. *Topological properties of a dense atomic lattice gas*. Phys. Rev. A **96**, 041603 (2017). (Cited on page **124**)

[344] L. Henriet, J. S. Douglas, D. E. Chang, and A. Albrecht. *Critical open-system dynamics in a one-dimensional optical-lattice clock*. Phys. Rev. A **99**, 023802 (2019). (Cited on page **124**)

List of figures

List of tables

List of abbreviations

0D zero-dimensional. 106
1D one-dimensional. 3, 6, 10, 25–30, 33, 34, 36, 41, 45, 48, 49, 57, 60, 67, 71–74, 76–78, 80–82, 85, 86, 89, 90, 92, 105, 106, 112, 121, 122
2D two-dimensional. 3, 15, 17, 24–27, 30, 36, 37, 41, 45, 47, 49, 53, 71, 73, 76, 77, 80, 86, 90, 100, 101, 103, 105, 106, 109, 111–113, 115, 119, 121–123
3D three-dimensional. 10, 15, 105, 109

AM amplitude-modulation. 33, 36, 37, 74
AOM acousto-optical modulator. 28, 30, 31
ASEP asymmetric exclusion process. 60

BCS Bardeen–Cooper–Schrieffer. 1
BEC Bose–Einstein condensate. 1, 7, 17
BH Bose–Hubbard. 3, 5–9, 12, 31, 35, 36, 38, 41–43, 45, 46, 49, 52, 53, 74, 81, 84, 85, 92, 121, 122
BP brane parity. 41, 49–53, 121
BR Baik–Rains. 58, 59, 90, 91

CDT crossed dipole trap. 16

DMD digital micromirror device. 21–23, 32–35, 37–40, 46, 72, 73, 77, 78, 82, 84
DN diagonal-neighbor. 28, 47
DOF degree of freedom. 2, 21, 23, 25–27, 31, 77, 109, 122
DSF dynamical structure factor. 63–65, 71, 74–76, 85, 87, 89, 92
DW domain wall. 64, 65, 67, 69, 71–82, 84–86, 88–92, 121, 122

EIT electromagnetically induced transparency. 119, 123
EM electromagnetic. 8, 10–12, 96–100, 102, 103, 111, 112, 118, 119, 123
EMCCD electron-multiplying charge-coupled device. 18, 22, 106–108, 115

FCS full counting statistics. 3, 11, 87, 88, 91, 92, 121, 123
FH Fermi–Hubbard. 71, 92
FWHM full width at half maximum. 23

GE Gibbs ensemble. 61, 62
GGE generalized Gibbs ensemble. 61
GHD generalized hydrodynamics. 3, 60–63, 67, 68, 70, 76, 79, 81, 83, 86
GOE Gaussian orthogonal ensemble. 58, 59, 90, 91
GUE Gaussian unitary ensemble. 58, 59, 90–92

HFS hyperfine state. 11, 12, 16, 21–23, 39, 102, 113
HWP half-wave plate. 22, 29, 30

KPZ Kardar–Parisi–Zhang. 3, 57–60, 62, 64, 67, 71, 75, 77, 85–92, 121

L1 Lattice 1. 28–30, 32, 33, 35, 46, 73, 74, 82
L2 Lattice 2. 28–30, 32, 33, 35, 36, 46, 73, 74
L3 Lattice 3. 22, 29–31, 36, 38, 45, 106, 111, 112
LDA local-density approximation. 8, 11, 62

MF mean-field. 41–45, 48, 51
MI Mott insulator. 1, 3, 7, 8, 17, 23, 30, 31, 36, 38, 41, 42, 45–53, 72, 76, 77, 81, 88, 92, 106, 111–113, 116, 121, 123
MOPA master oscillator power amplifier. 16
MOT magneto-optical trap. 15
MW microwave. 2, 12, 15–17, 21, 23, 35, 38–40, 72, 73, 77, 81, 82, 84, 96, 106, 113

NA numerical aperture. 18, 34, 35, 109, 115–117
NN nearest-neighbor. 6, 8, 28, 34, 42, 46, 47, 50, 53, 68, 72

PBS polarizing beam splitter. 29, 30
PCF photonic-crystal fiber. 28, 30
PDE partial differential equation. 57
PSF point spread function. 19, 20, 34, 35

QED quantum electrodynamics. 97, 100, 123
QGM quantum gas microscope. 2, 3, 5, 11, 45, 53, 75, 76, 85, 87, 106, 121
QPT quantum phase transition. 1, 3, 7, 41, 53, 122

QWP quarter-wave plate. 22, 72

ROI region of interest. 19, 20, 46, 49–51

SD standard deviation. 33, 38, 80, 90, 106–108, 111, 113, 116, 118
SEM standard error of the mean. 47, 48, 51, 52, 108
SF superfluid. 1, 7, 8, 17, 36, 38, 41–45, 47–52, 77, 121
SLM spatial light modulator. 12, 21, 119
SNR signal-to-noise ratio. 19, 51, 52, 71, 74, 81, 87, 88, 108, 115

TW Tracy–Widom. 58, 59, 90–92

w.l.o.g. without loss of generality. 24, 25

XXX isotropic Heisenberg. 3, 10, 60, 67, 70–72, 76, 77, 79, 81, 83–87, 89–91, 121, 122
XXZ Heisenberg. 3, 8–12, 67, 68, 71

Acknowledgements

Throughout the years, I have been blessed to be surrounded by a dedicated, knowledgeable and supportive group of people, without whom this work would not have been possible.

First, I would like to thank my supervisor, Immanuel Bloch, for the opportunity to pursue my Ph.D. at the *Single Atoms* experiment. His passion for many areas of physics and guidance towards the most interesting scientific directions were crucial to the findings of this thesis. I also appreciate him for the possibility of attending conferences, ensuring that the needs of the labs were always met and, generally, for fostering a great working environment in the group.

I would further like to thank Johannes Zeiher as direct supervisor during large parts of my Ph.D. His steady encouragement and optimism were a driving force behind trying new ideas and for overcoming challenges. With an extensive physical understanding and knowledge of the setup, paired with an openness for detailed discussions, his support played a key role. I would also like to thank Christian Groß, who led the lab in the beginning of the Ph.D., for my start in the group as a master's student and for his pragmatic advice on any physical or technical matters I faced.

I am most grateful for having the daily opportunity to work with the team of the *Single Atoms* lab. In particular, I would like to thank Antonio Rubio Abadal, who introduced me to working in a laser lab and navigating the group, spent countless hours explaining and discussing the physics both specific to our setup as well as its general context, and reliably had solutions to problems arising in the lab. I thoroughly enjoyed working with him on the spin superdiffusion project, which benefitted greatly from his physical and experimental insights. I would also like to thank Simon Hollerith, who was working on the Rydberg side of the experiment, for being highly supportive in the lab and always interested in discussing the latest results. His unwavering enthusiasm and commitment were a steady motivation to further our physical understanding. I am very fortunate to have also worked with Jun Rui, who introduced me to operating and modifying the main experiment, as well as assessing the measurement results. It was a great time working on the subradiant mirror project together, through which I learned and benefitted much from his focussed thought process and expansive knowledge of atomic physics.

During most of my Ph.D., I had the pleasure of having Kritsana Srakaew as lab partner, who joined shortly after I started and whose technical expertise and high motivation was invaluable when rebuilding the lattices for the system size upgrade.

I am particularly grateful for his unconditional support, for always seeing the most pragmatic approach in the lab, and for many inspiring but grounded physical and technical discussions. At the middle of my Ph.D., we were joined by Daniel Adler as a Ph.D. student and Pascal Weckesser as a postdoc. I highly appreciated the opportunity to work with Daniel on the tunable lattice project, which benefitted greatly from his technical adeptness and comprehensive attention to detail. I thank Pascal particularly for the insightful, supportive and motivating physics discussions, for helping structuring my thoughts and giving valuable feedback. I would also like to thank Suchita Agrawal, who started as the newest Ph.D. student towards the end of my Ph.D., for stimulating questions and discussions. I hope they will enjoy their time at MPQ and wish them all the best for the upcoming projects. In addition, I would like to acknowledge our master's students and interns, Simon Evered, Martin Link, Pierre Cussenot, Sarah Rößle and Anwei Zhu, for advancing the technology in our lab, for many discussions, and for sharing my journey in the *Single Atoms* lab.

I would also like to extend my thanks to our theory collaborators on the spin superdiffusion project. I thank Norman Yao, Bingtian Ye, Francisco Machado and Jack Kemp for introducing us to this interesting problem, performing extensive calculations and guiding our experimental efforts. Moreover, I am grateful to them and to Sarang Gopalakrishnan, for the support in interpreting the results.

I am also thankful to Anton Mayer for his suggestions and help in designing and producing the mechanical systems for the lattice upgrades. In addition, I would like to thank Karsten Förster for his efforts in designing various electronic systems, particularly his support in minimizing laser noise, and Olivia Mödl for helping to fix faulty devices on short notice. I would furthermore like to thank Kristina Schuldt, Doreen Seidl, Veronika Seidl and Ildiko Kecskesi for their overall administrative support and for organizing memorable group events.

A big thanks also goes out to the many other incredibly supportive group members, who are the core of what makes the group and MPQ such a unique place. I deeply appreciate the countless discussions about physics and beyond, and thank them for exchanging inspiring ideas, technical know-how and useful laboratory equipment. With the great progress in the existing experiments and the many new projects starting up, I am excitedly looking forward to their future findings.

Last but not least, I would like to say a special thanks to my family for the constant support throughout my studies and Ph.D.

Thank you!